ÉCOLE POLYTECHNIQUE
ParisTech

Laboratoire de Physique des Interfaces
et des Couches Minces

CNRS
dépasser les frontières

Thèse présentée pour obtenir le grade de
DOCTEUR DE L'ÉCOLE POLYTECHNIQUE
Spécialité : Physique des Plasmas

par
Laurent Kroely
laurent.kroely@polytechnique.edu

Process and material challenges in the high rate deposition of microcrystalline silicon thin films and solar cells by Matrix Distributed Electron Cyclotron Resonance plasma

Soutenue le 28 septembre 2010 devant le jury composé de :

Christophe Ballif	*Examinateur et président du jury*
Yvonnick Durand	*Invité*
Jean-Paul Kleider	*Rapporteur*
Patrick Leempoel	*Examinateur*
Françoise Massines	*Rapporteur*
Pere Roca i Cabarrocas	*Directeur de thèse*
Rutger Schlatmann	*Examinateur*
Marc Vermeersch	*Examinateur*

Table of contents

Table of contents

Introduction

The main goal of the fast-growing thin film photovoltaic (PV) industry is the reduction of the production costs. Solutions to fulfill this requirement are the increase of the panel efficiencies and sizes, and the improvement of the throughputs. For the latter issue, the deposition rate of the different layers of the modules is a key parameter.

The Laboratory of Physics of Interfaces and Thin Films (LPICM : Laboratoire de Physique des Interfaces et des Couches Minces), on the campus of the École Polytechnique, is a major actor of the development of photovoltaic research in France since many years. One of its axes of research since 2003 is the use of Matrix Distributed Electron Cyclotron Resonance (MDECR) plasma sources for the high rate deposition of amorphous and microcrystalline silicon solar cells.

The first PhD on this topic, from 2003 to 2007, was focused on amorphous cells and this work was then dedicated to microcrystalline cells.

It took place in the frame of a national project called ATOS (Association Tandem Optimisées pour le Solaire) about the development of $10\,\text{cm} \times 10\,\text{cm}$ tandem modules deposited at high rate. Three research laboratories (LPICM, LGEP : the Laboratory of Electrical Engineering of Paris, and LAAS : the Laboratory of Analysis and Architecture of Systems) and three industrial partners (Saint Gobain Recherche, Total Gas & Power and Solems) were collaborating in this project selected in 2005 for the solar PV program of the National Agency for Research (ANR : Agence Nationale de la Recherche). The project started in December 2005 and lasted three years, until November 2008, with a total budget of more than 3 million euros.

This manuscript is divided in four chapters :

Chapter I will introduce the readers to our field of research and in particular, give a historical overview of the various technologies which have been developed to reach high deposition rates. This review will help us to better understand the extremely restricting requirements for the fast deposition of high efficiency microcrystalline silicon cells on large areas.

Chapter II will present some of the main characterization techniques that have been used during this work. This chapter will therefore be a "toolbox" for the rest of our study.

Chapter III is about the MDECR technology. A brief historical review will show the evolution of the different types of ECR sources and underline the advantages of the recent MDECR technique over the previous ones. The two plasma reactors used during this work will be described in detail.

Chapter IV is the core of this work and is divided in four parts. The first two parts are general points about the microcrystalline silicon material and the microcrystalline silicon solar cells respectively. The third part corresponds to the various parametric scans we carried out to analyze the impact of the different deposition parameters on the material properties and on the solar cell characteristics. These initial studies allowed us to optimize the material quality. Finally, the fourth part will list all the investigations we performed to rule out or solve the potential limitations of our material and cell quality.

The results are then summarized in the conclusion, and perspectives of future work are given.

The steps of this doctoral work can be summed up as follows :

From plasmas . . .

After my Master in Plasma Physics, one of the first tasks of my PhD was to assemble a new MDECR reactor. To have the opportunity to assemble such a complex equipment gives a very deep understanding of the associated technological issues and it is very rewarding to work with it afterwards. Furthermore, this equipment was non-commercial, had been custom-designed by the technical team of our laboratory in order to meet the specific requirements of our application.

. . . to materials . . .

The MDECR configuration allows to couple a very high level of electrical power to the plasma and thus, is a very efficient solution to increase the deposition rate for amorphous or microcrystalline silicon films. Great efforts were then dedicated to monitor and characterize the material quality. In this perspective, a lot of characterization techniques have been implemented during this work. Indeed, we found out that such a strategy of multiple characterizations is an absolute necessity and is the best approach to optimize such a complex material.

. . . to solar cells

Finally, the deposition conditions leading to interesting material properties have been selected to grow the intrinsic layer of p-i-n devices. For this, the different layers, interfaces and processing steps have been studied and improved, and various structures and substrate types have been used.

We will try to emphasize this very unique *global* approach throughout this manuscript.

Notations :

In this manuscript, hydrogenated microcrystalline silicon will be abbreviated μc-Si:H or simply μc-Si. Similarly, the symbol for hydrogenated amorphous silicon will be a-Si:H or simply a-Si. *All* the materials analyzed during this work were hydrogenated.

Also, the non-intentionally doped materials are called intrinsic throughout the manuscript although this is a misuse of language as the deposited amorphous and microcrystalline silicon layers are always slightly n-doped.

Chapter I

Context : High rate deposition of microcrystalline silicon films and solar cells

Contents

1   Introduction

High rate deposition of microcrystalline silicon (µc-Si) is a key research topic in both laboratories and companies. Indeed, due to the low absorption coefficient of this material, layers of more than $1\,\mu m$ are needed to absorb efficiently the red part of the sun spectrum. Therefore, high deposition rates (R_d) are required to have deposition times suitable for industrial production, especially in the case of in-line manufacturing of tandem modules, for which the front amorphous cell is only $\sim 0.3\,\mu m$ thick or even less. Obviously, greater deposition rates also mean greater throughputs and as a result, reduced costs.

To overcome the challenge of fast growth of microcrystalline silicon, many solutions have been proposed.

Different methods of deposition have been tried, the two main ones being Hot Wire Chemical Vapor Deposition (HW-CVD) and Plasma Enhanced Chemical Vapor Deposition (PE-CVD). In the latter category, many types of plasma sources have been tried : Radio-Frequency and Very High Frequency Capacitively Coupled Plasmas (RF-CCP and VHF-CCP), Expanding Thermal Plasmas (ETP), high density and low pressure plasmas like Inductively Coupled Plasmas (ICP), Surface Wave Plasmas (SWP), Electron Cyclotron Resonance plasmas (ECR) and other microwave plasmas.

This review will only focus on low-temperature methods (i.e. $< 600\,°C$ in order to be compatible with glass substrates). Other methods to obtain microcrystalline silicon exist but are too slow or unsuitable for industrial low-cost mass production of solar cells, e.g. because they require high temperatures. One can cite laser annealing of amorphous silicon (a-Si), thermal annealing of a-Si in an oven at $\sim 600\,°C$, nickel catalyzed crystallization of a-Si and the Layer-By-Layer (LBL) technique. The last technique consists in a repeated cycle of deposition of a thin amorphous layer which is then exposed to a hydrogen plasma to crystallize it.

Then, microcrystalline silicon can be obtained from various feed gases, like silane (SiH_4), disilane (Si_2H_6), gases containing chlorine such as silicon tetrachloride ($SiCl_4$) or dichlorosilane (SiH_2Cl_2) and gases containing fluorine such as silicon tetrafluoride (SiF_4), SiH_2F_2, SiH_3F. The presence of fluorine results in an electronegative plasma with interesting properties (such as nanocrystal formation [1]) and is known to enhance the etching of the amorphous phase and to result in films of higher quality (thinner amorphous incubation layer and larger grains). All these gases can be diluted in H_2, Ar or He for example. Other gases can be added in order to obtain doped layers : phosphine (PH_3) for n-doped layers and tri-methyl-boron ($B(CH_3)_3$) or diborane (B_2H_6) for p-doped layers. Adapting the gas mixture can help to promote the deposition rate : e.g. by adding helium [2], argon or SiH_2Cl_2.

We will report on the performance of microcrystalline (µc) cells and also of tandem cells associating a front amorphous cell with a back microcrystalline cell. Indeed, since efficiencies as high as the best µc-Si cells (i.e. slightly over $10\,\%$) can be reached by stabilized a-Si cells, which are less expensive to deposit, the commercial future of µc-Si lies in tandem junctions made at high rate [3].

The cell effiencies cited here for the different techniques are only given as examples. One has to keep in mind that light trapping (i.e. the front surface roughness, anti-reflection coatings and the back reflector) is a crucial issue in µc cells. The thicknesses or sizes of the cells may also vary from one group/article to another.

The goal of this section is not to make an exhaustive historical review of high rate deposition of microcrystalline silicon but rather to illustrate the challenges of this field with the results of some of the leading research groups and companies in the world. This section also aims at emphasizing the strong difference between achieving a high deposition rate and obtaining a high efficiency microcrystalline solar cell at high rate. Indeed, even if the optical, structural and electrical properties of the material measured by several diagnostics seem to be of device-grade quality, it does not guarantee that a cell made with it will show good characteristics. As a result, there are many papers proposing solutions to achieve high deposition rates and much less actually achieving good performance for the corresponding cells.

2   Hot Wire Chemical Vapor Deposition (HW-CVD)

The basic principle of this method is that a metal filament is heated up to typically $1500\,°C -$ $2000\,°C$ in order to thermally dissociate the silane gas. It is usually said that there are no ions created but Nong-Moon Hwang *et al.* have evidenced the presence of charged particles [4] and have emphasized their potential role in the crystallization. In any case, the ion bombardment of this technique, if any, is much lower than in the other methods. To increase R_d in this technique, the silane flow, the filament temperature, the filament-substrate distance and the number of filaments seem to be key parameters.

Good µc solar cells can be obtained at low R_d. Example 1 : $6.6\,\%$ at $5\,\text{Å/s}$, which was the world record in 2003 for an all-HWCVD cell (i.e. intrinsic layer as well as doped layers made by HWCVD) [5]. Example 2 : $9.4\,\%$ demonstrated in 2002 (V_{oc} of $600\,mV$, substrate temperature of $\sim 185\,°C$ and $R_d < 1\,\text{Å/s}$) [6]. Deposition rates as high as $\sim 60\,\text{Å/s}$ have been demonstrated with a reasonable crystalline fraction of $\sim 30\,\%$ estimated by Raman spectroscopy [7] but the solar cells at $R_d > 10\,\text{Å/s}$ seem to have quite low performance so far (e.g. $2.8\,\%$ at $15\,\text{Å/s}$ in [7] and $4.4\,\%$ at $13\,\text{Å/s}$ in [8] where they used four filaments in order to enhance R_d).

An explanation proposed to interpret the limitations of the material grown by HWCVD is that it has a too low density in absence of ion bombardment. Indeed, it is generally accepted that a flux of ions with moderate impact energies helps to densify the growing film. The other main challenges of this method are : the large area non-uniformity, the contamination of the films by tungsten, the periodic replacement of the wires and the possibility of degradation of the film quality due to overheating by the radiation of the filament.

This overview will be focusing on PE-CVD as it was the method used during this work.

3   Plasma Enhanced Chemical Vapor Deposition (PE-CVD)

3.1   Radio-Frequency Capacitively Coupled Plasmas (RF-CCP)

Capacitively Coupled Plasmas (CCP) are plasma sources with a very simple geometry : they consist in two parallel plane electrodes. The most common ones use an alternative electric field in the Radio-Frequency (RF) range ($13.56\,MHz$ being the standard).

The usual pressures of a few hundreds of mTorr lead to very low deposition rates : typically $1-2\,\text{Å/s}$. To overcome this limit, a new regime of process conditions has been explored.

The High Pressure Depletion regime (HPD)

To increase the deposition rate, one needs to increase the (RF or VHF) power in order to promote the dissociation of the injected silane molecules. But doing so, the sheath voltage drop increases and as a result, the enhanced impact energy of the ions leads to a poor quality material, due to too high defect densities. In order to lower the ion bombardment energy, the operating pressure has to be increased : typically in the $1-10\,\text{Torr}$ range. The collisions

in the sheath will thus avoid energetic ion impacts. This new deposition regime has been called "High Pressure Depletion".

Working at higher pressures seems to be quite universally helpful as it has been successfully implemented by several research groups in RF-CCP discharges and in VHF-CCP ones (see 3.2 below) as well as in industrial-type reactors (e.g. results of Oerlikon Solar in [9]). Although empirically validated and widely accepted, a detailed theoretical explanation is probably still lacking. One can summarize the usual consensus on the requirements for fast growth of µc-Si as follows :

- favoring the formation of SiH_3 radicals which have a long diffusion length at the surface of the growing film,
- keeping a high atomic hydrogen flux to passivate the surface,
- avoiding too energetic ion bombardment,
- preventing the short lifetime radicals from reaching the surface because they form high defect density materials,
- avoiding the formation of higher radicals and powders.

The success of the HPD conditions is said to be due to the fact that when the silane molecules are very efficiently dissociated, the annihilation reaction $SiH_4 + H \rightarrow SiH_3 + H_2$ is avoided. This reaction reduces the atomic hydrogen concentration and can be responsible for the apparition of an amorphous phase.

Following is a short list of achievements :

As early as in 1998, it allowed to demonstrate deposition rates approaching $10\,\text{Å/s}$: e.g. $9.3\,\text{Å/s}$ obtained in [10] by increasing the pressure to $4\,\text{Torr}$ (at $350\,°C$) in order to fulfill the above-mentioned requirements.

In 2001, a 6.2% cell prepared at $9\,\text{Å/s}$ at temperatures lower than $200\,°C$ was obtained in the Institute of Photovoltaics in Jülich in Germany [11] by varying the pressure between 1 and $8\,\text{Torr}$. At a slightly lower $R_d = 6\,\text{Å/s}$, they also obtained a 7.1% single junction and an initial 11.1% a-Si:H/µc-Si:H tandem junction.

In 2003, the National Institute for Advanced Industrial Science and Technology (AIST) in Tsukuba in Japan used the HPD regime with a mesh in order to further reduce the ion damages [12]. They could deposit crystallized materials at almost $60\,\text{Å/s}$ and they processed an 8.1% cell at $12\,\text{Å/s}$.

In 2006, the Jülich group optimized their process at high pressure and high power density (excitation frequency of $40.68\,\text{MHz}$) to deposit cells at $10\,\text{Å/s}$ with 9.2% efficiencies, the ones at $20\,\text{Å/s}$ still showing 7.9% efficiencies. Then, in collaboration with the manufacturer Applied Films [13], they upscaled their deposition method in a $\sim 1\,\text{m}^2$ commercial equipment (excitation frequency of $13.56\,\text{MHz}$) and obtained a $30 \times 30\,\text{cm}^2$ tandem module at 10% (initial) at a rate close to $5\,\text{Å/s}$.

The best efficiency with this technique in our laboratory is 8.3% at $3\,\text{Å/s}$ from a mixture of Ar, H_2 and SiF_4 at $2.7\,\text{Torr}$ and with an RF power density of $0.44\,\text{W/cm}^2$ [14].

Although they are not giving a lot of informations about their PECVD technology and their growth rates, one can also cite here the noteworthy results of the Kaneka Corporation. In 1999, they reported the first microcrystalline cell above 10% : $\eta = 10.1\%$ processed at a

temperature of less than $550\,^\circ$C [15]. In 2002, they reached $14.1\,\%$ initial efficiency for an a-Si/intermediate transparent layer/µc-Si tandem cell of $1\,\mathrm{cm^2}$ and an average initial efficiency of $11.2\,\%$ for $91 \times 46\,\mathrm{cm^2}$ modules [16]. With this know-how, commercial production of these "micromorph" (also called "hybrid") modules was started as early as in April 2001.

3.2   Very High Frequency Capacitively Coupled Plasmas (VHF-CCP)

For these Capacitively Coupled Plasmas, the excitation frequency to sustain the discharge is typically ranging from $27\,\mathrm{MHz}$ to $300\,\mathrm{MHz}$. These higher frequencies result in a better coupling of the power with the bulk of the plasma and thus, lead to greater electron densities and higher dissociation of the SiH_4 molecules. Also, increasing the frequency decreases the sheath thickness and consequently, the ion energy. A "softer" ion bombardment seems to favor the growth of device-grade µc-Si.

Historically, the VHF technique has been the one allowing to obtain the first entirely microcrystalline solar cell with a high efficiency : This result has been published in 1994 by the Institute of Microtechnology (IMT) of the University of Neuchâtel in Switzerland [17]. They used a frequency of $70\,\mathrm{MHz}$ and obtained a $4.6\,\%$ cell at $1\,\mathrm{\mathring{A}/s}$.

Only 10 years later, Mitsubishi Heavy Industries (see [18]) published some very promising results with this deposition method. For a small surface of $5\,\mathrm{cm^2}$, they could manufacture $8.8\,\%$ µc single junction cells at $25\,\mathrm{\mathring{A}/s}$. Then, they managed to overcome the problem of non-uniformity on larger scales (i.e. when the wavelength of excitation becomes comparable to the dimension of the electrodes) with a specific ladder-shaped electrode, with phase-modulation methods and with a higher process pressure. With these solutions, they obtained tandem modules of $40 \times 50\,\mathrm{cm^2}$ with initial efficiencies as high as $11.1\,\%$ (estimated to go down to $9.8\,\%$ when stable) for which the µc-Si layer was deposited at $21\,\mathrm{\mathring{A}/s}$. They explain the high quality of their material by the properties of the VHF plasmas, i.e. high density, low electron temperature and low ion energy.

The High Pressure Depletion regime (HPD)

The so-called High Pressure Depletion (HPD) regime is also valid for VHF plasmas. The pressures are then typically ranging from 7 to $10\,\mathrm{Torr}$ instead of the usual $\sim 0.3\,\mathrm{Torr}$.

For example, in 2003, the AIST group reported efficiencies of $8.2\,\%$ at $21\,\mathrm{\mathring{A}/s}$ ($7\,\mathrm{Torr}$) and $7.9\,\%$ at $30\,\mathrm{\mathring{A}/s}$ ($8\,\mathrm{Torr}$) at $70-100\,\mathrm{MHz}$ [19]. But problems of inhomogeneity appeared when extended to greater areas.

At $10\,\mathrm{Torr}$, the same group has developed a new design of cathode with interconnected multi-holes which generate high density plasma spots (due to electron confinement by the electrode pattern). The resulting deposition rates were as high as $76\text{-}79\,\mathrm{\mathring{A}/s}$ with defect densities of $4-6\times10^{15}\,\mathrm{cm^{-3}}$ ([20] in 2004 and [21] in 2007). But to our knowledge, no cell result has been reported for this deposition technique.

In 2008, impressive results were published by Sobajima *et al.* of the Osaka University : Their VHF ($100\,\mathrm{MHz}$) reactor had already allowed them to deposit $9\,\%$ cells at $3.8\,\mathrm{\mathring{A}/s}$. By further increasing the power and keeping a very high pressure of $24\,\mathrm{Torr}$ (total gas flow of $800\,\mathrm{sccm}$), they demonstrated a cell of $6.30\,\%$ at $81\,\mathrm{\mathring{A}/s}$ [22].

3.3   Expanding Thermal Plasmas (ETP)

Also called plasma jets, this type of source consists of a thermal plasma expanding in a low pressure deposition chamber (at typically several hundred mTorr). The thermal plasma is created in a small tube or nozzle at high pressure (at several tens to more than one thousand Torr) : it can be an RF discharge or a DC cascaded arc. The vector gas (argon and/or hydrogen) then reacts with silane injected in the low pressure chamber. It is estimated that the main radicals reaching the substrate are SiH_3 and that the deposition process is basically ion free.

This type of plasma source has been successfully applied to high rate deposition of µc-Si. The deposition conditions were optimized at the Eindhoven University of Technology in the Netherlands to reach up to $37 \, \text{Å/s}$ [23] with a high temperature of $300 \, °C$. The material obtained with this type of plasma source seems to show many similarities with ours. They deposited cells at $2.1 \, \text{Å/s}$ at $T_{substrate} = 250 \, °C$ at $152 - 380 \, \text{mTorr}$ with a resulting $1.9 \, \%$ performance. At a higher rate of $\sim 13 \, \text{Å/s}$ and with a corrected temperature of $300 \, °C$, they obtained a $1.1 \, \%$ cell.

We can also cite the impressive results of Chae *et al.* [24] who have reached deposition rates of $10 \, 000 \, \text{Å/s}$ in 2001 with a DC-RF hybrid ETP source ! Their huge deposition rate is said to be obtained from clusters of around $1 \, \text{nm}$ size. But they mention that the substrate temperature rises from the room temperature to $700 \, °C$ within 30 seconds and do not give cell results. More recent publications could not be found.

3.4   The microwave plasmas

They use an electric field at even higher frequencies, $2.45 \, \text{GHz}$ being the standard one. This mode of excitation allows to couple very high level of electrical power to the plasma and thus, results in high density plasmas. As a consequence of an enhanced dissociation, it is a common result that microwave (MW) plasmas allow to obtain crystallized materials at lower hydrogen dilutions than in the standard RF-CCP reactors [25], or even from pure silane.

3.4.1   Without magnetic field

The group of Hajime Shirai from the Saitama University uses an innovative design of MW reactor : the microwave power is injected with a spoke antenna and no magnetic field is used. The typical operating pressure is $\sim 80 \, \text{mTorr}$. Deposition rates as high as $65 \, \text{Å/s}$ were achieved [25]. The ellipsometric spectra of such films are fitted with a crystalline fraction of $65 \, \%$ but have a low maximum of the imaginary part of the pseudo-dielectric function (~ 10.5) and a too high void fraction in the bulk layer ($\sim 20 \, \%$). This original type of source has been first described in 1998 [26] and deposition rates higher than $5 \, \text{Å/s}$ were demonstrated in this first paper. The performances of the cells reported later are quite low : $4.5 \, \%$ at $13 \, \text{Å/s}$ in 2003 [27], then $2.8 \, \%$ (due to a low Fill Factor of 0.35) at $\sim 30 \, \text{Å/s}$ in 2006 [28]. In 2010, a new gas mixture of SiH_2Cl_2 and H_2 was studied and seemed to lead to better material properties but the cell efficiencies stayed below $0.6 \, \%$ at $15 \, \text{Å/s}$ [29].

Recently, Jia *et al.* from the AIST developed a microwave discharge which allowed them to reach an impressive growth rate of $7 \, 000 \, \text{Å/s}$ [30]. But this discharge is a very particular one : they deposit on a $0.3 \, \text{mm}$ diameter quartz fiber in a very small chamber. The working

gas is a mixture of SiH_4 (30 sccm) and He operated at 2 Torr, without any substrate heating and with a microwave power of 120 W. Their geometry is obviously not adapted to the production of solar cells, but it is a noteworthy result as it still demonstrates that it is possible to crystallize the material very fast (although this may be specific to the high gas temperature of $500-1000\,°C$).

More industrially relevant are the results of United Solar Ovonic Corporation in collaboration with the National Renewable Energy Laboratory (NREL) in a three-year project (2001–2004) [31]. They could reach R_d as high as $20-30\,\text{Å/s}$ and did n-i-p cells with a µc n-doped layer on stainless steel substrates. They could reach a 4.9 % active-area efficiency at $\sim 30\,\text{Å/s}$ (J_{sc} of $15.8\,\text{mA/cm}^2$, V_{oc} of 480 mV, FF of 65 %) and 7.2 % for a tandem cell (J_{sc} of $8.5\,\text{mA/cm}^2$, V_{oc} of 1.32 V, FF of 64 %) [32]. Although they do not say in detail what their microwave source is, it is still worth listing these results as they are among the best µc cells obtained from a microwave plasma published.

3.4.2   Electron Cyclotron Resonance plasmas (ECR)

The most common geometry consists in injecting the microwaves by a wave-guide through a dielectric window in a cylindrical chamber surrounded by electromagnets. The axial magnetic field provides a magnetic confinement and the microwave power is absorbed in the resonant region where the electron cyclotron frequency (defined as $\omega_e = q_e B/m_e$ where q_e is the elementary charge, B is the magnetic field intensity and m_e is the electron mass) matches the MW frequency (more explanations can be found on pages 58 to 59).

The electrons heated in the resonant zone are dissociating the silane molecules which are then diffusing to the substrate. With the so-called remote configuration, the ion energy can be independently controlled by biasing the substrate holder.

Despite the high dissociation levels achievable with the ECR concept, only few deposition rates and solar cell results have been reported [33].

Dalal *et al.* from the Microelectronics Research Center of the Iowa State University obtained growth rates of $\sim 3\,\text{Å/s}$ and up to $10\,\text{Å/s}$ in the case of a dilution in helium. They obtained n-i-p amorphous cells on stainless steel of 6.8 % in 1998 [34]. For microcrystalline cells, they published an efficiency of 5.7 % in 2000 [35], but their n-i-p cell was illuminated through chromium contacts with a transmission of only 20 % and the correction for this is not clear. They obtained a 4.7 % cell in 2003 [2]. It was an n-i-p structure deposited at a rate of $\sim 3\,\text{Å/s}$ on stainless steel with amorphous buffer layers at the n-i and i-p interfaces. The size of the ITO contact is not given. Its characteristics were a V_{oc} of 480 mV, a fill factor of 70 % and a current density of $14\,\text{mA/cm}^2$ (without light trapping or back reflector ; with a very low response in the red). Their deposition conditions were a pressure of 5 mTorr, a microwave power of only ~ 200 W, a temperature of $275-325\,°C$ and a mixture of H_2 and SiH_4. The former is introduced near the ECR zones while the latter is injected close to the substrate holder.

4   Conclusion

As a conclusion, we would like to emphasize once again the striking difference between being able to deposit a microcrystalline film on glass at high rate and making a high efficiency device with this material incorporated as the intrinsic layer. Many articles stop after the first step and the characterization of their material by a few diagnostics, and do not publish results about the corresponding solar cells.

This review only focused on the most well-known techniques and for a wider list of methods, the reader can check the very complete article by J. K. Rath of 2003 [33].

A wide range of reactors based on different principles of plasma generation have been empirically developed and improved in the last fifteen years. It seems that only very few solutions have been found to address the numerous issues specific to the growth of microcrystalline silicon at high rate and uniformly on large areas. The most successful and mature technologies seem to be the RF and VHF CCP reactors, when used in the so-called High Pressure Depletion process conditions. Similarly, we can notice that only a few research groups and industrial companies throughout the world fulfilled these goals. This underlines the difficulty of the task but also, the opportunities of major furture breakthroughs for new emerging technological solutions, e.g. innovative geometries for the electrodes could be promising candidates.

To our knowledge, the best microcrystalline cell obtained from an ECR plasma source published has an efficiency of **4.7 %** (see detailed description above and in [2]).

Matrix Distributed Electron Cyclotron Resonance (MDECR) is the technique explored in this study.

Bibliography

[1] S. Kasouit, J. Damon-Lacoste, R. Vanderhaghen, and P. Roca i Cabarrocas. Contribution of plasma generated nanocrystals to the growth of microcrystalline silicon thin films. *Journal of Non-Crystalline Solids*, 338-340:86–90, June 2004.

[2] V.L. Dalal, J.H. Zhu, M. Welsh, and M. Noack. Microcrystalline Si:H solar cells fabricated using ECR plasma deposition. *IEE Proceedings – Circuits, Devices and Systems*, 150(4), August 2003.

[3] Jef Poortmans and Vladimir Arkhipov, editors. *Thin Film Solar Cells : Fabrication, Characterization and Applications.* Wiley, 2006.

[4] Sung-Soo Lee, Min-Sung Ko, Chan-Soo Kim, and Nong-Moon Hwang. Gas phase nucleation of crystalline silicon and their role in low-temperature deposition of microcrystalline films during hot-wire chemical vapor deposition. *Journal of Crystal Growth*, 310(15):3659 – 3662, 2008.

[5] E. Iwaniczko, Y. Xu, R. E. I. Schropp, and A. H. Mahan. Microcrystalline silicon for solar cells deposited at high rates by hot-wire CVD. *Thin Solid Films*, 430(1-2):212 – 215, 2003. Proceedings of the Second International Conference on Cat-CVD (Hot Wire CVD) Process.

[6] Stefan Klein, Friedhelm Finger, Reinhard Carius, and Jan Lossen. Improved deposition rates for µc-si:h at low substrate temperature. *Thin Solid Films*, 501(1-2):43 – 46, 2006. Proceedings of the Third International Conference on Hot-Wire CVD (Cat-CVD) Process.

[7] Y. Ide, Y. Saito, A. Yamada, and M. Konagai. Microcrystalline silicon thin film solar cells prepared by hot wire cell method. In *Photovoltaic Energy Conversion, 2003. Proceedings of 3rd World Conference on*, volume 2, pages 1772–1775 Vol.2, May 2003.

[8] J. K. Rath, A. J. Hardeman, C. H. M. van der Werf, P. A. T. T. van Veenendaal, M. Y. S. Rusche, and R. E. I. Schropp. Deposition of HWCVD poly-si films at a high growth rate. *Thin Solid Films*, 430(1-2):67 – 72, 2003. Proceedings of the Second International Conference on Cat-CVD (Hot Wire CVD) Process.

[9] G. Bugnon, A. Feltrin, F. Meillaud, J. Bailat, and C. Ballif. Influence of pressure and silane depletion on microcrystalline silicon material quality and solar cell performance. *Journal of Applied Physics*, 105(6):064507, 2009.

[10] Lihui Guo, Michio Kondo, Makoto Fukawa, Kimihiko Saitoh, and Akihisa Matsuda. High rate deposition of microcrystalline silicon using conventional Plasma-Enhanced Chemical Vapor Deposition. *Japanese Journal of Applied Physics*, 37(Part 2, No. 10A):L1116–L1118, 1998.

[11] B. Rech, T. Roschek, J. Müller, S. Wieder, and H. Wagner. Amorphous and microcrystalline silicon solar cells prepared at high deposition rates using RF (13.56 Mhz) plasma excitation frequencies. *Solar Energy Materials and Solar Cells*, 66(1-4):267 – 273, 2001.

[12] Michio Kondo. Microcrystalline materials and cells deposited by RF glow discharge. *Solar Energy Materials and Solar Cells*, 78(1-4):543 – 566, 2003. Critical review of amorphous and microcrystalline silicon materials and solar cells.

[13] B. Rech, T. Repmann, M.N. van den Donker, M. Berginski, T. Kilper, J. Hüpkes, S. Calnan, H. Stiebig, and S. Wieder. Challenges in microcrystalline silicon based solar cell technology. *Thin Solid Films*, 511-512:548–555, 2006. EMSR 2005 - Proceedings of Symposium F on Thin Film and Nanostructured Materials for Photovoltaics - Symposium F.

[14] Q. Zhang, E. V. Johnson, Y. Djeridane, A. Abramov, and P. Roca i Cabarrocas. Decoupling crystalline volume fraction and V_{oc} in microcrystalline silicon pin solar cells by using a µc-Si:F:H intrinsic layer. *Physica Status Solidi (RRL) - Rapid Research Letters*, 2(4):154–156, 2008.

[15] K. Yamamoto, M. Yoshimi, Y. Tawada, Y. Okamoto, A. Nakajima, and S. Igari. Thin-film poly-Si solar cells on glass substrate fabricated at low temperature. *Applied Physics A : Materials Science & Processing*, 69:179–185, 1999.

[16] Kenji Yamamoto, Masashi Yoshimi, Yuko Tawada, Susumu Fukuda, Toru Sawada, Tomomi Meguro, Hiroki Takata, Takashi Suezaki, Yohei Koi, Katsuhiko Hayashi, Takayuki Suzuki, Mitsuru Ichikawa, and Akihiko Nakajima. Large area thin film Si module. *Solar Energy Materials and Solar Cells*, 74(1-4):449 – 455, 2002.

[17] J. Meier, R. Flückiger, H. Keppner, and A. Shah. Complete microcrystalline p-i-n solar cell – Crystalline or amorphous cell behavior ? *Applied Physics Letters*, 65(7):860–862, 1994.

[18] Hiromu Takatsuka, Matsuhei Noda, Yoshimichi Yonekura, Yoshiaki Takeuchi, and Yasuhiro Yamauchi. Development of high efficiency large area silicon thin film modules using VHF-PECVD. *Solar Energy*, 77(6):951 – 960, 2004. Thin Film PV.

[19] T. Matsui, M. Kondo, and A. Matsuda. Microcrystalline silicon solar cells grown at 20-30 å/s by high-pressure silane-depletion plasma. In *Photovoltaic Energy Conversion, 2003. Proceedings of 3rd World Conference on*, volume 2, pages 1548–1551, May 2003.

[20] Chisato Niikura, Michio Kondo, and Akihisa Matsuda. Preparation of microcrystalline silicon films at ultra high-rate of 10 nm/s using high-density plasma. *Journal of Non-Crystalline Solids*, 338-340:42–46, 2004.

[21] Chisato Niikura, Naho Itagaki, and Akihisa Matsuda. High rate growth of high-quality microcrystalline silicon films from plasma by interconnected multi-hollow cathode. *Surface and Coatings Technology*, 201(9-11):5463 – 5467, 2007. Proceedings of the Fifth Asian-European International Conference on Plasma Surface Engineering - AEPSE 2005, Proceedings of the Fifth Asian-European International Conference on Plasma Surface Engineering.

[22] Y. Sobajima, S. Nakano, M. Nishino, Y. Tanaka, T. Toyama, and H. Okamoto. Microstructures of high-growth-rate (up to 8.3 nm/s) microcrystalline silicon photovoltaic layers and their influence on the photovoltaic performance of thin-film solar cells. *Journal of Non-Crystalline Solids*, 354:2407–2410, May 2008.

[23] C. Smit, A. Klaver, B.A. Korevaar, A.M.H.N. Petit, D.L. Williamson, R.A.C.M.M. van Swaaij, and M.C.M. van de Sanden. High-rate deposition of microcrystalline silicon with an expanding thermal plasma. *Thin Solid Films*, 491(1-2):280 – 293, 2005.

[24] Y. K. Chae, H. Ohno, K. Eguchi, and T. Yoshida. Ultrafast deposition of microcrystalline Si by thermal plasma chemical vapor deposition. *Journal of Applied Physics*, 89(12):8311–8315, 2001.

[25] H. Jia, J. K. Saha, N. Ohse, and H. Shirai. High-density microwave plasma of SiH_4/H_2 for high rate growth of highly crystallized microcrystalline silicon films. *Eur. Phys. J. Appl. Phys.*, 33:153–159, 2006.

[26] Hajime Shirai, Takeshi Arai, and Hiroyuki Ueyama. The generation of high-density microwave plasma and its application to large-area microcrystalline silicon thin film formation. *Japanese Journal of Applied Physics*, 37(Part 2, No. 9A/B):L1078–L1081, 1998.

[27] Go Ohkawara, Masanobu Nakajima, Hiroyuki Ueyama, and Hajime Shirai. Relationship between microstructure and photovoltaic performance in microcrystalline silicon film solar cells fabricated by a high-density microwave plasma. *Thin Solid Films*, 427(1-2):27 – 32, 2003. Proceedings of Symposium K on Thin Film Materials for Large Area Electronics of the European Materials Research Society (E-MRS) 2002 Spring Conference.

[28] Haijun Jia, Jhantu K. Saha, Naoyuki Ohse, and Hajime Shirai. Toward the fast deposition of highly crystallized microcrystalline silicon films with low defect density for Si thin-film solar cells. *Journal of Non-Crystalline Solids*, 352(9-20):896 – 900, 2006. Amorphous and Nanocrystalline Semiconductors - Science and Technology - Proceedings of the 21st International Conference on Amorphous and Nanocrystalline Semiconductors - Science and Technology.

[29] Jhantu Kumar Saha, Naoyuki Ohse, Kazu Hamada, Hiroyuki Matsui, Tomohiro Kobayashi, Haijun Jia, and Hajime Shirai. Fast deposition of microcrystalline Si films from SiH_2Cl_2 using a high-density microwave plasma source for Si thin-film solar cells. *Solar Energy Materials and Solar Cells*, 94(3):524 – 530, 2010.

[30] Haijun Jia, Hiroshi Kuraseko, Hiroyuki Fujiwara, and Michio Kondo. Ultrafast deposition of microcrystalline silicon films using high-density microwave plasma. *Solar Energy Materials and Solar Cells*, 93(6-7):812 – 815, 2009. 17th International Photovoltaic Science and Engineering Conference.

[31] S. Guha and J. Yang. Microcrystalline silicon solar cells. Technical report, National Renewable Energy Laboratory (NREL) and United Solar Ovonic Corporation, August 2005. www.nrel.gov/docs/fy05osti/38355.pdf.

[32] B. Yan, G. Yue, Yang J, K. Lord, A. Banerjee, and S. Guha. Microcrystalline silicon solar cells made using RF, MVHF, and microwave at various deposition rates. In *Photovoltaic Energy Conversion, 2003. Proceedings of 3rd World Conference on*, volume 3, pages 2773 – 2778 Vol.3, 12-16 2003.

[33] J. K. Rath. Low temperature polycrystalline silicon: a review on deposition, physical properties and solar cell applications. *Solar Energy Materials and Solar Cells*, 76(4):431 – 487, 2003.

[34] Vikram L. Dalal, Tim Maxson, Kay Han, and Sohail Haroon. Improvements in stability of amorphous silicon solar cells by using ecr-cvd processing. *Journal of Non-Crystalline Solids*, 227-230(Part 2):1257 – 1261, 1998.

[35] V.L. Dalal and K. Erickson. Microcrystalline Si and (Si,Ge) solar cells on plastic substrates. In *Photovoltaic Specialists Conference, 2000. Conference Record of the Twenty-Eighth IEEE*, pages 792 – 795, 2000.

Chapter II

Diagnostics

Contents

Introduction

To process an entire cell is very time-consuming. For example, it requires to coordinate the schedules of the two reactors involved (for the deposition of the doped layers and the intrinsic layer). Thus, it is not an efficient optimization method to process a cell with every deposition condition tried. As a consequence, we are looking for techniques which can predict whether the material deposited (e.g. on glass or on monocrystalline silicon) will result in a good device or not.

As our strategy for the optimization of the microcrystalline solar cells has been to characterize the material with a very large set of diagnostics, this chapter cannot present them all. Only the main ones will be described.

We will start with our method to measure in-situ our substrate temperature : pyrometry. We will then review some techniques used to monitor the material structural and chemical properties : spectroscopic ellipsometry, Raman spectroscopy, Fourier Transform Infra-Red spectroscopy, X-Ray Diffraction and Secondary Ion Mass Spectrometry. A third group of diagnostics allowed us to evaluate the electrical quality of the films : steady-state photoconductivity, the Steady-State Photocarrier Grating method and Time Resolved Microwave Conductivity. Finally, we will explain how we characterize the cells in our laboratory.

1   Pyrometry

The reader who would like to have more details and informations on pyrometry can look for them in the remarkable book by DeWitt and Nutter [1], on which this section is based.

1.1   Theory of radiation thermometry

1.1.1   Principle

Radiation thermometry, also called pyrometry, is a method to measure the temperature of a surface. The optical system of the instrument, called a radiation thermometer or a pyrometer, collects the radiation flux emitted by the target, filters it and transmits the selected bandwidth to a detector which delivers an electric signal.

The calibration of the pyrometer carried out by its manufacturer consists in using a black body and in recording the intensity received on the detector as a function of the known temperature of the black body. The result of this calibration process is a table of the temperature of the black body T_{BB} as a function of the measured signal S_m : $T_{BB}(S_m)$. Then, measuring the unknown temperature of any black body is very easy, just by finding the temperature corresponding to the measured signal.

But in most cases, the surfaces of interest do not emit like a perfect black body. So how does a pyrometer measure the temperature when the surface is not a black body ?

To explain this, let us note I, the radiance per wavelength interval unit. (The radiance being the energy per time unit per surface unit per solid angle unit.) Then, the spectral-directional emissivity ε_λ of a material is defined as follows :

$$\varepsilon_\lambda(\lambda, \theta, T) = \frac{I(\lambda, \theta, T)}{I_{BB}(\lambda, T)} \tag{II.1}$$

where $I(\lambda, \theta, T)$ and $I_{BB}(\lambda, T)$ are the radiances per wavelength interval unit of the material of interest and of a black body respectively, measured at the same wavelength λ, at the same temperature T and in the direction θ. The spectral-directional emissivity is thus a quantity ranging from 0 to 1 and which can simply be seen as a correction factor to the black body. **Remark :** Since we will only deal with measurements in the direction perpendicular to the substrate throughout this section, the dependence on the angle will be omitted in the rest of the discussion.

Then, to know the temperature of any material, the measured signal S_m will be corrected by dividing it by the value of the spectral emissivity which has to be provided by the user to the software analyzing the recording : $S_{corrected} = S_m/\varepsilon_\lambda$. As a result, the temperature of the material T is calculated by the software using the table obtained during the calibration : $T(S_{corrected})$.

1.1.2   The difficulties and advantages of pyrometry

Although the principle of the measurement could seem simple, it is only valid provided the spectral emissivity ε_λ is known, which is one of the major challenges of pyrometry. Indeed, this ratio can be quite misleading because it depends on the material, the wavelength,

the surface roughness, the angle of observation, the oxidation of the surface (if any, e.g. for metals), and . . . on the temperature, which is precisely the parameter we want to determine !

Important remark : The spectral emissivity must be distinguished from the total emissivity ε_t defined as :

$$\int_0^\infty I(\lambda, T)\,\mathrm{d}\lambda = \int_0^\infty \varepsilon_\lambda(\lambda, T) I_{BB}(\lambda, T)\,\mathrm{d}\lambda = \varepsilon_t(T) \int_0^\infty I_{BB}(\lambda, T)\,\mathrm{d}\lambda \qquad \text{(II.2)}$$

which is very often the parameter found in tables or given by companies, but which is of no use for our one-wavelength measurements.

Apart from the crucial problem of the spectral emissivity, the proper use of pyrometry requires to keep other potential sources of error in mind. The environment has to be taken into account. For example, the deduced temperature can be overestimated if other sources of heat are reflected by or emit through the surface. Similarly, the deduced temperature will be underestimated if the radiations at the considered wavelength are absorbed on their path to the pyrometer, e.g. by dusts.

The advantages of this technique are that it is non intrusive, contact-free and time-resolved. It can be installed in-situ provided that the reactor has the suitable geometry of course, in order to view directly the surface of the sample. This cost-effective diagnostic can easily be implemented on production lines as a tool of control of the process. The drawbacks are that it is not straightforward to analyze and that some artefacts can be misleading.

1.2   Our pyrometer

Our pyrometer is the model "Infratherm IN 5/5 plus" from the Impac company. It records the radiation emitted at $5.14\,\mu\text{m}$. Its temperature range is $100\,^\circ\text{C}$ to $1300\,^\circ\text{C}$ and its accuracy is $2\,^\circ\text{C}$.

In our MDECR reactor, we can take advantage of our very specific configuration : in the absence of a counter-electrode, the pyrometer was installed on the flange of the microwave applicators to perform in-situ measurements of the temperature of the substrates (see Figures III.13 page 70 and III.17 page 76). With the design of the optical system, the radiation flux received on the detector is independent of the distance between the instrument and the target. In our case, the surface observed by the pyrometer is a spot of around $19\,\text{mm}$ in diameter.

To install the pyrometer on the vacuum vessel, we have a port with a CaF_2 window which is not perfectly transparent at $5.14\,\mu\text{m}$. To account for that, the emissivity has to be multiplied by a correcting factor of 0.945 .

1.3   Validity of our measurements

Deposition on the window is very often a problem in research or industrial reactors because the attenuation in the collected signal leads to an underestimation of the temperature. In our configuration, we are far enough from the plasma so that no deposition is observed.

One problem of our configuration could have been that the radiation from the surface is observed through the plasma. Hopefully none of the gases we used are emitting or absorbing ligth at the recorded wavelength : no step when the plasma is turned on or off has ever been observed.

What is more, we are not affected by the risk of overestimation of the temperature due to emission through the measured object. Indeed, the glass substrates that we used (Corning 1737 1.1 mm thick) can be considered as completely opaque at 5.14 µm so that the pyrometer never "sees" the radiation emitted by the heated substrate holder.

Then comes the central question of the error produced by the uncertainty on the spectral emissivity. *At room temperature*, the spectral emissivity at 5.14 µm has been measured by the glass manufacturer to be 0.97 . The formula relating the radiance per wavelength interval unit of a black body I_{BB} at a certain wavelength λ to its temperature T is the well-known Planck's law (1901) :

$$I_{BB}(\lambda, T) = \frac{2hc^2}{\lambda^5} \frac{1}{e^{\frac{hc}{\lambda kT}} - 1} \tag{II.3}$$

where h is the Planck constant, k the Boltzmann constant and c the speed of light.

For our conditions, at a wavelength of 5.14 µm and at a typical temperature around 500 °K, $e^{\frac{hc}{\lambda kT}} \sim 270$ and as a result, the Wien's approximation can be applied :

$$I_{BB}(\lambda, T) \sim \frac{2hc^2}{\lambda^5} e^{-\frac{hc}{\lambda kT}} \tag{II.4}$$

Using this simplified formula, the real temperature T_r as a function of the apparent temperature T_m can be expressed as :

$$T_r = \frac{1}{\frac{1}{T_m} + \frac{\lambda k}{hC} \ln\left(\frac{\varepsilon_{\lambda r}}{\varepsilon_{\lambda m}}\right)} \tag{II.5}$$

where T_m is measured with a wrong spectral emissivity $\varepsilon_{\lambda m}$ set in the software of the pyrometer while the real spectral emissivity is $\varepsilon_{\lambda r}$.

1.4   The temperature at the end of the heating phase (without plasma)

Now we can apply this expression to our typical conditions to have an idea of the accuracy of our measurements : The usual temperature measured at the end of the heating phase is $T_m = 230\,°C$ obtained with a fixed emissivity $\varepsilon_{\lambda m} = 0.945$ corresponding to an emissivity arbitrarily set to 1 and corrected for the presence of the CaF_2 window (see 1.2). The real temperature T_r as a function of the real emissivity $\varepsilon_{\lambda r}$ is plotted in Figure 1.4 .

Figure 1.4 shows us that if we assume that the spectral emissivity of our *heated* glass remains between 1 and 0.9, then its real temperature is between 230 °C and 240 °C. As can be seen of the graph, setting the highest emissivity possible means we are measuring a *minimal* temperature.

In any case and despite all its difficulties, pyrometry can at least be used to check the repeatability of the temperature of the process : During my PhD, I have had the opportunity
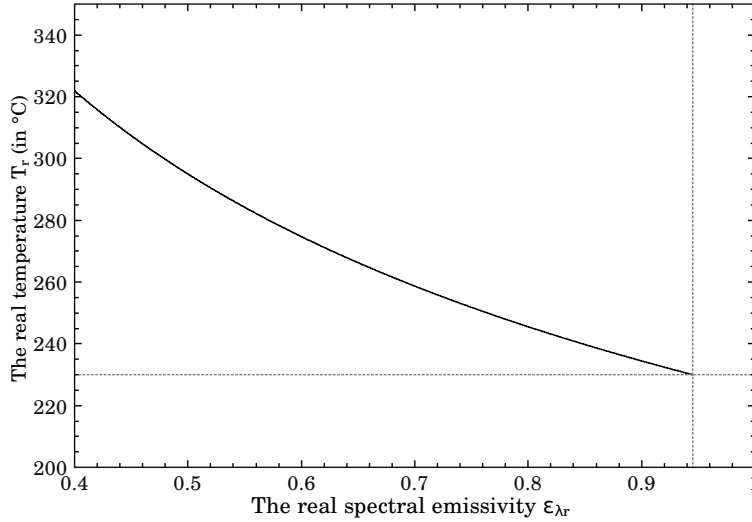
Figure II.1 – *Error induced on the temperature by the uncertainty on the spectral emissivity for $T_m = 230\,°C$ and $\varepsilon_{\lambda m} = 0.945$.*

to use three different substrate holders (see page 72 for more details). Depending on where the thermocouples were, they indicated temperatures ranging from $350\,°C$ to $650\,°C$ to give the same temperature of $230\,°C$ at the surface of the glass sample. Such huge discrepencies led us to conclude that with our low pressure process and with our configuration (i.e. absence of counter-electrode), a pyrometer is the necessary tool to evaluate the temperatures of the samples, which is a crucial parameter for the growth of microcrystalline silicon by MDECR [2, 3].

2   Ellipsometry

The crystalline fraction is one of the most important characteristics of microcrystalline films. The four techniques which can be used to determine the crystalline fraction are : high-resolution transmission electron microscopy (HRTEM), X-ray diffraction (XRD) [4], spectroscopic ellipsometry (SE), and Raman spectroscopy.

Ellipsometry was used to obtain the total thickness of the films and their structural compositions, i.e. the crystalline fraction, the amorphous fraction and the void fraction, in our case.

2.1   Theory of ellipsometry

This technique probes the material dielectric properties by analysing the state of polarisation of a light beam after its interaction (reflection) with the thin film (see Figure II.2).

The experimental data recorded during a spectroscopic ellipsometry measurement consist in two values at each wavelength. For example, the angles Δ and ψ can be used to write the ratio of the complex Fresnel reflection coefficients parallel (r_p) and perpendicular (r_s) to the plane of incidence :

$$\rho = \frac{r_p}{r_s} = \tan(\psi)\exp(i\Delta) \tag{II.6}$$

Equivalently, one can use the real and imaginary parts of the complex pseudodielectric function $\langle \varepsilon \rangle$, related to ρ by :

$$\langle \varepsilon \rangle = \langle \varepsilon_r \rangle + i \langle \varepsilon_i \rangle \tag{II.7}$$

$$= \sin^2(\Phi)\left(1 + \frac{(1-\rho)^2}{(1+\rho)^2}\tan^2(\Phi)\right) \tag{II.8}$$

where Φ is the angle of incidence.
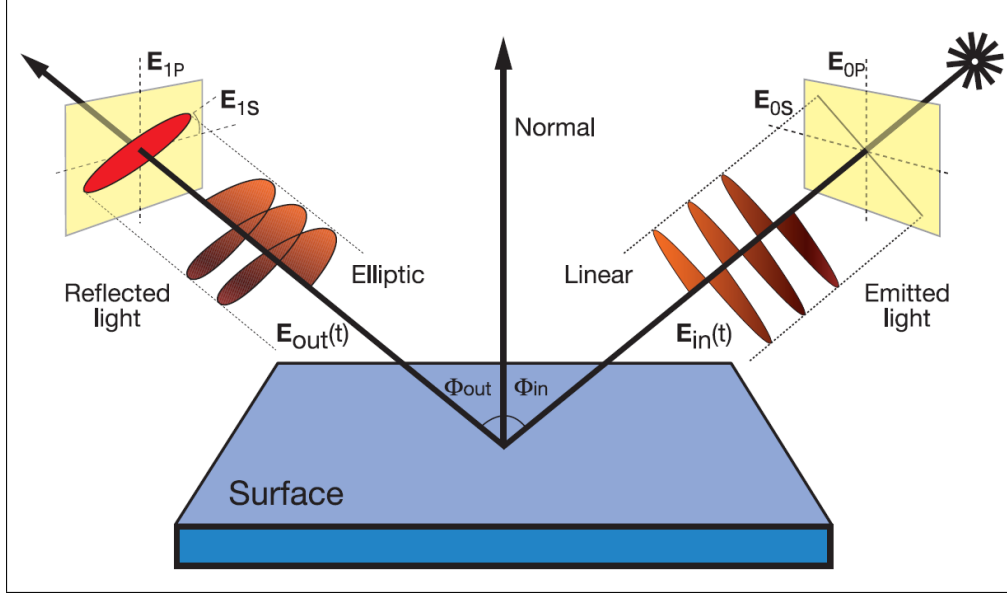
Figure II.2 – *Drawing of the reflection of the incoming linearly polarized beam (light source on the top right corner) on the sample. The electric field is decomposed into parallel and perpendicular components, noted with the subscripts P and S respectively. (Taken from* http://www.horiba.com *)*

To obtain the informations on the film thickness and composition, one has to design an adapted model. For our films, a three-layer model (see Figure II.3) generally gives satisfactory accuracy and each layer can be composed of amorphous silicon (Si), fine-grain polycrystalline Si, large-grain polycrystalline Si and voids, whose dielectric functions are taken from a data base [5]. The layer thicknesses deduced show very good agreement with high resolution transmission electron microscopy (HRTEM) as demonstrated in [6]. To represent the complex microcrystalline silicon material, which is a mixture of crystallized grains, amorphous tissue and voids, the Bruggemann Effective Medium Approximation (B-EMA) is used, which gives the composite dielectric function ε_B by solving :

$$0 = \sum f_j \frac{\varepsilon_j - \varepsilon_B}{\varepsilon_j + 2\,\varepsilon_B} \tag{II.9}$$

where f_j is the volumic fraction of the jth component and ε_j is its dielectric function taken from the data base.

The complex Fresnel reflection coefficients can be *calculated* from such a model with the hypothesis of uniform and isotropic layers. Finally, the parameters of this model (i.e. the thicknesses of the layers and the volumic fractions of the different components) are adjusted with a Levenberg-Marquardt algorithm to match the experimental data.

Figure II.3 – *Schematic of the typical three-layer model used during this work. The nine adjustable parameters of this model are the thicknesses of the layers (d_1, d_2 and d_3) and the crystalline (small grains), amorphous and void fractions of each layer (F_c, F_a and F_v respectively).*
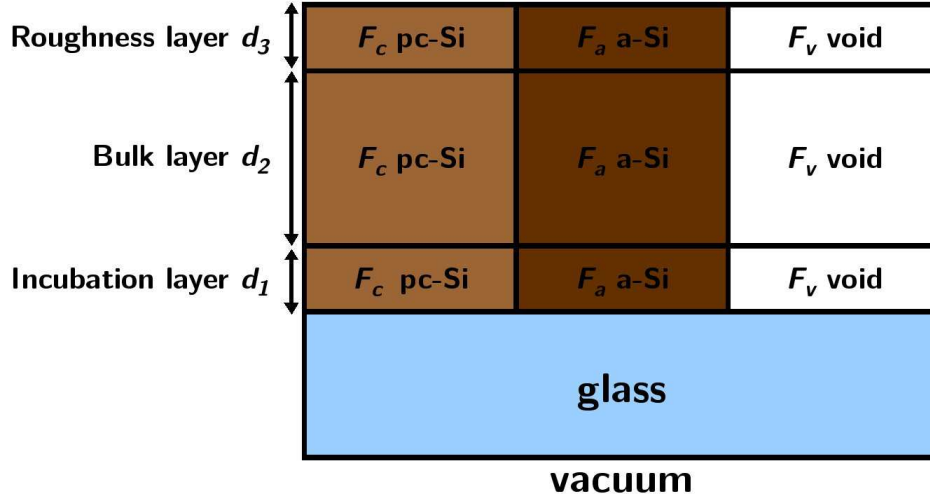
To find the best fit, the figure of merit used is the so-called reduced χ^2 which takes the experimental errors into account [7], i.e. more weight is attributed to accurate points :

$$\chi^2 = \frac{1}{n_l - m - 1} \sum \frac{\left[\rho_{exp}(\lambda_j) - \rho_{calc}(\lambda_j, \mathbf{z}) \right]^2}{\delta\rho(\lambda_j)^2} \tag{II.10}$$

where n_l is the number of experimental points, m is the number of varied parameters, $\mathbf{z}$ is the vector of the m parameters and $\delta\rho$ is the experimental error. This biased estimator has been demonstrated to avoid the errors associated with an unbiased estimator [8].

What is more, this figure of merit is quasi-independent of the chosen representation (i.e. (Δ,ψ) or $(\langle\varepsilon_r\rangle,\langle\varepsilon_i\rangle)$ etc.) and is a meaningful quantitative indication of the "goodness of the fit". Also, the errors (corresponding to the confidence intervals) for each parameter are calculated by the software, as well as the normalized cross-correlation coefficients.

As a final remark, it can be noted that the physical origin of the void fraction is difficult to determine from ellipsometry alone as it can arise from the hydrogen content, from cavities and/or from a lower density than the reference material whose dielectric function is used. With elaborate models, one can distinguish the void fraction from the hydrogen fraction like in [9] and [10], where they use a tetrahedron model combined with the Bruggeman effective medium approximation.

2.2   The ellipsometer

The ex-situ spectroscopic ellipsometer used during this work was a phase modulated UVISEL from the company Horiba Jobin-Yvon. Its range goes from 826.6 nm (1.5 eV) to 263.8 nm (4.7 eV) and the spectra were taken with an energy step of 0.01 eV. Its main parts are briefly described in Figure II.4. The adjustment of the models to the experimental data was performed with DeltaPsi2, the software platform of Horiba Jobin-Yvon.
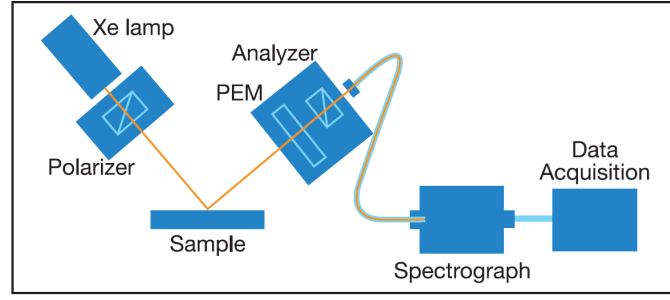
Figure II.4 – *Principle of the UVISEL phase modulated ellipsometer : The linearly polarized beam interacts with the sample and the Photoelastic Modulator (PME) adds a 50 kHz phase shift between the parallel and perpendicular components of the electric field, which is analysed. (Taken from the brochure of the UVISEL ellipsometer at* http://www.horiba.com *)*
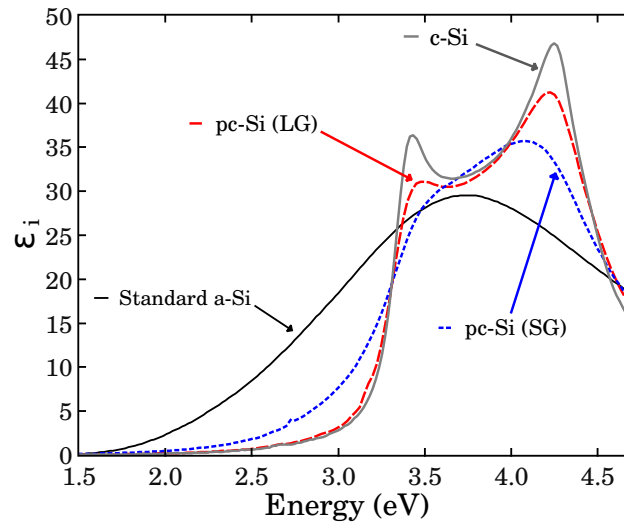
Figure II.5 – *Imaginary parts of the pseudodielectric functions $\langle \varepsilon_i \rangle$ of standard amorphous silicon (a-Si), small grain and large grain polycrystalline silicon (pc-Si SG and LG) and of monocrystalline silicon (c-Si) [5].*
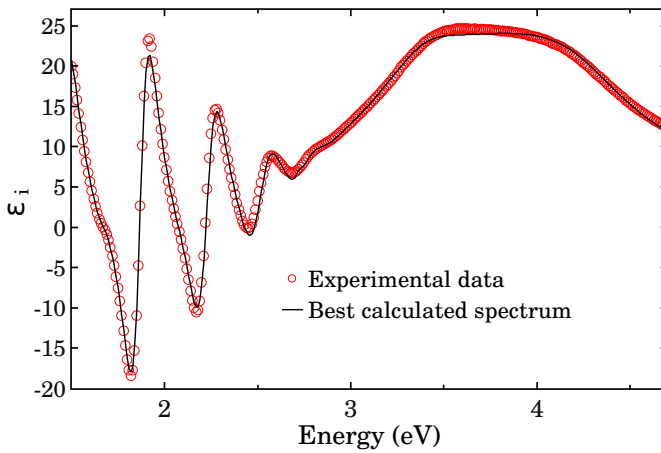
Figure II.6 – *Microcrystalline film deposited by MDECR : experimental data points and adjusted spectrum (graph on the left) and results of the fit (right table). The figure of merit is $\chi^2 = 1.4$.*

2.3   Microcrystalline silicon characterization with ellipsometry

Our most typical model consists of three layers, each of them containing three phases (amorphous silicon, small grain crystalline silicon and void), which corresponds to nine parameters to adjust (see Figure II.3). As a consequence, we always payed attention to the correlations between the parameters.

The basic "bricks" to perform this adjustment are shown in Figure II.5. The changes between c-Si and pc-Si are due to the finite grain sizes [11]. Finally, an example of such a fit is given on Figure II.6. This graph can be decomposed in two parts. At high energies (greater than around $3\,\text{eV}$), the film is opaque and thus, the ellipsometric signal is characterising the surface and the bulk. At lower energies, the film is more transparent and the reflection on the substrate gives rise to interference fringes. Also, one can see the two peaks E_1 and E_2 at $3.4\,\text{eV}$ and $4.2\,\text{eV}$ respectively, which are due to singularities in the Brillouin zone called Van Hove singularities. As shown on the graph, it is often difficult to adjust our theoretical model to the experimental data in this region.

3   Raman Spectroscopy

3.1   Principle

Raman spectroscopy is probably the most widely used technique to evaluate the most important microstructural parameter of microcrystalline silicon : its crystalline volume fraction.

The principle of this technique is to illuminate the sample with incident monochromatic photons. Most of the photons will be scattered without any energy exchange (Rayleigh scattering) and a small fraction will be scattered at a shifted wavelength after their interaction with the solid phase. This interaction taking place consists in the creation or in the absorption of a phonon. These phenomena are respectively referred to as Stokes and anti-Stokes inelastic diffusion.

The oscillating electric field $E(t)$ of the incoming laser beam induces an electric dipole moment μ_{ind} in the illuminated diatomic molecule which is proportional to it :

$$\mu_{ind}(t) = \alpha E(t) \tag{II.11}$$

where α is the polarisability. This is due to the fact that the electrical forces on the positively charged nuclei and on the negatively charged electrons are in opposite directions. Equation II.11 is of course a simplified expression as it should be written with vectors and a polarizability tensor, which is a 3×3 matrix [12].

The polarizability depends on the bond length and this bond length varies with time at the frequency of the vibration mode of the molecule. For the vibration to be Raman-active, the derivative of the polarizability with respect to the molecule bond length at the rest position has to be non-zero. A discussion comparing the selection rules of Raman spectroscopy and infra-red absorption, can be found in Section 4.2 page 37.

Thus, Raman spectroscopy gives informations about the chemical environment of the atoms in the film by testing their vibrational modes.

3.2   Raman peaks

The positions of the peaks are related to the inter-atoms forces and distances, to their masses and to their chemical environments. For a crystalline solid, due to the momentum conservation law, only phonons with zero momentum will be excited because of the very small momentum of the incoming photons. Therefore, only the $64\,\mathrm{meV}$ phonon (at $520\,\mathrm{cm^{-1}}$) will appear in the spectrum of monocrystalline silicon since it is the only one having a zero momentum. In disorded solids such as hydrogenated amorphous silicon, the selection rule is relaxed and other peaks appear.

Here, we will list the main Raman-active peaks used during this work :

- **$310\,\mathrm{cm^{-1}}$:** Longitudinal Acoustic mode in a-Si:H [13, 14].
- **$380\,\mathrm{cm^{-1}}$:** Longitudinal Optical mode in a-Si:H [13]. Some authors propose that it should be included in the fit for a proper estimation of the crystalline fraction. Indeed, the tail of this additional Gaussian function can have an influence on the other Gaussian functions at higher wavenumbers.
- **$480\,\mathrm{cm^{-1}}$:** Transverse Optical mode in a-Si:H [13].
- **$\sim 500\,\mathrm{cm^{-1}}$:** An additional intermediate peak can sometimes be included. It is interpreted as a signature of the grain boundaries, of crystallites smaller than $10\,\mathrm{nm}$ [15], or of a hexagonal structure induced by twin boundaries or stacking faults (seen on TEM images in [4]).
- **$520\,\mathrm{cm^{-1}}$:** Transverse Optical (TO) mode of crystalline silicon. It corresponds to a phonon of $\sim 64\,\mathrm{meV}$.
- **$\sim 2080\,\mathrm{cm^{-1}}$ and $2100\,\mathrm{cm^{-1}}$:** Doublet peaks of Si–H_x stretching modes [16].

These peaks can be seen on some typical spectra shown on Figure II.7. In the case of a thin film ($\alpha d < 1$), the signal from the glass substrate is going to artificially increase the amorphous component [17].

3.3   Our setup

Our equipment is a system from the company Horiba Jobin Yvon. It consists of a red Helium-Neon laser ($632.8\,\mathrm{nm}$) connected by an optical fibre to a microscope. The unpolarized incident beam is focused on the sample and the backscattered light is analyzed by a monochromator with a Charge Coupled Detector (CCD). A computer with the software LabSPEC is used to display and analyze the recorded data.

The laser beam probes the whole thickness of the samples. Indeed, the extinction coefficient for small grain polycrystalline silicon at its wavelength is 0.0556 [5], corresponding to an absorption coefficient $\alpha \sim 1.1 \times 10^4\,\mathrm{cm^{-1}}$ and the thicknesses of the analyzed films are $\leqslant 1\,\mathrm{\mu m}$, often $\sim 0.3\,\mathrm{\mu m}$.

Compared spectra have systematically been recorded at the same place of the sample (to avoid problems in the case of inhomogeneous films) and in the same conditions (i.e. with the same magnification, the same integration time and averaging over the same number of spectra to reduce noise).
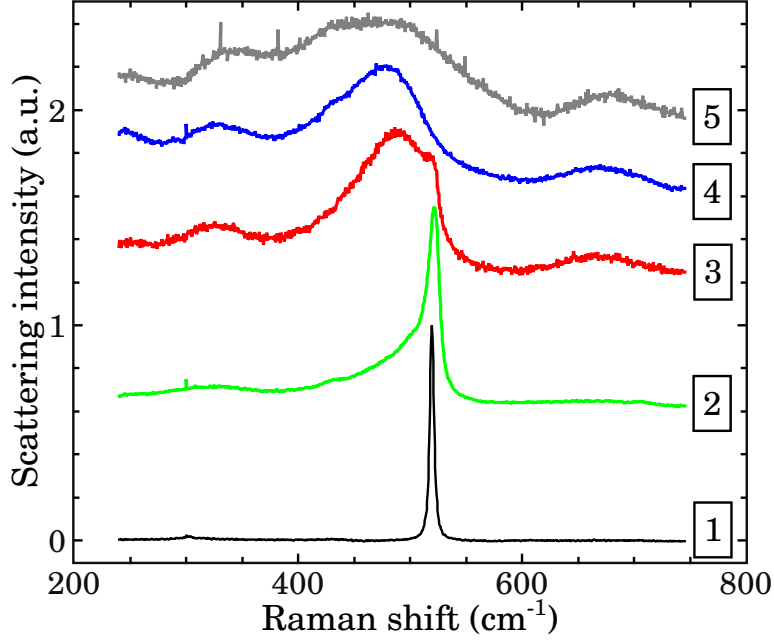
Figure II.7 – *Spectra of monocrystalline silicon (curve 1), of highly crystallized microcrystalline silicon (curve 2), of moderately crystallized microcrystalline silicon (curve 3), of amorphous silicon (curve 4) and of a bare Corning 1737 glass substrate (curve 5), all normalized to the same maximum intensity and shifted for clarity.*

3.4   Quantitative estimation of the crystalline fraction

One of the methods to do so, exposed in [18], is to remove a typical amorphous spectrum and to consider that the remaining area represents the crystalline fraction. We used another method during this work, which consists in fitting the experimental spectra with several Gaussian peaks corresponding to the above list.

The crystalline and amorphous integrated scattered intensities, I_c and I_a, can be written as :

$$I_c = \rho_c \, \Sigma_c \, V_{exp} \tag{II.12}$$
$$I_a = (1 - \rho_c) \, \Sigma_a \, V_{exp} \tag{II.13}$$

- where ρ_c is the crystalline volumic fraction, which is the quantity we would like to estimate,
- where Σ_c (Σ_a) is the crystalline (amorphous) integrated Raman cross section over the measured wavenumber range,
- and where V_{exp} is the total scattering volume.

The crystalline volume fraction can then be deduced as :

$$\rho_c = \frac{I_c}{I_c + y \, I_a} \tag{II.14}$$

where $y = \Sigma_c/\Sigma_a$ is the Raman emission cross-section ratio [19].

So that the two steps are :

1. to define a method to treat the spectrum, i.e. to remove the baseline if any and to separate the spectrum into the two components I_a and I_c,

34

2. and then, to find the value of y.

It is common practice to simply take $y = 1$ and to name the obtained value the Raman crystalline volume fraction. For a more detailed approach, the value of y has been reported to vary as a function of the crystallite size and of the laser wavelength [20], which implies that one would have to get an estimation the crystallite size by another diagnostic (e.g. X-Ray Diffraction). The values taken for y can vary between 0.88 to 0.1 (the latter being suitable for large-grain polycrystalline silicon) [19], although greater values have sometimes been proposed, as 1.7 in [21]. The authors of [18] and those of [14] take it equal to 0.8. They say it varies from ~ 0.9 to ~ 0.7 for crystallite sizes varying from 5 to 15 nm.

Then, the peaks can be adjusted with Gaussian or Lorentzian [22] functions. It has been proposed that Gaussian is suitable for small grain sizes and that an asymmetrical Lorentzian is better for crystallites average sizes greater than ~ 13 nm [20]. Other authors are fitting the crystalline peak as a mixture of a Lorentzian and a Gaussian function, the percentage of the mixture being an additional parameter of the fit [13].

As a conclusion, one of the great weaknesses of Raman spectroscopy is probably the diversity of methods used to analyze the spectra. In this work, we will fit our data with Gaussian functions and with $y = 0.8$.

3.5   Interpretation of the spectra

3.5.1   Interpretation of a shift in the crystalline peak position

Three parameters can affect the crystalline peak position.

Stress can cause such a shift. A positive shift of the crystalline peak is attributed to a compressive stress and a shift to lower wavenumbers, to a tensile stress [23]. For an isotropic stress, the following relation between the stress strength τ and the wavenumber shift $\Delta\omega$ has been proposed [24] :

$$\tau = 2.49 \times 10^9 (\mathrm{cm}^2/\mathrm{dyn}) \times \Delta\omega (\mathrm{cm}^{-1}) \tag{II.15}$$

The grain size can also play a role [19, 25] : Small grains shift the TO mode to lower wavenumbers. For [22], a decrease of the grain size (from 150 Å to 47 Å) induces broader crystalline peaks with maxima shifted at lower frequencies and they attribute these phenomena to a progressive relaxation of the zero momentum $\boldsymbol{k} \sim \boldsymbol{0}$ selection rule (see also [26]). Zi *et al.* [27] proposed a quantification of the dependence of the Raman shift $\Delta\omega$ as a function of the crystallite size L (in nanometers) with the hypothesis of spherical shape crystallites and based on a bond-polarizability model :

$$\Delta\omega(L) = -47.41 \left(\frac{0.543}{L} \right)^{1.44} \tag{II.16}$$

Different values of the pre-factor ($-52.3 \, \mathrm{cm}^{-1}$) and the exponent (1.586) have later been proposed [28]. In any case, the smallest crystallite size measured by X-ray diffraction during this work was 7.4 nm (in the direction perpendicular to the substrate) and this would correspond to a shift of only $-1.1 \, \mathrm{cm}^{-1}$.

Finally, the third factor is local heating of the low thermal conductivity silicon matrix by the focused laser during the measurement. Its consequence is a shift of the peak to lower values with increasing temperature ($-0.028\,\mathrm{cm}^{-1}\,{}^{\circ}\mathrm{C}^{-1}$ [17]).

3.5.2   Interpretation of the width of the crystalline peak

The width of the TO mode is related to the grain size. Indeed, for small grain sizes, the zero momentum selection rule is relaxed and the width of the peak increases [22]. Full Widths at Half Maximum (FWHM) of $\sim 12\,\mathrm{cm}^{-1}$ would correspond to crystallites of $\sim 60-70\,\mathrm{\AA}$ (as determined by X-Ray Diffraction) according to [25].

Local heating by the laser can also increase the peak width [13, 26].

4   Fourier-Transform Infra-Red Spectroscopy (FTIR)

FTIR is a technique which allows to identify and to quantify some of the species and some of their chemical configurations present in the studied layers. Indeed, the infra-red (IR) spectra of hydrogenated amorphous and microcrystalline silicon exhibit various absorption bands which can be related to the vibrational modes of hydrogen (and carbon and oxygen, if any) in the silicon matrix. The only vibration modes which are infra-red active are the ones involving a change of the dipole moment of the bond, that is to say, of its polarization.

Our device is a single beam Nicolet 6700 with Mercury Cadmium Telluride (MCT) detector cooled by liquid nitrogen. Its spectral range is $2.5\,\mu\mathrm{m}-15.4\,\mu\mathrm{m}$, often given in wavenumbers : $650\,\mathrm{cm}^{-1}-4000\,\mathrm{cm}^{-1}$ (corresponding to energies ranging from $0.08\,\mathrm{eV}$ to $0.5\,\mathrm{eV}$). The spectra are obtained from an average of 32 scans with a step of $1.9\,\mathrm{cm}^{-1}$. The chamber is purged with nitrogen during the measurement to lower the effect of the absorption bands of H_2O and CO_2.

The films must be deposited on IR transparent substrates. To fulfill the FTIR requirements, we used high resistivity ($10\,000\,\Omega\,\mathrm{cm}-20\,000\,\Omega\,\mathrm{cm}$), Float Zone (for very low oxygen concentrations) and both sides polished monocrystalline silicon substrates. The absorption of the substrate is removed with the measurement of a bare c-Si wafer.

4.1   List of the absorption peaks

The position of a peak depends on its environment : it can be influenced by the local density of the film, local dipole-dipole interactions with surrounding atoms etc.

- $\sim 640\,\mathrm{cm}^{-1}$: $Si-H_n$ wagging mode [29]. It is possible to quantify the hydrogen content in amorphous films [30, 31] and even in microcrystalline films [32] with this peak but it is unfortunately out of the range of our device.
- $\sim 820-920\,\mathrm{cm}^{-1}$: doublet SiH_2 and SiH_3 bending modes [16, 33, 29].
- $950\,\mathrm{cm}^{-1}$: $Si-OH$ bonds [29].
- $980-1060\,\mathrm{cm}^{-1}$: $Si-O$ stretching band. It shifts to higher wavenumbers with higher concentrations of oxygen and added to that, the FWHM decreases from $200\,\mathrm{cm}^{-1}$ to $94\,\mathrm{cm}^{-1}$ [29]. In [34], Kilper *et al.* consider that a peak at $\sim 1050\,\mathrm{cm}^{-1}$ shows up for oxygen concentrations higher than 1.4×10^{20} atoms/cm^3.

- $\sim \mathbf{1300 - 1950\,cm^{-1}}$: peaks due to atmospheric water in the device.
- $\sim \mathbf{2000\,cm^{-1}}$: Low Stretching Mode (LMS) related to only monohydrides Si$-$H [31]. Indicates H in a compact environment according to [34] or isolated H according to [30]. This mode can be shifted at a higher wavenumber ($\sim 2100\,cm^{-1}$) in the presence of oxygen atoms [29].
- $\sim \mathbf{2100\,cm^{-1}}$: High Stretching Mode (HSM). Some authors attribute this mode to only dihydrides, while others also include clustered monohydrides at the surface of voids and di- and trihydrides [30, 31].
- $\mathbf{2080\,cm^{-1}}$ **and** $\mathbf{2100\,cm^{-1}}$: narrow doublet of stretching modes (see discussion below)
- $\mathbf{2240 - 2250\,cm^{-1}}$: Vibration mode involving oxygen and hydrogen, described as $O_{2...3}-Si-H$ in [35], as O_3-Si-H in [36] or O_x-Si-H_y in [33].
- $\mathbf{3000 - 3600\,cm^{-1}}$: Si$-$OH bonds inside the film (not on the surface) [29].
- $\mathbf{> 3650\,cm^{-1}}$: bands due to isolated OH bonds on the surface [29]. It indicates the presence of remaining water in the device.

For more details, one can read [33] for a decomposition of the $2000 - 2100\,cm^{-1}$ modes with a great number of peaks.

The narrow peaks at $2080\,cm^{-1}$ and $2100\,cm^{-1}$

For some of our samples, a doublet of narrow peaks is clearly identified at these wavelengths and the study of their origin and their evolution with time by combined Raman and FTIR spectroscopies was a rich topic of this PhD (see Section 4.3.5 page 160).

Their interpretation is still under debate :

- In [33] they are attributed to mono-, di-, and trihydrides on crystalline surfaces, i.e. in the grain boundaries in the bulk.
- In [37] the peak at $2080\,cm^{-1}$ is attributed to a monohydride structure on a (111) oriented plan coupled to the surrounding monohydrides.

For the authors of [33], the presence of two Narrow High Stretching Modes (NHSMs) at $2083\,cm^{-1}$ and $2103\,cm^{-1}$ indicates a highly crystallized but not dense material which will undergo oxidation with time through the interconnected voids. They proposed that high efficiency cells can only be obtained with materials not showing this typical signature.

4.2   Raman vs FTIR

This section aims at concisely summarizing the similarities and differences between Raman and FTIR spectroscopies.

They are both based on the vibrating dipole formed by bonded atoms.

- In Raman spectroscopy, both the incident and analyzed light are in the *visible* range. What is used is the low energy shift between the two, which probes vibration modes. The polarizability of the bond has to change : more precisely, the derivative of the polarizability with respect to the varying bond length has to be non-zero at the rest position. However, the selection rules can be less strict in the amorphous and crystallized

phases of hydrogenated microcrystalline silicon, due to the lack of order. Therefore, the absence of the peaks has to be checked experimentally.

- In FTIR, a mode of vibration will be absorbing if it corresponds to a change in the dipole moment, i.e. a change of its polarization.

The two phenomena are mutually exclusive for molecules which have a center of symmetry (e.g. CO_2) : in such a case, the vibrations which are symmetric (antisymmetric) with respect to the center of symmetry are Raman-active but IR-inactive (Raman-inactive but IR-active).

In general, a bond will have a strong Raman signal if it is covalent while it will have a strong FTIR signal if it is ionic (e.g. O–H, N–H).

An Si–H bond has a dipole moment because the hydrogen electronegativity is greater than the silicon one (2.1 vs 1.8), but it has a small electronic polarizability (1.36×10^{-24} cm^3 vs 1.96×10^{-24} cm^3 for Si–Si bonds in the amorphous phase [31]). This is due to the fact that the polarisability of hydrogen itself is very low because it only has one strongly bound valence electron. Thus, hydrogen is only indirectly seen in Raman because its vibrations change the polarizability of the surrounding silicon atoms. As a result, the Raman sensitivity is lower than the FTIR one.

On the other hand, Raman does not need a water-free (water is a weak Raman scatterer) and CO_2-free environment and can be carried out directly on a cell while films for FTIR have to be on high resistivity c-Si.

5 X-Ray Diffraction (XRD)

5.1 Presentation

This diagnostic has been used on two sets of samples during this work and the interpretation of these results allowed us to better understand our materials.

This technique is used to probe the following film characteristics :

- It allows to identify the different crystallographic phases present in planes *parallel* to the film. They are indicated by the positions of the diffraction peaks (see Graph IV.16 page 113). This way, a preferred crystalline orientation (also called "texture") can be put into evidence.
- The crystalline fraction of the film can be estimated.
- From the peak width, the crystallite size in the direction *perpendicular* to the layer can be estimated with the Scherrer formula, as discussed below.
- It can reveal the presence of tilted bonds at $2\theta \sim 26.6\,°$.
- Stress may be evaluated from the variations of the peak positions corresponding to variations of the inter-plane distances. With the corresponding elastic coefficients, the stress forces may be deduced.

The equipment used to perform these measurements was a Philips X'Pert X-ray diffractometer. The electrons emitted by a heated tungsten filament are accelerated in a $40\,kV$ potential and bombard a copper target which emits X-rays. The lines Cu-$K_{\alpha 1}$ and Cu-$K_{\alpha 2}$ at $1.540598\,\text{Å}$ and $1.544426\,\text{Å}$ respectively are selected by a graphite monochromator. The relative intensities of the two lines are $I(K_{\alpha 1})/I(K_{\alpha 2}) = 0.5$. The Cu-$K_\beta$ line is almost

completely suppressed by a nickel foil. The measurements were carried out by varying the angles of the emitter and the detector with a 2θ step of $0.02\,°$. Peaks will appear at the angles θ in the spectra whenever planes parallel to the film surface result in constructive interferences satisfying the Bragg condition :

$$2\,d\sin(\theta) = \lambda \tag{II.17}$$

where d is the inter-plane distance and λ is the K_α wavelength. Similarly, *all* the angles showing a zero diffracted signal correspond to *destructive* interferences taking place.

The main peaks of interest are the following :

	Inter-plan distance d	2θ
Signal of glass	–	broad band around $23\,°$
Tilted bonds	–	$26.6\,°$
First Scattering Peak of a-Si	–	$27.6\,°$
(111)	$3.14\,\text{Å}$	$28.39\,°$
(220)	$1.92\,\text{Å}$	$47.29\,°$
Second Scattering Peak of a-Si	–	$\sim 52\,°$
(311)	$1.64\,\text{Å}$	$56.01\,°$

Notation : The (110) crystallographic orientation is detected by its (220) peak because the double of the inter-plane distance allows to observe the peak at lower 2θ. In this manuscript, (220) will be used to specifically refer to the peak monitored by the X-ray diffractometer and (110) will be used the rest of time, to refer to this family of planes in general.

5.2   Preferred crystallographic orientation

To quantify the preferred crystallographic orientation, the areas under the peaks have to be compared to randomly oriented crystalline silicon powder, which has no "texture". For such a powder of silicon, the relative intensities of the (111), (220) and (311) peaks are 1, 0.55 and 0.3 respectively, according to the American Standard for Testing Materials (ASTM) card number 27-1402 [38, 39]. Thus, these normalization factors, which correct for the different atom densities in these planes, have to be used to properly deduce the main orientation in the planes parallel to the layer.

Discussion : What is the "best" crystallographic orientation for solar cells ?

The planes (111) and (110) are believed to be the ones which are etched (by atomic hydrogen) and deposited the fastest [38]. Can the ratio of these two main orientations be used as a quality indicator ?

To explain the (110) preferred orientation often observed in device quality µc-Si:H (e.g. [40, 41]), the authors of [42] performed in-situ Reflection High Energy Electron Diffraction (RHEED) in their RF-CCP deposition system and saw the film evolve from amorphous (incubation layer) to randomly oriented (nucleation) to preferentially (110) oriented. They proposed that the tilted (111) bonds can act as seeds for the nucleation of (110) crystallites.

Photoluminescence measurements on microcrystalline samples deposited by Hot Wire CVD have brought some experimental evidence of the higher quality of the (110)-oriented films [36].

The arguments developed to explain these results are based on the fact that the grain boundaries of (110) columns grow without broken bonds but with tilted (110) bonds which are electrically inactive, unless they are contaminated by impurities (e.g. oxygen). The same argument is developed in [43] to explain that materials with small grains which are not (110)-oriented could result in low V_{oc} solar cells due to charged grain boundaries.

There are several reports of experimental results proving that the (111) orientation is more sensitive to impurity contamination during air exposure than the (110) orientation [36, 44]. But there seems to be an optimum to be found because highly (110) oriented films, *without any (111) peak detected*, show enhanced oxygen, nitrogen and carbon contamination when stored at air [45]. Since there is no improvement in electron mobility in the highly (110) oriented films as compared to moderately (110) oriented films [45], optimization of the deposition conditions to obtain moderately (110) oriented materials could be a path for solar cell improvement.

On top of these explanations, we can also propose a simple argument : since the (111) planes are the denser ones, it may be more difficult for atomic hydrogen to diffuse through them (to rearrange the network) and also, for molecular hydrogen to exit through them, so that these crystallites could suffer from greater densities of weak or strained bonds and defects.

5.3   The Scherrer equation

Due to the finite size of the crystallites in the direction perpendicular to the reflecting planes, the interferences at the angles close to the angles satisfying the Bragg condition will not be completely destructive and the peaks will have a certain width which can be related to the crystallite sizes *perpendicular* to the substrate.

The Scherrer formula (1918) expresses the crystallite size D perpendicular to the diffracting planes as (pages $96-102$ of [46] and $491-538$ of [47]) :

$$D = \frac{K\lambda}{\beta \cos(\theta_B)} \tag{II.18}$$

• where K is a factor depending on the crystallite shape and orientation, which can take values down to 0.7 and up to 1.7 (typical values from 0.85 to 0.99). For unknown shape and distribution, K is often set to unity, which introduces a 20 % error in D at most [17, 47]. We chose to take $K = 1$ in this work.
• λ is the wavelength of the X-ray source (in Angströms).
• β is the full width at half maximum (FWHM) of the peak (in *radians* and in terms of 2θ, not of θ) corrected from the instrument broadening (see discussion below).
• θ_B is the Bragg angle.

There are several ways to correct the peak width. One of them, the Warren correction (see [47] for a detailed discussion about this approximation), is to consider that the observed FWHM β_{obs} is the sum of two contributions :

$$\beta_{obs}^2 = \beta_i^2 + \beta^2 \tag{II.19}$$

where β_i is the instrument induced broadening and can be determined by measuring a reference sample in the same conditions. For example, with a monocrystalline susbstrate, β will be very small and one can consider that $\beta_{obs} = \beta_i$.

In this work, for a quick estimation and relative comparisons of the crystallite sizes, we did not attempt to correct for the instrumental broadening.

5.3.1   Limitations of the Scherrer equation

We have already mentioned that the determination of the value of K and the correction for the instrumental broadening are both challenging. The latter comes from sources of non-ideality such as a not perfectly parallel and not perfectly monochromatic X-ray beam. Indeed, there are always convergent and divergent rays and the width of the $K\alpha$ line is around $0.001\,\text{Å}$. These could explain the discrepencies found in [38] between the grain sizes evaluated from the Scherrer equation and from TEM observations.

We can add that this measurement is an average over the shapes of all the crystallites having one orientation and is therefore inaccurate in the case of a size distribution. Furthermore, mechanical stress increases the peak width and thus, can lead to an underestimation of the grain size [38].

6   Secondary Ion Mass Spectrometry (SIMS)

This diagnostic has been used quite intensively during this PhD and is therefore be explained in this chapter.

6.1   Principle

The goal of this technique is to analyze the chemical composition of our samples. It is a destructive diagnostic which gives the profiles of the different species studied as a function of depth. A simplified representation of the equipment can be seen on Figure II.8. The sample is placed in a very low pressure chamber ($< 10^{-9}$ Torr obtained by a cryogenic pump) and sputtered by an oblique beam of energetic primary ions (accelerations in the range $0.5 - 15\,\text{keV}$). The diameter of the primary ion beam is typically of a few microns and it is scanned to sputter a crater of $100\,\mu\text{m} \times 100\,\mu\text{m}$ to $200\,\mu\text{m} \times 200\,\mu\text{m}$ in our measurements. The ejected atoms or groups of atoms have a certain probability to be ionized, positively or negatively, depending on their electronic affinity and of the surrounding matrix. These secondary ions will be accelerated in the electric field present in the analysis chamber between the sample and the extraction electrode and will be counted by an electron multiplier or a Faraday cup of a mass spectrometer.

To detect negative (respectively positive) secondary ions, positive cesium Cs^+ (respectively positive oxygen O_2^+) ions are used as primary ions.

In order not to charge the analyzed sample, it should preferably be conductive. We carried out SIMS measurements on layers deposited on doped monocrystalline silicon or on ZnO.

6.2   Quantification

The raw outcome of the measurement is a signal in counts per second as a function of the sputtering time. The sample is taken out and the depth of the crater is measured by a
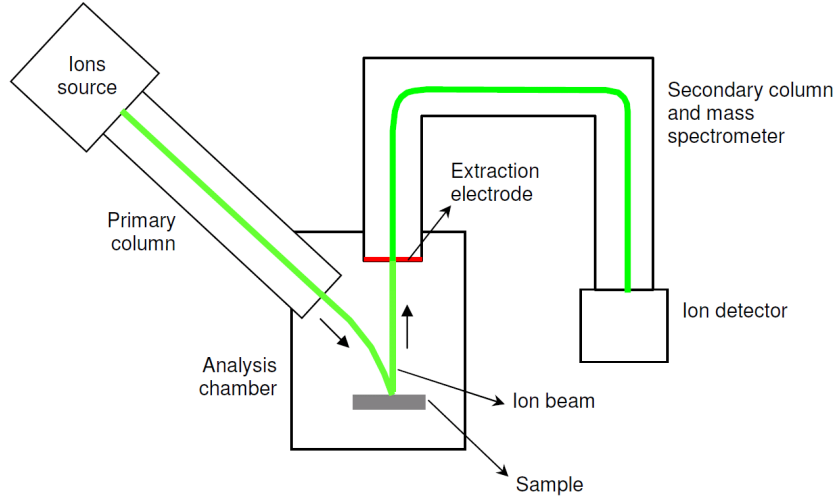
Figure II.8 – *Simplified drawing representing the different parts of a SIMS equipment, taken from* www.probion.fr/en.html .

profilometer. The sputtering time can then be converted into the depth, assuming a constant sputtering rate.

To convert the signal S_s of the species of interest s (in counts per time unit) in a concentration C_s (in atoms per volume unit), a reference sample is used. It has to be the same matrix as the measured sample because the ionization rate strongly depends on the chemical environment of the sputtered species. So in our case, monocrystalline reference samples were used. A known quantity per surface unit (also called "dose") of the species of interest, N_s^{ref}, is implanted in it. The reference sample is then sputtered in the same conditions as the ones used for the sample. From this, the signals of silicon and of the species of interest, S_{Si}^{ref} and S_s^{ref}, are obtained as a function of the sputtering time. The noise signal deep in the implanted reference sample indicates the limit of detection. The concentration in the measured sample is then obtained as :

$$C_s = RSF \times \frac{S_s}{S_{Si}} \tag{II.20}$$

where the Relative Sensitivity Factor (RSF) is defined as :

$$RSF = \frac{N_s^{ref} \times S_{Si}^{ref}}{S_s^{ref\ tot} \times R_s} \tag{II.21}$$

where R_s is the sputtering rate and $S_s^{ref\ tot}$ is the integration of the signal of the species s over the complete sputtering time in the reference sample :

$$S_s^{ref\ tot} = \int S_s^{ref}(t)\, \mathrm{d}t \tag{II.22}$$

These equations show us that any error in the sputtering rate evaluation by profilometry will result in an error in the deduced concentration in the sample.

6.3   Difficulties

Although it could seem to be a simple diagnostic (sputtering with energetic ions and collecting the charged species ejected), one must be aware of some misleading phenomena that can take place, in order to avoid wrong interpretations.

The depth resolution can be affected by several factors. For too high ion bombardment, atoms below the surface can be ejected. This artefact is called "mixing". To avoid it, the primary beam energy can be reduced below 1 keV. Another issue can be that the bottom of the crater can be curved. An answer to this is to spatially filter the secondary ions by a diaphragm at the entrance of the secondary column : for our measurements, only the ions coming from the flat $\sim 30\,\mu m$ diameter disk in the center of the crater are taken into account. Finally, a roughness can appear during the sputtering for some materials, for example due to different sputtering rates for grains with different crystallographic orientations. This phenomenon does most likely not occur in the typical conditions used for our measurements because the bombardment of our material leads to the amorphization of its surface. One can see that often the solutions lead to a reduced signal. As a consequence, there is a compromise, an optimum to be found.

Deducing the sputtering rate by measuring the depth of the crater with a profilometer is not an extremely accurate method and thus, a discrepency of around $\pm 10\,\%$ with the expected thickness is often noticed.

Finally, the formula II.20 is valid only for species present in small quantities (around $1\,\%$ or lower). Indeed, for higher concentrations, the measured signals of the species may not be proportional to their concentrations anymore. This is due to the so-called "matrix effect", where species present in high concentrations will have an effect on the ionization rate and on the sputtering rate of the matrix species and of the contamination species.

List of mass interferences

The mass resolution necessary to distinguish two atomic or molecular ions of masses M_1 and M_2 is defined as $M_1/(M_1-M_2)$. A mass interference can happen when two species (atomic or molecular) have very close masses. This artefact leads to an overestimation of the monitored species.

In this section, we have listed the most common mass interferences encountered in our hydrogenated silicon layers. The relative abundances of the different isotopes are written $A_{species}$ or are the percentages between parentheses.

Other lists of mass interferences can be found in the Appendix G of [48] and the most complete and practical one is the work of Burdo and Morrison [49].

- **Nitrogen :** Since the yield of formation of negative ions N^- is low and because of the strong interference with $^{28}Si^{2-}$, nitrogen is generally monitored under the form of a molecular ion with an element of the matrix : e.g. $^{28}Si^{14}N$ for our measurements. For this latter molecular ion, if carbon is also present, there is a risk of overestimation with $^{30}Si^{12}C$ ($A_{^{30}Si}$ is $3.10\,\%$), $^{29}Si^{12}CH$ ($A_{^{29}Si}$ is $4.67\,\%$) and $^{28}Si^{12}CH_2$. These interferences explain the apparent peak of N in the p-doped layers which contain carbon when they are made with trimethylboron (TMB, $B(CH_3)_3$).
- **Fluorine :** There is only one fluorine isotope, of atomic mass 19. The most likely mass interference is with $^{16}OH_3$. Mass interferences with ^{18}OH ($A_{^{18}O}$ of $0.2\,\%$), $^{17}OH_2$ ($A_{^{17}O}$ of $0.038\,\%$) or $^{13}C^{13}C^{12}C^{2-}$ ($A_{^{13}C}$ of $1.10\,\%$) are not very likely. The apparent fluorine peak often seen in the microcrystalline p-doped layers is thus difficult to explain. This peak is also present in an all-ARCAM stack on flat ZnO (Figure IV.80 page 178) and should therefore not be a problem.

- **Aluminum :** There is only one isotope, of mass 27. It can be overestimated due to the sputtering of $^{12}C_2H_3$, $^{12}C^{14}NH$ or $^{11}B^{16}O$ if there is boron.
- **Phosphorous :** There is only one isotope, of atomic mass 31. It will strongly interfere with ^{30}SiH (A$_{30Si}$ of 3.10 %). The apparent variations of the M=31 profile will then be related to the variations of the hydrogen concentration in the hydrogenated silicon matrix. The solution if one wants to obtain the concentration of phosphorous is to go at high mass resolution.
- **Iron :** The main (91.8 %) isotope of Fe, ^{56}Fe, interfers with $^{28}Si_2$. One can monitor the second most abundant isotope : ^{54}Fe (5.8 %).
- **Zinc :** The yield of formation of the negatively charged ion Zn^- is small. To measure it as a positively charged ion would require to switch from Cs^+ to O_2^+ primary ions so that it was measured as $^{64}Zn^{16}O^-$. As a result, it can interfere with $^{68}Zn^{12}C$ (A$_{68Zn}$ is 18.8 %) or $^{28}Si_2{}^{12}C_2$.

Some mass interferences can be suppressed by filtering the species according to their energy. Indeed, an atom and a molecular species of the same mass will not be ejected from the bombarded sample with the same energy distribution.

7   Steady-state photoconductivity (SSPC)

The goal of this measurement is to deduce the mobility-lifetime product of the electrons, written $\mu_e \tau_e$. To do so, the sample with coplanar contacts is polarized with a DC voltage and illuminated by a monochromatic constant flux of photons F_{dc} with an energy higher than the bandgap. In our case, we used a light-emitting diode at 640 nm, which can produce fluxes between 10^{12} and 10^{15} photons $\cdot$ cm^{-2} $\cdot$ s^{-1}. The constant photocurrent I_{photo} is measured.

For an elementary layer of thickness $\mathrm{d}z$ at a depth z, we have :

$$\mathrm{d}I_{photo}(z) = L \cdot E \cdot \sigma_{photo}(z) \cdot \mathrm{d}z \qquad (\text{II.23})$$

where L is the length of the contacts, E is the electric field and σ_{photo} is the photoconductivity.

Assuming a model of transport by free carriers above the mobility edge, the conductivity at the depth z can be written as :

$$\sigma_{photo}(z) = e \, \mu_n^0 \, \Delta n(z) + e \, \mu_p^0 \, \Delta p(z) \qquad (\text{II.24})$$

where e is the elementary charge, μ_n^0 and μ_p^0 are the band mobilities of the free electrons and holes respectively, and Δn and Δp are the densities of free carriers in excess defined as $\Delta n = n - n_0$ and $\Delta p = p - p_0$, where n_0 and p_0 are the densities of electrons and holes in the dark.

Now, making the assumptions that $\mu_p^0 \ll \mu_n^0$ and that $n_0 \ll n$, equation II.24 can be simplified as a one-carrier equation :

$$\sigma_{photo}(z) = e \, \mu_n^0 \, n(z) \,. \qquad (\text{II.25})$$

$n(z)$ can be written as $n(z) = \tau_n^R \, G(z)$, with the electron recombination time τ_n^R and the generation rate G :

$$G(z) = (1 - R) \, F_{dc} \, \exp(-\alpha z) \, \alpha \qquad (\text{II.26})$$

where R is the reflection coefficient at the air/silicon interface due to the difference of optical indexes, F_{dc} is the photon flux, α is the absorption coefficient of the silicon layer taken at the wavelength of the photon flux and obtained from the spectroscopic ellipsometry measurement in our case.

The photocurrent is then :

$$I_{photo} = \int_0^t \mathrm{d}I_{photo}(z) = L\,E\,e\,\mu_n^0\,\tau_n^R\,(1-R)\,F_{dc}\,(1-\exp(-\alpha t)) \qquad \text{(II.27)}$$

where t is the total thickness of the layer (known from the ellipsometry model).

The $\mu\tau$ product of the majority carrier is finally deduced as :

$$\boxed{\mu_n^0\tau_n^R = \frac{I_{measured} - I_{dark}}{L\,E\,e\,(1-R)\,F_{dc}\,(1-\exp(-\alpha t))}} \qquad \text{(II.28)}$$

The $\mu\tau$ product is an important parameter, e.g. for an electric field E, the average distance d a free carrier travels before recombining is proportional to $d \propto \mu^0\tau^R E$ [50]. But the illumination flux has to be taken into account for proper interpretation of the results. Indeed, the $\mu\tau$ products *decrease* when the generation rate *increases* because of the enhanced splitting of the Fermi quasi-levels [51].

Apart from these precautions, SSPC is a good illustration of the complexity of microcrystalline silicon as the $\mu\tau$ values depend on the film microstructure and can be affected by contamination :

- Microstructure : The higher the crystalline fraction, the higher the $\mu\tau$ value. For example, the values found in [52] as a function of the crystalline fractions F_c given by ellipsometry are : $2 \times 10^{-5}\,\mathrm{cm^2\,V^{-1}}$ for F_c of $30\,\%$; $8 \times 10^{-5}\,\mathrm{cm^2\,V^{-1}}$ for F_c of $67\,\%$; $7 \times 10^{-4}\,\mathrm{cm^2\,V^{-1}}$ for F_c of $79\,\%$ and $3 \times 10^{-4}\,\mathrm{cm^2\,V^{-1}}$ for F_c of $96\,\%$. Note that all these films were probably affected by n-type contaminations.
- Contamination : The $\mu^0\tau^R$ products greatly depend on the position of the Fermi level. In case of incorporation of oxygen during or after the deposition, the unintentional n-type doping results in greater values of $\mu_e^0\tau_e^R$ [53]. Oxygen is going to induce negatively charged deep defects in the grain boundaries and to affect the transport of holes. The "normal" values for intrinsic microcrystalline silicon seem to be around $1 \times 10^{-7}\,\mathrm{cm^2\,V^{-1}}$ [45] or even higher than $10^{-6}\,\mathrm{cm^2\,V^{-1}}$ [54].

Furthermore, there is a strong dependence of the photoconductivity as a function of the generation rate. In highly photosensitive semiconductors like amorphous and microcrystalline silicon, if the illumination conditions result in $p_0 \ll \Delta n$, it implies that $\sigma_{photo} \propto G^{1/2}$, which is called the bimolecular recombination regime [55]. The experimental values reported are $\sigma_{photo} \propto G^{0.50-0.85}$ in [56] or $\sigma_{photo} \propto G^{0.5-1}$ in [57]. As a result, the values of $\mu\tau$ should be given with the illumination flux for absolute comparisons.

As a conclusion, we will mainly use this diagnostic for relative comparisons within a series of samples.

8   The Steady-State Photocarrier Grating method (SSPG)

This technique was first proposed by Ritter and coworkers in 1986 [57]. Its goal is to extract the ambipolar diffusion length L_{amb}, which is the hole diffusion length L_d in our case, since for microcrystalline silicon, holes are the limiting species for transport. However, the measurement is performed with coplanar contacts and therefore gives the diffusion length *parallel* to the substrate, which is not the direction of interest for solar cells.

Very good values for high quality materials, for a generation rate of $\sim 1.5\times 10^{21}\,\mathrm{cm}^{-3}\,\mathrm{s}^{-1}$ are $\sim 150\,\mathrm{nm}$ for a-Si:H and $\sim 300\,\mathrm{nm}$ for μc-Si:H [56].

The typical experimental setup is shown in Figure II.9 In our case, the light source is a Helium-Neon laser at 677 nm. The laser beam is split and one of the beams is attenuated. This way, it represents a small perturbation to the uniform illumination of the other beam. The superposition of the two coherent beams creates interferences between the two coplanar contacts. The step of the interference fringes Λ can be varied by changing the angle of the incident beams. The half-wavelength plane can be rotated to obtain parallel or perpendicular polarizations. In the first case, the interferences are present, in the second case, they disappear. A DC voltage is applied to the contacts and the current is measured with and without interferences.

The quantity used to obtain the diffusion length is the ratio of the collected photogenerated currents with and without interferences as a function of the interference step Λ [58] :

$$\beta = \frac{J_{coherent}}{J_{incoherent}} = 1 - \frac{2\,\Phi}{\left(1 + \frac{4\,\pi^2 L_d{}^2}{\Lambda^2}\right)^2} \tag{II.29}$$

where $\Phi = \alpha \times \gamma_0^2 \times \gamma_{dark}$:

- α is the exponent of the power law dependence of the photoconductivity as a function of the generation rate : $\sigma_{photo} \propto G^\alpha$.
- γ_0 is the grating quality factor. It can be affected by misalignments in the experimental setup and/or by the roughness of the sample surface. Its value goes from 1 (in the case of an ideal grating) to 0.
- $\gamma_{dark} = \sigma_{photo}/(\sigma_{photo} + \sigma_{dark})$ and should be very close to unity for good quality films.

Values of Φ close to 1 indicate that the grating is very sharp, i.e. with well-defined fringes, while lower values correspond to "blurred" fringes, e.g. due to surface or internal scattering. In [59], their grating quality parameter γ_0 falls from 0.9 to 0.5 at the amorphous – microcrystalline transition due to the increase of the surface roughness. Their Φ values can range from 0.16 to 0.9 .

The assumptions behind this formula are that the light is absorbed uniformly on the whole thickness of the film and that there is no surface recombination. These two phenomena would result in a gradient in the direction perpendicular to the film surface. Correcting factors can be added to the formula II.29 to take into account the gradient of the carriers along the depth of the film due to surface recombination (see [58] for more details).

In our case, the fit was performed over the two parameters Φ and L_d. α and γ_{dark} have to be determined separately to get γ_0.
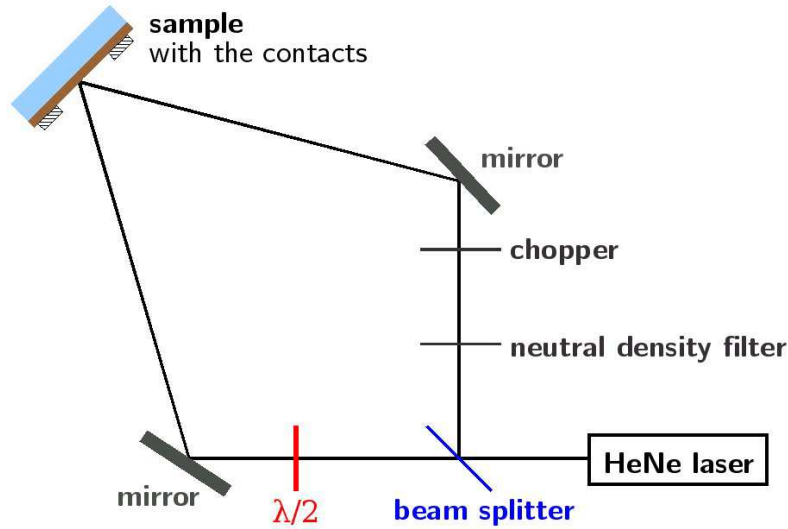
Figure II.9 – *Typical configuration of the SSPG experimental setup. The element labelled $\lambda/2$ is a half wavelength retardation plate used to change the polarization of the beam. The collected current is measured by a lock-in amplifier system at the frequency of the chopper.*

It can be intuitively understood that the illuminated zones are characterized by a high level of photogenerated carriers and that these will diffuse towards the zones of destructive interferences and also drift due to the electric field. As a consequence, β will be close to 1 as long as the diffusion length of holes is greater than the interference step and in such cases, the photocarrier density will be uniform between the two coplanar contacts. For higher values of Λ, β will drop (see Figure IV.50 page 140).

One can also see that the greater the contrast between the illuminated zones and the zones of destructive interferences, the higher the sensitivity (i.e. the greater the β variations). For this reason, this technique is less sensitive with µc-Si than with a-Si due to the higher dark conductivity of the former. As a consequence, SSPG measurements for microcrystalline silicon are usually made at higher generation rates. Since there is no light induced degradation in highly crystallized µc-Si:H and only a very small dependence of the ambipolar diffusion as a function of the generation rate, the measurement is still valid. Indeed, L_d scales as a power law of the generation rate [56] : the authors found an exponent of the power law in the range -0.18 to $+0.8$. (For a-Si, their exponent is always negative.)

Validity of SSPG

First developed for amorphous silicon, the possibility to apply SSPG to microcrystalline silicon to extract the ambipolar length has been studied in detail in [56]. To assess the validity and the quality of an L_d measurement, one needs to know the quality factor γ_0 which measures light scattering due to the roughness of the sample surface and other problems in the experimental setup. For the SSPG technique to be valid on microcrystalline silicon, the diffusion length has to be distinguished from the dielectric relaxation length. The latter strongly decreases with the generation rate while the former does not depend a lot on it so that this dependency should be systematically measured [56]. Finally, diffusion has to be the dominant phenomenon with respect to drift. This can be checked by varying the applied voltage : the ratio β is independent of the voltage when diffusion is dominant.

9   Time Resolved Microwave Conductivity (TRMC)

This technique has been used to characterize a few samples during this work and we will only briefly outline its basic principle here.

To obtain information on the opto-electronic properties of semiconductors, this method exposes the sample to a laser pulse. During and after the pulse of the YAG laser (duration : a few nanoseconds ; wavelengths : 1064, 532 or 266 nm), the photogenerated carriers diffuse, recombine, either in the bulk or at the interfaces and are trapped, in deep defects or in bandtail states. Then, the sample reaches back its thermodynamic equilibrium. The photo-generated carriers induce a transient change of the conductivity, and thus, of the complex dielectric function of the material. This variation of the dielectric function is probed by recording the evolution of the reflectivity of the sample to microwaves. The amplitude of the change of the reflection coefficient is directly related to the sum of the electron and hole mobilities. It has to be made clear that what is measured is the *local* mobilities inside the crystallites [60].

The experimentral setup has been described in detail elsewhere [61] and one of the advantages of this technique is that is does not require any electrode to be deposited on the sample. The measured quantity is the time variation of the electrical output of the detector, ΔV, which is proportional to the reflected microwave power. The mobility can be extracted from it, provided the maximum excess carrier density ΔN_{max} and the sensitivity of the experimental setup S are known (see [61]) :

$$\Delta V = S \times \mu_{eff} \times \Delta N_{max} \tag{II.30}$$

S is deduced from the measurement of a reference sample of known mobility. μ_{eff} is an effective mobility : it is the sum of the mobility of holes and electrons and it is averaged over the film thickness. It is not sensitive to boundaries between small grains, but to column barriers [62].

This method was first used to study monocrystalline silicon [63] and then its usefulness for silicon thin films has been established, e.g. for in-situ [64] and ex-situ characterizations of transport in microcrystalline silicon [65, 62, 66].

In addition to their mobility, an effective lifetime of the carriers can be deduced from the time evolution of the reflected microwave signal. This lifetime value depends on the pho-togenerated carrier density and must consequently be measured at low laser flux. There are typically two slopes of decay of the reflectivity. Indeed, after the pulse, the high photo-generated carrier concentrations (densities of $10^{15} - 10^{18} \, \text{cm}^{-3}$ depending on the laser power) induce a splitting of the Fermi quasi-levels, which then decays when the carriers recombine. The first slope depends on the incident flux of the laser and is attributed to recombination in levels around $0.2 \, \text{eV}$ from valence or conduction band edges. The second slope is almost independent of the laser flux and corresponds to recombination in deeper states. This latter slope results in lifetime values comparable to other techniques.

10   Characterization of the solar cells

Once the stack of doped and intrinsic layers is finished and the contacts have been evaporated, we systematically perform spectral response and then current – voltage curves measurements before and after annealing.

10.1   Spectral response

The goal of spectral response characterization is to retrieve detailed informations about the cell efficiency. It measures the collected current per unit of incident illumination power as a function of the wavelength. Thus, the spectral response is in Amperes per Watt (A/W). It can be converted in the measurement of the average number of eletron-hole pair collected per incident photon, called the quantum efficiency. In this work, we will use the latter form.

All the quantum efficiencies given in this manuscript are *external* ones (EQE). That is to say they include the partial reflexion of the incoming photons due to the differences in optical indexes at the interfaces (air/glass, glass/TCO, TCO/cell) and the absorption of the glass and TCO.

The experimental setup and the measurement procedure can be briefly described : A white source is filtered by 12 different filters from a turning filter-wheel and its beam is chopped. This beam is focused on the solar cell and the collected current is amplified with a lock-in system at the frequency of the chopper. A commercial diode of known EQE (given by the manufacturer) is first used. The current values as a function of the filters are stored by the software as a calibration of the lamp intensity and to check its stability.

We carried out all our spectral response measurements with the addition of a white bias light (not chopped) from a second source to be in conditions of homogeneous photogeneration throughout the intrinsic layer.

The EQE at $0\,V$ (short-circuit conditions) is then multiplied by the solar spectrum and integrated over the wavelengths to give the short-circuit current [67] :

$$J_{sc} = q \int EQE(\lambda) \times S_{sun}(\lambda)\,\mathrm{d}\lambda \qquad (II.31)$$

with q, the elementary charge and S_{sun}, the spectral flux density of photons.

In this measurement, two aspects of the material and device are probed : the absorption and then, the collection.

Since the absorption coefficient in silicon strongly depends on the wavelength, the EQE will therefore provide informations on the collection of the photocarriers generated along the depth of the intrinsic layer. The blue region will mainly characterize the p-i interface region. In the red, the main limiting factor will probably be the transport of holes until the p-doped contact. Furthermore, analysis of the evolution of the spectral response when an additional bias voltage is applied can bring interesting informations on the profile of the internal electric field.

10.2   J(V) curves

Figure II.10 – *Characteristics of a J(V) curve. (See text for details.)*

The experimental setup is quite simple : A halogen light bulb (Solux "4700 °K" of 50 W) is supplied by a variable DC power supply whose voltage is adjusted in order to reproduce the short-circuit current value obtained from the EQE measurement (see equation II.31). During the measurement, the cell is cooled down by a fan. A mask with the same diameter as the metal dot (4 mm) defines the illuminated area and avoids lateral collection. This procedure ensures to be close to the Standard Test Conditions (STC), which are defined by an incident power density of $1000\,\mathrm{W\cdot cm^{-2}}$, a temperature of 25 °C and an Air Mass 1.5 spectrum (which corresponds to the irradiance at an altitude of 0 m received from the sun being at an angle of 42 ° above the horizon, without any cloud).

A Keithley 2400 SourceMeter controlled by a computer is used to provide voltage sweeps and to record the current. Figure II.10 illustrates the typical curve obtained and its characteristics : the short-circuit current density J_{sc} and the open-circuit voltage V_{oc} are shown, as well as the series and parallel resistances R_s and R_p, and the fill factor FF defined as :

$$R_s \;=\; \frac{1}{\left(\frac{\mathrm{d}J}{\mathrm{d}V}\right)_{J=0}} \tag{II.32}$$

$$R_p \;=\; \frac{1}{\left(\frac{\mathrm{d}J}{\mathrm{d}V}\right)_{V=0}} \tag{II.33}$$

$$FF \;=\; \frac{V_{max} \times J_{max}}{V_{oc} \times J_{sc}} \tag{II.34}$$

A Labview program then analyzes the curves and give us the characteristics of the cells. The efficiency of the cell is given by :

$$\boxed{\eta = \frac{FF \times V_{oc} \times J_{sc}}{P_{sun}}} \tag{II.35}$$

where P_{sun} is the sun power illumination per unit surface.

11   Conclusion

Being limited to three depositions per day forced us to develop a strategy based on multiple characterizations. The question of the best diagnostic or of the best property of the material on which the process of optimization should be based has been a crucial matter throughout these three years of work. This is the reason why we tried to emphasize the difficulties and limits of each diagnostic in this chapter. Similarly, throughout Chapter IV, we will try to compare the results given by the different methods and to explain the discrepencies.

Since our cells have always shown low efficiencies, our goal was to find diagnostics revealing a problem in the material or in the device. Indeed, once a source of limitation is clearly identified, it can be monitored while varying the deposition conditions in order to analyze its evolution and eventually, to suppress it completely.

But as we will see, the improvement of some of the material characteristics, evidenced by diagnostics such as ellipsometry, SIMS or SSPG, did not always result in an improvement of the corresponding cells.

Some other diagnostics will be introduced directly in the Chapter IV when the associated results will be given.

Bibliography

[1] D. P. DeWitt and Gene D. Nutter, editors. *Theory and Practice of Radiation Thermometry*. Wiley-Interscience, 1988.

[2] P. Roca i Cabarrocas, P. Bulkin, D. Daineka, T. H. Dao, P. Leempoel, P. Descamps, T. Kervyn de Meerendre, and J. Charliac. Advances in the deposition of microcrystalline silicon at high rate by distributed electron cyclotron resonance. *Thin Solid Films*, 516(20):6834–6838, August 2008.

[3] Thien Hai DAO. *Dépôt de couches minces de silicium à grande vitesse par plasma MDECR*. PhD thesis, École Polytechnique, May 2007.

[4] L. Houben, M. Luysberg, P. Hapke, R. Carius, F. Finger, and H. Wagner. Structural properties of microcrystalline silicon in the transition from highly crystalline to amorphous growth. *Philosophical Magazine A*, 77, 1998.

[5] Jr. G. E. Jellison, M. F. Chisholm, and S. M. Gorbatkin. Optical functions of chemical vapor deposited thin-film silicon determined by spectroscopic ellipsometry. *Applied Physics Letters*, 62(25):3348–3350, 1993.

[6] P. Roca i Cabarrocas, S. Hamma, A. Hadjadj, J. Bertomeu, and J. Andreu. New features of the layer-by-layer deposition of microcrystalline silicon films revealed by spectroscopic ellipsometry and high resolution transmission electron microscopy. *Applied Physics Letters*, 69(4):529–531, 1996.

[7] G. E. Jellison Jr. Data analysis for spectroscopic ellipsometry. *Thin Solid Films*, 234:416–422, October 1993.

[8] G. E. Jellison. Use of the biased estimator in the interpretation of spectroscopic ellipsometry data. *Appl. Opt.*, 30(23):3354–3360, 1991.

[9] A. Fontcuberta i Morral, P. Roca i Cabarrocas, and C. Clerc. Structure and hydrogen content of polymorphous silicon thin films studied by spectroscopic ellipsometry and nuclear measurements. *Physical Review B (Condensed Matter and Materials Physics)*, 69(12):125307, 2004.

[10] A. Fontcuberta i Morral and P. Roca i Cabarrocas. Etching and hydrogen diffusion mechanisms during a hydrogen plasma treatment of silicon thin films. *Journal of Non-Crystalline Solids*, 299–302(1):196–200, April 2002.

[11] H. Touir and P. Roca i Cabarrocas. Optical dispersion relations for crystalline and microcrystalline silicon. *Phys. Rev. B*, 65(15):155330, Apr 2002.

[12] John R. Ferraro, Kazuo Nakamoto, and Chris W. Brown. *Introductory Raman Spectroscopy*. Academic Press, second edition, 2003.

[13] G. Viera, S. Huet, and L. Boufendi. Crystal size and temperature measurements in nanostructured silicon using Raman spectroscopy. *Journal of Applied Physics*, 90(8):4175–4183, 2001.

[14] A. T. Voutsas, M. K. Hatalis, J. Boyce, and A. Chiang. Raman spectroscopy of amorphous and microcrystalline silicon films deposited by low-pressure chemical vapor deposition. *Journal of Applied Physics*, 78(12):6999–7006, 1995.

[15] Z. Iqbal, A. P. Webb, and S. Veprek. Polycrystalline silicon films deposited in a glow discharge at temperatures below 250 °C. *Applied Physics Letters*, 36(2):163–165, 1980.

[16] M. H. Brodsky, Manuel Cardona, and J. J. Cuomo. Infrared and Raman spectra of the silicon-hydrogen bonds in amorphous silicon prepared by glow discharge and sputtering. *Phys. Rev. B*, 16(8):3556–3571, Oct 1977.

[17] C. Godet, B. Marchon, and M. P. Schmidt. Characterization of microcrystallinity in hydrogenated silicon thin films. *Thin Solid Films*, 155(2):227–242, December 1987.

[18] C. Smit, R. A. C. M. M. van Swaaij, H. Donker, A. M. H. N. Petit, W. M. M. Kessels, and M. C. M. van de Sanden. Determining the material structure of microcrystalline silicon from Raman spectra. *Journal of Applied Physics*, 94(5):3582–3588, 2003.

[19] R. Tsu, J. Gonzalez-Hernandez, S. S. Chao, S. C. Lee, and K. Tanaka. Critical volume fraction of crystallinity for conductivity percolation in phosphorus-doped Si:F:H alloys. *Applied Physics Letters*, 40(6):534–535, 1982.

[20] E. Bustarret, M. A. Hachicha, and M. Brunel. Experimental determination of the nanocrystalline volume fraction in silicon thin films from Raman spectroscopy. *Applied Physics Letters*, 52(20):1675–1677, 1988.

[21] E. Vallat-Sauvain, C. Droz, F. Meillaud, J. Bailat, A. Shah, and C. Ballif. Determination of Raman emission cross-section ratio in hydrogenated microcrystalline silicon. *Journal of Non-Crystalline Solids*, 352(9-20):1200 – 1203, 2006. Proceedings of the 21st International Conference on Amorphous and Nanocrystalline Semiconductors.

[22] Z. Iqbal, S. Veprek, A. P. Webb, and P. Capezzuto. Raman scattering from small particle size polycrystalline silicon. *Solid State Communications*, 37(12):993–996, March 1981.

[23] B. Kalache, A. I. Kosarev, R. Vanderhaghen, and P. Roca i Cabarrocas. Ion bombardment effects on microcrystalline silicon growth mechanisms and on the film properties. *Journal of Applied Physics*, 93(2):1262–1273, 2003.

[24] B. Pivac, K. Furić, D. Desnica, A. Borghesi, and A. Sassella. Raman line profile in polycrystalline silicon. *Journal of Applied Physics*, 86(8):4383–4386, 1999.

[25] I. H. Campbell and P. M. Fauchet. The effects of microcrystal size and shape on the one phonon Raman spectra of crystalline semiconductors. *Solid State Communications*, 58(10):739 – 741, 1986.

[26] H. Richter, Z. P. Wang, and L. Ley. The one phonon Raman spectrum in microcrystalline silicon. *Solid State Communications*, 39(5):625 – 629, 1981.

[27] Jian Zi, H. Büscher, C. Falter, W. Ludwig, Kaiming Zhang, and Xide Xie. Raman shifts in Si nanocrystals. *Applied Physics Letters*, 69(2):200–202, 1996.

[28] V. Paillard, P. Puech, M. A. Laguna, R. Carles, B. Kohn, and F. Huisken. Improved one-phonon confinement model for an accurate size determination of silicon nanocrystals. *Journal of Applied Physics*, 86(4):1921–1924, 1999.

[29] Pavel V. Bulkin, Pieter L. Swart, and Beatrys M. Lacquet. Electron cyclotron resonance plasma enhanced chemical vapour deposition and optical properties of SiO_x thin films. *Journal of Non-Crystalline Solids*, 226(1-2):58 – 66, 1998.

[30] A. A. Langford, M. L. Fleet, B. P. Nelson, W. A. Lanford, and N. Maley. Infrared absorption strength and hydrogen content of hydrogenated amorphous silicon. *Phys. Rev. B*, 45(23):13367–13377, Jun 1992.

[31] A. H. M. Smets, W. M. M. Kessels, and M. C. M. van de Sanden. Vacancies and voids in hydrogenated amorphous silicon. *Applied Physics Letters*, 82(10):1547–1549, 2003.

[32] U. Kroll, J. Meier, A. Shah, S. Mikhailov, and J. Weber. Hydrogen in amorphous and microcrystalline silicon films prepared by hydrogen dilution. *Journal of Applied Physics*, 80(9):4971–4975, 1996.

[33] A. H. M. Smets, T. Matsui, and M. Kondo. Infrared analysis of the bulk silicon-hydrogen bonds as an optimization tool for high-rate deposition of microcrystalline silicon solar cells. *Applied Physics Letters*, 92(3):033506, 2008.

[34] T. Kilper, W. Beyer, G. Bräuer, T. Bronger, R. Carius, M. N. van den Donker, D. Hrunski, A. Lambertz, T. Merdzhanova, A. Mück, B. Rech, W. Reetz, R. Schmitz, U. Zastrow, and A. Gordijn. Oxygen and nitrogen impurities in microcrystalline silicon deposited under optimized conditions: Influence on material properties and solar cell performance. *Journal of Applied Physics*, 105(7):074509, 2009.

[35] F. Finger, R. Carius, T. Dylla, S. Klein, S. Okur, and M. Günes. Stability of microcrystalline silicon for thin film solar cell applications. *IEE Proc. – Circuits Devices Syst.*, 150(4):300–308, August 2003.

[36] K. Brühne, M. B. Schubert, C. Köhler, and J. H. Werner. Nanocrystalline silicon from hot-wire deposition – a photovoltaic material? *Thin Solid Films*, 395(1-2):163 – 168, 2001.

[37] V. A. Burrows, Y. J. Chabal, G. S. Higashi, K. Raghavachari, and S. B. Christman. Infrared spectroscopy of Si(111) surfaces after HF treatment: Hydrogen termination and surface morphology. *Applied Physics Letters*, 53(11):998–1000, 1988.

[38] E. Vallat-Sauvain, U. Kroll, J. Meier, A. Shah, and J. Pohl. Evolution of the microstructure in microcrystalline silicon prepared by very high frequency glow-discharge using hydrogen dilution. *Journal of Applied Physics*, 87(6):3137–3142, 2000.

[39] Soo Young Yoon, Seong Jin Park, Kyung Ho Kim, Jin Jang, and Chae Ok Kim. Structural and electrical properties of polycrystalline silicon produced by low-temperature Ni silicide mediated crystallization of the amorphous phase. *Journal of Applied Physics*, 87(1):609–611, 2000.

[40] R. B. Bergmann and J. H. Werner. The future of crystalline silicon films on foreign substrates. *Thin Solid Films*, 403-404:162–169, February 2002.

[41] Takuya Matsui, Masaharu Tsukiji, Hiroyuki Saika, Toshihiko Toyama, and Hiroaki Okamoto. Correlation between Microstructure and Photovoltaic Performance of Polycrystalline Silicon Thin Film Solar Cells. *Jpn. J. Appl. Phys.*, 41:20–27, 2002.

[42] T. Kitagawa, M. Kondo, and A. Matsuda. In situ observation of low temperature growth of crystalline silicon using reflection high-energy electron diffraction. *Journal of Non-Crystalline Solids*, 266-269(Part 1):64 – 68, 2000.

[43] J. H. Werner, R. Dassow, T. J. Rinke, J. R. Kohler, and R. B. Bergmann. From polycrystalline to single crystalline silicon on glass. *Thin Solid Films*, 383:95–100, February 2001.

[44] M. Fonrodona, D. Soler, J. M. Asensi, J. Bertomeu, and J. Andreu. Studies on grain boundaries in nanocrystalline silicon grown by hot-wire CVD. *Journal of Non-Crystalline Solids*, 299-302(Part 1):14 – 19, 2002.

[45] M. Goerlitzer, P. Torres, N. Beck, N. Wyrsch, H. Keppner, J. Pohl, and A. Shah. Structural properties and electronic transport in intrinsic microcrystalline silicon deposited by the VHF-GD technique. *Journal of Non-Crystalline Solids*, 227-230(Part 2):996 – 1000, 1998.

[46] B. D. Cullity. *Elements of X-Ray Diffraction.* Addison-Wesley, 1956. Pages 96 – 102.

[47] Harold P. Klug and Leroy E. Alexander. *X-ray diffraction procedures for polycrystalline and amorphous materials.* John Wiley, 1954. Chapter 9 : Crystallite-size determination from line broadening, page 491 to 538 of the second printing of 1959.

[48] R. G. Wilson, F. A. Stevie, and C. W. Magee. *Secondary Ion Mass Spectrometry: A Practical Handbook for Depth Profiling and Bulk Impurity Analysis.* John Willey & Sons, 1989.

[49] R. A. Burdo and G. H. Morrison. Table of Atomic and Molecular Lines for Spark Source Mass Spectrometry of Complex Sample-Graphite Mixes. Technical Report #1670, Materials Science Center, Cornell University, Ithaca, New York, 1971.

[50] M. Goerlitzer, P. Torres, C. Droz, and A. Shah. Extension of the a-Si:H electronic transport model to μc-Si:H: use of the $\mu^0\tau^0$ product to correlate electronic transport properties and solar cell performances. *Solar Energy Materials and Solar Cells*, 60(2):195 – 200, 2000.

[51] S. Okur, M. Günes, O. Göktas, F. Finger, and R. Carius. Electronic transport properties of microcrystalline silicon thin films prepared by VHF-PECVD. *Journal of Materials Science: Materials in Electronics*, 15:187–191, 2004.

[52] P. St'ahel, S. Hamma, P. Sládek, and P. Roca i Cabarrocas. Metastability studies in silicon thin films: from short range ordered to medium and long range ordered materials. *Journal of Non-Crystalline Solids*, 227-230(Part 1):276 – 280, 1998.

[53] C. Droz, M. Goerlitzer, N. Wyrsch, and A. Shah. Electronic transport in hydrogenated microcrystalline silicon: similarities with amorphous silicon. *Journal of Non-Crystalline Solids*, 266-269(Part 1):319 – 324, 2000.

[54] J. P. Kleider, C. Longeaud, R. Brüggemann, and F. Houzé. Electronic and topographic properties of amorphous and microcrystalline silicon thin films. *Thin Solid Films*, 383(1-2):57 – 60, 2001.

[55] Monica Brinza, Jan Willekens, Mohammed L. Benkhedir, Evguenia V. Emelianova, and Guy J. Adriaenssens. Photoconductivity methods in materials research. *Journal of Materials Science: Materials in Electronics*, 16:703 – 713, 2005.

[56] M. Goerlitzer, N. Beck, P. Torres, J. Meier, N. Wyrsch, and A. Shah. Ambipolar diffusion length and photoconductivity measurements on "midgap" hydrogenated microcrystalline silicon. *Journal of Applied Physics*, 80(9):5111–5115, 1996.

[57] D. Ritter, E. Zeldov, and K. Weiser. Steady-state photocarrier grating technique for diffusion length measurement in photoconductive insulators. *Applied Physics Letters*, 49(13):791–793, 1986.

[58] D. Ritter, K. Weiser, and E. Zeldov. Steady-state photocarrier grating technique for diffusion-length measurement in semiconductors: Theory and experimental results for amorphous silicon and semi-insulating GaAs. *Journal of Applied Physics*, 62(11):4563–4570, 1987.

[59] S. Okur, M. Günes, F. Finger, and R. Carius. Diffusion length measurements of microcrystalline silicon thin films prepared by hot-wire/catalytic chemical vapor deposition (HWCVD). *Thin Solid Films*, 501(1-2):137 – 140, 2006. Proceedings of the Third International Conference on Hot-Wire CVD (Cat-CVD) Process.

[60] R. Brenot, R. Vanderhaghen, B. Drévillon, P. Roca i Cabarrocas, R. Rogel, and T. Mohammed-Brahim. Transport mechanisms in hydrogenated microcrystalline silicon. *Thin Solid Films*, 383(1-2):53 – 56, 2001.

[61] Romain Brenot. *Corrélation entre mode de croissance et propriétés de transport du silicium microcristallin, établie par réflectométrie micro-onde et ellipsométrie.* PhD thesis, École Polytechnique, February 2000.

[62] Samir Kasouit. *Mécanismes de croissance et transport dans le silicium microcristallin fluoré. Application aux transistors en couches minces et transfert technologique.* PhD thesis, École Polytechnique, October 2003.

[63] M. Kunst and G. Beck. The study of charge carrier kinetics in semiconductors by microwave conductivity measurements. *Journal of Applied Physics*, 60(10):3558–3566, 1986.

[64] R. Brenot, R. Vanderhaghen, B. Drévillon, and P. Roca i Cabarrocas. Real-time measurement of the evolution of carrier mobility in thin-film semiconductors during growth. *Applied Physics Letters*, 74(1):58–60, 1999.

[65] R. Brenot, R. Vanderhaghen, B. Drevillon, I. French, and P. Roca i Cabarrocas. Time resolved microwave conductivity measurements for the characterization of transport properties in thin film microcrystalline silicon. *Thin Solid Films*, 296(1-2):94 – 97, 1997. European Materials Research Society 1996 Spring Meeting, Symposium B: Thin Film Materials for Large Area Electronics.

[66] Yassine Djeridane. *Synthèse de nanocristaux par plasma froid et leur rôle dans la croissance de couches minces de silicium microcristallin : Application aux transistors.* PhD thesis, École Polytechnique, May 2008.

[67] Jenny Nelson. *The Physics of Solar Cells.* Imperial College Press, 2003.

Chapter III

The Matrix Distributed Electron Cyclotron Resonance plasma

Contents

1   Introduction

MDECR can either stand for Matrix Distributed Electron Cyclotron Resonance (ECR) or for Multi-Dipolar ECR. With helicon sources and inductively coupled plasmas (ICP), MDECR belongs to the family of the low pressure, high density plasmas.

In this chapter, we will first expose the general basic principle of ECR sources, then briefly list the different kinds of reactors based on this plasma generation technique. This will allow us to emphasize the advantages of the MDECR configuration as compared to the former technologies. The two MDECR reactors used during this PhD will be presented. The second one, which has been assembled during this project, will be described in great detail.

2   The Electron Cyclotron Resonance (ECR) effect

Before presenting the different types of plasma sources based on this effect, we will explain its basic principle here.

The trajectory of an electron in a uniform static magnetic field of strength B_0 is well known. The result of the Lorentz force is a helicoidal trajectory around the magnetic lines with a frequency f_{Larmor} and a radius r_{Larmor} given by :

$$
\begin{aligned}
f_{Larmor} &= \frac{q_e\, B_0}{2\,\pi\, m_e} & \text{(III.1)} \\
r_{Larmor} &= \frac{m_e\, v_\perp}{q_e\, B_0} & \text{(III.2)}
\end{aligned}
$$

where q_e is the elementary charge, m_e is the eletron mass and $v_\perp$ is the electron velocity in the plane perpendicular to the magnetic field.

A linearly polarized electric field is superposed to the magnetic field. Its frequency is in the microwave range, $f_{MW} = 2.45\,\text{GHz}$, which is an industrial standard and which corresponds to a wavelength of $\sim 12\,\text{cm}$ in vacuum. If the electron gyration frequency matches the electric field frequency, a resonant absorption will take place.

This can be understood by decomposing the linearly oscillating electric field into two rotating contributions : a right-hand and a left-hand circularly polarized component (see Figure III.1). If $f_{Larmor} = 2.45\,\text{GHz}$, the component of the electric field rotating in the same way as the electron will *constantly* accelerate it while the other component will have a null effect when averaged over one period.

The condition $f_{MW} = f_{Larmor}$ indicates that the resonant absorption will take place at the specific value of the magnetic field of $\sim 875\,\text{Gauss}$. The electrons will be trapped in the magnetic field and acquire sufficiently high velocities to dissociate or ionize the silane molecules in order to sustain the discharge and to create the reactive species. For this, the pressure has to be low enough, typically lower than $\sim 10\,\text{mTorr}$, so that the electron can be
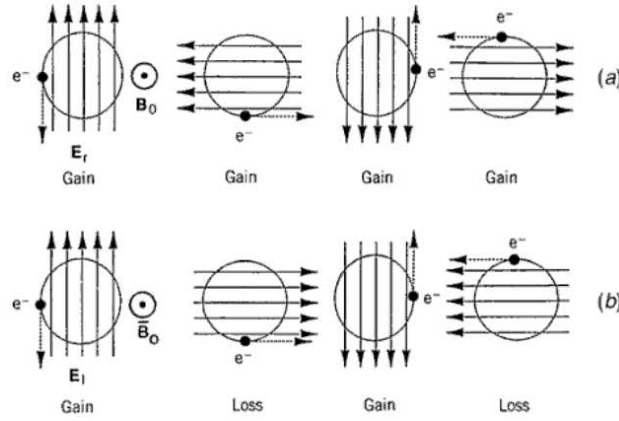
Figure III.1 – *Explanation of the ECR heating : The drawings are separated by a fourth of a period. Line (a) shows the right-hand polarized component which continuously increases the electron energy. Line (b) shows the left-hand polarized component which alternatively accelerates and slows down the electron. Taken from page 497 of [1].*

accelerated during a sufficient number of rotations and can pass several times in the ECR region before any collision. The mean free path of the electrons l_{eN} must be much larger than their Larmor radius :

$$l_{eN} = \frac{1}{\sigma_{eN} \cdot N} \gg r_{Larmor} \tag{III.3}$$

where σ_{eN} is the total electron cross section and N is the total gas density.

3   The different types of ECR plasmas

Now that the basic principle has been explained, we are going to review chronologically some of the reactor configurations proposed to take advantage of this phenomenon.

3.1   The divergent ECR reactors

The typical geometry of such reactors is shown in Figure III.2. The microwave power is guided by a rectangular or cylindrical waveguide and is injected into the vessel through a quartz or alumina window. A first set of electro-magnets near this window defines the Electron Cyclotron Resonance absorption zone. The plasma then diffuses until the substrate holder in what is sometimes called the "extraction chamber". A second set of magnets is sometimes used at the level of the substrate holder in order to correct for the diverging magnetic lines of the first magnets [2].

The leading country for the early development of this technology has been Japan. High plasma densities, in the range of $10^{11}\,\mathrm{cm}^{-3}$ have been reached [2]. But several limiting factors are also challenging. Indeed, the size is difficult to expand (less than 50 centimeters diameter usually). Furthermore, deposition on the dielectric window or damage of this window by the process gases (e.g. etching gases) is a serious issue. Such a deposition can result in a decrease of the plasma density by as much as $50\,\%$ in 5 minutes in some cases [3]. The chemical erosion of the quartz window has been demonstrated to be a problem in high density, hydrogen-rich Surface-Wave plasmas [4].
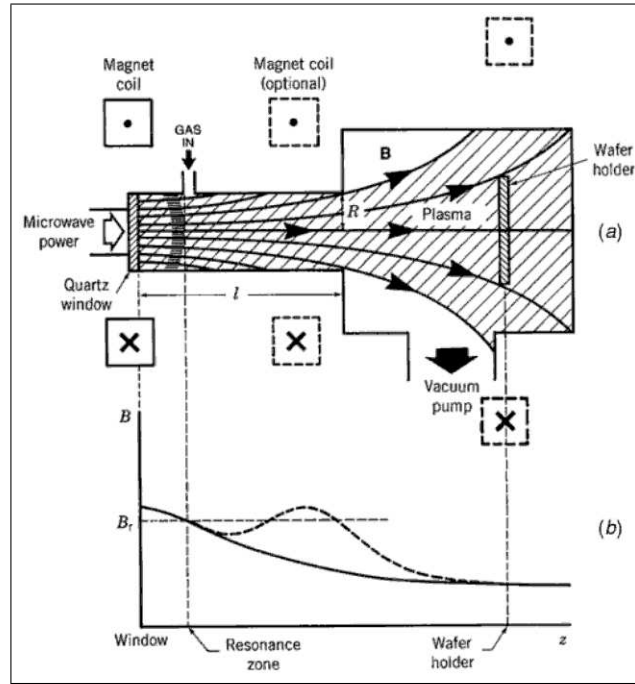
Figure III.2 – *Top graph : Typical configuration of a divergent ECR reactor with one (or more) zone(s) of microwave power absorption and the extraction chamber. Bottom graph : Magnetic field variation showing the resonant value of the magnetic field. Taken from page 493 of [1].*

3.2   The Distributed ECR (DECR) reactors

This configuration was first proposed by Pichot and co-workers in 1988 [5] in order to avoid the issues associated with the use of hot filaments and in order to scale up the treated surface without decreasing the plasma density. Densities of $10^{11} - 10^{12}\,\mathrm{cm}^{-3}$ could be reached and it enabled to process substrates of 200 mm in diameter.

This configuration is based on microwave injection along linear applicators (10 to 40 cm long) placed near the 875 Gauss ECR regions as illustrated in Figure III.3. The typical geometry of such reactors is a cylindrical vessel with magnets all around, inside the walls. Water cooled microwave applicators are on the periphery also and the plasma diffuses to the center. While the uniformity along the radius in atomic gases was satisfactory, in the case of reactive gases, it was not as optimal so that the size expansion was limited. An additional issue was the possible interactions between the antennas.

Furthermore, to reach a good homogeneity of the plasma along the MW applicators, it is necessary to have constant amplitude standing wave patterns in the axis of the antennas. To do so, the microwaves have to propagate along the antenna with low attenuation and to be reflected at its end [7].

3.3   The Integrated Distributed ECR (IDECR) reactors

This geometry is derived from the DECR one (see Figure III.4). The magnets are inside the water cooled microwave applicators [9] and a plane uniform plasma is generated. In Figure III.4, H_2 is injected near the magnets and SiH_4 near the substrate holder and deposition rates for microcrystalline silicon of 3 Å/s were demonstrated [8].
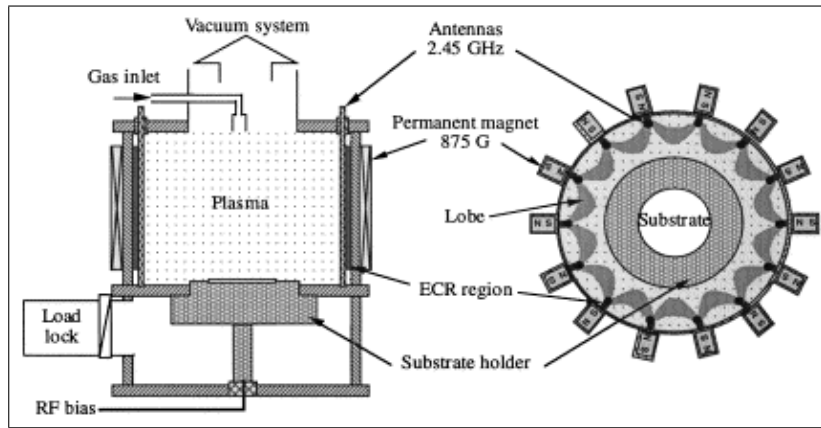
Figure III.3 – *Distributed ECR typical configuration : side view on the left and top view on the right (taken from [6]).*
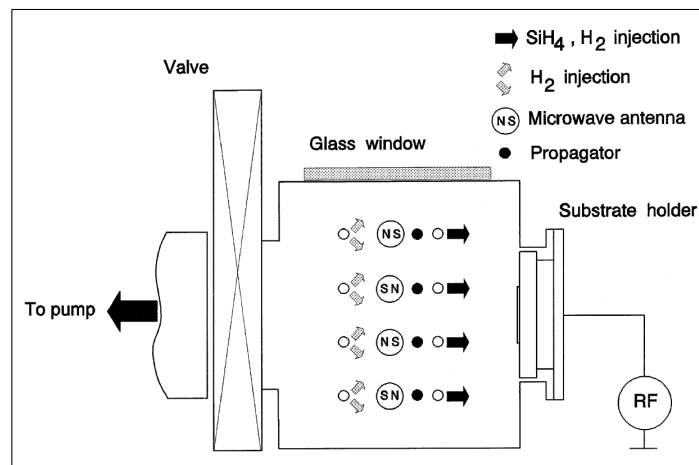

Figure III.4 – *Integrated Distributed ECR geometry (taken from [8]).*

Other geometries have been proposed, such as the Microwave Plasma Disk reactors developed by Asmussen and co-workers [10].

3.4   The MDECR reactors

The idea of multipolar magnetic field confinement was first proposed by Sadowski in 1967 in a spherical configuration for controlled thermonuclear reactions [11]. Its first realization for the production of large uniform low temperature plasmas is attributed to Limpaecher and MacKenzie in 1972 [12]. In this early system, the electrons were provided by heated filaments and densities up to $10^{12} \, cm^{-3}$ were produced (see Chapter 10 page 273 of [13] for a complete overview and [14] for a study of the chemistry of a silane plasma in such a configuration).

Matrix Distributed or Multi-Dipolar ECR reactors were later developed as a combination of multipolar magnetic confinement and microwave plasma in order to overcome the difficulties of DECR [15]. The first patent about MDECR plasmas has been released in 1999 [16] as a solution to the need of the industrial company Saint Gobain to process non-plane surfaces. The first two reactors have been done by the company Metal Process. A second patent was released more recently, in 2002, about plasma creation for surface treatment [17].
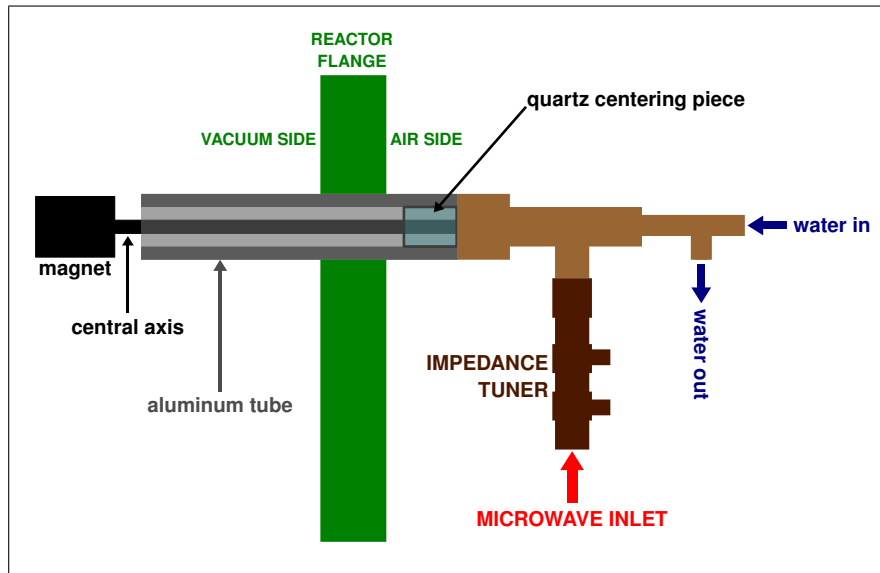
Figure III.5 – *Drawing of a microwave applicator. The aluminum tube is transparent to show the central coaxial line and the quartz window.*

3.4.1   The microwave applicators

The idea of this type of ECR plasma source is to split the microwave power into independent elementary sources. These can then be arranged e.g. in a hexagonal or square pattern, in order to provide a high density uniform plasma on areas that can be expanded just by increasing the number of microwave applicators.

These microwave applicators, also called "antennas", are described in Figure III.5. One can see that the position of the antenna, its "depth" inside the reactor, can be varied easily, e.g. in order to change the substrate–magnet distance. The microwave power is brought to the antenna by a coaxial cable connected to it and injected inside the vacuum chamber via a coaxial feedthrough which ends with a permanent magnet. To do so, the matching of the impedance of each antenna has to be optimized manually with a sliding stub for the used conditions (microwave power, plasma composition in case of a mixture of several gases and plasma pressure). The central axis has a diameter of 6 mm and is screened by an aluminum cylinder (transparent on the drawing) with an internal diameter of 16 mm. The central coaxial line then ends up by a cylindrical permanent magnet magnetized along its axis (made of a samarium-cobalt alloy Sm_2Co_{17} and covered by stainless steel). Water is circulating inside the central axis until the magnet in order to cool it down (see Figure IV.52 page 145 for a zoom on this part).

The magnetic field of the magnet will trap the electrons and limit their loss on the walls. We can see that as opposed to the DECR configuration, here, there is no propagation of the microwaves inside the plasma : the electric field of up to 200 W is absorbed in a small volume around the magnet satisfying the ECR condition. The electric field is very intense at the back of the magnet, at the end of the aluminum cylinder but the electrons heated there will be lost on the surface of the applicator [18, 19]. On the contrary, the electrons on the side of the magnet will be heated and trapped efficiently.

The hot (or "primary") electrons are trapped in the lobes around one magnet or between two magnets of opposite magnetic polarities [20]. Their lifetime is greatly enhanced by this trapping (mean free paths larger than 1 m in argon for pressures below 1 mTorr [21]). Their
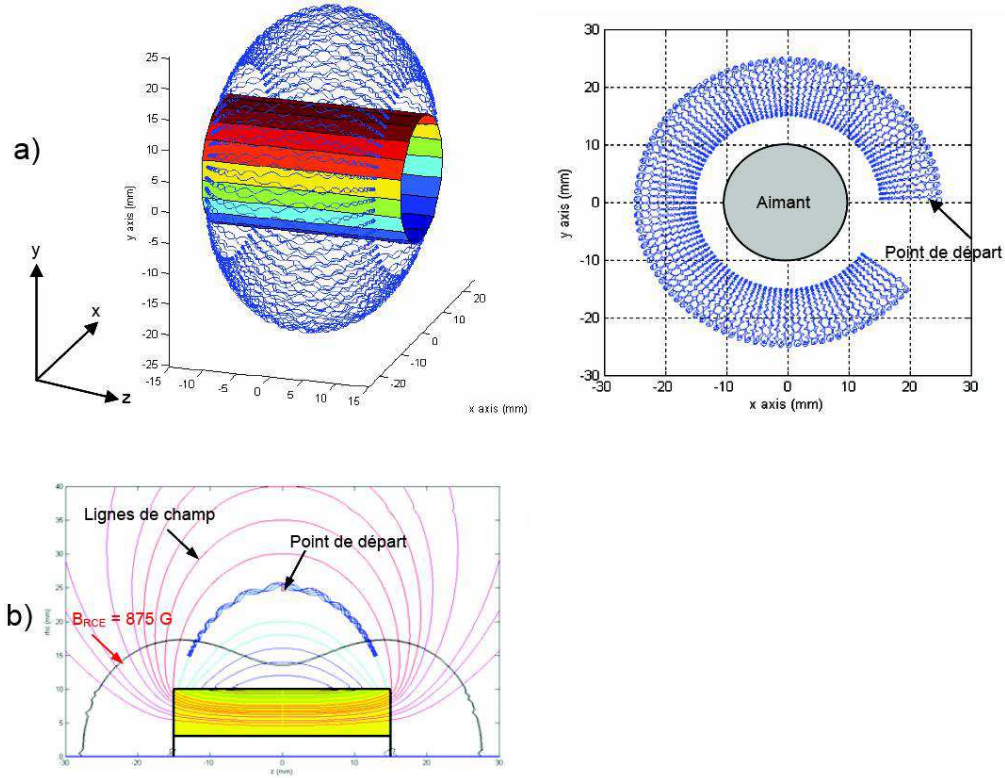
Figure III.6 – *This simulation, taken from [18], shows the trajectory of a hot electron of 40 eV during 5×10^{-12} s. The magnet has a length of 30 mm and a diameter of 20 mm like in our microwave applicators. Top left graph : side view. Top right graph : top view showing the initial position of the electron. Bottom graph : cross section with the magnetic lines and the ECR region at $B = 875$ G.*

trajectories have been simulated by a Particle In Cell (PIC) model in absence of electric field [18]. The results for a cylindrical magnet in absence of collisions are reproduced in Figure III.6. We can see the mirror points and the drift of the trapped electron due to the curvature of the magnetic lines and to the gradient of magnetic field strength. In absence of collision and without ECR heating, the electron energy is constant. Their PIC model has also been combined with a Monte Carlo approach in order to simulate more realistic trajectories with elastic and inelastic collisions (see page 117 of [18]).

The magnetic confinement structure created by a row of such magnets can be seen in Figure III.7. It can be concluded that in both cases (i.e. same polarities or alternating polarities), the 875 Gauss regions where the ECR effect will take place are very similar. We can see that compared to the divergent ECR configuration, where the lines of magnetic field tend to direct the charged particles towards the substrate holder (Figure III.2), here, the presence of the magnets maintains the charged particles, in particular, the hot electrons, in their surrounding.

In argon for a planar magnetron-like magnetic structure and microwave injected by a linear applicator (DECR type), the authors of [21] evidenced the presence of two electron populations in the lobe : hot and cold electrons. They performed combined Langmuir probe and Optical Emission Spectroscopy measurements assuming Maxwellian distributions and found temperatures of $3-6$ eV for cold electrons and temperatures as high as 17 eV for hot electrons. The densities of the latter population are $\sim 2 \times 10^9$ cm^{-3}, representing $\sim 5-20\%$ of the electrons.
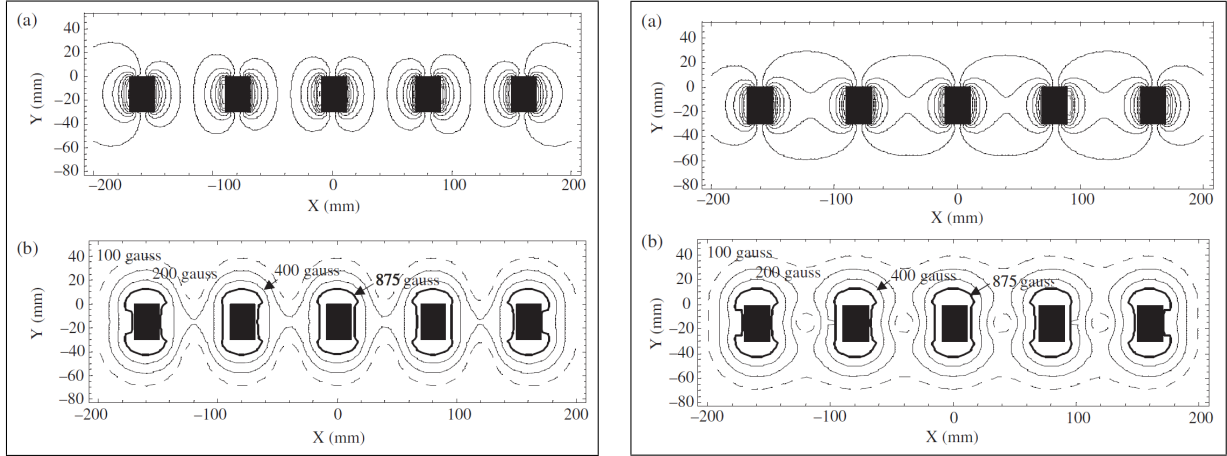
Figure III.7 – *Row of magnets with the same polarities on the left graphs and with alternating polarities on the right graphs. The graphs (a) show the magnetic field lines while the graphs (b) show the lines of constant magnetic field intensity. Taken from [22].*

A new version of the applicators has been released in 2003 with an integrated tuner and improved cooling. Furthermore, this principle is still being developed and has recently been extended to new microwave sources, free from magnetic field, to produce high density, uniform, large scale plasma at higher pressures of $0.2 - 2.5$ Torr [23, 24].

3.4.2   Advantages of the MDECR configuration

The MDECR technology is a versatile plasma source as it can be sustained in a wide pressure range $\sim 0.5 - 20$ mTorr and provide plasma densities in a large range $5 \times 10^9 - 5 \times 10^{11}$ cm^{-3} (in argon, and the high value is obtained with a MW power of 2 kW) [7].

These high densities achievable are of course of great interest to increase the deposition rates of amorphous and microcrystalline silicon because they result in highly dissociated plasmas. As a result, the trend of the deposition rate is to scale linearly with the gas flow [25] provided that the MW power is high enough. But usually, the quality of the material (i.e. its crystallinity for example) degrades when the deposition rate is enhanced [26]. So there is obviously an optimum to find.

The dimensions of the plasma can be easily extended to the desired area without any physical or technical obstacle, just by repeating the pattern of elementary MW sources [15]. For example, a few rows of antennas could be used for high rate uniform deposition in a roll-to-roll industrial process. Furthermore, since each antenna is independent of the others, one has a great freedom, e.g. to compensate the edge effects by feeding the MW applicators near the walls a higher power to compensate for the losses. Another original possibility of this technology is to adapt the height of the antennas in a 3-D network in order to treat non-flat surfaces.

If the magnet – substrate distance is sufficient, if the edge effects are avoided and if the gas injection is uniform, there is no reason for thickness or properties inhomogeneities.

Another clear advantage as compared to divergent ECR reactors is that the dielectric window is inside of the MW applicators, far from the plasma, and therefore, cannot be coated nor etched.

64

An additional interesting characteristic is that this type of plasma source allows the independent control of the plasma density (which mainly depends on the MW power) and of the ion energy (which is defined by the Radio-Frequency power fed to the substrate holder). Thus, they have the ability to deliver high-current densities (tens of mA/cm^2) at low ion energy (a few tens of eV). Furthermore, due to the low pressure, the sheath is non-collisional which is a crucial advantage for etching applications where highly anisotropic bombardment is required. The energy distribution of the ions reaching the growing surface is thus very narrow. We can take the Debye length λ_D as an order of magnitude of the sheath width :

$$\lambda_D = \left(\frac{\varepsilon_0\, k\, T_e}{n\, q_e^2} \right)^{1/2} \tag{III.4}$$

where ε_0 is the permittivity of free space, k is the Boltzmann constant, T_e is the electron temperature, n is the plasma density and q_e is the electron charge. This gives a value of $\sim 0.2\,$mm for estimated values at the level of the substrate holder : $n = 5 \times 10^9\,$cm^{-3} and $T_e = 3\,$eV.

Dust formation is a wide-spread problem encountered when trying to obtain high-rate microcrystalline silicon in Capacitively Coupled Plasmas (CCP) (either Radio-Frequency or Very High Frequency). Due to the very low working pressure, the MDECR plasmas can be considered dust-free although some mechanisms of formation of particles based on the enhanced lifetime in the magnetic field have been proposed [27]. Additionally, the low pressure makes the chemistry of this type of plasma quite "simple" : it reduces secondary reactions between the radicals. On the other hand, the plasma-wall interactions probably become very important, at least in our research-scale reactor. These considerations can be illustrated by calculating the order of magnitude of the radicals mean free path in the weakly magnetized diffusion plasma. It is given by $kT/P\sigma$. We will assume a gas temperature T of $400\,°$K and a pressure P of $5\,$mTorr. For the cross section σ, we will choose the simplest model of hard sphere collisions between neutral SiH_2 radicals, taken as the average radicals in our highly dissociated plasma. The collision diameter of this molecule is $3.8\,$Å (found in [28]). Finally, we get a mean free path of $\sim 7.2\,$cm, which is close to the magnet-substrate holder distance.

For research purposes, the geometry of the MDECR reactors is also convenient to implement some real time, in-situ diagnostics on the surface of the sample (e.g. ellipsometry and pyrometry).

3.4.3   Limitations of the MDECR configuration

One limitation related to the very unique microwave applicators is that each antenna has to be manually tunned. This tunning is different for every condition (gas mixture, gas flow rates, pressure, MW power etc.). When a new condition is tried, it can take more than 30 seconds to optimize the reflected power. Thus, the effective power absorbed by the plasma can change during this initial phase and this is particularly important for the study of the incubation layer in microcrystalline silicon deposition.

Due to the very fast deposition rates achievable with this technique, the walls and antennas get covered by a thick layer of silicon and some cleaning procedures (manually or by an etching plasma) have to be applied to avoid any problem of flaking for example, which can induce pin-holes if the substrate is horizontal.

3.4.4   Applications of MDECR plasmas

The MDECR technology can be used for many applications as it is a dense plasma which can provide high fluxes of ions. We can list some applications : plasma-based ion implantation (PBII) [7], anisotropic etching, sputtering and other surface treatment, cleaning plasmas, negative hydrogen ions H^- production [20], thin film deposition (SiO_2 [29, 30], SiO_xN_y optical filters and layers with gradient index [31, 32], high rate deposition of hydrogenated amorphous silicon solar cells [33]).

4   Description of the MDECR reactor Domex

I had the unique opportunity to work on two MDECR reactors during my PhD : Domex and then ATOS.

Domex was installed in July 2003 and disassembled in July 2007. It was a collaboration between two companies (Dow Corning and Metal Process) and the École Polytechnique.

Since this reactor has been described in detail elsewhere [33] and since I worked with it only around four months, it will only be described very rapidly here. Furthermore, several elements of it (such as the MW applicators, the turbo-molecular pump, the gas lines and bottles, the microwave and Radio-Frequency generators, the computer controlling them etc.) have been used in the new reactor ATOS and will be presented in detail in the next section.

One important difference with the new reactor ATOS is its geometry. As one can see in the pictures of Figures III.8 and III.9, the antennas in Domex are vertical and the substrate holder is horizontal. This configuration sometimes led to shunted solar cells due to pin-holes formed by little flakes falling from the covered antennas. This problem has been completely solved by the geometry of ATOS.

I used the reactor Domex with six antennas forming a circle in the top flange. The central port, at the vertical of the substrate, was occupied by the pyrometer, enabling us to record the surface temperature of the sample. Films and cells of $2.5\,\mathrm{cm} \times 2.5\,\mathrm{cm}$ were processed. The system of plate bringing the samples from the load-lock to the deposition chamber was unfortunately not working anymore, and thus, the whole reactor had to be exposed to air between each sample.

The main limitation of this reactor was its substrate holder. The highest temperatures it could provide for a glass substrate were around $\sim 230\,^\circ\mathrm{C}$, measured by the pyrometer with an emissivity fixed to 1. To increase this initial temperature, we often used a so-called "pre-heating" procedure, which consisted in injecting a gas and in almost completely closing the gate valve in front of the pump in order to obtain a pressure of around 1 Torr. With this procedure, the improved thermal contact between the heated substrate holder and the substrate allowed to go up to $\sim 280\,^\circ\mathrm{C}$. The disadvantage of this pre-heating procedure is that one has then to set the gas flows for deposition, to adjust the gate valve and to turn on the MW and RF generators as fast as possible. During these settings, the substrate temperature *sharply drops*, thus resulting in a lack of control or reproducibility of the substrate temperature at the beginning of the deposition.

Another possibility to increase the substrate temperature is to glue it to the heated substrate holder with silver paste. This option is also not satisfactory as it could result in contamina-
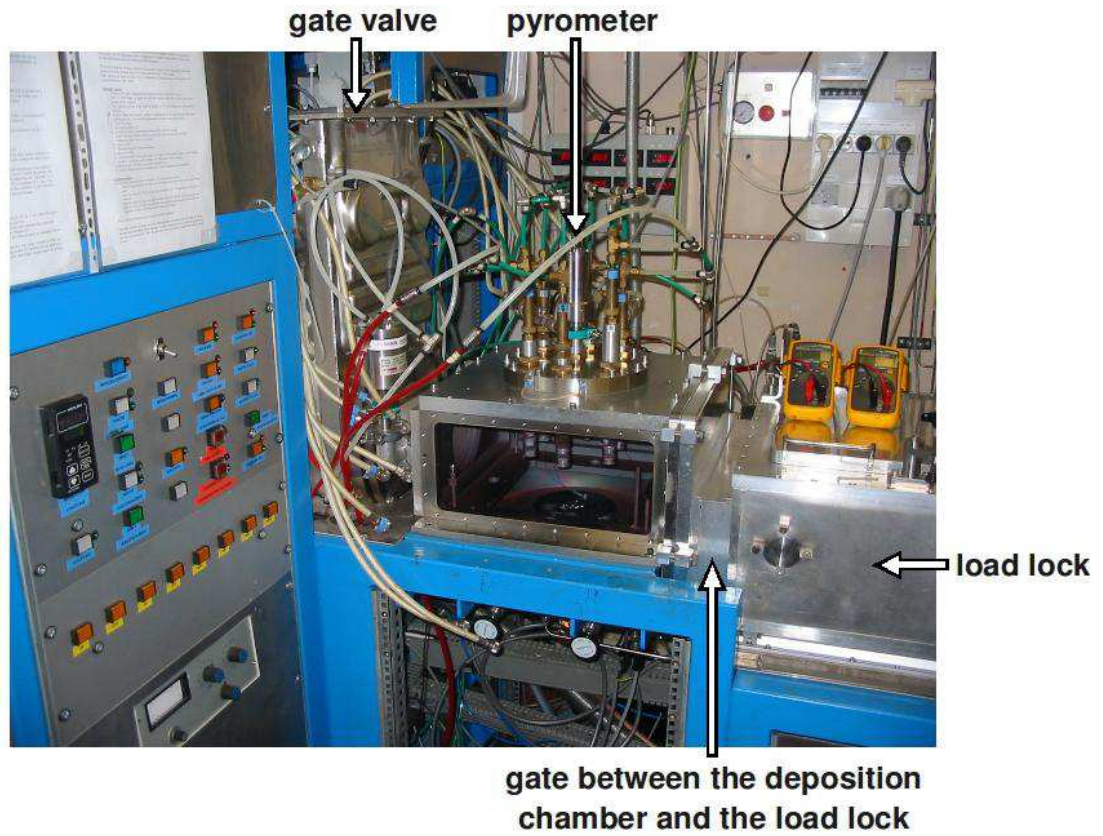
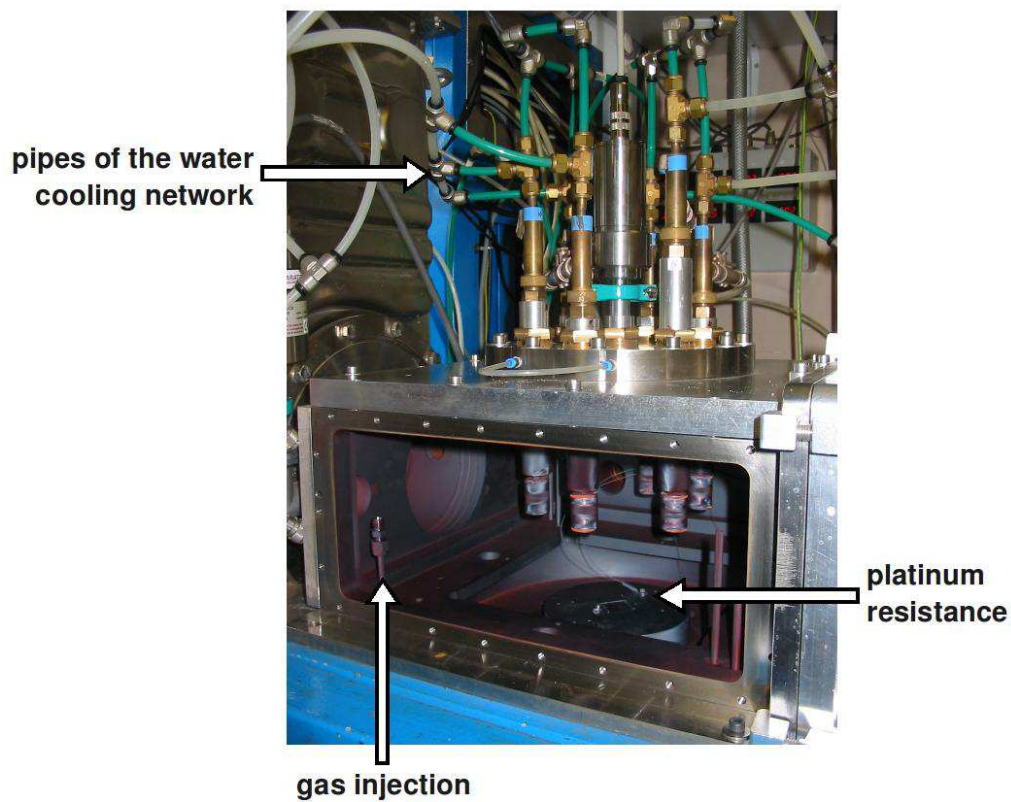Figure III.8 – *Side view of the reactor Domex.*

Figure III.9 – *Zoom on the deposition chamber. The exhaust going to the turbomolecular pump can be seen on the left.*

tions of the samples but it resulted in temperatures as high as $\sim 305\,°C$. The enhancement of the temperature from $\sim 230\,°C$ to $\sim 305\,°C$ illustrates the poor thermal contact at low pressures in the range of a few mTorr.

5   Description of the MDECR reactor ATOS

5.1   Introduction

It has already been mentioned that the geometry of ATOS is different from the previous one. Indeed, this time, in order to avoid any pin-hole problems, the antennas are horizontal and the substrate holder is vertical. This way, no flakes can fall on the surface of the substrate.

Since temperature had been found to be a crucial parameter to obtain a crystallized material [26], the other very important improvement of the reactor ATOS is a much more powerful substrate holder with a guaranteed very high temperature homogeneity (see details below).

5.2   General description

Two drawings of the reactor ATOS are shown on Figures III.10 and III.11. One can see that the vessel has the shape of a "cross". It is made of stainless steel and, before the addition the load-lock, its volume was 28 liters and its internal surface exposed to the plasma was estimated to be around $4000\,cm^2$. The distance between the magnets and the substrate holder is $10.5\,cm$ and the distance between two applicators is $8\,cm$.

The flange on the left of Figure III.11 has seven microwave applicators (six antennas on the periphery form a hexagone and the seventh one is in the center). The magnetic polarities of the antennas on the border are alternating (i.e. North-South-North etc.) in order to form a completely closed magnetic configuration. This can be clearly seen on the picture of Figure III.12.

This flange also has a port to install the pyrometer in order to perform in-situ optical measurements of the substrate surface temperature, which is shown in broad outline on Figure III.13. The pyrometer integrates the radiations coming from an area of the glass substrate of less than $19\,mm$ diameter. Other in-situ diagnostics can be implemented : two ports on the side of the substrate holder allow to perform in-situ ellipsometry (spectroscopic or real-time multi-wavelengths) and the bottom flange has three ports for Optical Emission Spectroscopy measurements.

The magnetron generator can deliver a maximum power of $2\,kW$. The total power is split in 8 using the patented microwave power splitter developed by Pelletier and Moisan [34] (See Figure III.14). Coaxial cables are connected to seven of these eight ways by a circulator and a water-cooled load, allowing to protect the MW generator from the reflected power of the antennas and to dissipate it. One channel is not used and two water-cooled loads are thermally dissipating the corresponding excess of microwave power. These loads can only dissipate $100\,W$ each so that for safety, we never used total powers higher than $1.5\,kW$. Each coaxial cable is connected to one MW applicator through a coaxial impedance adaptator which has to be manually tuned for every deposition condition in order to reduce the reflected MW power.
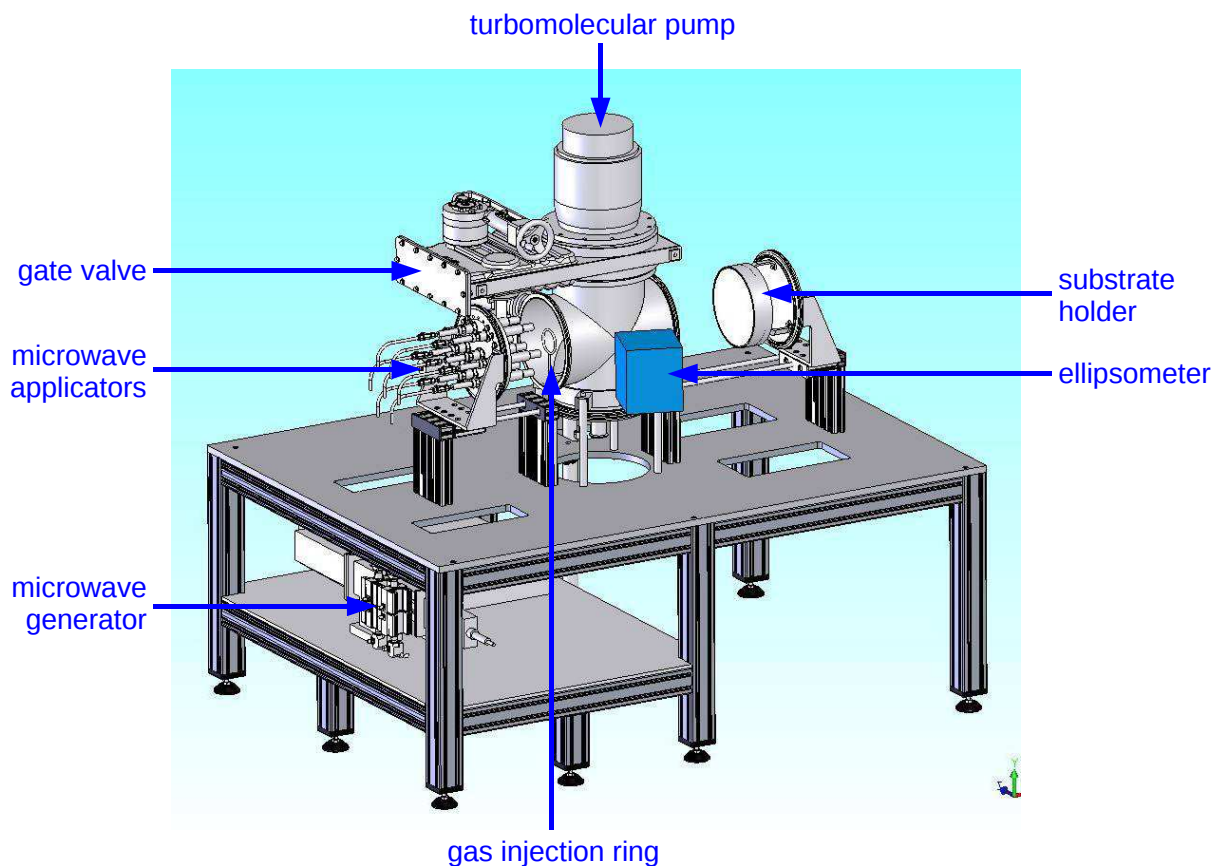
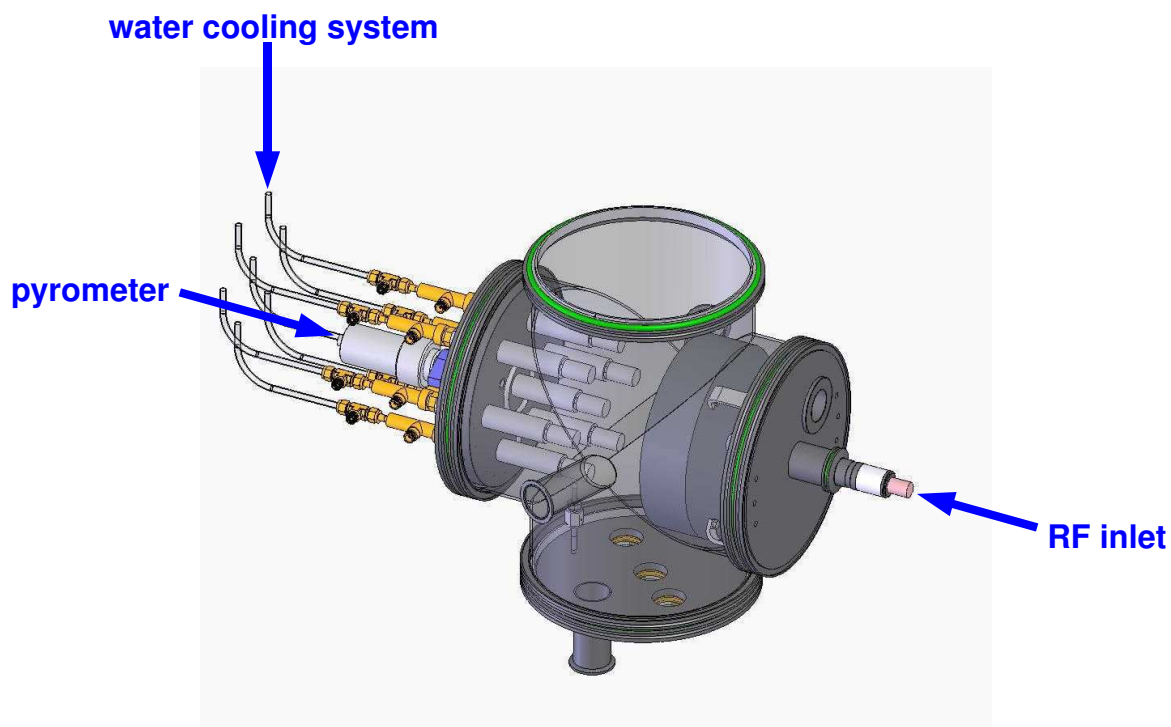Figure III.10 – *General view of the MDECR reactor ATOS open.*

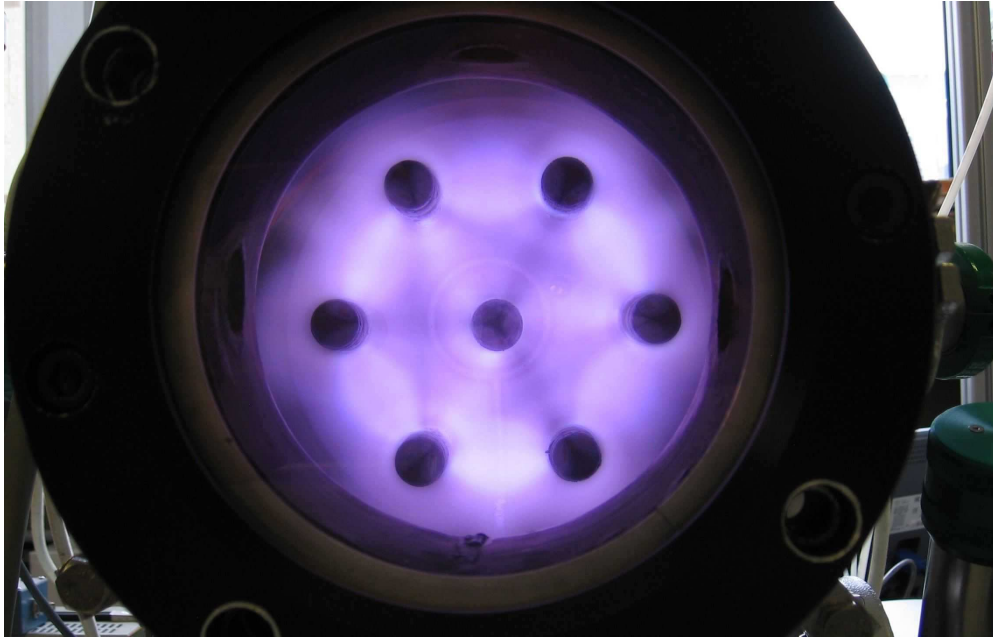Figure III.11 – *Closer view on the vessel.*

69

Figure III.12 – *Magnetic structure : The substrate holder has been removed and the flange replaced by a window to take this picture. We can see the lobes of intense light emission between the six magnets with alternating polarities on the periphery. Three other lobes with the central antenna can be seen. All these lobes show where the hot electrons are trapped. The regions between two magnets with the same polarity appear as darker. Finally, the gas ring and the port of the pyrometer can also be seen.*
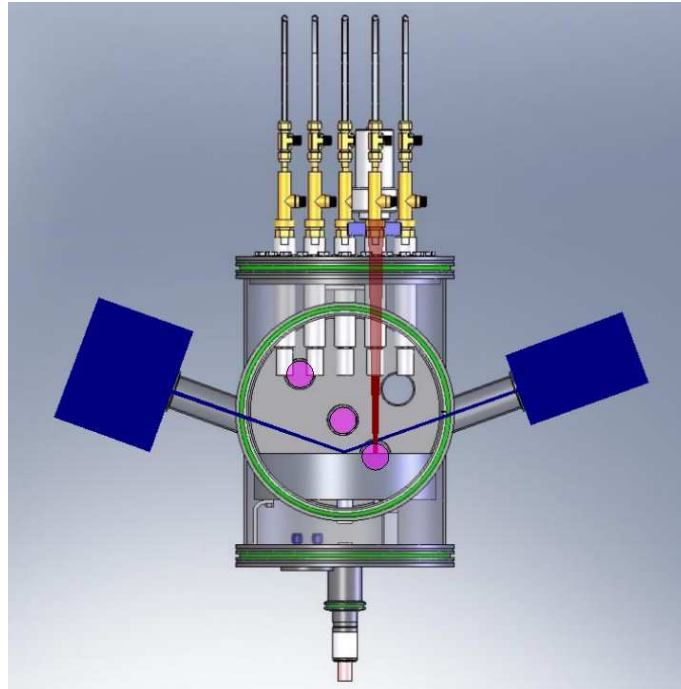
Figure III.13 – *Top view of the reactor in its first configuration, without load-lock. Three in-situ diagnostics are represented : Two ports on the side of the reactor allow to perform ellipsometry (in blue). Three windows in the bottom flange can be used to carry out Optical Emission Spectroscopy measurements (in magenta). The pyrometer is installed on the flange of the antennas to collect the radiations emitted by the surface of the sample.*
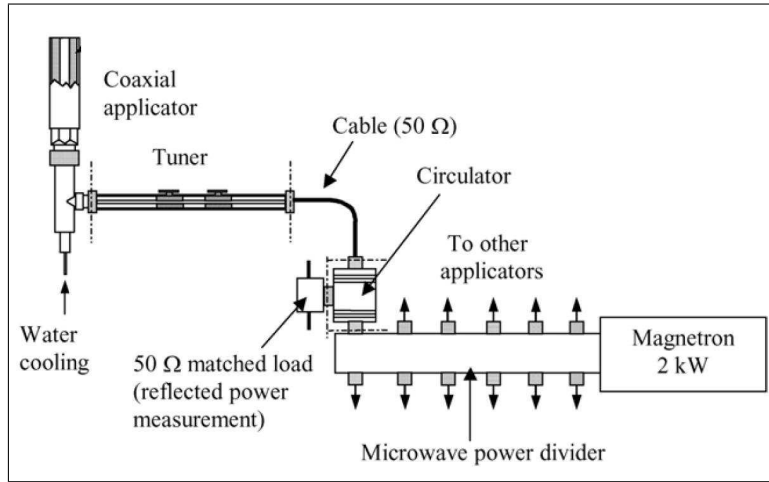
Figure III.14 – *Illustration of the microwave distribution taken from [24]. Our setup divides the power in eight ways instead of the twelve shown and the MW applicator is also different from ours.*

On Figures III.10, III.11 and III.12, one can also see the gas injection ring. Holes directed towards the substrate ensure a high dissociation of the molecules since the gases have to pass through the ECR zones. It has been previously shown that the deposition rate and the properties of the material can crucially depend on the gas injection geometry in MDECR [35]. The different gases available are : O_2, Ar, SiF_4, H_2, GeH_4, SiH_4, tri-methyl-boron $B(CH_3)_3$ diluted in SiH_4, and SF_6. The line of SiH_4 is equipped with two different mass flow controllers whose maximum flow rates are 200 sccm and 8 sccm, the latter being used to obtain accurate small flow rates.

Gas purifiers have been added on the hydrogen and silane lines in November 2008. The H_2 gas purifier removes the H_2O, O_2, CO, CO_2 and non-methane hydrocarbons (NMHC) impurities to levels lower than 1 ppb. The SiH_4 gas purifier removes the H_2O, O_2, CO, CO_2 and H_2 impurities to levels lower than 1 ppb.

The primary vacuum (~ 50 mTorr) is reached with a primary pump. The background pressures are then obtained with a turbomolecular pump (Alcatel ATH 1600M with a capacity of 1600 liters/s for N_2 and a rotation speed of up to 39 000 rotations per minute). This pump is on top of the main vessel and has a gate valve (VAT) in front of it which can be partially closed to increase the pressure inside the reactor. The pressure inside the reactor is monitored with a cold cathode Penning gauge for the background pressure and a capacitance manometer (baratron gauge) during the process. We explored plasma pressures in the range of $\sim 1 - 30$ mTorr. The lowest pressures achievable without heating were around 5×10^{-8} Torr. Without the load-lock, such low pressures could only be reached after several days without depositions and without opening the reactor at air. With the load-lock, the lowest pressure was the same but could be reached faster. With all the substrate holders, the minimum pressure at the end of the heating phase (to the usual temperature $T_{pyrometer} \sim 230\,^\circ$C) was $\sim 3 \times 10^{-7}$ mTorr and usually $\sim 1 \times 10^{-6}$ mTorr.

The gas residence time in seconds can be written as :

$$\tau_{res} = \frac{21.5 \times P \times V}{T \times F} \tag{III.5}$$

where P is the pressure in mTorr, V is the reactor volume in liters, T is the temperature in $^\circ$K and F is the total gas flow rate in sccm (cubic centimeters per minute in standard

conditions). To have an order of magnitude, we can apply this formula with a flow rate of 42 sccm of pure silane, a pressure of 5 mTorr and a gas temperature of 500 °K, which gives a gas residence time of 140 msec.

The top plate of the substrate holder is connected to a 13.56 MHz Radio-Frequency generator (Dressler CESAR1310 – Maximum power of 1000 W) through an automatic matching box. The microwave and RF powers are set on the corresponding generators which are then controlled by the computer to turn on the plasma. The gas injection is also controlled by the same computer connected to the valves and the mass flow controllers. The gas bottles are in a shelter outside of the building and a pressure switch automatically closes all the valves if the pressure inside the vessel reaches 100 Torr.

5.3   The substrate holders

During my PhD, three different substrate holders have been implemented in ATOS. Indeed, the heating element of the first one failed after six months so that we temporarily replaced it by the substrate holder of the other MDECR reactor of the laboratory. Finally, when we installed the load-lock, we also designed a new substrate holder with a smaller thermal mass and heated by three halogen lamps (maximal power : 500 W each ; luminous flux : 9500 lm ; voltage : 230 V ; length : 118 mm) in order to be able to deposit more samples per day.

$10\,cm \times 10\,cm$ susbstrates could be used with the three substrate holders.

5.3.1   The first substrate holder

This substrate holder was designed in order to provide a very high surface temperature with a high homogeneity. Its diameter was 240 mm. Its surface was in Inconel 600, an alloy containing more than 72 % of nickel. This alloy is suitable for temperatures as high as 600 °C and has a good thermal conductivity. The resistive heater enabled to reach a surface temperature as high as ~ 630 °C with a radial uniformity of ± 1 % at this highest temperature (as simulated by the manufacturer). As a result, the so-called phase of "pre-heating" or the use of silver paste (described in Section 4 page 66) were not necessary anymore, which was a successful improvement.

The temperature on this substrate holder could be measured by two K-type thermocouples : one close to the heating element and the other one in the top RF-biased plate (see Figure III.17 below).

The main drawback of this substrate holder was its very long heating and cooling phases of more than 1H30 and at least 2H30 respectively due to its high thermal mass (around 14 kg). We were thus limited to two samples per day (which has to be compared with e.g. six samples per day for the previous reactor with its load-lock and its transferring plate).

It unfortunately failed after six months, due to a short circuit between the resistive heater and the surrounded grounded part. Since the resistive heater was welded *inside* of a disk of the substrate holder, it was impossible to fix.
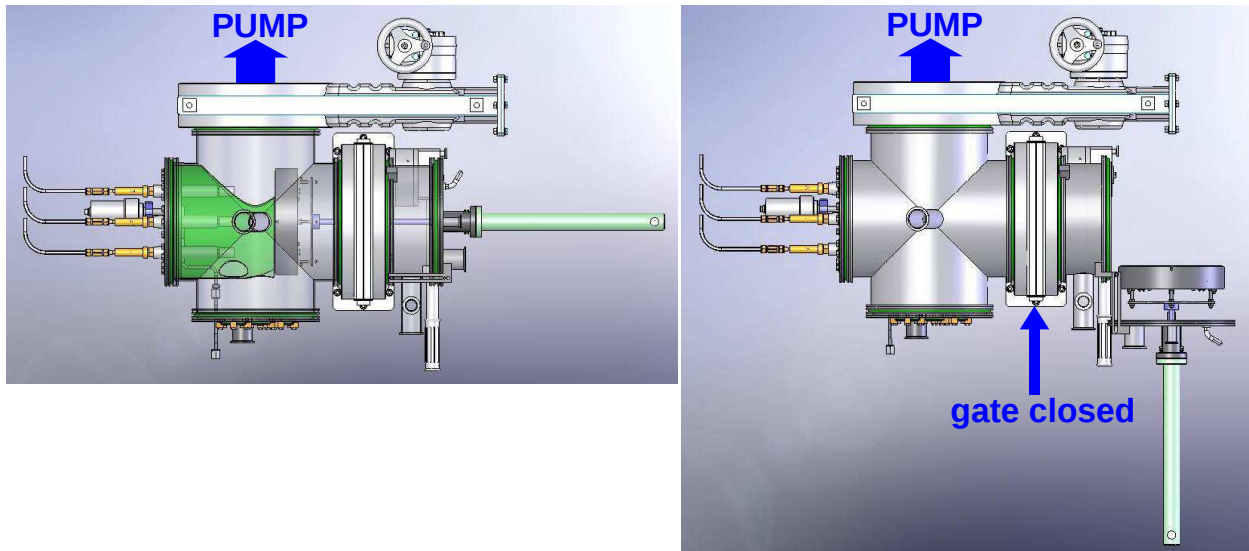
Figure III.15 – *Side views of the improved ATOS reactor with the load-lock. On the left : Transparent view with the substrate holder in the typical deposition position. On the right : The substrate holder has been moved backwards and switched to horizontal position to clamp a new substrate. In this position, the gate valve is closed and only the load-lock is exposed to air.*

5.3.2   The second substrate holder

This second substrate holder was used during almost 9 months in replacement of the previous broken one. It was taken from another MDECR reactor of the laboratory. It was a bit smaller (diameter of 220 mm) and allowed us to reach the usual temperature of $\sim 230\,°C$ for the surface of the glass sample, as measured by the pyrometer and had the advantage of having a much smaller thermal mass, as compared to the first substrate holder. As a result, it enabled us to deposit three samples a day.

5.3.3   The third substrate holder

For this third substrate holder, we tried to reduce the thermal mass (less than 8 kg for a diameter of 240 mm) and we decided to change the heating source : Three lamps allow to reach the usual temperature of $230\,°C$ indicated by the pyrometer. This substrate holder has only one thermocouple, located just below the surface and a few millimeters away from the edge of the metallic frame holding the substrates. Another improvement is that the substrate holder can be switched to a horizontal position for an easy installation of the substrates (see Figure III.15).

5.4   The load-lock

The third substrate holder corresponds to the installation of the load-lock, in February 2009. A manual gate valve was added, as can be seen on Figure III.15 and the primary pump was connected to the load-lock. Not to expose the main chamber at air anymore allowed to reduce the oxygen content in the films by a factor of 10 (see results of Section 4.3.4 page 158).

An issue appeared after this improvement of the reactor : Indeed, the reflected Radio-

Frequency power on the substrate holder is always high. This change in the matching of the RF power could be due to stray plasmas inside or behind the new substrate holder or to the long cable connecting the moveable substrate holder to the flange. This is a serious problem as it prevented us from repeating the previous conditions which used a high RF power.

6   Characterizations of the reactor ATOS

6.1   Leak rate

We made several leak rate measurements in various conditions. It consists in a basic static vacuum test : we completely close the gate valve in front of the turbomolecular pump and we record the pressure increase given by the baratron gauge as a function of time. The pressure change ΔP in mTorr per minute is then converted to a leak rate Q in sccm (cubic centimeters per minute in standard conditions) with the formula :

$$Q = \frac{V_{reactor}}{760}\Delta P \tag{III.6}$$

where $V_{reactor}$ is the volume of the reactor in liters (estimated to be around 28 L before the load-lock and around 39 L with the load-lock). This formula corresponds to the situation of a test at room temperature. When we heat the substrate holder at the usual temperature, the leak rate has to be corrected by a factor 0.52 corresponding to a gas temperature of 250 °C.

This series of checks has been initiated in July 2008 (i.e. without load-lock) because of abnormally high background pressures. We found that a leak had appeared because of the bending of one element of the nitrogen injection (used to put the vessel at atmospheric pressure). The static pressure evolution with the leak is the curve 1 in Figure III.16, whose corresponding leak rate is 180×10^{-4} sccm. We fixed this leak and the improvement down to 3×10^{-4} sccm can be seen on the curve 2. This level is similar to the value found in another MDECR reactor in our laboratory [31].

What remains unexplained is the leak rate with heating. The curve 3 has been recorded in the exact conditions of the process of a cell. We started to heat just after having closed the reactor and we waited to reach the usual temperature of the glass substrate surface (~ 230 °C). The found leak rate is 177×10^{-4} sccm. To know the minimum leak rate achievable with heating, we carried out the following sequence : we pumped the reactor during more than 24 hours, heated during ~ 4 hours, pumped one whole night and heated again during ~ 4 hours before starting the measurement. The result is the curve 4, which has $Q \sim 50 \times 10^{-4}$ sccm. Such a sequence should ensure that the vessel is completely degased. Later, an even stricter experiment has been carried out to be sure that the reactor is completely degased : It was left at the usual temperature (330 °C indicated by the thermocouple at the surface of the substrate holder) one whole night (12 hours) and the leak rate was not improved at all (curve not shown).

If it is not degasing, then this pressure increase would correspond to a real air leak but it is not very likely that a leak appears only when the reactor is heated. Careful helium leak detections have been performed on the heated reactor and have not revealed any leak.
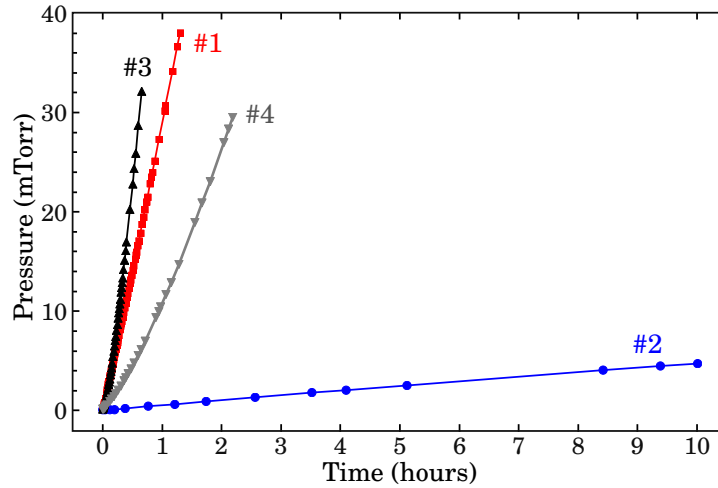
Figure III.16 – *Static vacuum tests in various conditions (see explanations and results in the text) : without heating for the curves 1 and 2, and with heating for the curves 3 and 4. The curve 3 reproduces the sequence of the processing of a cell and the pressure increase corresponds to a leak rate of $177 \cdot 10^{-4}$ sccm.*

As a comparison, the leak rate in the ARCAM reactor with heating has been estimated to be $\sim 6 \times 10^{-5}$ Torr/min, corresponding to $\sim 5.3 \times 10^{-4}$ sccm and the one of the other MDECR reactor of the laboratory is $\sim 1 \times 10^{-5}$ Torr/min, i.e. $\sim 7 \times 10^{-4}$ sccm (without heating).

The authors of [36] estimate that their cell performance starts to drop at an air leak fraction of 140 ppm to 200 ppm as compared to their total gas flow. Their process uses $1.7 - 3.5$ sccm of SiH_4 and 360 sccm of H_2 and their deposition rate is 5 Å/s. We often used pure silane conditions with a moderate flow of 42 sccm. With this value, the threshold of $140 - 200$ ppm would correspond to $\sim 60 - 84 \times 10^{-4}$ sccm, which is lower than our value of 177×10^{-4} sccm obtained in conditions imitating the process of a cell.

The same tests have been repeated with the flange of the antennas replaced by a blank flange and the same unexplained increase by a factor ~ 40 when heating has been found. The goal was to rule out any risk of leak from the water cooling system of the antennas (see Section 4.1 page 145).

6.2   Temperature measurements

Measuring temperatures at the low pressures typically used in MDECR is challenging. In addition to the thermocouples inside the substrate holders (the first substrate holder had two : see Figure III.17 ; the two other substrate holders had only one), we used two other methods that we will briefly describe here. Pyrometry was used to estimate the temperature of the surface of the glass substrates (see Section 1 page 25) and platinum resistance thermometers were glued on the substrate holder to determine the temperature of its surface with the known dependency of their resistance as a function of temperature (measurement of the current applying a constant 5 V tension).

There is a large temperature gradient in the substrate holders, from the heating filament or lamps down to their surface. This can be illustrated by the different temperatures recorded by the two thermocouples of the first substrate holder : e.g. $\sim 650\,°C$ close to the resistive filament and $\sim 350\,°C$ in the top plate corresponding to a surface temperature of $\sim 300\,°C$
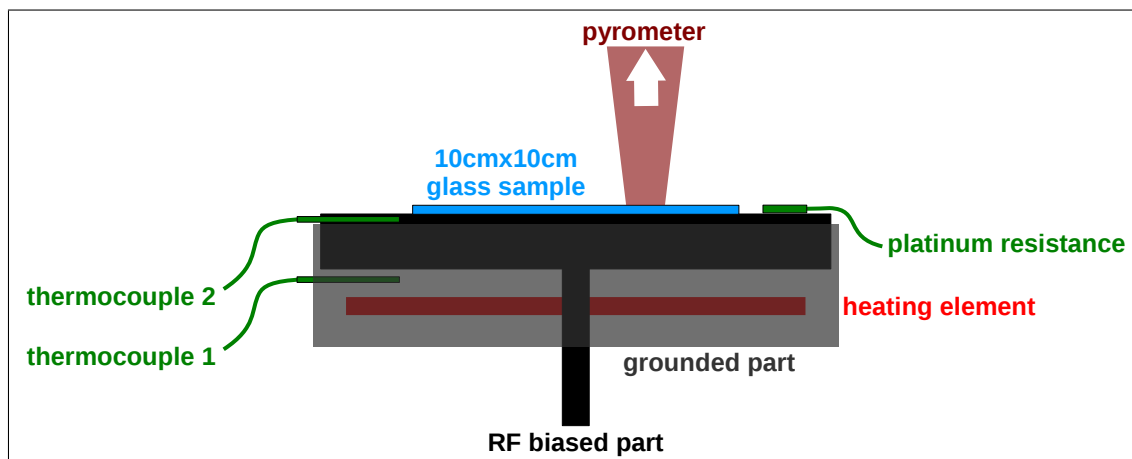
Figure III.17 – *Side view of the first substrate holder showing the different ways of measuring the temperature. See text for more explanations.*

given by the platinum resistance and a temperature of the glass of 230 °C given by the pyrometer.

With the second substrate holder, the temperature indicated by the thermocouple was 535 °C to reach 230 °C indicated by the pyrometer. So that for the same substrate temperature, the temperatures indicated by the thermocouples of the different substrate holders can be very different. This illustrates how temperature can be a very misleading information because it crucially depends on where it is measured. Therefore, we explored the use of pyrometry, which is a very interesting and powerful tool to ensure the reproducibility of the temperature conditions.

6.2.1   Plasma induced substrate heating

It is well known that temperature is a crucial parameter for growth of μc-Si:H thin films. In our low pressure reactor, pyrometry can be a powerful tool to study the real temperature of interest, which is the substrate surface temperature. This section reports some early results obtained in the reactor Domex for inert-gas plasmas (pure argon in Figure III.18). The glass substrate is not glued and thus, its temperature is much lower than the one of the platinum resistance thermometers glued at the surface of the substrate holder (~ 296 °C vs 213 °C). The injection of 100 sccm of pure argon (resulting in a gas pressure of 1.4 mTorr) has no effect on the temperature measured by the pyrometer (Phase 1). A total microwave power of 1 kW is fed to the plasma (Phase 2). Without biasing the substrate holder, the temperature increase in these conditions is of ~ 20 °C in around 4 minutes. The RF power is then injected so as to result in a DC bias voltage of -80 V (Phase 3) and the substrate temperature increases by another ~ 33 °C in 5 minutes 30 seconds. This evidences the central role of ions in the plasma induced substrate heating and reveals that a significant part of the intrinsic layer of the microcrystalline cells is probably grown under *transient* conditions of substrate temperature.

In the case of a pure hydrogen plasma (23 sccm of H_2, a plasma pressure of 7 mTorr, an RF power of 41 W corresponding to a bias of $+30$ V), the pyrometer recorded a temperature increase from 216 °C to 251 °C in 3 minutes and 20 seconds (graph not shown).

As a comparison, in Radio-Frequency plasmas, one of the very successfull methods to increase the deposition rate is the so called "High Pressure Depletion" regime. This regime involves
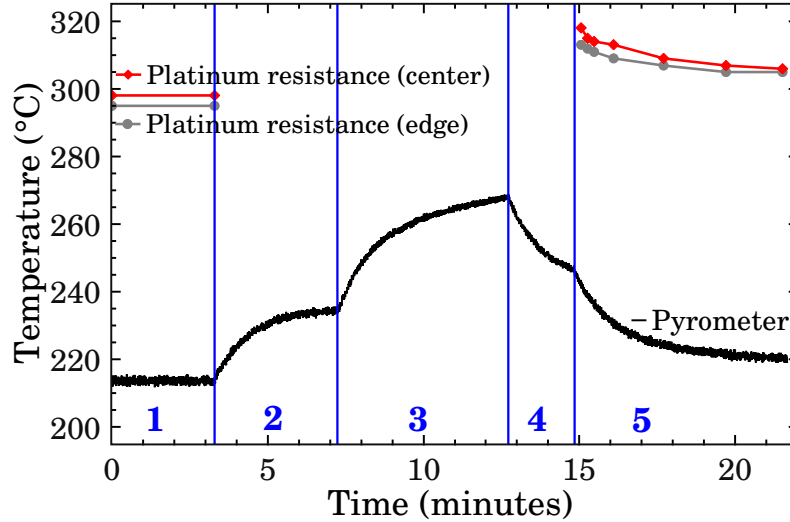
Figure III.18 – *Comparison of the temperature of the glass substrate recorded by the pyrometer and the one of the substrate holder surface measured by two platinum resistance thermometers (near its center and near its edge). Phase 1 is the end of the heating phase. In phase 2, the microwave power is injected to ignite the argon plasma. Then in phase 3, the RF power is supplied to the substrate holder. The phases 4 and 5 correspond to the RF and microwave powers being successively turned off.*

a high power density. As a result, temperature increases of the substrate holder as high as 65 °C have been reported [37]. In the showed graph of [37], this transient of temperature lasts around 30 minutes, which corresponds to a 2 µm deposition in their conditions.

6.3   Homogeneity in thickness

The homogeneity in thickness for the microcrystalline depositions has been studied with the first eight samples on $10 \times 10 \, cm^2$ glass substrates from the first series in the new ATOS reactor. The average thickness decrease between the center and the bottom left corner (a few millimeters from the border) was 19 %, the worst sample being 23 % thinner in the corner. These thickness variations are not related to the nature of the MDECR source. Possible reasons are :

- the presence of the walls, which are quite close from the antennas (as close as $\sim 4 \, cm$),
- the fact that the antenna in the center is shorter ($\sim 2.6 \, cm$ difference),
- and the gas injection geometry.

In the case of an industrial-scale reactor with a matrix of ECR antennas, with a uniform gas injection and with an equal microwave power on each applicator, the diffusion plasma would result in a film with a highly homogeneous thickness provided the walls of the vessel are sufficiently far away from the substrate. Indeed, the fact that each antenna is an independent source and that all of them are identical would ensure that the composition of the diffusion plasma is homogeneous above a minimal antennas – substrate holder distance.

For example, for SiO_2 deposition, the homogeneity in thickness on a 200 mm wafer can be as good as $\pm 3.3 \%$ for a square matrix of 16 applicators of $24 \, cm \times 24 \, cm$ [30].

7   Conclusion

Microwave reactors are used and studied in our laboratory since 1995. Six reactors have been successively designed. The first two ones were Integrated Distributed Electron Cyclotron Resonance (IDECR) reactors. The four others were then Matrix Distributed ECR (MDECR) ones. MDECR reactors are used in several French research groups but our laboratory is the only one working on photovoltaic applications with this technology, thus making our reactor a unique prototype in the world.

We have presented the general principle of Electron Cyclotron Resonance (ECR) and the historical evolution of the various types of reactors based on this effect. The advantages of the MDECR configuration, selected for this work, have been emphasized throughout this chapter. The main ones of interest for photovoltaic applications are the following :

- The magnetic confinement of the hot electrons allows to create highly dissociated plasmas, which results in high deposition rates.
- The size of the reactor can be easily scaled up to deposit on large substrates, just by repeating the pattern of antennas.
- The low process pressure ensures the absence of powders.
- The MDECR configuration enables the independent control of the ion flux (mainly defined by the MW power) and the ion bombardment energy (corresponding to RF power on the substrate holder).

Then, the reactor ATOS has been described in detail and some basic characterizations have been presented. Assembling such a complex equipment has been an important task of my PhD. Its maintenance and its improvement (e.g. the installation of the load-lock) have been constant goals during this project.

The next chapter will expose the results obtained with these two MDECR reactors (Domex and ATOS) for the high rate deposition of hydrogenated microcrystalline silicon thin films and solar cells.

Bibliography

[1] M. A. Lieberman and A. J. Lichtenberg. *Principles of Plasma Discharges and Materials Processing.* Wiley, second edition, 2005.

[2] Satoshi Nakayama. ECR (electron cyclotron resonance) plasma for thin film technology. *Pure Appl. Chem.*, 62(9), 1990.

[3] S. M. Gorbatkin and L. A. Berry. Contamination by sputtering in mirror field electron cyclotron resonance microwave plasma sources. *Journal of Vacuum Science & Technology A: Vacuum, Surfaces, and Films*, 10(5):3104–3113, 1992.

[4] Satoru Somiya, Hirotaka Toyoda, Yoshihiko Hotta, and Hideo Sugai. Suppression of Oxygen Impurity Incorporation into Silicon Films Prepared from Surface-Wave Excited H_2/SiH_4 Plasma. *Japanese Journal of Applied Physics*, 43(11A):7696–7700, 2004.

[5] M. Pichot, A. Durandet, J. Pelletier, Y. Arnal, and L. Vallier. Microwave multipolar plasmas excited by distributed electron cyclotron resonance: Concept and performance. *Review of Scientific Instruments*, 59(7):1072–1075, 1988.

[6] E. Dufour-Gergam, F. Meyer, F. Delmotte, M. C. Hugon, B. Agius, P. Warren, and D. Dutartre. Electrical properties of silicon nitride films grown on a SiGe layer by distributed electron cyclotron resonance plasma-enhanced chemical vapor deposition. *Thin Solid Films*, 294(1-2):214 – 216, 1997.

[7] S. Béchu, O. Maulat, Y. Arnal, D. Vempaire, A. Lacoste, and J. Pelletier. Multi-dipolar plasmas for plasma-based ion implantation and plasma-based ion implantation and deposition. *Surface & Coatings Technology*, 186:170–176, 2004.

[8] P. Bulkin, R. Brenot, B. Drévillon, and R. Vanderhaghen. Structure and transport properties of integrated distributed electron cyclotron resonance grown micro-crystalline silicon. *Journal of Non-Crystalline Solids*, 231(3):268 – 272, 1998.

[9] Pavel Bulkin, Nicolas Bertrand, and Bernard Drévillon. Deposition of SiO_2 in integrated distributed electron cyclotron resonance microwave reactor. *Thin Solid Films*, 296(1-2):66 – 68, 1997. European Materials Research Society 1996 Spring Meeting, Symposium B: Thin Film Materials for Large Area Electronics.

[10] J. Asmussen and M. Dahimene. The experimental test of a microwave ion beam source in oxygen. *Journal of Vacuum Science & Technology B: Microelectronics and Nanometer Structures*, 5(1):328–331, 1987.

[11] M. Sadowski. Plasma confinement with spherical multipole magnetic field. *Physics Letters A*, 25(9):695 – 696, 1967.

[12] Rudolf Limpaecher and K. R. MacKenzie. Magnetic Multipole Containment of Large Uniform Collisionless Quiescent Plasmas. *Review of Scientific Instruments*, 44(6):726–731, 1973.

[13] Michel Moisan and Jacques Pelletier. *Microwave Excited Plasmas.* Elsevier, 1992.

[14] Jérôme Perrin. *Physico-Chimie d'un Plasma Multipolaire de Silane et Processus de Déposition du Silicium Amorphe Hydrogéné.* PhD thesis, Université Paris VII, December 1983.

[15] J. Pelletier and T. Lagarde. Chemical vapor deposition in high-density low-pressure plasmas: reactor scale-up and performance. *Thin Solid Films*, 241:240–246, April 1994.

[16] T. Lagarde and J. Pelletier. Procédé de production de plasmas élémentaires en vue de créer un plasma uniforme pour une surface d'utilisation et dispositif de production d'un tel plasma, 4 août 1999. Number FR 99 10 291.

[17] A. Lacoste, S. Béchu, J. Pelletier, and Y. Arnal. Dispositif de confinement de plasma, 28 mars 2002. Number FR 02 03 900.

[18] Tan Vinh Tran. *Caractérisation et modélisation des plasmas micro-ond multi-dipolaires – Application à la pulvérisation assistée par plasma multi-dipolaire.* PhD thesis, Université Joseph Fourier, Décembre 2006. Download at http://tel.archives-ouvertes.fr/tel-00139610/en/.

[19] G. J. M. Hagelaar, K. Makasheva, L. Garrigues, and J.-P. Boeuf. Modelling of a dipolar microwave plasma sustained by electron cyclotron resonance. *Journal of Physics D: Applied Physics*, 42(19), 2009.

[20] Jr. A. A. Ivanov, C. Rouillé, M. Bacal, Y. Arnal, S. Béchu, and J. Pelletier. H$^-$ ion production in electron cyclotron resonance driven multicusp volume source. *Review of Scientific Instruments*, 75(5):1750–1753, 2004.

[21] T Lagarde, Y Arnal, A Lacoste, and J Pelletier. Determination of the EEDF by Langmuir probe diagnostics in a plasma excited at ECR above a multipolar magnetic field. *Plasma Sources Science and Technology*, 10(2), 2001.

[22] A Lacoste, T Lagarde, S Béchu, Y Arnal, and J Pelletier. Multi-dipolar plasmas for uniform processing: physics, design and performance. *Plasma Sources Science and Technology*, 11(4):407–412, 2002.

[23] L. Latrasse, A. Lacoste, J.C. Sánchez-López, A. Bès, M. Rayar, and J. Pelletier. High deposition rates of uniform films in tetramethylsilane-based plasmas generated by elementary microwave sources in matrix configuration. *Surface and Coatings Technology*, 203(16):2343 – 2349, 2009.

[24] L Latrasse, A Lacoste, J Sirou, and J Pelletier. High density distributed microwave plasma sources in a matrix configuration: concept, design and performance. *Plasma Sources Science and Technology*, 16(1), 2007.

[25] P. Bulkin, A. Hofrichter, R. Brenot, and B. Drévillon. Deposition of microcrystalline silicon in an integrated distributed electron cyclotron resonance PECVD reactor. *Thin Solid Films*, 337:37–40, 1999.

[26] P. Roca i Cabarrocas, P. Bulkin, D. Daineka, T. H. Dao, P. Leempoel, P. Descamps, T. Kervyn de Meerendre, and J. Charliac. Advances in the deposition of microcrystalline silicon at high rate by distributed electron cyclotron resonance. *Thin Solid Films*, 516(20):6834–6838, August 2008.

[27] Maria Calafat, David Escaich, Richard Clergereaux, Patrice Raynaud, and Yvan Segui. Particle formation in acetylene very low-pressure high density magnetized plasmas. *Applied Physics Letters*, 91(18):181502, 2007.

[28] J. Perrin, O. Leroy, and M. C. Bordage. Cross-Sections, Rate Constants and Transport Coefficients in Silane Plasma Chemistry. *Contributions to Plasma Physics*, 36(1), 1996.

[29] Pavel Bulkin, Nicolas Bertrand, and Bernard Drévillon. Deposition of SiO$_2$ in integrated distributed electron cyclotron resonance microwave reactor. *Thin Solid Films*, 296:66–68, March 1996.

[30] Roelene Botha. *Deposition of thin films in a high-density low-pressure plasma system: the influence of the SiH$_4$ injection on the deposition kinetics and material properties of SiO$_2$*. PhD thesis, École Polytechnique, 2008.

[31] Bicher Haj Ibrahim. *The deposition of multilayer and gradient index thin films by MDECR-PECVD*. PhD thesis, École Polytechnique, April 2007.

[32] Alfred Hofrichter. *Dépôt plasma de couches minces d'alliages de silicium à fonctionnalités optiques et mécaniques sur polycarbonate*. PhD thesis, École Polytechnique, March 2001.

[33] Thien Hai DAO. *Dépôt de couches minces de silicium à grande vitesse par plasma MDECR*. PhD thesis, École Polytechnique, May 2007.

[34] J. Pelletier, A. Lacoste, T. L. Lagarde, M. Moisan, Y. Arnal, and Z. Zakrzewski. PCT WO01/20710, U.S. Patent 6 727 656. April 27, 2004.

[35] D. Daineka, P. Bulkin, G. Girard, J.-E. Bourée, and B. Drévillon. High density plasma enhanced chemical vapor deposition of optical thin films. *Eur. Phys. J. Appl. Phys.*, 26, 2004.

[36] T. Kilper, W. Beyer, G. Bräuer, T. Bronger, R. Carius, M. N. van den Donker, D. Hrunski, A. Lambertz, T. Merdzhanova, A. Mück, B. Rech, W. Reetz, R. Schmitz, U. Zastrow, and A. Gordijn. Oxygen and nitrogen impurities in microcrystalline silicon deposited under optimized conditions: Influence on material properties and solar cell performance. *Journal of Applied Physics*, 105(7):074509, 2009.

[37] B. Rech, T. Repmann, M.N. van den Donker, M. Berginski, T. Kilper, J. Hüpkes, S. Calnan, H. Stiebig, and S. Wieder. Challenges in microcrystalline silicon based solar cell technology. *Thin Solid Films*, 511-512:548–555, 2006. EMSR 2005 - Proceedings of Symposium F on Thin Film and Nanostructured Materials for Photovoltaics - Symposium F.

Chapter IV

Microcrystalline silicon films and solar cells

Contents

Introduction

Chapter I gave a historical review of the plasma sources developed to attempt to solve the challenges of high rate deposition of microcrystalline silicon cells and gave the latest state-of-the-art achievements in research groups and industrial companies. Therefore, the results reported in this chapter have to be compared with them.

Chapter II explained the principles of some of the most important diagnostics used in this chapter.

Chapter III showed all the advantages of the Matrix Distributed Electron Cyclotron Resonance technology and presented the two reactors used during this work.

This chapter, which is the core of our work, will now give all the results obtained during this PhD. It is organized in four parts. The first two parts (page 83 and 94) will expose general points on microcrystalline silicon films and cells respectively. The third part (page 100) will summarize the characterization results obtained during parametric studies and show the successive improvements of the material quality. Finally, the fourth part (page 145) is a discussion on all the potential sources of limitation of our cells.

1   Microcrystalline silicon

1.1   Definition

Microcrystalline silicon (sometimes also called nanocrystalline silicon) is a heterogeneous material. It contains a crystalline phase appearing as crystallites of variable crystallographic orientations and variable sizes : typically between 10 nm and 50 nm. These crystallites can be separated by grain boundaries saturated with weakly bonded hydrogen or can be embedded in an amorphous or disordered phase. "Cracks" can also appear between the nanocrystals. In some cases, the crystallites can be included in bigger columnar structures.

One of the great difficulties of microcrystalline silicon is that very different materials, i.e. very different microstructures, can be obtained depending on the methods and conditions of deposition and labelled "microcrystalline". As a consequence, comparing results from different research groups can be tricky. For example, the crystalline volumic fraction of the films can vary from 30 % to 100 %.

What is more, a second difficulty is that a structural inhomogeneity along the growth axis is often observed. For example, the material is often more crystallized on the top than at the interface with the substrate. This evolution can be monitored by in-situ ellipsometry for example [1].

Finally, a third difficulty is that a significant substrate dependence of the nucleation process is often reported. Possible explanations are :

- The diffusion coefficients of the radicals vary for different substrates.
- The defects of the substrate surface can act as nucleation sites.
- Epitaxy can take place on a crystalline substrate.
- The exposition of the first layers to hydrogen will depend on the permeability of the substrate to hydrogen, e.g. hydrogen will be accumulated if it cannot diffuse inside the substrate.

1.2   Microcrystalline silicon history in a nutshell

Here are a few dates of the microcrystalline silicon history :

1968 : S. Veprek and V. Maracek managed to obtain µc-Si at low temperature using chemical transport in hydrogen plasma.
1979 : First demonstration of the possibility to deposit µc-Si directly from a silane plasma by S. Usui and M. Dikuchi.
1981 : Second demonstration of µc-Si deposition by silane plasma by Spear and coworkers.
1991 and 1992 : Preliminary works of Lucovsky and Faraji about the use of µc-Si as the intrinsic layer for solar cells.
1994 : First successful use of µc-Si as the absorber layer of solar cells by the research group of the Institute of Microtechnology of the University of Neuchâtel, Switzerland [2]. The popularity of µc-Si started to grow after it was first established that this material is very stable against light-induced degradation and could be used in solar cells despite its natural slightly n-doped type.
April 2001 : Kaneka Corporation started the production of amorphous/microcrystalline (a-Si/µc-Si) tandem modules in Japan.
End of 2008 : With Oerlikon Solar turn-key equipment, Inventux Technologies (near Berlin, Germany) is the first company in Europe to start the production of a-Si/µc-Si tandem modules. The efficiency reached in April 2010 is 9.2% stabilized for their $\sim 130\,\mathrm{W}$ modules of $1.4\,\mathrm{m}^2$ and with a full capacity production of $33\,\mathrm{MW}$ per year.

These few non-exhaustive milestones help to underline that the application of this material as the intrinsic layer for solar cells is rather recent and that its future for industrial mass production lies in the combination with an amorphous cell in the so-called tandem structure.

1.3   The advantages of microcrystalline silicon

Hydrogenated microcrystalline silicon (µc-Si:H) has many advantages as compared to hydrogenated amorphous silicon (a-Si:H). One of its most interesting properties is that unlike the famous Staebler-Wronski effect in a-Si:H, it shows almost no light-induced degradation. For exemple, the photocurrent of µc-Si:H films has been found to stay unchanged under light soaking, while the one of device quality a-Si:H drops by a factor of 10 in [3]. But, illustrating

the difficulty of making statements universally true for the whole range of microstructures of this material, this will not be perfectly true for films with low crystallinity as observed in [4] where the photosensitivity of their moderately crystallized films (crystalline fraction $\leq 30\,\%$ estimated by Raman spectroscopy) decreases by a factor of almost 10. In [5], a film with a crystalline fraction of 30 % (from ellipsometry) shows an irreversible degradation induced by light-soaking (decrease of the dark conductivity and of the mobility-lifetime product, and enhancement of the sub-gap absorption) while the films with crystalline fractions of 67 % and higher are stable. As a conclusion, the optical and electrical properties are stable for crystalline fractions above $\sim 50-60\,\%$ [5, 6].

The lower band-gap of μc-Si:H ($\sim 1.1\,\mathrm{eV}$) as compared to a-Si:H ($\sim 1.7\,\mathrm{eV}$) allows to absorb photons of lower energies. The combination of a top amorphous cell with a bottom micro-crystalline cell is thus often used to collect a greater part of the sun spectrum (until the red and infra-red) and to boost the thin film cell efficiencies. The other optical properties will be detailed in Section 1.6.

For p-doped and n-doped layers, μc-Si has a greater doping efficiency than a-Si and for intrinsic layers, it has higher room temperature dark conductivities ($10^{-7}-10^{-5}\,\mathrm{S{\cdot}cm^{-1}}$ vs $10^{-9}-10^{-11}\,\mathrm{S{\cdot}cm^{-1}}$ for a-Si:H) and lower activation energies ($0.4-0.6\,\mathrm{eV}$ vs $0.7-0.9\,\mathrm{eV}$ for a-Si:H). What is more, the mobility-lifetime products and ambipolar diffusion lengths are also greater for optimized μc materials.

On the other hand, the electrical properties of μc-Si are not as good as those of polycrystalline silicon (poly-Si), but one can argue that its deposition techniques are much easier than the high temperature (oven above $600\,^\circ\mathrm{C}$) or laser annealing procedures necessary to obtain poly-Si. Indeed, μc-Si can be deposited in the same PECVD reactors as the ones developed for amorphous silicon, just by changing the process parameters. Since it does not require high temperatures, it is compatible with a great diversity of substrate types, including flexible ones, which is of great interest for industrial or custom-designed applications, e.g. for roll-to-roll production.

1.4   The drawbacks of microcrystalline silicon

This type of material presents two main drawbacks.

First, this material is characterized by a low absorption coefficient of light, due to its indirect band-gap. The absorption is then a three particle process, involving a photon and a phonon resulting in an exciton (i.e. an electron-hole pair) creation. Thus, microcrystalline p-i-n junctions must have thick intrinsic layers of $1\,\mu\mathrm{m}-3\,\mu\mathrm{m}$ (to be compared with the typical $0.3\,\mu\mathrm{m}$ thick absorber layer of amorphous cells).

The second drawback is the difficulty to obtain deposition rates higher than a few Angströms per second while maintaining the material optical and electrical quality. This can be quantified for example by measuring the average surface reaction probability β in microcrystalline deposition conditions and in amorphous deposition conditions, which are $\beta \sim 0.2$ and ~ 0.4 respectively [7]. Another way to illustrate this difference is to increase the hydrogen dilution in a silane and hydrogen mixture in order to observe the transition from a-Si:H growth to μc-Si:H growth : in [8], the deposition rate drops from 7 to $0.3\,\mathrm{\mathring{A}/s}$. As a consequence, it is easy to understand that improving the growth rate of μc-Si:H is a crucial goal for industrial production of cost-effective solar cells. The use of an MDECR plasma is a solution to

reach the required deposition rates (up to $28\,\mathring{\text{A}}/\text{s}$ with $100\,\text{sccm}$ of pure silane have been demonstrated [9]).

Another consequence of the above-mentioned limitations is that the optimization of the light trapping schemes is a very important research topic for further improvement of the performance of these cells.

Finally, we can also mention that due to its crystalline order and to the presence of grain boundaries or even "cracks" [10], this material suffers from a high sensitivity to contaminations, both *during* the growth and *after* the deposition, when stored at ambient air. In particular, the surface adsorption of oxygen or water, or their diffusion inside the material can lead to wrong interpretations of the electrical characterizations so that care must be taken to avoid them.

1.5   Industrial goals

We already emphasized that a high deposition rate is a necessary condition to fulfill for industrial applications. Two other conditions can be mentioned : a high homogeneity over large areas has to be achieved, in terms of material properties and of film thickness (better than $\pm 10\,\%$ over $1\,\text{m}^2$) and the gas utilization has to be efficient. In addition to these requirements, the process must have a high repeatability, e.g. not to shift with time due to a dependence on the state of the walls. This also brings up the question of the cleaning procedure, which should happen as rarely as possible and be as fast as possible in order to maximize the utilization time of the equipment.

Other important large area industrial applications of microcrystalline silicon are light sensors and thin-film transistors (TFT). For the latter application, a crucial requirement is that the film must be completely crystallized right from the start (i.e. without a less crystallized incubation layer) in order to limit the off-current.

1.6   Optical properties

The optical characteristics of microcrystalline silicon are similar to those of crystalline silicon, enhanced by the internal scattering phenomenon at the grain boundaries. Another common feature of µc-Si is the presence of a surface roughness due to the presence of cristallites and/or columns, thus enhancing the optical path of light in the film. The optical absorption of microcrystalline silicon as a function of the photon energy/wavelength can be seen in Figure IV.1.

Three parts can be distinguished in this graph :

1. Above the gap energy ($E_g \sim 1.1\,\text{eV}$) : This high absorption part involves band-to-band electronic transitions. For energies above $1.7\,\text{eV}$, the experimental values for µc-Si are often higher than the c-Si curve, which can be explained by the presence of a higher absorption direct band-gap amorphous fraction (if any), by internal scattering and by the presence of grain boundaries. For energies below $1.7\,\text{eV}$, µc-Si exhibits a significantly higher absorption coefficent than a-Si, which means that low energy photons can be absorbed, provided the layer is thick enough. These two points are of great interest for photovoltaic applications.
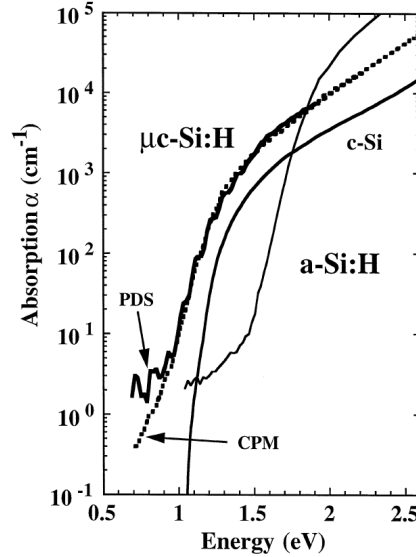
Figure IV.1 – *Superposition of the absorption coefficients of amorphous, microcrystalline and monocrystalline silicon as a function of the photon energy (taken from [11]).*

2. Between $\sim 0.8 - 1.1\,\text{eV}$: Below the band-gap energy, the Urbach tail of exponentially decreasing absorption is due to the presence of strained bonds in the disordered semiconductor and corresponds to electronic transitions involving the bandtail states. This part of the absorption can be fitted as $\alpha(E) \propto \exp\left(\frac{E - E_g}{E_0}\right)$, where the Urbach parameter E_0 corresponds to the width of the absorption edge. A too high (above $\sim 35 - 40\,\text{meV}$) value of E_0 can indicate a too high density of bandtail states, which can decrease the electric field inside the intrinsic layer.

3. At energies lower than $\sim 0.8\,\text{eV}$: The absorption is related to defects in the gap, i.e. recombination centers. This is justified by the increase of α in this region upon annealing [12]. As a consequence, this value is a very interesting indicator of the quality of the material. Typical values of a device grade material at $0.8\,\text{eV}$ are $\alpha = 0.1 - 0.3\,\text{cm}^{-1}$ or even below (corrected for surface roughness scattering), or $\alpha = 1 - 3\,\text{cm}^{-1}$ (as measured).

Such graphs can be obtained by the diagnostics of Constant Photocurrent Method (CPM) and Photothermal Deflection Spectroscopy (PDS), which have unfortunately not been used during this work. For experimental measurements, the band-gap of µc-Si seems to be smaller than the one of c-Si because its curve is shifted up. This artefact is due to light scattering on the rough surface and/or in the bulk, and can be significantly reduced or even eliminated by polishing the surface, as demonstrated in [13].

1.7   Electrical properties

To study the transport properties of microcrystalline silicon, one has to keep in mind that the material is heterogeneous, anisotropic and that its properties may vary with thickness.

Indeed, we have already mentioned that this material is *heterogeneous* : it is a complex combination of crystallites, grain boundaries, amorphous tissue and voids. The bonds responsible for the band tails are thought to be localized at the grain boundaries. The properties of µc-Si:H are usually *anisotropic* and since we are working on the optimization of solar cells, we care about transport perpendicular to the substrate. The transport parallel

to the substrate is the suitable parameter to focus on when optimizing thin film transistors for example. *The thickness dependence* of the electronic properties is often related to the variation of the crystalline fraction during the growth. This has been evidenced for example in [14] by combining in-situ ellipsometry and Time Resolved Microwave Conductivity (TRMC) : The deduced mobility is seen to increase at the beginning of the growth, following the crystalline fraction, but when the latter saturates, around 200 nm, the mobility keeps on increasing, thus indicating that the crystalline volume fraction is not the only parameter controlling the electrical properties.

The density of states (DOS) in µc-Si also strongly depends on the particular microstructure of the studied sample and does not show as clearly the same features as in a-Si (i.e. exponential band tails corresponding to the variations in bond lengths and bond angles, and two Gaussian distributions of deep states attributed to unsaturated dangling bonds). The smaller the grains, the higher the grain boundary concentration and as a consequence, the higher the DOS. In the case of large grains, the DOS is usually lower than for a-Si.

1.7.1   The grain boundaries

The grain boundaries are composed of remaining amorphous tissue and/or tilted bonds, with deviations in their angles and lengths. They may also contain impurities such as carbon, nitrogen and/or oxygen which are migrating there during the crystallization process or which penetrate after the deposition if the film is exposed to ambient air. As a consequence, in the grain boundaries, the density of states is modified with the appearance of tails in the gap and a shift of the conduction (resp. valence) band energy E_C (E_V) to higher (lower) energies. An interesting order of magnitude to keep in mind is that in a very simplified geometry where the crystallized grains are assumed to be cubic and to all have the same size of 20 nm, there are $\sim 10^{17}$ crystallites per cubic centimeter, which has to be compared to the defect density, i.e. there is less than one defect per crystallite.

The grain boundaries can either cause shunt leakage and thus, reduce the V_{oc} if they are charged, or they can act as barriers of low local conductivity. This later phenomenon can be measured by an Atomic Force Microscopy (AFM) mapping combined with a conductive cantilever : a decrease of the local conductivity in the grain boundaries has been put into evidence and this decrease can be as strong as a factor 100 for the *column* boundaries [15].

1.7.2   Transport parallel and perpendicular to the substrate

Significant discrepencies between parallel and perpendicular transport properties can arise due to the presence :

- of the grain boundaries,
- of too high concentrations of defects in the column joints,
- and/or due to the presence of an amorphous incubation layer formed at the beginning of the deposition.

For example, the diffusion lengths L_d parallel and perpendicular to the substrate have been compared when measured by the Steady-State Photocarrier Grating method (SSPG) and by the Surface Photovoltage method (SPV) respectively and showed to be around 3 to 4 times greater in the perpendicular direction in [16]. This ratio obviously depends on the microstructure of the studied samples and in particular, on the presence of columns. The

same research group later found that it is possible to obtain isotropic µc-Si (i.e. same conductivities and diffusion lengths values in both directions) in films deposited at a lower temperature of 150 °C [17]. Varying the power, another group [18] found that L_d in the perpendicular direction can be higher, equal or lower than the value in the direction parallel to the substrate.

1.7.3   The models of electrical transport

Some models have been adapted from the understanding of the behavior of polycrystalline silicon [19]. It is the so-called "homogeneous model" and it proposes that the transport properties are controlled by the potential barriers which build up at the grain boundaries due to charged trapping defects and which have to be overcome by carriers. Other explanations are based on the confinement due to the lower band-gap energy of the crystallites (1.1 eV) as compared to the amorphous tissue surrounding them (1.7 eV).

Other models are adapted from amorphous silicon. For example, the evolution of the $\mu\tau$ product as a function of the Fermi level position of various µc-Si:H samples has been found to be very close from the behavior of undegraded a-Si:H [18]. Similarly, based on their electrical measurements, the authors of [20, 21] propose that the same transport mechanisms as for amorphous silicon [22] are valid for microcrystalline silicon, i.e. that it is controlled by the exponential tail states which are trapping centers and by amphoteric dangling bonds (either positively or negatively charged, or neutral) acting as recombination centers, which are most likely located at the grain or column boundaries.

Some authors have also proposed that the transport is limited by defects *inside* the crystallites [23].

1.7.4   Consequences for microcrystalline cells

While the diffusion lengths of holes parallel to the substrate in intrinsic µc-Si:H can be up to typically ~ 300 nm [24, 25], it is much too low in doped µc-Si:H to use diffusion limited p-n junctions. From the drift lengths at an electric field of 1 V/µm, one can see that µc-Si is a suitable material for collection over a thickness of several microns. Thus, the microcrystalline solar cells have a p-i-n structure which will be described in detail below (Section 2 page 94).

Furthermore, the ratio μ_e/μ_h of the electron mobility over the hole mobility is typically around 3 to 10 for µc-Si:H. (The value of this ratio is the same for polycrystalline silicon, but is ~ 100 for a-Si:H.) Thus, it is better to illuminate a microcrystalline silicon cell through the p-doped side for the optimum collection of the photogenerated holes.

1.8   Growth mechanisms

This section aims at reviewing briefly the main categories of growth models which have been proposed to account for the formation of microcrystalline silicon at low temperature (~ 200 °C) by Plasma Enhanced Chemical Vapour Deposition. Indeed, with the unique properties of PECVD, it is possible to obtain a crystalline material at low temperature which is otherwise only obtained by annealing amorphous silicon at 600 °C or more.

The models presented in this section mainly correspond to the hypotheses used to explain the growth of µc-Si:H in RF-CCP reactors, which has been and is still the dominant technology to deposit silicon thin films for solar cells. Considering the very unique characteristics of our MDECR plasma, exposed in the previous chapter, it is not clear that the same ideas can apply in our situation. For example, with microwaves, a very high dissociation degree of the SiH_4 molecules can be reached, so that the ratio of Si radicals to SiH_3 radicals can be one hundred times greater than the typical one in RF plasmas [26]. What is more, the very high sticking probabilities of the Si, SiH and SiH_2 radicals as compared to SiH_3 may well be a difficulty to obtain good materials.

From a thermodynamic point of view, it can be shown that µc-Si:H is more stable, i.e. has a lower free energy, than a-Si:H [27]. This gain of free energy depends on the hydrogen content and it is proposed that it is maximized for a highly hydrogenated amorphous layer. Another thermodynamic model is based on a critical elastic energy (i.e. on a critical value of extensive stress) : in this model, a lattice expansion above 1 to 2 % is said to induce amorphous growth [28]. The model of Street [29] can also be listed in this category and proposes that µc is formed above a critical value of the hydrogen chemical potential.

A correlation between a high density of atomic hydrogen and the appearance of a crystalline phase has indeed been experimentally encountered for a wide range of deposition conditions. Thus, it is accepted that hydrogen plays a major role in several of the proposed models [30]. Yet, its role is not clear. As a consequence, the most commonly studied parameter is the silane concentration, that is to say, the silane dilution in hydrogen.

The predictions for the improvement of the material quality and of the deposition rate will be listed for each model.

1.8.1   The surface models

Some models have proposed that the surface phenomena such as physisorption, desorption, diffusion, abstraction and incorporation, can help to understand the formation of microcrystalline silicon.

1.8.1.1   The selective etching model

This model has been proposed quite early (see [31] in 1989) and considers the film formation as the result of a balance or a competition between etching and deposition. The underlying idea is that etching has a positive effect on the quality of the microcrystalline film since the disordered phase and defects (i.e. weak and strained bonds) are preferentially etched. One has to realize that in this model, the reason for the appearance of a crystalline phase well below the melting temperature of silicon is not explained as hydrogen only etches the amorphous phase but does not "create" an ordered phase.

Such an etching has clearly been seen in Layer-By-Layer experiments [32] and increases with the duration of the hydrogen plasma treatment. But in their conditions, the highest etching rates do not correspond to the highest crystalline fractions of the films, which does not fit with this model.

In [31], etching is not systematically associated with hydrogen. Indeed, they also propose reactions where a silicon radical arrives on the surface, reacts and goes back in the plasma phase as a Si_2H_x molecule.

According to this model, a slow growth is not required to obtain a crystallized film. The deposition rate of microcrystalline silicon can be increased as long as the etching rate is also enhanced in order to guarantee the film quality. It also predicts that the film crystallinity should decrease when the substrate temperature is increased due to the less efficient hydrogen etching at high temperatures. This last point does not fit with our experimental results (see Section 3.7 page 130), thus indicating that it is not the dominant growth mechanism in the explored range of temperature.

1.8.1.2   The surface diffusion model

This model, introduced by Matsuda in 1983, proposes that the diffusion of the incoming radicals (mainly SiH_3) on a fully hydrogen passivated surface will allow them to find the best sites to stick and will result in an organized material [30]. Thus, a high atomic hydrogen flux is important to ensure a full coverage of the growth surface and also to favor the diffusion of the radicals by locally heating the surface due to their exothermic reactions. According to this model, the final defect density of the material depends on the density of remaining dangling bonds. Especially at high deposition rates, the latter is said to depend on the ratio of the SiH_3 precursors and of the short lifetime precursors (Si, SiH and SiH_2) [33].

This kind of model can help us to find reasons for the low quality of our microcrystalline silicon. Indeed, in MDECR, many radicals with high sticking coefficients (SiH_x with $x \leqslant 2$) are created. Those radicals are believed to basically just stick where they arrive on the surface, unlike SiH_3 which diffuses until it finds a stable site or a dangling bond. What is more, the fast deposition rates achieved with this high density plasma source may also prevent the diffusing species from finding the suitable site.

According to this model, a temperature increase of the growth surface will result in an enhanced diffusion of the radicals and should therefore improve the quality of the material, but it will be detrimental at too high temperatures because of the resulting lower passivation of the surface by hydrogen atoms.

1.8.2   The volume or growth zone model

It is a model where all the reactions taking place at the surface as well as a few nanometers below are said to be the key parameters leading to the re-arranging of the film, the sub-surface relaxation and to the formation of a microcrystalline material. In particular, the role of hydrogen is crucial, as it provides chemical annealing. Thus, the sub-surface thickness can be defined by the ratio of the diffusion coefficient of atomic hydrogen divided by the growth rate. In this model, nucleation takes place in a porous sub-surface layer as demonstrated by Layer By Layer (LBL) depositions [34]. It can be noticed that this corresponds to the thermodynamic model of [27]. The temperature of the surface and of the volume of the layer is of crucial importance for this mechanism as it controls the penetration depth of atomic hydrogen and the mobility of molecular hydrogen to escape from the growing layer [35, 36]. The effect of energetic ion bombardment also has to be taken into account as they can damage the film on depths as thick as tens of nanometers.

As etching of the walls or of the counter-electrode covered by silicon can take place during the pure hydrogen plasma and would result in chemical transport of silicon under high hydrogen

dilution, some care has to be taken for the proper interpretation of LBL experiments [30, 37]. But their validity has been demonstrated even in a multichamber reactor [38].

The growth zone model predicts that the increase of the deposition rate has to be balanced by a higher temperature in order to allow for the fast diffusion of molecular hydrogen out of the layer. Otherwise, issues of porosity, too high hydrogen concentration, formation of "bubbles" or delamination of the layer from the substrate could occur.

1.8.3   The role of hydrogen

The crucial role of hydrogen will be emphasized repeatedly throughout this manuscript.

For PECVD, the three main solutions to provide sufficient H radicals are :

- A high hydrogen dilution (typically 5 % of SiH_4 in H_2 in [31] for example)
- A high dissociation of the silane molecules, with or without added hydrogen. Indeed, one has to keep in mind that what really matters is the ratio of silane radicals and hydrogen atoms *in the plasma*. This latter parameter can be quite different from the ratio of the gas flow rates depending on the type of plasma source and on the power [39]. As a consequence, diagnostics to determine this ratio inside the plasma are of great interest.
- The Layer-By-Layer technique, which consists in cycles of growth with silane and hydrogen or with pure silane, and then, during the second phase of the cycle, of exposure of the film to a pure hydrogen plasma.

The possibility to deposit microcrystalline silicon without hydrogen dilution has been demonstrated in our lab several years ago [40]. A high hydrogen dilution was thought to be necessary in RF-CCP reactors to obtain µc-Si but this consensus was questioned by recent results of van den Donker *et al.* [41], who obtained µc-Si from pure SiH_4 in RF-CCP by avoiding the formation of an amorphous incubation layer. They obtained cells with 9.5 % efficiency in pure silane.

We can now list the main effects attributed to hydrogen :

- The passivation of dangling bonds, which is of crucial importance in the grain boundaries,
- The etching of weaker distorted or strained bonds and the preferential etching of the amorphous phase, which favors the crystallization,
- The enhancement of the diffusion of radicals on the surface,
- The so-called phenomenon of chemical annealing : The exothermic H recombinations, when taking place at the film surface, result in higher diffusion lengths of the precursors and when taking place in the sub-surface, allow for the re-organization of the silicon network [42] and has been said to "liquify" the sub-surface region in order to interpret the results of Layer-By-Layer (LBL) experiments [32].
- From a plasma point-of-view, hydrogen is also responsible for chemical transport, where silicon and impurities (if any) from the walls are etched, "recycled" in the plasma and further deposited.

1.9   Conclusion : Method of study

To sum up the first part of this chapter, we can say that all these considerations lead to the conclusion that the comparison of the different samples has to be very methodic and careful. Indeed, microcrystalline silicon is well known to evolve during the deposition, to be inhomogeneous along the axis of growth, so that only films of very close thicknesses should be compared for the results to be valid. Otherwise, misleading conclusions could be made in choosing the deposition conditions producing the best material. Also, since the homogeneity of our microcrystalline films is not perfect on our $10\,\text{cm} \times 10\,\text{cm}$ glass substrates, great care has been devoted to systematically perform all the measurements (e.g. ellipsometry, Raman spectroscopy, etc.) on the exact same spot of the sample.

Many aspects of microcrystalline silicon are still open questions, such as the different explanations for the electrical transport or the growth mechanisms. As a consequence, basic research is still needed to evidence the crucial parameters to improve solar cells made with this material. This also allows new breakthroughs to be generated, for example, with non-standard plasma sources.

2   Microcrystalline silicon solar cells

Introduction

The three main challenges for the future mass production of high performance microcrystalline (µc) solar cells are :

- the increase of the deposition rate,
- the development of efficient light trapping solutions,
- their uniform deposition on large area substrates.

The unique properties of the MDECR technology, exposed in the previous chapter, make it a great candidate to fulfill these requirements.

Due to the electrical properties of the microcrystalline silicon material reviewed in the previous section, and in particular, to the diffusion lengths of the minority carriers which are generally lower than the thickness of a few micrometers necessary for an efficient light absorption, the microcrystalline solar cells cannot be based on a p-n junction but have to be p-i-n structures in order not to rely on the diffusion only, but to benefit from a drift-assisted collection.

The next section aims at briefly exposing how the microcrystalline solar cells have been processed during this work.

2.1   The p-i-n structure

This section will describe the different steps to make a p-i-n solar cell in our lab. The order of the letters refers to the order of deposition and is sometimes also called the "superstrate" configuration. This has been by far the most common structure studied during this project. Only a few attempts of n-i-p structures have been carried out.
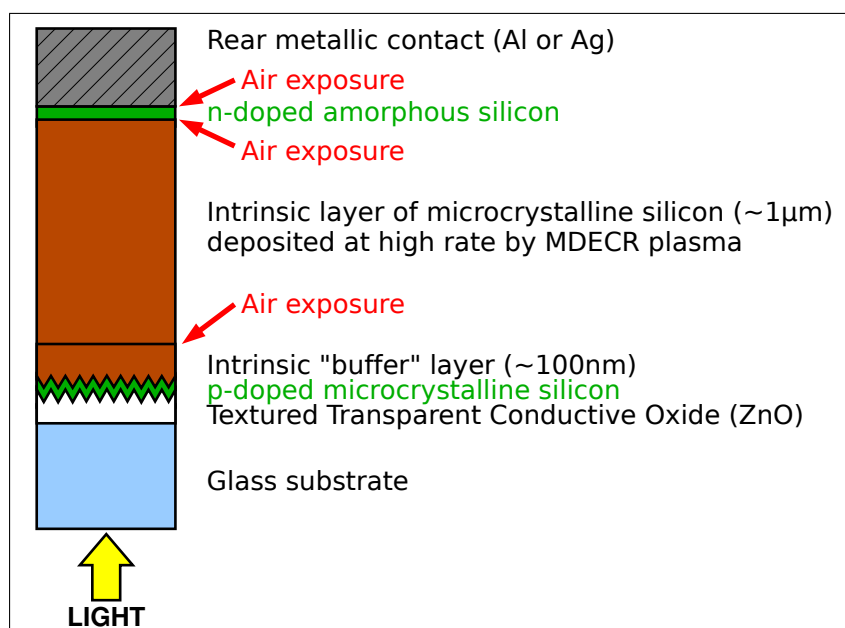

Figure IV.2 – *Structure of our p-i-n cells.*

2.1.1   The Transparent Conductive Oxide (TCO)

The requirements for this layer are that it must be highly transparent (i.e. the absorption should be below $6\% - 7\%$ over the range $400\,\text{nm} - 1100\,\text{nm}$), with a low resistivity (lower than $\sim 10\,\Omega\,\square$) and its surface texture has to be optimized to enhance the light scattering in order to provide the greatest optical path of light through the cell (the typical rms roughness should be $\sim 50\,\text{nm} - 150\,\text{nm}$).

For the p-i-n configuration, the other roles and requirements of the TCO are to help to minimize the amount of reflected light with its matching of the refractive indexes (in the visible range : $n_{\text{Corning 1737 glass}} \sim 1.5$, $n_{\text{ZnO}} \sim 2$ and $n_{\text{µc-Si}} \sim 3.7$). Furthermore, it should be stable against the deposition conditions used for the cell (e.g. temperature and diffusion of atomic hydrogen).

For the µc solar cells produced during this work, we used zinc oxide (ZnO) provided by the Photovoltaic Institute (IPV) in Jülich, Germany. Indeed, Indium Tin Oxide (ITO) is not stable when exposed to a silane plasma and tin oxide (SnO_2) can be reduced by the hydrogen-rich plasma required for deposition of µc-Si, especially at high temperatures ($> 200\,°\text{C}$) [43]. ZnO can be sputtered or deposited by Low Pressure Chemical Vapour Deposition (LP-CVD) or Metal-Organic Chemical Vapour Deposition (MO-CVD). The ZnO obtained by LP-CVD and MO-CVD is naturally textured but the one we used is obtained by sputtering and therefore, is flat. We textured it by chemical wet etching in a 0.5%-diluted hydrochloric acid (HCl) bath for 30 seconds. The resulting rms roughness, measured by Atomic Force Microscopy, is in the $100 - 150\,\text{nm}$ range (i.e. a peak-to-valley roughness of about $400\,\text{nm}$) for a total thickess of $\sim 700\,\text{nm}$. When intrinsic, the direct band-gap of ZnO is around $3.3\,\text{eV}$ at room temperature but we used aluminum doped zinc oxide (ZnO:Al) in order to boost its conductivity, in which case the gap can increase up to $3.7\,\text{eV}$ [44].

2.1.2   The doped layers

The n and p-doped layers are made in another reactor named ARCAM, which is a multi-chamber RF-CCP reactor (described in detail in [45]). As a consequence, the samples are taken out at air twice to transfer them as fast as possible for the deposition of the next layer (see Figure IV.2). This is a common problem that a lot of research teams have to face. Thus, the study of the influence of adsorption and oxidation at the surface of microcrystalline films is very important in our conditions (see [6] and [46]) although this problem would not arise in an integrated industrial production line.

The optimized doped layers used during this work can result in 8.3% efficiency for highly crystallized solar cells deposited at low rate from the decomposition of a mixture of SiF_4, H_2 and Ar in another RF-CCP reactor of our laboratory [47]. This guarantees the high quality of the doped layers as well as the possibility to achieve high perfomance despite air exposures.

2.1.3   The p-doped layers

They are doped by adding boron atoms into the silicon matrix. It can be provided by a small flow rate of tri-methyl-boron ($B(CH_3)_3$) or of diborane (B_2H_6) added to the usual SiH_4/H_2 mixture. Due to the incorporation of carbon atoms from the dissociation of TMB,

the gap of the corresponding layer will be larger than when diborane is used, so that the advantage of doping with TMB is to reduce the absorption inside this layer.

It is much easier to dope μc-Si:H than a-Si:H. This is the reason why μc-Si was historically first used as a "transparent" doped layer for amorphous p-i-n structures. The activation energy of p-type μc-Si can be below 50 meV (while the minimum for amorphous doped silicon is around 300 meV) and the conductivity, as high as $\sim 2\,\mathrm{S\,cm^{-1}}$ for a 24 nm-thick layer in [43].

The thickness of the p μc layer is fixed at around 30 nm for all our cells. High crystallinity and high conductivity are crucial requirements for this layer. What is more, it will act as a seed layer for the growth of the intrinsic layer on top so that its crystallinity, crystallographic orientation and roughness can have a great influence on the final cell performance.

2.1.4   The n-doped layers

The top layer is made with the addition of phosphine (PH$_3$) to silane in order to incorporate phosphorous atoms in the matrix. It is amorphous in our case, with a fixed thickness of ~ 30 nm, which should help to encapsulate the intrinsic μc layer and to avoid its post-oxidation.

2.1.5   Optimization of the interfaces

As shown in Figure IV.2, we sometimes added what we call a "buffer layer" or performed interface treatments.

The motivation for the "buffer layer" is to protect the p-i interface from any oxidation and to encapsulate the p-doped layer and the TCO, which could be damaged by atomic hydrogen diffusing from the high density MDECR plasma. The positive effect of such a buffer layer has been reported several times, e.g. in [48] where a 10.3 % solar cell at 11 Å/s is obtained in a VHF system by introducing an intrinsic μc-Si:H buffer layer deposited by How Wire CVD (HW-CVD) at the p-i interface. Probably due to the ion-free very "soft" deposition, this additionnal layer allowed them to improve their spectral response in the blue and to increase their V$_{oc}$.

The V$_{oc}$ of μc-Si solar cells is believed to be mainly governed by interface effects and not by bulk recombinations. This fits with the buffer layers improving this parameter and with the absence of reduction of the V$_{oc}$ for thick cells [11].

The interface treatments also aimed at improving the quality of the interfaces and in particular, at removing the oxide layer which can be formed during the transfer between the two reactors.

2.1.6   The back contacts

Metallic back contacts are then deposited by thermal evaporation just after the deposition of the n-doped a-Si:H layer, which corresponds to a third air exposure. The metal can be silver or aluminum. The former is a better reflector in the red so that it allows to boost the optical path of light and thus, to increase the spectral response above 650 nm [49].

2.1.7   Annealing

This step usually consists in annealing the cell at $150\,°C$ during $30-40$ minutes in an oven. A higher temperature could induce the diffusion of the metal contact inside the silicon stack. The goals of this procedure are to improve the adhesion between the metal contacts and the n-doped layer, to correct some of the structural defects of the material and to activate the doping effect of the passivated B–H complexes in the p layer [43].

2.2   The n-i-p structure

This configuration is also sometimes called the "substrate" configuration. We have carried out a few attempts of n-i-p structures, on metallic substrates or on TCOs. Some authors do n-i-p with a microcrystalline n-doped layer [49, 50, 51] and in some cases, it has been reported to tremendously improve the fill factor [52], but in our case, we have always used an amorphous n-doped layer. The p layer is then covered by sputtered Indium Tin Oxide, in order to illuminate the stack through the p layer.

This configuration is said to have several advantages. The first one is a lower sensitivity to temperature. For example, a higher optimum temperature of their n-i-p was found by the authors of [53] as compared to their p-i-n. This is interesting in the case of MDECR because high temperatures of $\sim 230\,°C$ are often used to produce microcrystalline films at high rate. The boron diffusion is also a much higher risk as compared to the phosphorus diffusion. The second advantage is that an amorphous incubation layer at the beginning of the intrinsic layer growth is an obstacle to hole collection in the case of a p-i-n configuration while it may have a less detrimental impact on top of an amorphous n layer.

One drawback of this structure is that is requires an additional process step : Indeed, the highly conductive µc p-doped layer has to be etched (by the Reactive Ion Etching technique) after the sputtering of the contacts, otherwise the cells suffer from very low parallel resistances.

2.3   What is the "best" crystalline fraction for solar applications ?

The interest of being close to the a-Si to µc-Si transition regime was first reported in [49]. There seems to be a wide consensus that such materials with moderate crystalline fractions give the best cells (e.g. [54, 54, 49]). When approaching the transition, µc-Si:H is characterized by an increasing hydrogen content and an enhanced internal stress [8, 38]. For example, in [55], the authors measured the hydrogen content for an amorphous film, a film at the transition, and a microcrystalline film. Their respective atomic percentages of hydrogen characterized by Elastic Recoil Detection Analysis (ERDA) were $\sim 12\,\%$, $\sim 18\,\%$ and $\sim 6\,\%$, illustrating that the films at the transition are very rich in hydrogen (bonded and also molecular hydrogen in microcavities).

During this work, we almost always looked for the conditions leading to the highest crystalline fraction and therefore, we would like to give here a detailed discussion on the open question of the relation between the cell performance and the crystalline fraction.

Before even listing some explanations and arguments, we can simply give some counter-examples, i.e. highly crystallized material leading to good performance solar cells. In our

laboratory, films with $\sim 80\%$ crystallinity (from Raman spectroscopy) deposited with SiF_4 as a precursor, led to V_{oc} as high as $523\,mV$ and efficiencies of 8.3% [47]. Also, the Kaneka Company reported a 10.1% µc cell with more than 90% crystalline fraction measured by spectroscopic ellipsometry [56].

The known issues associated with high crystalline fractions can be listed as follows :

- A general trend of a decrease of the V_{oc} with the increase of the crystalline fraction has been identified ([57] or Figure 4 of [58] for example). The drop of the V_{oc} for highly crystallized films has been explained by their lower band-gap, their higher carrier mobilities, their higher mid-gap defect density and their broader band tails by comparing experimental characterizations and simulations of these cells [59, 60] : Due to the smaller gap, the higher free carrier densities result in higher trapped hole densities near the p/i interface. This induces a concentration of the electric field near the p/i interface and the collapse of the electric field in the rest of the intrinsic layer.
- If recombination is the dominant phenomenon determining the V_{oc}, it could be difficult to reach high values without passivation of the crystallite surfaces with amorphous material. Conversely, in the case of reduced crystalline fractions of 32% (deduced from Raman spectroscopy), a V_{oc} above $600\,mV$ could be demonstrated in [61] and remarkably, the J_{sc} of this cell was maintained at $22\,mA/cm^2$ (Efficiency of 9.8%).
- If highly crystallized, the passivation of the grain boundaries and the presence of interconnected cracks getting oxidized during air-exposure become crucial issues for the electronic properties of the films.

The known issues associated with materials close to the a-Si/µc-Si transition can be listed as follows :

- Although microcrystalline is often said to be perfectly stable against light-soaking, such a statement may not hold for materials consisting of a significant fraction of amorphous tissue (see the detailed discussion and the references of Section 1.3 page 84). But it has to be kept in mind that in the case of a tandem structure, this phenomenon will probably anyway not take place because of the absorption of the high energy photons in the front amorphous cell.
- For the optimum absorption in the red and the near infra-red, a high crystalline fraction is required. This is even more striking in the case of a tandem cell and precisely, developing an intrinsic µc material for the bottom cell of a tandem structure was our goal during this project.
- Since µc-Si is often evolving during its growth, it sometimes requires profiled deposition conditions (e.g. by reducing the H_2 dilution) to stay at the edge of the a-Si/µc-Si regime throughout the layer (e.g. [62] for the HW-CVD technique).
- Furthermore, it has to be kept in mind that the amorphous/microcrystalline transition is not an absolute criteria (e.g. it strongly depends on temperature [63]) so that the best a-Si/µc-Si transition in the parameter space has to be searched anyway.

These two lists surely underline that it is not easy to rule out one of the two types of material and that the question of the solar cell performance as a function of the crystallinity is still an open debate. Similarly, the increase of the cell quality with the grain size could seem to be common sense but e.g. the authors of [64] report that there is no influence of the grain size on the V_{oc} in their case and it is possible to obtain high efficiency cells even with small grain size, as proven in [65] with 8.9% with $18\,nm$ grains.

2.4   Conclusion on the microcrystalline solar cells

This second part of the chapter exposed some general points about microcrystalline silicon solar cells and explained in detail the different steps of their processing in our laboratory. The specificities of the material listed in the first part of this chapter have been linked with potential problems in the cells (e.g. grain boundary passivation, less crystallized incubation layer). The requirements and potential risks for each layer and interface of the complex stack have been given and our choices (e.g. p-i-n structure and high crystallinity material) have been explained.

The next part of this chapter will now show the results of the characterizations of the films and cells deposited under various deposition conditions.

3   Optimization of the deposition conditions of the microcrystalline films and solar cells

This part will review the systematic studies we carried out varying one of the deposition parameters at a time in order to better understand their influence. The first two sections will expose the first results in the new ATOS reactor as a starting point, then the effects of the different deposition parameters on the properties of the films and on the performance of the solar cells will be analyzed.

3.1   First series of microcrystalline silicon depositions in the new ATOS reactor : pure silane

The optimization of the microcrystalline silicon material in the new reactor ATOS started in November 2007. The deposition conditions for the first series were quite similar to those tested previously in the reactor Domex. (Their description can be found in Section 4.2.1 page 146.) We used pure silane with flow rates ranging from 55 to 65 sccm, gas pressures of 4.6 or 9 mTorr (yielding to plasma pressures of ~ 3.6 and 5.6 mTorr), microwave powers of 1.4 or 1.5 kW, RF powers adjusted to result in a bias value of -50 V or -10 V and apparent temperatures measured by the pyrometer of $230 - 275\,°$C (corresponding to temperatures of $647 - 716\,°$C indicated by the thermocouple at the back of the substrate holder and temperatures of $350 - 410\,°$C indicated by the thermocouple at the surface of the substrate holder).

During this first series of trials, maximum values of the imaginary part of the pseudo-dielectric function $\langle \varepsilon_i \rangle_{max}$ as high as 20.8 could be achieved as well as a sample with a 85 % crystalline fraction.

The electrical properties of four of these samples have been characterized in the Laboratory of Electrical Engineering of Paris (LGEP, see Table IV.1 and Figure IV.3). The sample A071116a shows a high dark conductivity and a low activation energy after deposition, probably indicating the presence of donor-type contaminations. The three other samples show satisfactory values of σ_{dark} and E_a after deposition which are typical of an intrinsic material. But maybe because the material is not dense enough, they systematically exhibit lower activation energies after one month of air exposure, indicating that the material is prone to post-oxidation. The low diffusion lengths (measured parallel to the substrate) of the three intrinsic samples prove that the material quality is poor.

The densities of states (DOS) have been measured by the diagnostic of modulated photocurrent (MPC) with a DC photon flux of 10^{15} cm^{-2}·s^{-1} at a wavelength of 660 nm for ten different temperatures and varying the frequency of the modulated light intensity. To obtain the DOS, an electron mobility $\mu_e = 10$ cm^2·V^{-1}·s^{-1} and an electron capture coefficient $C_n = 4 \times 10^{-8}$ cm^3·s^{-1} have been assumed. Figure IV.3 shows the enveloppes of the curves of two samples, which represent their DOS. The curves at the different temperatures for the sample A071119a did unfortunately not overlap in the band-tail region so that it was impossible to plot the DOS of this sample. Table IV.1 shows that the defect densities of the samples A071116a and A071116b are satisfactory, while the one of A071119b is too high.

The conditions of the sample A071116b were selected to deposit the intrinsic layer of two p-i-n cells. Indeed, on glass, this sample showed interesting properties, e.g. its intrinsic nature

Sample Name	σ_{dark}	$E_a\,(t=0)$	$E_a\,(t \sim 1\,\mathrm{month})$	$\mu\tau$	L_d	MPC-DOS	F_c(IL)
A071116a	$3.1 \times 10^{-5}\,\mathrm{S\,cm^{-1}}$	$0.28\,\mathrm{eV}$	$0.26\,\mathrm{eV}$	$3.7 \times 10^{-5}\,\mathrm{cm^2\,V^{-1}}$	$85\,\mathrm{nm}$	$9 \times 10^{15}\,\mathrm{cm^{-3}\,eV^{-1}}$	$0\,\%$
A071116b	$7.5 \times 10^{-7}\,\mathrm{S\,cm^{-1}}$	$0.43\,\mathrm{eV}$	$0.38\,\mathrm{eV}$	$7.6 \times 10^{-5}\,\mathrm{cm^2\,V^{-1}}$	$40\,\mathrm{nm}$	$5 \times 10^{15}\,\mathrm{cm^{-3}\,eV^{-1}}$	$24\,\%$
A071119a	$1.4 \times 10^{-7}\,\mathrm{S\,cm^{-1}}$	$0.53\,\mathrm{eV}$	$0.28\,\mathrm{eV}$	$5.4 \times 10^{-5}\,\mathrm{cm^2\,V^{-1}}$	$45\,\mathrm{nm}$	$-$	$0\,\%$
A071119b	$2.2 \times 10^{-6}\,\mathrm{S\,cm^{-1}}$	$0.39\,\mathrm{eV}$	$0.34\,\mathrm{eV}$	$7.6 \times 10^{-6}\,\mathrm{cm^2\,V^{-1}}$	$40\,\mathrm{nm}$	$8 \times 10^{16}\,\mathrm{cm^{-3}\,eV^{-1}}$	$30\,\%$

Table IV.1 – *Electrical properties of four of the first samples. σ_{dark} are the dark conductivities at room temperature. E_a are the activation energies. The mobility-lifetime products $\mu\tau$ have been measured at $303°K$ with a flux of 10^{14} photons $s^{-1}\,cm^{-2}$. L_d are the diffusion lengths. The column MPC-DOS gives the density of states at $0.6\,eV$ below the condution band. In addition to the electrical properties, the last column shows the crystalline fraction in the incubation layer (IL) from the ellipsometric models.*
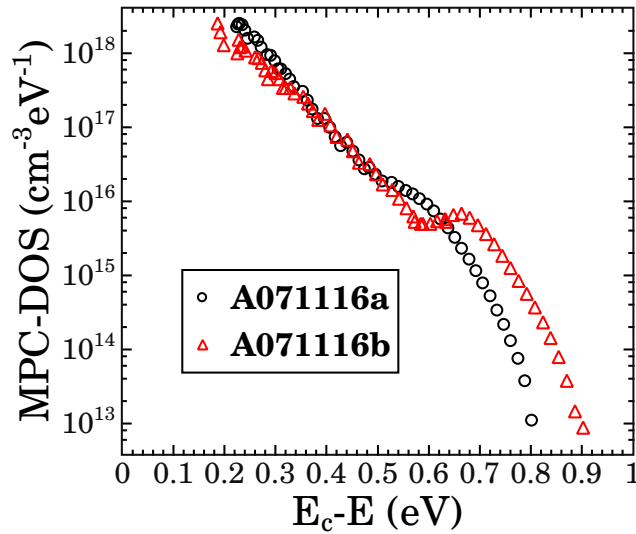

Figure IV.3 – *Densities of states below the conduction band (at the energy E_c) given by the technique of modulated photocurrent (MPC).*

and a crystallized interface with the glass substrate (see Table IV.1). The deposition time was only 14 minutes to grow the i layer of $\sim 1.3\,\mu\mathrm{m}$. Despite the feedback loop regulating the power injected to heat the resistive filament of the first substrate holder, the thermocouple close to its surface recorded a temperature increase of $\sim 34\,°\mathrm{C}$ from the initial temperature of $\sim 350\,°\mathrm{C}$. It is reasonable to believe that the temperature of the surface of the sample is increasing even more because it is directly exposed to the ion bombardment and because of the poor thermal conductivity and the small mass of the glass substrate.

The cells were deposited on textured ZnO with a $21\,\mathrm{nm}$ µc-Si p layer and an $18\,\mathrm{nm}$ a-Si n layer. A "buffer layer" was added to one of the two cells to see if it could help to improve its performance : it consisted in a $72\,\mathrm{nm}$ intrinsic µc layer made in the ARCAM reactor in order to protect the p-i interface from oxidation when transfered to the reactor ATOS and in order to protect the ZnO from the hydrogen-rich MDECR plasma. The characteristics of these first cells after 30 minutes of annealing at $150\,°\mathrm{C}$ are shown in the Figure IV.4 and in the Table IV.2. One can see that the buffer layer helps to greatly improve R_p and V_{oc}. Despite the clear benefit of adding such a layer, the cell still shows poor performance : the spectral response curves show a lack of efficiency in the red part of the spectrum as well as a collection problem revealed by a significantly enhanced current when a bias in applied.
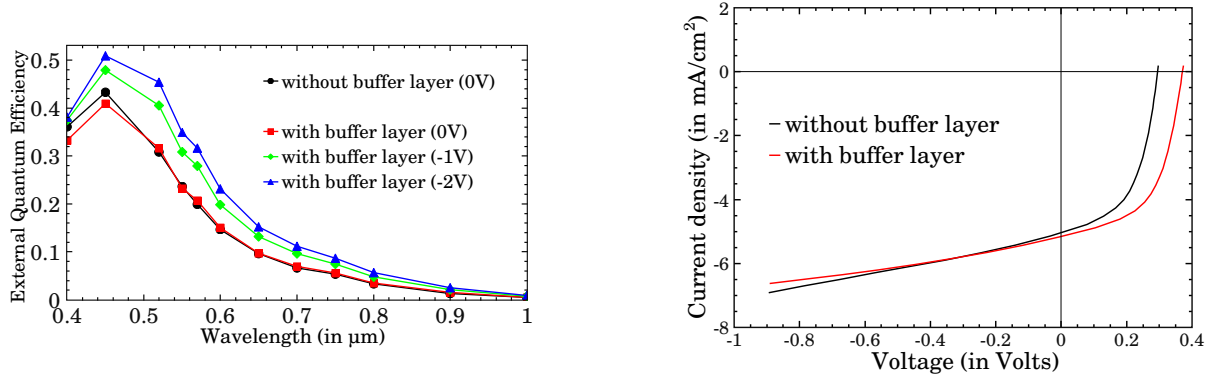
Figure IV.4 – *Characterization of the first two µc p-i-n cells in the new reactor ATOS. On the left : Spectral Responses taken for different bias values. On the right : J(V) curves.*

	Buffer layer	FF	R_p	R_s	J_{sc}	V_{oc}	Efficiency
A071121a	No	53 %	515 $\Omega\,cm^2$	14.1 $\Omega\,cm^2$	5.1 mA/cm^2	295 mV	0.78 %
A071121b	Yes : 72 nm	55 %	649 $\Omega\,cm^2$	15.7 $\Omega\,cm^2$	5.2 mA/cm^2	370 mV	1.05 %

Table IV.2 – *Results of the first two µc p-i-n cells in the new reactor ATOS.*

3.2 Second series of microcrystalline silicon depositions in the new ATOS reactor : different gas mixtures

3.2.1 Characterization of the material

After the depositions with pure silane, we explored different gas mixtures : hydrogen or silicon tetrafluoride (SiF$_4$) were added to compare the obtained films and cells. For this series, a high substrate-holder surface temperature ($\sim 410\,°C$ instead of the usual $\sim 350\,°C$) and a quite low RF power of $\sim 20\,W$ ($V_{bias} = -15\,V$) were used. The gas pressure was fixed for all the gas mixtures to a quite high value of 9 mTorr. These plasma conditions resulted in deposition rates ranging from 11.8 to 17.5 Å/s.

The reduced ion bombardment energy seems to have a great effect on the relative intensities of the amorphous and crystalline contributions in the Raman spectra. The low RF power helped to enhance the crystalline peak. This trend will be confirmed in the detailed study on the ion energy effect (Section 3.5 page 110).

These films were also compared with a µc-Si film grown in a RF-CCP reactor with a mixture of SiF$_4$, Ar and H$_2$, which is a high quality material as it results in cells with efficiencies as high as 8.3 % [47]. Table IV.3 summarizes the electrical measurements carried out on these five samples in the coplanar configuration with aluminum contacts.

Sample name	Gas mixture	σ_{Dark}	E_a	$\mu\tau$	L_d	$D(E_c - 0.6\,eV)$
A080104b	SiH$_4$ = 55 sccm	7.7×10^{-6} S·cm^{-1}	0.43 eV	4.2×10^{-7} cm^2 V^{-1}	50 nm	1.6×10^{16} cm^{-3} eV^{-1}
A080107	SiH$_4$/SiF$_4$ = 55/1 sccm	9.0×10^{-8} S·cm^{-1}	0.43 eV	4.3×10^{-8} cm^2 V^{-1}	105 nm	6.5×10^{17} cm^{-3} eV^{-1}
A080109	SiH$_4$/H$_2$ = 55/100 sccm	8.0×10^{-6} S·cm^{-1}	0.39 eV	1.1×10^{-6} cm^2 V^{-1}	70 nm	1.9×10^{16} cm^{-3} eV^{-1}
A080110b	SiH$_4$ = 55 sccm	6.3×10^{-6} S·cm^{-1}	0.38 eV	1.4×10^{-6} cm^2 V^{-1}	110 nm	1.4×10^{16} cm^{-3} eV^{-1}
I080121	SiF$_4$/Ar/H$_2$ (RF-CCP)	1.2×10^{-6} S·cm^{-1}	0.43 eV	5.4×10^{-6} cm^2 V^{-1}	150 nm	–

Table IV.3 – *Dark conductivities σ_{Dark}, activation energies E_a, $\mu\tau$ products (at 303°K with a flux of 10^{14} photons $s^{-1}\,cm^{-2}$), diffusion lengths L_d and density of states 0.6 eV below the conduction band $D(E_c - 0.6\,eV)$ of the four MDECR samples with different gas compositions compared to a CCP sample (last line).*
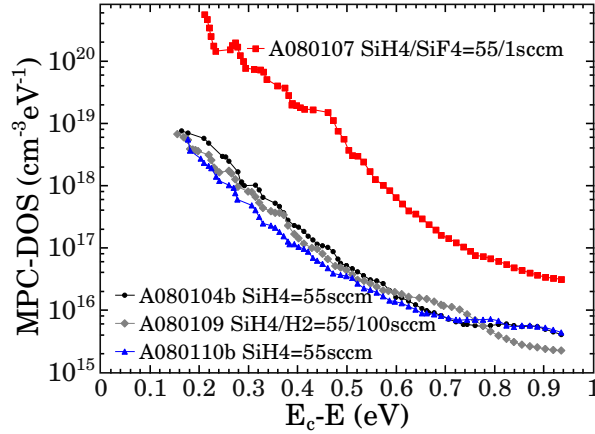
Figure IV.5 – *Modulated photocurrent densities of states (MPC-DOS) of the four samples with different gas mixtures.*

Unfortunately, there is a reproducibility issue in the depositions and/or in the measurements of the samples of Table IV.3. Indeed, A080104b and A080110b have been deposited in the same conditions but their L_d values are as different as 50 nm and 110 nm respectively and their $\mu\tau$ products differ by a factor of 3.

Nevertheless, the comparison of the MDECR samples with the RF-CCP reference sample showed that the former were very sensitive to air contamination : Their conductivity values go up by one to four orders of magnitude when exposed to ambient air (as compared to values recorded under vacuum) while the RF-CCP sample conductivity is stable. The $\mu\tau$ products of the MDECR samples are also always lower than the RF-CCP value.

The densities of states (DOS) have been measured by the diagnostic of modulated photocurrent (MPC) with a DC photon flux of $10^{15}\,\mathrm{cm^{-2}\,s^{-1}}$ at a wavelength of 660 nm for ten different temperatures and varying the frequency of the modulated light intensity. To obtain the DOS, an electron mobility $\mu_e = 10\,\mathrm{cm^2\,V^{-1}\,s^{-1}}$ and an electron capture coefficient $C_n = 4 \times 10^{-8}\,\mathrm{cm^3\,s^{-1}}$ have been assumed. The results of Figure IV.5 seem to show that the addition of 1 sccm of SiF$_4$ has a tremendous impact on the DOS. (This could also partially be due to an overestimated value of μ_e leading to such a global shift or to an underestimated value of C_n changing the shape of the curve.) This fits with its $\mu\tau$ product for the electrons being the lowest of the series. We can notice that the diffusion length of this sample is still high, which is not a contradiction as it characterizes the transport of holes and is therefore related to the defect density near the valence band. The three samples without SiF$_4$ have satisfactory and very close defect densities. When compared to those of the previous series, they seem to flatten for energies lower than the mid-gap, as is the case in the presence of deep defects corresponding to dangling bonds, which could be due to the higher temperature.

From the fits of the ellipsometry spectra, the addition of SiF$_4$ in small quantity did not significantly help to promote the crystallization of the incubation layer. Also, the large dilution in hydrogen (sample A080109) led to an increase of the bulk void fraction up to 18 % in these conditions. The ellipsometric spectra of the five samples of this series are superposed in Figure IV.6 for a comparison : the not yet optimized deposition conditions in the new reactor ATOS showed quite low maximum values of $\langle\varepsilon_i\rangle$. The best fit for the sample deposited in the RF-CCP reactor has a large grain crystalline fraction $F_{LG} = 12\,\%$ and a small grain crystalline fraction $F_{SG} = 84\,\%$ in its optical model and can be qualitatively seen as a goal to reach.
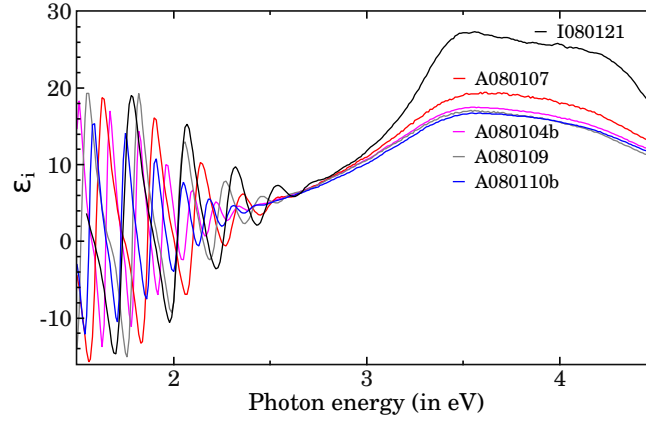
Figure IV.6 – *Superposition of the imaginary parts $\langle \varepsilon_i \rangle$ of the pseudo-dielectric functions of the five studied samples.*

3.2.2   Cells

n-i-p structures on glass covered with chromium, SnO_2 and ZnO and on stainless steel, and p-i-n structures on textured and non-textured ZnO have been tried with these gas mixtures but all of them exhibited efficiencies $\leqslant 0.5\,\%$. Their characteristics will therefore not be detailed here.

3.2.3   SIMS measurements

After the series of cells, a sample has been prepared to study the chemical composition of these materials.

It consists in a stack of five 120 nm-thick layers. All the microcrystalline layers have been deposited at a quite high pressure ($P_{gas} = 9$ mTorr) and with a quite low ion energy bombardment ($V_{bias} = -15$ V). The initial temperature of the substrate-holder surface was 361 °C and the microwave power was 1.5 kW. Its structure is the following :

Sample name : A080312
• **Substrate :** low resistivity c-Si
Hydrogen cleaning plasma of several minutes
• **Layer 1 :** µc-Si:H with 55 sccm pure SiH_4 ($P_{plasma} = 5.7$ mTorr)
Plasma stopped
• **Layer 2 :** µc-Si:H with 45 sccm pure SiH_4 ($P_{plasma} = 5.3$ mTorr)
Plasma stopped
• **Layer 3 :** µc-Si:H with 45 sccm SiH_4 + 75 sccm H_2 ($P_{plasma} = 8.4$ mTorr)
Addition of 1 sccm of SiF_4 without stopping the plasma
• **Layer 4 :** µc-Si:H with 45 sccm SiH_4 + 75 sccm H_2 + 1 sccm SiF_4 ($P_{plasma} = 8.2$ mTorr)
Plasma stopped
• **Layer 5 :** capping a-Si:H with 100 sccm pure SiH_4

Reducing the pure silane flow rate from 55 sccm to 45 sccm allowed to reach the highest crystalline fraction and the lowest void fraction at that time, which were respectively 89 % and 6.3 %, as obtained from the ellipsometric models.

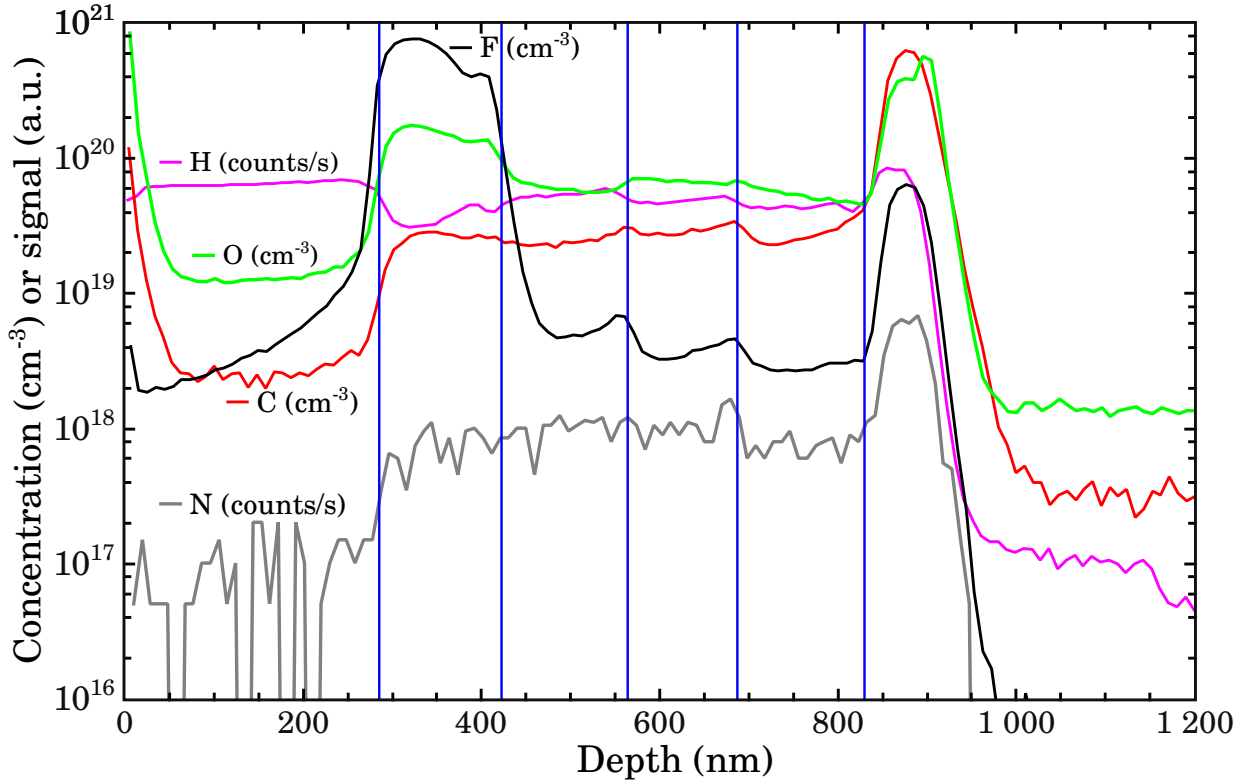The SIMS profiles of the stack are shown in Figure IV.7.

Figure IV.7 – *General remarks on the SIMS profiles of the sample A080312 : 1) The plasma unexpectedly stopped during the deposition of the layer 4, which explains the presence of a small dip in the F and O profiles and of a small peak in the H profile at an sputtering depth of around 390 nm. 2) It can be seen that the depth of the crater has been overestimated by $\sim 38\,\%$ as compared to the expected thickness of the stack. 3) The huge contaminations at the surface of the c-Si substrate could be due to a deposition of a very porous material having taken place by chemical transport during the 4'28" hydrogen plasma treatment (thickness of around 50 nm corresponding to a deposition rate of a bit less than 2 Å/s) : this underlines the striking importance to have a load-lock in order to avoid contaminations on the walls.*

The oxygen concentration, C_O, ranges from 4.7 to 7.1×10^{19} cm^{-3} in the first three µc layers. The addition of a small flow rate of silicon tetrafluoride to a silane/hydrogen mixture has proven to be an effective solution which can result in an impressive reduction of the oxygen incorporation for films deposited in RF-CCP reactors [66]. One of the main goals of this SIMS stack was to evidence a similar effect in our MDECR reactor. The oxygen level unfortunately increases with the addition of SiF$_4$, up to 1.8×10^{20} cm^{-3}. This can most likely be attributed to HF molecules etching and recycling oxygen from the walls which had been exposed to ambient air before the deposition in the absence of a load-lock at that time. If this oxygen increase is reproducible, it then explains why the cells made with 55 sccm of SiH$_4$ and 1 sccm of SiF$_4$ did not show improved performance.

Furthermore, in this layer 4, the concentrations of hydrogen and fluorine can be seen to evolve in opposite ways : H atoms are progressively replaced by F atoms. The fluorine incorporation reaches $\sim 8 \times 10^{20}$ cm^{-3} at its maximum, i.e. more than 1 %. But this value is probably slightly overestimated due to the mass interference with the molecular ion H$_3$^{16}O. At the interface of the layers 4 and 5, it takes almost 100 nm for the F signal to go down to its base level, indicating either recycling from the walls, thermal diffusion and/or hydrogen-assisted fluorine diffusion.

The role of the amorphous capping layer is to prevent any oxidation of the stack between the deposition and the SIMS measurement. In this layer, the tenfold decrease of the C level, as compared to the µc layers, and the lower O concentration ($C_O \sim 1.3 \times 10^{19} \, \text{cm}^{-3}$) cannot be explained only by the the fact that the deposition rate for the a-Si layer is higher than that of the µc layers. The microcrystalline conditions probably result in a more reactive surface and/or in more "recycling" of oxygen from the contaminated walls.

As a last remark about these SIMS profiles, one can see that the concentrations of H, C and F are not constant throughout each layer : their signals go down with deposition time. These "transient" variations could correspond to the heating of the layer by the ion bombardment, which would fit with the O signals going up due to a more reactive surface.

3.3   Series in argon dilution

The effect of the addition of argon to the gas phase has been studied in the reactor ATOS with the second substrate holder, without load-lock. The series consists of six samples on glass and two cells. The argon flow rate has been varied from 5 sccm to 90 sccm. The other gas flow rates have been fixed (50 sccm of SiH_4 and 100 sccm of H_2). To keep the initial gas pressure constant (5 mTorr), the position of the valve in front of the turbomolecular pump has been adjusted in order to adapt its pumping capacity. The RF power supplied to the substrate holder has been fixed to 79 W. This latter choice led to slightly smaller voltage drops in the sheath with higher argon flow rates ($V_{bias} = -48$ V for 5 sccm of Ar and $V_{bias} = -40$ V for 90 sccm of Ar), which can be explained by the higher electron densities obtained when adding argon.

One could expect that argon bombardment would help to promote the formation of large crystallized grains but using the large grain dielectric function [67] in the ellipsometry models never improved the figure of merit of the fits. Figure IV.8 shows the superposition of two samples as a qualitative comparison :

- the sample of the series with 15 sccm of Ar, which has the highest maximum value of the imaginary part of the pseudo-dielectric function $\langle \varepsilon_i \rangle_{max} = 24.3$ and whose bulk composition is a small grain (SG) crystalline fraction $F_{c\,SG} = 94\,\%$, an amorphous fraction $F_a = 2\,\%$ and a void fraction $F_v = 4\,\%$,
- and a film deposited in the RF-CCP reactor named Philix from the decomposition of a SiF_4, Ar, H_2 mixture whose bulk composition is $F_{c\,SG} = 49\,\%$, $F_{c\,LG} = 49\,\%$ and $F_v = 2\,\%$.

Although the addition of argon did not enable us to obtain larger crystallized grains, a systematic increase of the Raman crystalline signal with the argon flow rate has been evidenced (Figure IV.9).

The amplitudes of the changes found by ellipsometry are very small. The deposition rate goes down almost linearly from 15.8 Å/s to 15.3 Å/s when adding argon and the bulk composition is shown on Figure IV.10. The void fraction slightly increases at the expense of the crystalline fraction, which is very high for all the samples anyway. On the other hand, the incubation layers are all completely amorphous, except for 5 sccm of Ar (which results in $F_c = 6\,\%$) and all quite thick (i.e. between 28 and 31 nm).

Finally, the activation energy and dark conductivity values of these films have been found to be respectively abnormally low and high (Figure IV.11). These values could be explained by
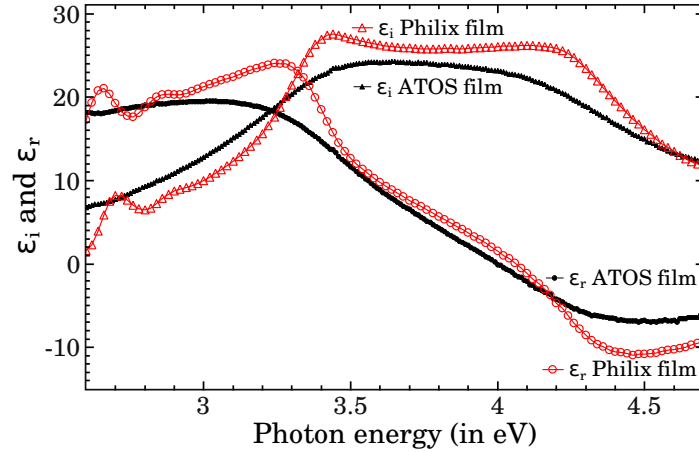
Figure IV.8 – *Superposition of an ATOS film whose best fit contains 94 % of small grains and of a Philix film, modelled with 49 % of small grains and 49 % of large grains.*
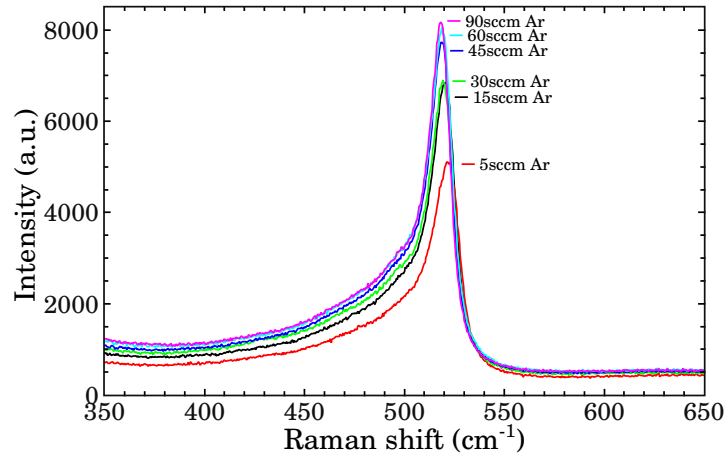

Figure IV.9 – *Effect of the argon dilution on the Raman spectra.*

the high oxygen concentrations present in the films before the installation of the load-lock. After this series, the condition with $5\,\mathrm{sccm}$ of Ar has been incorporated in a stack of several layers for SIMS characterization and the oxygen level was $C_O = 1.4 \times 10^{20}\,\mathrm{cm}^{-3}$. The other species levels were $C_C = 1.9 \times 10^{20}\,\mathrm{cm}^{-3}$, $C_F = 4 \times 10^{17}\,\mathrm{cm}^{-3}$ and $C_N = 6 \times 10^{15}\,\mathrm{cm}^{-3}$. The hydrogen signal has not been quantified but was 1.6 times higher than the signal in the reference ARCAM microcrystalline layer.

Two p-i-n cells have been deposited : with $5\,\mathrm{sccm}$ of argon and with $15\,\mathrm{sccm}$ of argon. Their structure was the following : Glass substrate / ZnO / p-doped µc-Si:H layer (ARCAM reactor) / 100 nm intrinsic µc-Si:H buffer layer (ARCAM reactor) / 1 µm intrinsic µc-Si:H layer (ATOS reactor) / one minute hydrogen plasma pre-treatment (ARCAM reactor) / n-doped a-Si:H layer (ARCAM reactor) / Aluminum contacts. They resulted in very low efficiencies of $0.2\,\%$ and $0.4\,\%$ for $5\,\mathrm{sccm}$ and $15\,\mathrm{sccm}$ of argon respectively. The $J(V)$ characteristics of the second cell was FF $= 40\,\%$, $R_p = 470\,\Omega\,\mathrm{cm}^2$, $R_s = 21\,\Omega\,\mathrm{cm}^2$, $J_{sc} = 4.4\,\mathrm{mA/cm}^2$ and $V_{oc} = 205\,\mathrm{mV}$.

Figure IV.12 shows the Raman spectra at high wavenumbers measured directly on the two cells. We can see that a signal at $2000\,\mathrm{cm}^{-1}$ is present and that the narrow peaks at $\sim 2080\,\mathrm{cm}^{-1}$ and $\sim 2100\,\mathrm{cm}^{-1}$ cannot be seen (see detailed discussion in Section 4.3.5 page 160). These are coarse indications that the material should be dense.
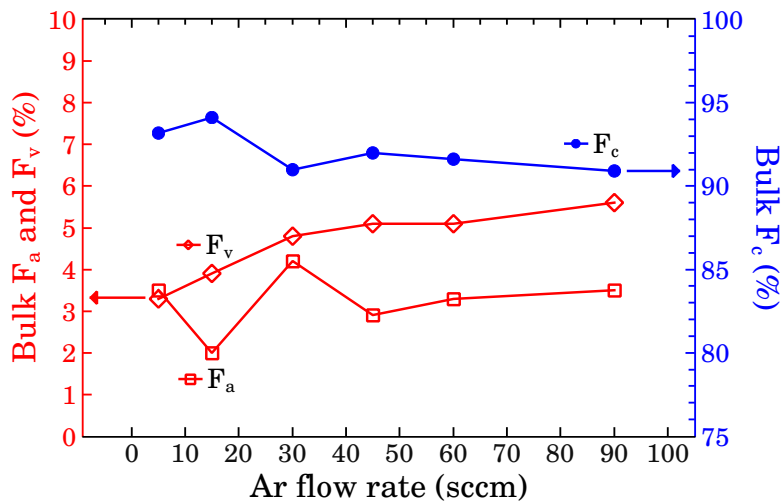
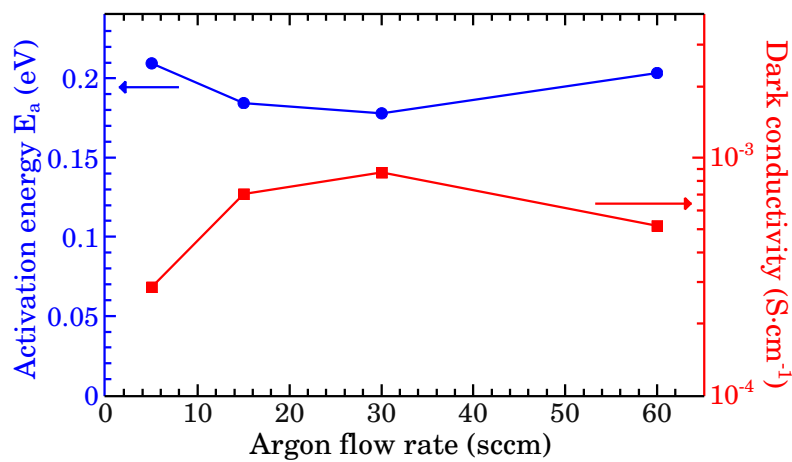Figure IV.10 – *Effect of the argon dilution on the bulk composition.*

Figure IV.11 – *For the studied set of deposition parameters, the values of the activation energy and the dark conductivity do not change a lot and could indicate a very severe oxygen contamination.*
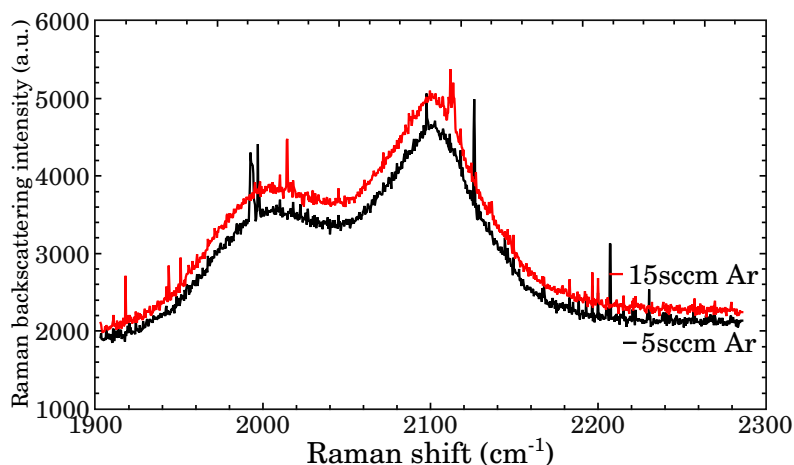

Figure IV.12 – *Raman spectra of the two cells with 5 sccm and 15 sccm of argon. The measurements have been carried out directly on the cells, without removing the top n-doped amorphous layer and it has been checked that the co-deposited films on monocrystalline silicon and on glass show similar shapes and no narrow twin peaks around 2100 cm^{-1} as well.*

As a conclusion, the results of this series were quite surprising to us. We wanted to see if argon could help to obtain large grains. We also expected that at some point, the bombardment of the argon ions would induce a strong amorphization of the growing film. Only weak changes were observed over a large range of the chemical composition of the gas. This illustrates one of the characteristics of the MDECR plasma which is that the process windows seem quite broad and that it is sometimes difficult to find conditions leading to new exciting material properties.

3.4   Series in bias

The two following series of depositions have been done in the reactor ATOS with the second substrate holder, without load-lock.

The motivation for these series is that among all the deposition parameters, the RF power is a very particular one : It controls the DC polarization potential of the substrate holder V_{bias} and thus, has the advantage of affecting directly and selectively one physical quantity, the ion bombardment energy. Indeed, in our low pressure plasma, the sheath is non-collisional and the ion energy is directly controlled by the voltage drop $V_{plasma} - V_{bias}$. Therefore, it is very satisfactory to study the influence of this parameter and this is why great efforts have been dedicated to characterize the samples of these series by many diagnostics.

In a study in an RF-CCP plasma, ions have been measured to represent up to 70% of the species contributing to the microcrystalline film growth [7], which is completely different from the value of 4% to 10% for amorphous films [68]. (But it has to be kept in mind that these values include the direct incorporation of ions containing silicon as well as the creation of growth sites, e.g. by H_x^+ ions). With other deposition technologies, one can obtain microcrystalline silicon without any ion bombardement as in the ion-free Hot Wire Chemical Vapor Deposition (HWCVD) technique. Such a striking difference underlines once more that there is not just one microcrystalline material, but a whole range of microcrystalline materials.

In a standard RF-CCP deposition system, one cannot control separately the power injected in the plasma and the ion bombardement energy. There is a general consensus on the fact that too high ion energies are detrimental for the film quality [69]. This is the reason for the interest for solutions providing milder ion energies : higher excitation frequencies such as Very High Frequency systems, higher pressures as in the High Pressure Depletion (HDP) regime, and the triode configuration, with an independently biased mesh.

Ion bombardment energy has an effect on the film density, on its crystallinity, on its stress, on its defect density and on the plasma induced heating during the growth. Reducing the ion energy is said to favor the formation of large grains [9, 70] and according to [70], it also leads to the formation of an amorphous incubation layer. Apart from the strictly physical effect of the heavy silicon-containing or argon ions, one must also consider the nature of the ions. The light hydrogen-based ions cannot be neglected. While the former can induce both an amorphization or a densification of the subsurface layer and create structural defects, the latter diffuse deeper and promote crystallization [35].
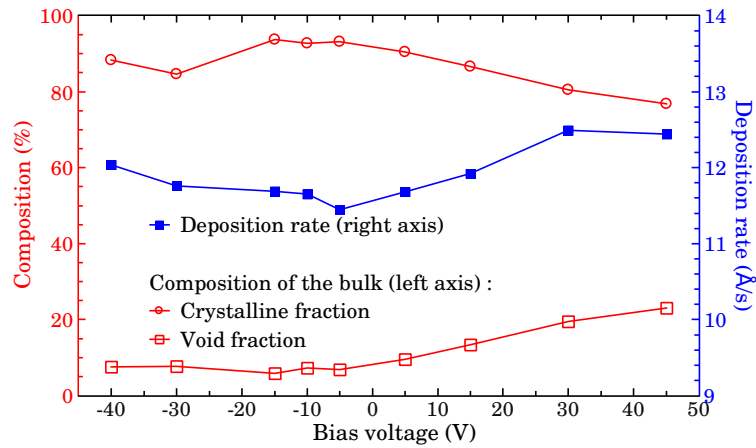
Figure IV.13 – *Effect of ion energy on the deposition rate and on the bulk composition obtained by ellipsometry.*

3.5 First series in bias

This series of films and cells has been done after the installation of the second substrate holder in the reactor ATOS, before the installation of the load-lock. The RF power applied to the substrate holder has been varied from $102\,W$ to $0\,W$, corresponding to polarisation voltages of $-40\,V$ to $+45\,V$ respectively, the latter being the floating potential. The other deposition parameters have been fixed : the pure silane flow rate, the temperature of the glass surface, the gas pressure, the plasma pressure and the microwave power were respectively $42\,sccm$, $\sim 230\,°C$, $9\,mTorr$, $4.75\,mTorr$ and $1.5\,kW$. Nine samples of around $290\,nm$ and two samples of around $1\,\mu m$ have been deposited to systematically investigate the effect of ion energy.

3.5.1 Ellipsometry

All the samples have been characterized by ex-situ spectroscopic ellipsometry. As shown in Figure IV.13, the deposition rates are ranging from 11.5 to $12.5\,\text{Å}/s$ and the crystalline fractions in the bulk vary from 77 to $94\,\%$. The minimum of growth rate corresponds to the maximum of crystalline fraction. From this graph, the sample at $-15\,V$ seems to be a good material for solar cells. An expected trend is confirmed in this graph : The void fraction increases when the ion energy decreases, indicating a lack of densification.

To understand the effect of ion energy on the crystallization process, we focused on the incubation layer. The results are shown in Figure IV.14. To obtain informations on the incubation layer is tricky. As far as ellipsometry is concerned, the models are not always sensitive to this part of the film when the layer is thick (typically $> 300\,nm$) and these results should therefore be considered carefully. For example, the sample at $+30\,V$ could be fitted with the same figure of merit χ^2 with an incubation layer thickness ranging between 150 and $220\,\text{Å}$ and with a crystalline fraction between 2.5 and $12\,\%$. Despite these uncertainties, the general trends were that high ion bombardment helps to grow a crystallized incubation layer (as in CCP [70]) but increases this layer thickness.

The interesting property of the sample at floating potential is that it exhibits the thinnest incubation layer of the series ($99\,\text{Å}$). We repeated another sample at floating potential with a shorter deposition time (three minutes instead of four) in order to have a thinner film
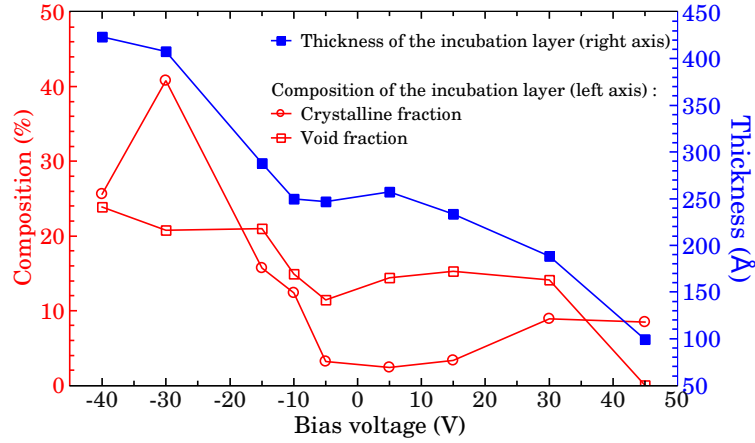
Figure IV.14 – *Effect of ion energy on the incubation layer thickness and composition obtained by ellipsometry.*

and to be more sensitive to the incubation layer. The best fit for this repetition gave an incubation layer thickness of $\sim 160\,\text{Å}$, thus indicating that it is difficult to be sure of the thicknesses and compositions close to the substrate even for films of 300 nm.

This sample at floating potential also has the surface with the greatest roughness of the series (140 Å) as well as the bulk with the highest F_v of the series (23 %). These two results of the optical model indicate that the material is not dense enough and contains a lot of hydrogen. Other authors [71] also observe an increase of the void fractions in their ellipsometric models with the decrease of the ion energies (up to $\sim 20\,\%$).

These results are confirmed by the 1 µm-thick films at $-5\,\text{V}$ and at floating potential : their bulk crystalline fractions are 90 % and 77 % and their bulk void fractions are 8 % and 22 % respectively.

As a last general remark on these ellipsometry data, we can emphasize that the non-monotonous evolution seen for the deposition rate, the crystalline fraction and the void fraction will also be found for many other properties (see next sections). It had also been evidenced in the previous reactor [72].

3.5.2   Raman spectroscopy

The Raman spectra of the nine samples of around 290 nm are superposed in Figure IV.15. The samples have been measured in the exact same conditions (same magnification, same acquisition time) and the raw signals are shown, without any normalization. A trend of the crystalline peak intensity as a function of the bias can be seen : the lower the ion energy, the higher the crystalline signal. This could at least partially be explained by a scattering effect of the surface roughness or of the crystallites.

This graph also illustrates a limit of the diagnostic of Raman spectroscopy : it is not sensitive to porosity. Indeed, ellipsometry revealed that the sample deposited at floating potential has a much too high void fraction while its Raman spectrum seems to be of high quality. The density of a microcrystalline film can also be qualitatively estimated with ellipsometry based on the maximum value of the imaginary part of its pseudo-dielectric function : while $\langle \varepsilon_i \rangle_{max} = 23$ at $-15\,\text{V}$, $\langle \varepsilon_i \rangle_{max}$ is only 16 at floating potential.
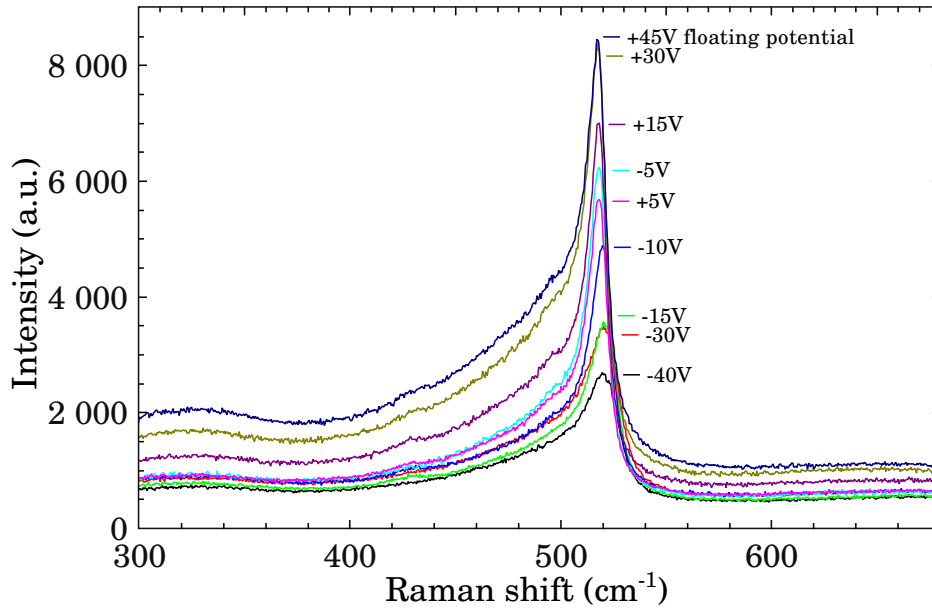
Figure IV.15 – *Superposition of the Raman spectra of the nine thin layers with their corresponding bias potentials.*

3.5.3   X-ray diffraction (XRD)

X-ray diffraction spectra have been measured on four samples deposited at different biases and of different thicknesses (Figure IV.16) in order to deduce their preferred crystallographic orientation and the sizes of their crystallites (Table IV.4).

Figure IV.16 shows the presence of three orientations : (111), (110), and (311), and the signal of the glass substrates. On the low angle side of the (111) peak, there seems to be something like a shallow hump around 27°. This could be due to planar faults (but it is less clear than those showed in Figure 26 of [73]), to the contribution of the amorphous fraction or maybe to very small (111) crystallites.

The peaks have been fitted with Voigt functions. Their areas, corrected by the normalization factors (see Section 5 page 38) give the relative fractions of the three orientations, reported in Table IV.4. One can see that at the minimum ion bombardment, the surface occupied by (111) crystallites in the plane parallel to the substrate is much greater than the (110) and (311)-oriented crystallites and that this domination gets greater for the thicker film. On the other hand, the ion bombardment seems to favor the (110) and (311) orientations : the film of 1.5 µm is very close to randomness and the one of 1 µm has dominant (311) and (110) textures.

These results are in opposition with the ones of [52]. They deposit µc-Si at high rate with a microwave glow discharge and obtain (111)-oriented films. They attribute this to the elevated level of ion bombardment energy causing a discontinuous growth of the grains and suppressing the (110) orientation. But despite the (111) orientation, which is often said not to be the best one, and a high microvoid density, indicated by Small Angle X-ray Scattering characterizations, they were still able to obtain 4.9 % cells at ∼ 30 Å/s.

Our trend agrees with the one of [74] (Fig. 5(b)), where their µc films deposited by ECR are strongly (110)-oriented without bias and get closer to random orientation or even (111)-oriented when a *positive* DC bias is applied.
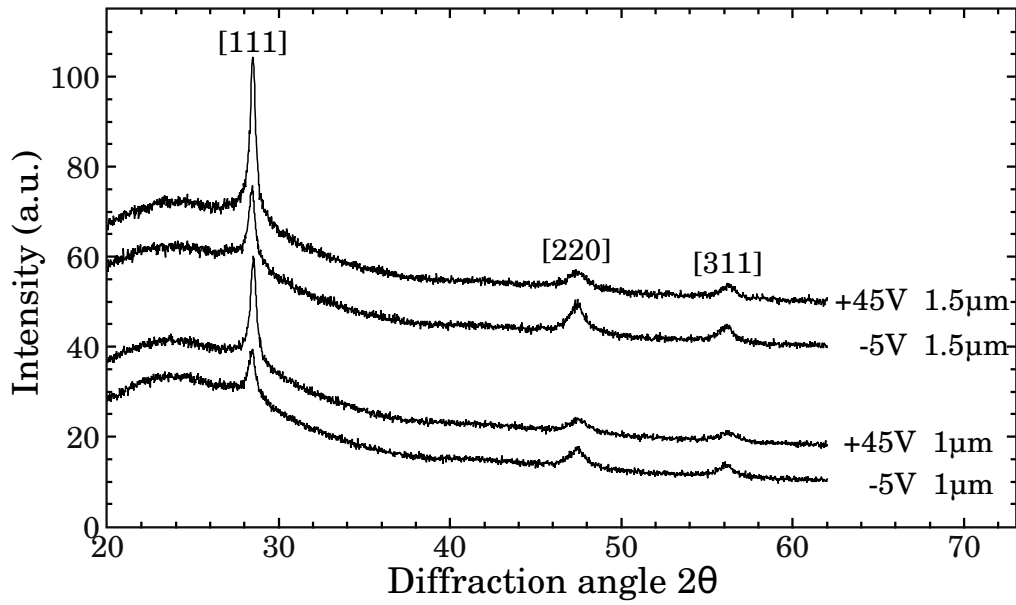
Figure IV.16 – *X-ray diffraction spectra of the four samples (shifted for clarity).*

Bias	Thickness	Fraction (111)	Fraction (110)	Fraction (311)	Size (111)	Size (110)	Size (311)
$-5\,$V	$1\,\mu$m	0.28	0.36	0.37	169 Å	94 Å	105 Å
$+45\,$V	$1\,\mu$m	0.46	0.26	0.27	207 Å	74 Å	79 Å
$-5\,$V	$1.5\,\mu$m	0.33	0.36	0.30	172 Å	90 Å	101 Å
$+45\,$V	$1.5\,\mu$m	0.59	0.20	0.20	201 Å	79 Å	98 Å

Table IV.4 – *Fractions occupied by the (111), (110) and (311) orientations in the planes parallel to the substrate and average sizes of the crystallites.*
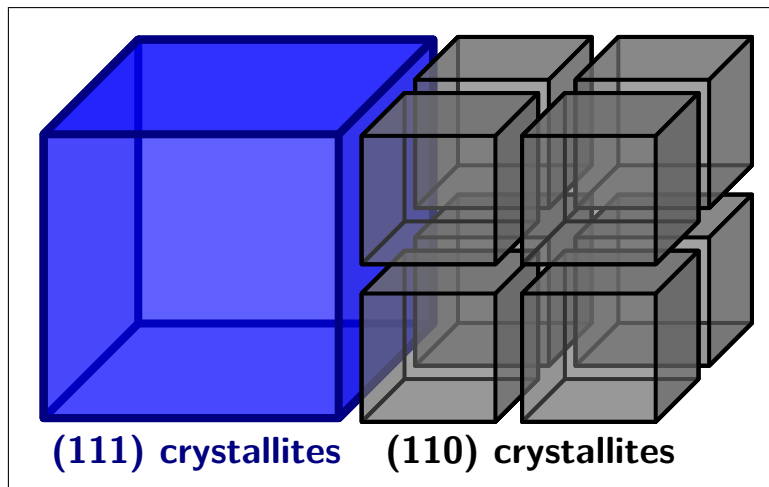

Figure IV.17 – *Possible way to represent the crystallites for the 1.5 μm thick sample at −5V.*

All the positions of the peaks are at higher 2θ than the theoretical values (see table page 39). This corresponds to smaller inter-plane distances. With ion bombardment, the peak positions get closer to the stress-free values, which is counterintuitive.

The average linear thermal expansion coefficient of the 1737 Corning glass is $3.8 \times 10^{-6}\,°\mathrm{C}^{-1}$ in the range 0–$300\,°\mathrm{C}$. The one of silicon is $\sim 3 \times 10^{-6}\,°\mathrm{C}^{-1}$ in the same range so no stress should be induced when the samples are cooled down from $\sim 250\,°\mathrm{C}$ to room temperature.

The Scherrer formula was then applied to obtain an estimation of the crystallite sizes. Despite all the approximations of this formula (see discussion in Section 5.3 page 40), the (111) crystallites clearly appear significantly bigger (by a factor of around 2 to 3). The effect of bias is to reduce the size of the (111) grains and to enhance the size of the (110) and (311) grains. Furthermore, it can be noted that the average grain sizes do almost not evolve from $1\,\mu\mathrm{m}$ to $1.5\,\mu\mathrm{m}$ (except for the (311) grains at $+45\,\mathrm{V}$).

Figure IV.17 is a simplified model designed to help us visualize the results for the (111) and (110) grains of the $1.5\,\mu\mathrm{m}$ thick sample at $-5\mathrm{V}$: the two orientations have the same surface in the plane parallel to the substrate but there is a factor of ~ 2 for their sizes perpendicular to the diffracting planes. For this image, we have *arbitrarily* assumed the grain shapes to be cubes. Despite this strong simplification, it helps us to realize that most of the grain boundaries are around (110) grains, which are said to be of greater quality than the (111) ones (see discussion page 39).

3.5.4   Exodiffusion

The hydrogen exodiffusion spectra of six of the nine thin ($\sim 290\,\mathrm{nm}$) samples have been measured and are shown in the top graph of Figure IV.18.

A first general remark is that we can clearly notice peaks at lower temperatures for the samples at $+15$, $+30$ and $+45\,\mathrm{V}$, indicating weaker Si-H bonds for low ion energies. Then, we can have a qualitative estimation of the total hydrogen content in the films by integrating their exodiffusion signals : The results are shown in the bottom graph of Figure IV.18. An impressive increase of the total amount of hydrogen by a factor ~ 4.6 is seen between the biases $-5\,\mathrm{V}$ and $+45\,\mathrm{V}$. The void fraction in the bulk obtained by ellipsometry, already shown in Figure IV.13, is magnified on this graph and superposed to exodiffusion data to emphasize the good agreement between the two diagnostics.

We also carried out deconvolutions of the spectra with gaussian peaks. It is impossible to fit all the samples with the same peaks but one peak was found to be present for all the films : Its maximum is between 400 and $430\,°\mathrm{C}$ and its area is shown in the bottom graph of Figure IV.18. It is usually attributed to hydrogen in cavities, in micro-voids [75].

3.5.5   Atomic Force Microscopy (AFM)

The surface of some samples of the series has been characterized by AFM. As an example, Figure IV.19 shows the surface topology of the $1\,\mu\mathrm{m}$ thick sample at $-5\,\mathrm{V}$. Even for this thick sample, one cannot see columnar structures of the order of magnitude of $\sim 200\,\mathrm{nm}$ as in [76]. The typical average size of the grains seen on this sample seems to be around $400\,\text{Å}$, which is greater than the XRD estimation of Table IV.4 because this latter technique is sensitive to coherence domains (i.e. perfect crystal planes).
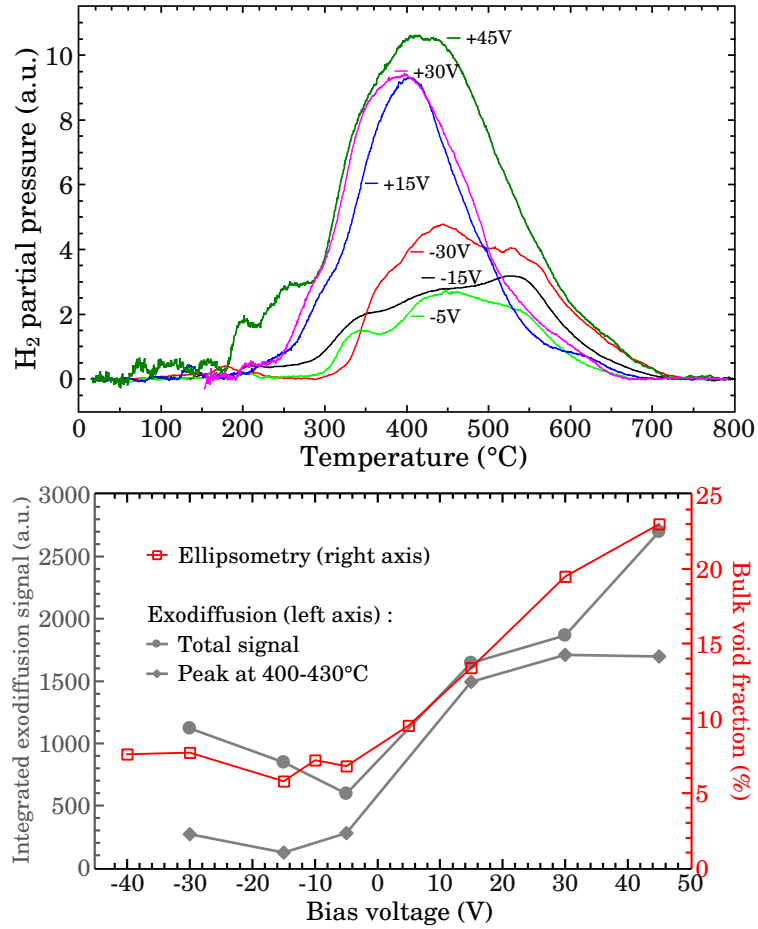
Figure IV.18 – Top graph : *Exodiffusion spectra of six of the nine thin samples of the series. The curves have been normalized by the volume of the layers.* Bottom graph : *Integrated areas of the total hydrogen signal and of the $400-430°C$ gaussian peak from their decompositions superposed with the bulk void fraction obtained from ellipsometry.*
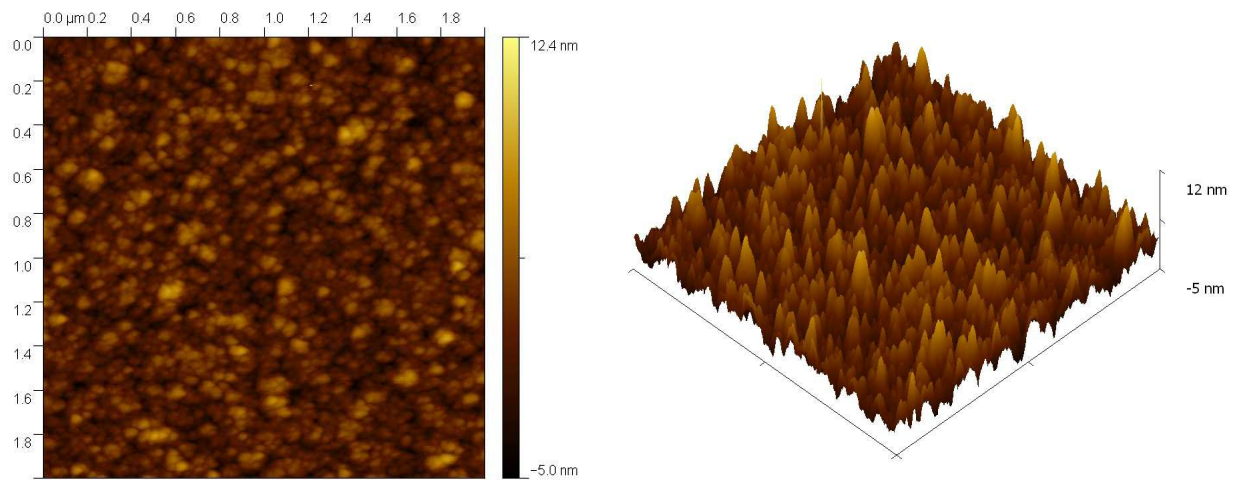

Figure IV.19 – *2-dimensional (graph on the left) and 3-dimensional (graph on the right) AFM images of the $1\,\mu m$ thick sample at $V_{bias} = -5\,V$. The scale of the images is $2\,\mu m \times 2\,\mu m$. The highest point is $12.4\,nm$ and the lowest point is $-5.0\,nm$. The root mean square roughness is $1.8\,nm$.*
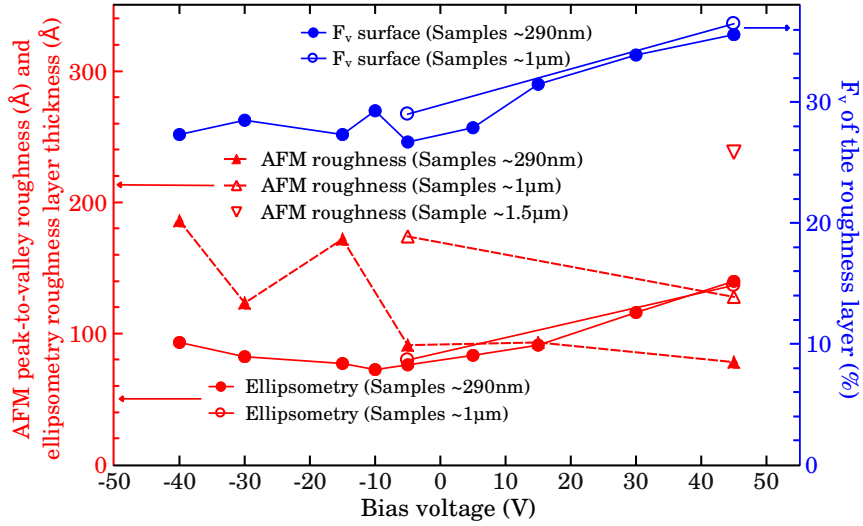
Figure IV.20 – *Characterization of the surface of samples of different thicknesses ($\sim 290\,nm$, $\sim 1\,\mu m$ and $\sim 1.5\,\mu m$) by Atomic Force Microscopy (peak-to-valley roughness) and by ellipsometry (top layer thickness on the left axis and top layer void fraction F_v on the right axis).*

The roughness values measured on these images are shown in Figure IV.20 and compared to ellipsometry results. Although the AFM peak-to-valley roughnesses and the ellipsometry top layer thicknesses are of the same order of magnitude, we notice that some trends are different : While ellipsometry indicates an increase of both the surface layer thickness and of its void fraction for low ion energies, the AFM roughness is stable or even decreasing (for $1\,\mu m$ thick samples) between $-5\,V$ and the floating potential. The thin sample at $+45\,V$ has the lowest AFM peak-to-valley roughness of $\sim 80\,\text{Å}$. Thus, a lack of densification at low ion bombardment energies cannot be seen with AFM. A second discrepency is that the ellipsometry results do not show any dependence on the thickness while AFM indicates an increase of the roughness during the film growth, e.g. multiplied by a factor of 2 from $290\,nm$ to $1\,\mu m$ at $-5\,V$.

3.5.6   Electrical characterizations

The activation energies (E_a) and the dark conductivities (σ_{Dark}) of the eleven samples have been measured and can be seen on Figure IV.21. The activation energies of most of the samples of this series are $\leqslant 0.3\,eV$, corresponding to an n-type doping. The SIMS measurements (Section 3.5.7.4 below) will indeed confirm too high concentrations of oxygen and nitrogen in these films. Very unexpectedly, the samples at floating potential, which seem to have normal activation energies (0.51 and $0.57\,eV$) and dark conductivities (4×10^{-6} and $6 \times 10^{-7}\,\text{S·cm}^{-1}$), have huge levels of oxygen contamination (up to $\sim 2 \times 10^{21}\,\text{cm}^{-3}$), illustrating the difficulty to rely on just one diagnostic to optimize the material. The very low values of E_a and high values of σ_{Dark} for V_{bias} between -15 and $-5\,V$ could be due to the fact that the doping efficiency of oxygen may be higher inside this more crystallized and more dense material. Maybe post-oxidation during a too long air exposure between the deposition and the measurement affected the characterization of some of the samples. Finally, the results for the $1\,\mu m$ thick samples are quite close to those of the thinner samples, indicating that the material does not change too much during its growth under these conditions.
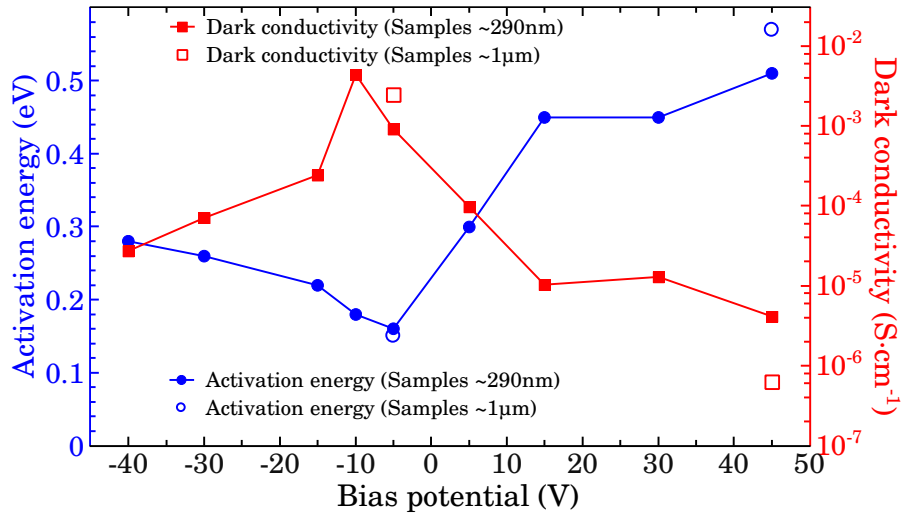
Figure IV.21 – *Activation energies and dark conductivities of the nine $\sim 290\,nm$ thick samples (solid symbols) and of the two $\sim 1\,\mu m$ thick samples (open symbols).*
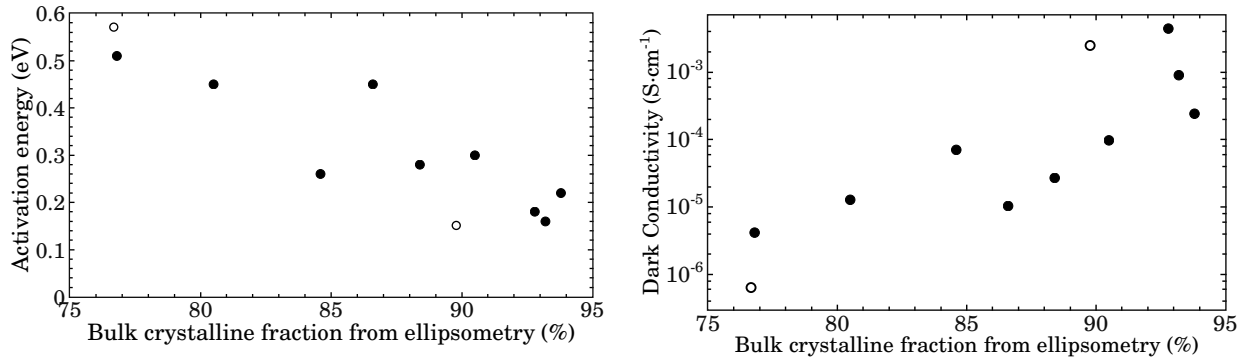

Figure IV.22 – *Activation energies and dark conductivities as a function of the bulk crystalline fraction : solid symbols are for $\sim 290\,nm$ samples and open symbols are for $\sim 1\,\mu m$ thick ones.*
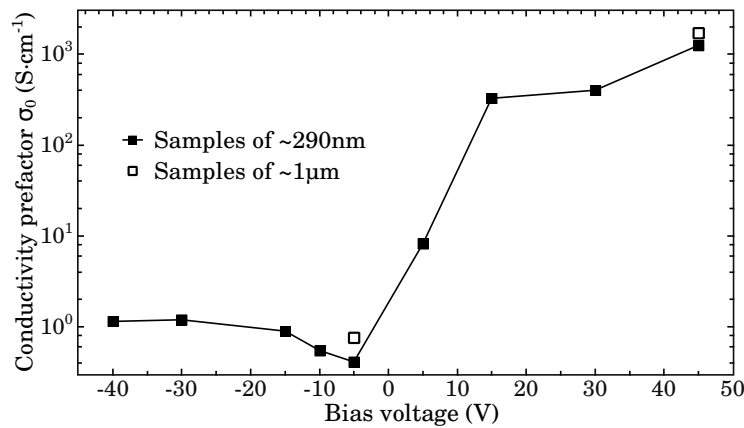

Figure IV.23 – *Effect of the bias on the conductivity pre-exponential factor σ_0.*
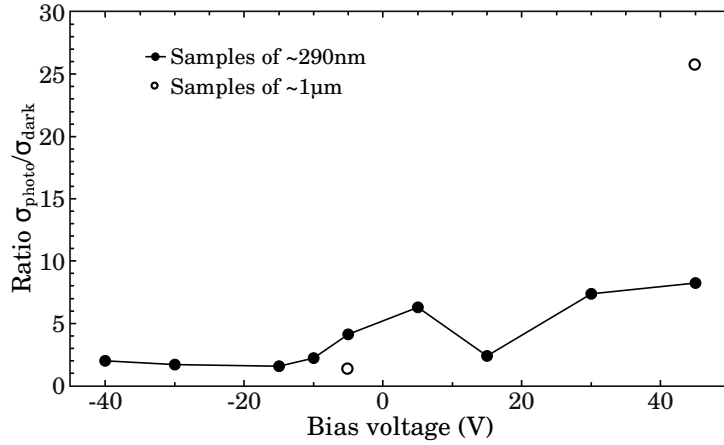
Figure IV.24 – *Effect of the ion bombardment energy on the photosensitivity.*

A non-monotonous behaviour as a function of the bias voltage is also found for the electrical properties. Such complex evolutions of the dark conductivity, of the conductivity prefactor and of the activation energy have also been seen in [77] and they explain them by the amorphous/crystalline ratio, the compressive stress, the crystallite sizes and the ratio of grain boundaries to crystallite volumes. Their minimum of dark conductivity corresponds to their minimum in crystallite sizes and therefore, to their maximum of inter-boundary material volumic fraction.

It is interesting to re-plot these results as a function of the bulk crystalline fraction (F_c) obtained by ellipsometry (Figure IV.22). The decrease of the activation energies and the increase of the dark conductivities as a function of F_c could correspond to a greater sensitivity of the highly crystallized films to oxygen contamination.

Figure IV.23 shows a variation over three orders of magnitude of the pre-exponential factor σ_0 defined by $\sigma_{Dark}(T) = \sigma_0 \cdot \exp(-E_a/k_B T)$. According to [76], this would correspond to transport by hopping through column boundaries for $V_{bias} < 5\,\mathrm{V}$ and transport through small grains for $V_{bias} > 5\,\mathrm{V}$. But it is difficult to confirm this interpretation of the evolution of σ_0 with the AFM images we have made. Indeed, no columnar formations can be seen on the surface of any sample of the series, even for the 1 µm thick ones (see Figure IV.19). When plotted as a function of the bulk crystalline fraction (graph not shown), a rough trend of decrease of σ_0 with increasing F_c is observed. Other authors [77] explain the increase of their σ_0 values with increasing ion bombardment energies by an enhanced compressive stress resulting in a denser film but this scenario does not fit with our experimental data. As a last remark, one can see that σ_0 does not vary a lot between 290 nm and 1 µm. One would expect that the microcrystalline material would evolve during its growth and progressively form columns, however, this is not observed for these deposition conditions.

Figure IV.24 shows the ratio of the photoconductivity (measured with a sun simulator) and the dark conductivity. The ratios for these films are extremely low (except the 1 µm thick film at floating potential). Although this measurement is a macroscopic one and does not tell us what is wrong in the material, it is a strong indication of its low quality. This limitation could explain the low efficiency cells obtained with these materials and these ratios are very far from the values of two or three orders of magnitude found by other groups [63] or in other reactors in our laboratory [66]. One also has to keep in mind that this measurement is not sensitive to the presence of an incubation layer because it is carried out in coplanar configuration.
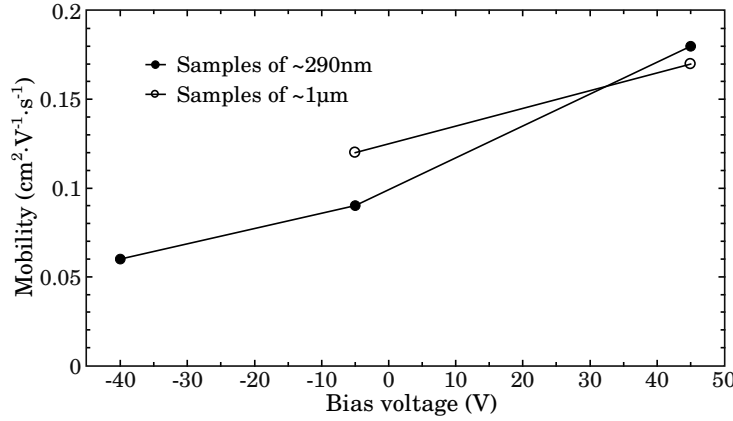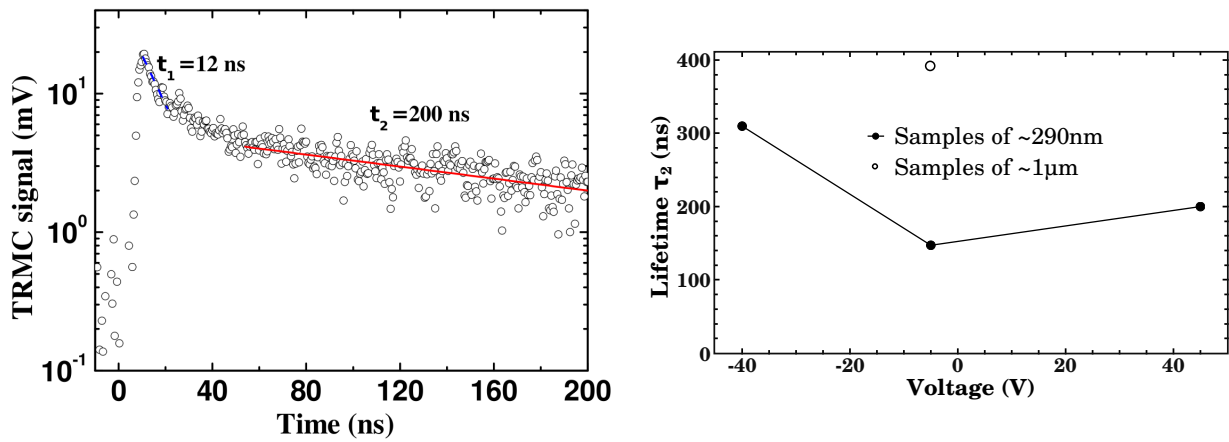
Figure IV.25 – *TRMC effective mobilities of some samples of the series in bias.*

Figure IV.26 – Left graph : *Typical TRMC transient signal obtained for the sample of 290 nm at floating potential.* Right graph : *Effect of the bias on the effective lifetime values τ_2.*

The local (i.e. intra-grain) mobilities have been measured for a few samples with the technique of Time Resolved Microwave Conductivity (TRMC : see Section 9 page 48). Those TRMC values (Figure IV.25) are found to be much lower than the highest values obtained in other reactors in the laboratory : e.g. $3.0\ \mathrm{cm^2\,V^{-1}\,s^{-1}}$ at a deposition rate of $0.45\ \mathrm{\mathring{A}/s}$ in [70] ; $6\ \mathrm{cm^2\,V^{-1}\,s^{-1}}$ at $\sim 2 - 3\ \mathrm{\mathring{A}/s}$ by the IDECR technique in [78] ; 1 and $2\ \mathrm{cm^2\,V^{-1}\,s^{-1}}$ by the IDECR technique in [40] ; $25 \pm 5\ \mathrm{cm^2\,V^{-1}\,s^{-1}}$ at $0.2\ \mathrm{\mathring{A}/s}$ in [14]. The trend of an enhancement of the mobility when reducing the bombardment energy had already been seen by increasing the pressure in two RF-CCP reactors in the laboratory [79, 7]. From the decay of the TRMC signal, one can extract an effective lifetime value, as shown in Figure IV.26. Again, these values seem very low compared to 100 nm layers deposited from a SiF_4, Ar, H_2 mixture in an RF-CCP reactor in our laboratory which had $\tau_2 = 1000\ \mathrm{ns}$ [79]. If the ion bombardment at $-40\,\mathrm{V}$ creates defects and dangling bonds, one would have expected a lower lifetime value, but it is difficult to compare these three samples anyway because the hydrogen contents and contamination levels are very different, and the crystalline fractions is not exactly the same either. Anyway, this diagnostic indicates that not only the devices, but first the material itself, has to be improved. On the other hand, in the RF-CCP reactor, some conditions having TRMC mobilities of $0.24\ \mathrm{cm^2\,V^{-1}\,s^{-1}}$ and $0.28\ \mathrm{cm^2\,V^{-1}\,s^{-1}}$ could still result in cells of $4.4\,\%$ and $2.1\,\%$ respectively, showing that the low mobility values of our films are not enough to explain our extremely low cell efficiencies.

3.5.7   Cells

The two conditions $V_{bias} = -5\,\mathrm{V}$ and $+45\,\mathrm{V}$ have been selected to be incorporated into cells.

3.5.7.1   Cells without buffer layer, without interface treatment

Two first cells have been made at $-5\,\mathrm{V}$ and at $+45\,\mathrm{V}$ with the simplest structure, i.e. without any buffer layer and without any interface treatment :

- Glass substrate covered with textured Juelich ZnO
- p-doped µc-Si:H layer made in the ARCAM reactor
- Air exposure
- intrinsic µc-Si:H layer made in the ATOS reactor (1 µm thick)
- Air exposure
- n-doped a-Si:H layer made in the ARCAM reactor
- Evaporation of the contacts.

The extremely low performance of these first cells can be seen in Figure IV.27 and Table IV.5. In particular, the spectral responses show a complete absence of response in the red. The quite high response at short wavelengths could indicate an inhomogeneous electric field localized at the p – i interface.

3.5.7.2   Cells with a buffer layer and an interface treatment

Here, we will present the effects of two improvements in the cell processing : We added a so-called "buffer layer", which was a 120 nm thick intrinsic µc-Si:H layer deposited in the ARCAM reactor on top of the p layer and we also performed a treatment on the ATOS layer by exposing it to a short (one minute) hydrogen plasma just before the deposition of the n layer.

Such a cell at $V_{bias} = -5\,\mathrm{V}$ has been made with a 1 µm thick ATOS layer. Its characteristics are FF = 46 %, $R_p = 655\,\Omega\,\mathrm{cm}^2$, $R_s = 22\,\Omega\,\mathrm{cm}^2$, $J_{sc} = 3.8\,\mathrm{mA/cm}^2$ and $V_{oc} = 262\,\mathrm{mV}$, resulting in a 0.47 % efficiency. One can see that the buffer layer and the interface treatment improved all the parameters except the current density (comparison with Table IV.5).

3.5.7.3   Series in thickness

To gain understanding on the origin of the low current density, we varied the ATOS intrinsic layer thickness. The buffer layer thickness was fixed to 120 nm. The spectral responses of these cells and their $J(V)$ parameters can be seen in Figure IV.28 and in Table IV.6 respectively.

We found out that the number of collected charges in the red *decreases* for thicker intrinsic layers. This means that the response in the red is not limited by the generation but by problems of charge transport. We unfortunately do not have values of hole diffusion lengths for these films. These three samples are thus unfortunately not showing the typical changes with thickness explained in [50]. The collection problems are quantified in the inset of Figure IV.28, where a negative voltage of $-1\,\mathrm{V}$ helps to increase the collected current by $\sim 40\,\%$ in the red. The fact that the enhancement in the blue is weaker (only $\sim 15\,\%$) could result from a concentration of the built-in electric field near the p-doped layer. What is
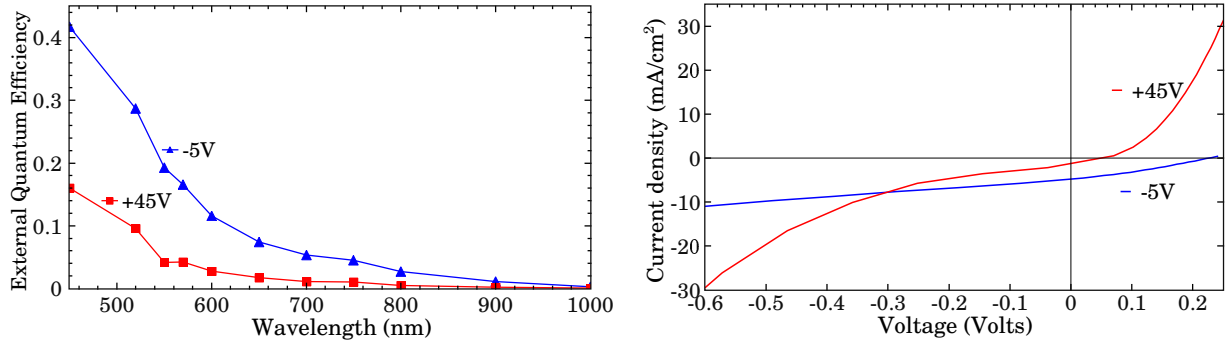
Figure IV.27 – *Spectral responses and $J(V)$ curves of the first two cells.*

	FF	R_p	R_s	J_{sc}	V_{oc}	Efficiency
$V_{bias} = -5\,V$	31 %	89 $\Omega\,cm^2$	37 $\Omega\,cm^2$	4.8 mA/cm^2	230 mV	0.33 %
$V_{bias} = +45\,V$	37 %	9.8 $\Omega\,cm^2$	3.1 $\Omega\,cm^2$	1.6 mA/cm^2	57 mV	0.03 %

Table IV.5 – *$J(V)$ characteristics of the first two cells of the series in bias.*
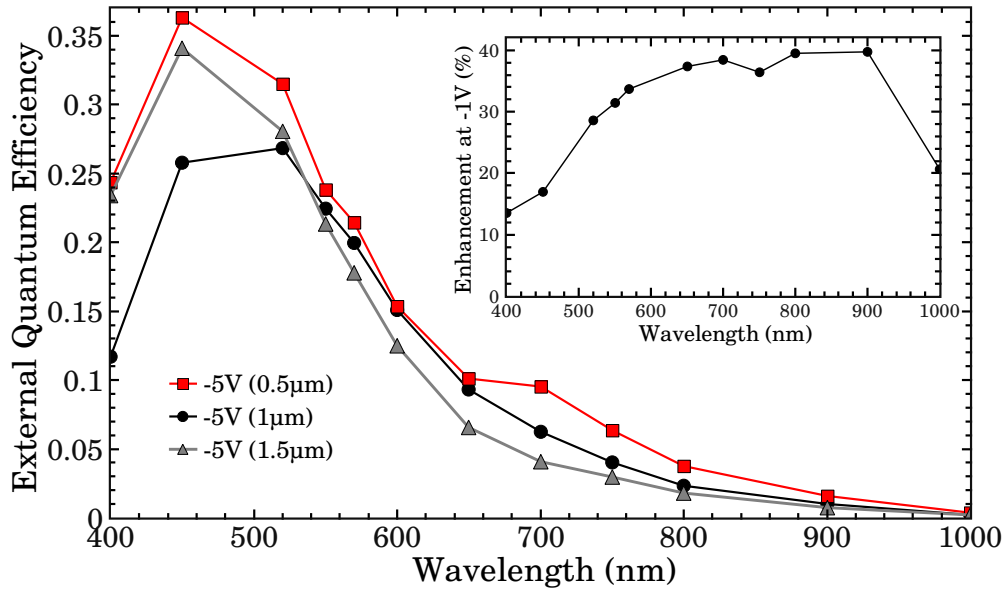
Figure IV.28 – *External quantum efficiencies (EQE) of three cells at $-5\,V$ with different thicknesses. The inset shows the collection enhancement under a negative bias of $-1\,V$ defined as $[\,EQE(-1\,V) - EQE(0\,V)\,] \times 100\,/\,EQE(0\,V)$ for the $1\,\mu m$ thick cell.*

V_{bias}	ATOS layer thickness	FF	R_p	R_s	J_{sc}	V_{oc}	Efficiency
$-5\,V$	0.5 µm	45 %	562 $\Omega\,cm^2$	3.7 $\Omega\,cm^2$	4.9 mA/cm^2	300 mV	0.67 %
$-5\,V$	1 µm	46 %	655 $\Omega\,cm^2$	22 $\Omega\,cm^2$	3.8 mA/cm^2	262 mV	0.47 %
$-5\,V$	1.5 µm	55 %	521 $\Omega\,cm^2$	22 $\Omega\,cm^2$	3.9 mA/cm^2	420 mV	0.91 %
$+45\,V$	1.5 µm	54 %	1525 $\Omega\,cm^2$	19 $\Omega\,cm^2$	4.2 mA/cm^2	309 mV	0.71 %

Table IV.6 – *Series in thickness : Three cells at $-5\,V$ and one cell at $+45\,V$, all with a $120\,nm$ buffer layer and a hydrogen treatment before the n layer.*

more, the fact that the thicker cell at $-5\,\mathrm{V}$ shows a high V_{oc} goes against a control and a limitation of this factor by recombinations in the bulk.

Table IV.6 also confirms that $V_{bias} = -5\,\mathrm{V}$ gives better cells than at floating potential for thicker cells with a buffer layer and an interface treatment (from the comparison of the last two lines).

3.5.7.4   Cells for SIMS

To characterize their chemical composition, one cell at $-5\,\mathrm{V}$ and one cell at floating potential have been deposited on non-textured ZnO in order to have a good resolution of the species variations at the interfaces and for the thin doped layers. It was the first time that SIMS measurements were carried out in "real conditions", i.e. on a device. It allowed us to directly correlate the cell performance with the presence of contaminations.

The structure of these two cells was the following :

- glass covered with flat ZnO:Al
- 3 minute argon plasma treatment on the ZnO
- p-doped µc-Si:H layer made in the reactor ARCAM
- intrinsic µc-Si:H buffer layer made in the reactor ARCAM (120 nm)
- air exposure during the transfer
- intrinsic µc-Si:H layer made in the reactor ATOS (1 µm)
- air exposure during the transfer
- no treatment for the cell at $-5\,\mathrm{V}$
  H_2 treatment for the cell at $+45\,\mathrm{V}$
- n-doped a-Si:H layer made in the reactor ARCAM
- evaporation of the aluminum contacts

The left graph of Figure IV.29 shows that this time, the collection in the cell deposited at $-5\,\mathrm{V}$ is only slightly enhanced by a negative voltage of $-0.5\,\mathrm{V}$ (around 10 %) and the right graph shows the much more stable reverse currents of these cells. The $J(V)$ characteristics confirm with these structures that $-5\,\mathrm{V}$ is the better condition of the two.

The SIMS measurements have been carried out only one day after deposition, in order to avoid post-oxidation. The profiles are shown on Figures IV.30 and IV.31, and are summarized in Table IV.7. The 120 nm of ARCAM material can be considered as a reference, although for some elements, the variation at the p-i interface is not sharp enough to be sure that the real value is reached, so that it could be overestimated.

These results show the high levels of contaminations of the MDECR material before the installation of the load-lock as compared to the RF-CCP reference. What is more, the ion bombardment has a tremendous effect on the chemical composition of the film, at least for the selective incorporation of certain species : while C and O atoms are incorporated at very high levels at floating potential ($\sim 2 \times 10^{21}\,\mathrm{cm}^{-3}$), the N concentration remains constant. It should be noted that very surprisingly, the films at floating potential had normal values of activation energy and dark conductivity.

The hydrogen concentrations (C_H) in the ARCAM material and in the ATOS material at $-5\,\mathrm{V}$ and $+45\,\mathrm{V}$ are respectively $\sim 2.4 \times 10^{21}\,\mathrm{cm}^{-3}$, $\sim 4.6 \times 10^{21}\,\mathrm{cm}^{-3}$ and $\sim 8.8 \times 10^{21}\,\mathrm{cm}^{-3}$. Assuming an atomic density of $5 \times 10^{22}\,\mathrm{cm}^{-3}$, these values correspond to atomic concentrations of 5 %, 9 % and 18 % respectively. The comparison of the two MDECR materials by

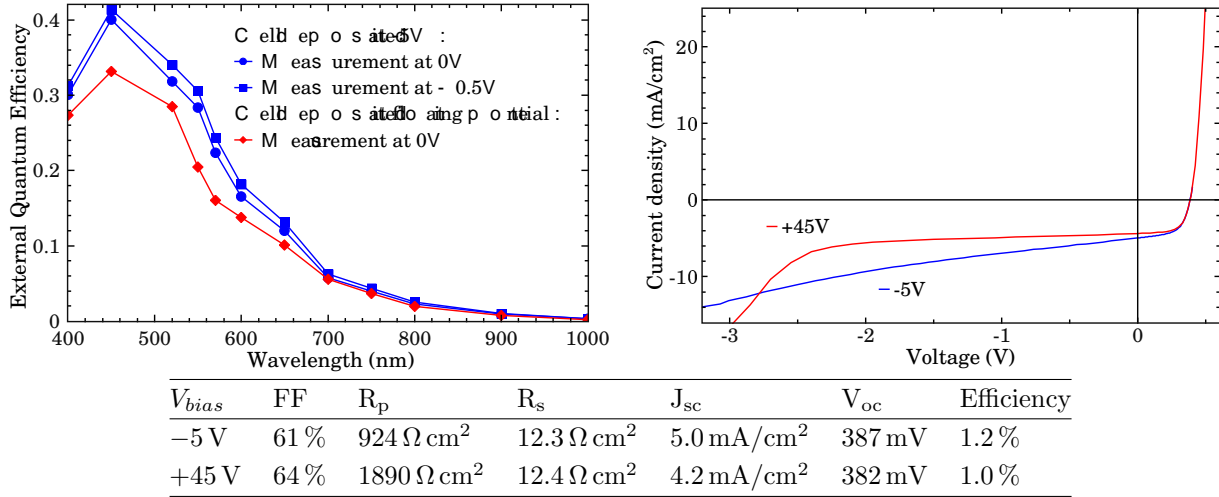| V_{bias}	FF	R_p	R_s	J_{sc}	V_{oc}	Efficiency
$-5\,V$	$61\,\%$	$924\,\Omega\,cm^2$	$12.3\,\Omega\,cm^2$	$5.0\,mA/cm^2$	$387\,mV$	$1.2\,\%$
$+45\,V$	$64\,\%$	$1890\,\Omega\,cm^2$	$12.4\,\Omega\,cm^2$	$4.2\,mA/cm^2$	$382\,mV$	$1.0\,\%$

Figure IV.29 – *Spectral responses, $J(V)$ curves and characteristics of the two cells on non-textured ZnO for SIMS.*

exodiffusion gave an estimation of the hydrogen ratios of ~ 4.6 (see Section 3.5.4). Here with SIMS, a factor of ~ 2 is found. The difference between the two techniques is that SIMS only measures the signal of atomic hydrogen (H^- secondary ions) while for exodiffusion, hydrogen is detected in its molecular form. Thus, the presence of molecular hydrogen in the film at floating potential could at least partially explain this difference and would fit with the signal at temperatures lower than $250\,°C$ seen in Figure IV.18. The ratio of the void fractions in the bulk was 3.4 for the ellipsometric models.

The apparent peak of N in the p-doped layer is explained by a mass interference (see Section 6.3 page 43). It is much more difficult to explain the signal of mass 31 in the p layer. Indeed, this signal has been measured separately at a higher mass resolution of 4000 in order to distinguish ^{31}P from ^{30}SiH. Thus, it could only interfere with molybdenum, iron or niobium, which is not likely.

One of the main results of this series of SIMS is the huge "tail" of oxygen signal at the Si/ZnO interface. It is seen for both cells although less clearly at $+45\,V$ because of the huge level of oxygen present in the ATOS layer. It cannot be explained by a mixing artefact or by the roughness of the crater because it takes place over a large depth of $\sim 0.5\,\mu m$ and because the variations of the other species are sharp. The only two possible explanations are a phenomenon of diffusion of oxygen from the ZnO or the sputtering of the ZnO before the Si/ZnO interface : The latter effect could happen if bubbles are present at the p/ZnO interface or if the sputtering by the primary cesium ions is inhomogeneous, inducing the formation of holes. Due to such bubbles or holes, the ZnO would be prematurely sputtered, leading to an increase of the oxygen signal. In order to better understand the origin of the oxygen profile, we decided to study the topology of the bottom of the craters. As we will see in a later SIMS experiment (Section 4.4.4.2 page 177), the appearance of the bottom of the craters can be very different during the sputtering of the silicon layers and after the sputtering of the silicon layers, i.e. once in the ZnO. Here, all the characterizations have been made for craters sputtered until the ZnO.

First, the roughness of the bottom of the craters has been characterized with a profilometer. The peak-to-valley roughness has been found to be around $20\,nm$ and no deep holes have been detected in the ZnO with this technique.
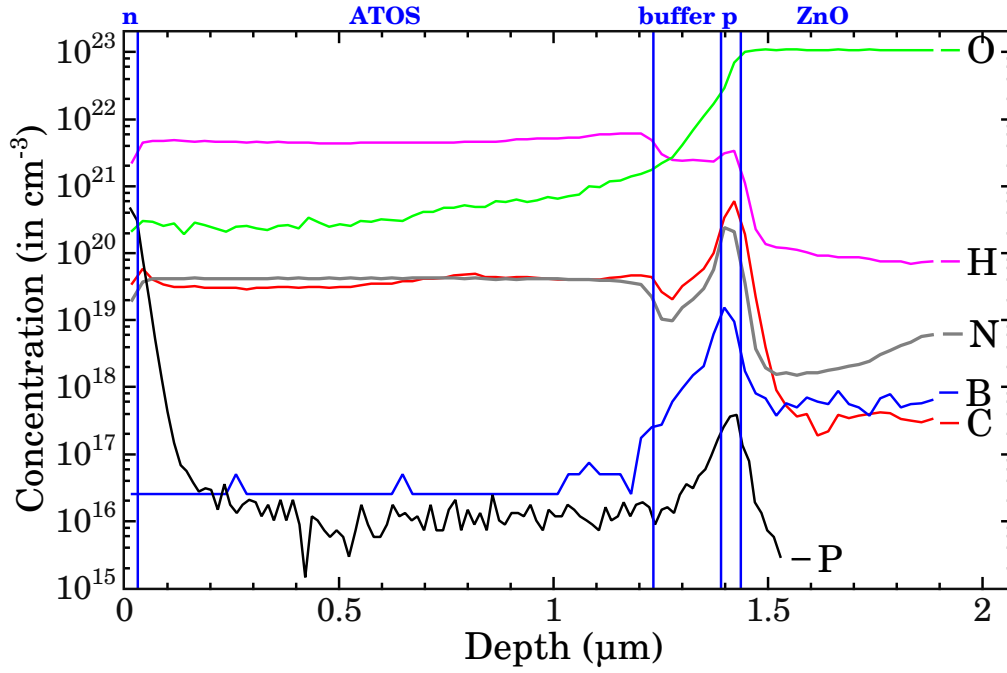
Figure IV.30 – *SIMS profiles of the −5 V cell.*
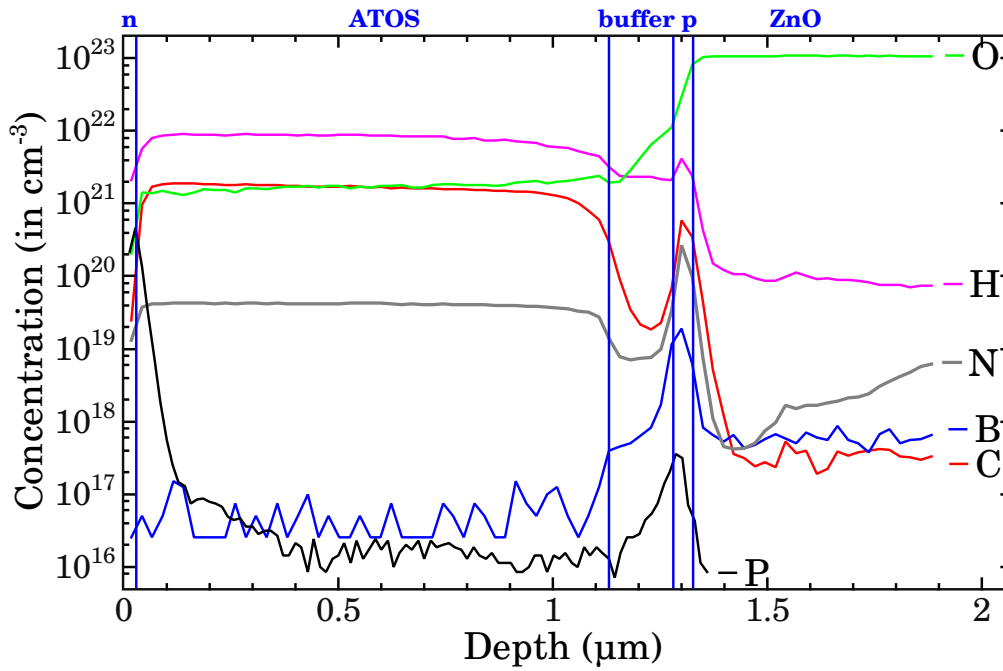
Figure IV.31 – *SIMS profiles of the +45 V cell.*

Species	ATOS −5V (cm^{-3})	ATOS +45V (cm^{-3})	ARCAM (cm^{-3})	ATOS +45V / ATOS −5V	ATOS −5V / ARCAM	ATOS +45V / ARCAM
H	4.6×10^{21}	8.8×10^{21}	2.4×10^{21}	2	1.9	3.8
C	3.8×10^{19}	1.6×10^{21}	2.0×10^{19}	42	1.9	80
O	2.3×10^{20}	1.6×10^{21}	O tail	7	–	–
N	4.1×10^{19}	4.1×10^{19}	7.4×10^{18}	1	5.5	5.5

Table IV.7 – *Comparison of the chemical compositions obtained by SIMS for the two ATOS intrinsic layers and the ARCAM intrinsic buffer layer.*

The Scanning Electron Microscopy (SEM) technique is a much more powerful tool and has also been used to further characterize the morphology of the craters. Figure IV.32 evidences features in the craters which look like elongated "cracks".

Then, we completed this study with the Atomic Force Microscopy (AFM) diagnostic, performed on the same crater as the SEM measurements. The results shown on Figure IV.33 reveal two types of structures : the elongated "cracks" of the SEM images are confirmed by the AFM technique and big holes having depths of several hundreds of nanometers ($\sim 300-500\,\text{nm}$) are also seen. The typical horizontal dimensions of the "cracks" in their elongation axis is a bit more than $1\,\mu\text{m}$ and their depths as measured by the tip are ranging from 20 to $60\,\text{nm}$.

The tail of oxygen was so puzzling that we had a quick second SIMS measurement done on the sample, which confirmed it is a reproducible feature (superposed in Figure IV.34). This time, we also recorded the aluminum and zinc species. O and Al both increase, but the shape of the signal is different from the first measurement, by a factor as high as 4. The mass chosen for zinc was 68 (relative abundance of this isotope : $18.8\,\%$). The main isotope, of mass 64, would probably have been a better choice, in order to have a higher signal. Zinc has a very low probability to be sputtered as a negative ion and as shown in the inset, the signal of mass 68 can be very well superposed with the carbon profile from the first measurement so that we think this indicates a mass interference with $^{28}\text{Si}_2{}^{12}\text{C}$.

At this stage, we concluded that the signals of oxygen before the ZnO are probably not due to a real phenomenon of diffusion but result from the formation of holes during the sputtering or to the presence of "bubbles" at the Si/ZnO interface. Indeed, the fact that the shapes of the oxygen tails are different and that the signals of aluminum and boron also increase before the Si/ZnO interface are arguments in favor of this hypothesis. For this latter explanation, one has to accept that the efficiency of formation of ions Zn^- from the $18.8\,\%$ abundance isotope is so small that this element is not seen in Figure IV.34 and that the dominant element of mass 68 is the molecular ion $^{28}\text{Si}_2{}^{12}\text{C}^-$ even though the carbon concentration is quite low in the ARCAM buffer layer ($2 \times 10^{19}\,\text{cm}^{-3}$). To avoid these doubts about the mass 68, zinc will always be detected under the form of the molecular ion ZnO^- in all the measurements thereafter.

As a conclusion, we can notice that the cell at floating potential has an efficiency of $1\,\%$ despite the huge O, C and N contaminations and that the spectral responses of the two cells above $700\,\text{nm}$ are superposed. Furthermore, the cells on non-textured ZnO and with aluminum back contacts are better than the ones on textured ZnO with silver back contacts so that maybe, the ZnO roughness and/or the hydrogen treatment are detrimental for our cell performance. It has indeed been reported [80] that a ZnO with sharp V-shaped roughness can induce the growth of a porous material with cracks. These are generally thought to result in shunts although it has also been observed [81] that a cell presenting such "cracks" (which could either be amorphous tissue or voids) on its TEM cross section image had a higher V_{oc} as compared to a "dense" cell ($530\,\text{mV}$ and $486\,\text{mV}$ respectively).

The tail of oxygen was a very exciting discovery, enabled by the fact that we carried out a SIMS measurement directly on a cell for the first time in our laboratory. A real diffusion of oxygen from the ZnO could have been a global explanation of the very low efficiencies of all our cells. Therefore, it had to be further studied : other experiments have been dedicated to this suspicion of oxygen diffusion and have clearly confirmed the presence of holes (Section 4.4.4.2 page 177).
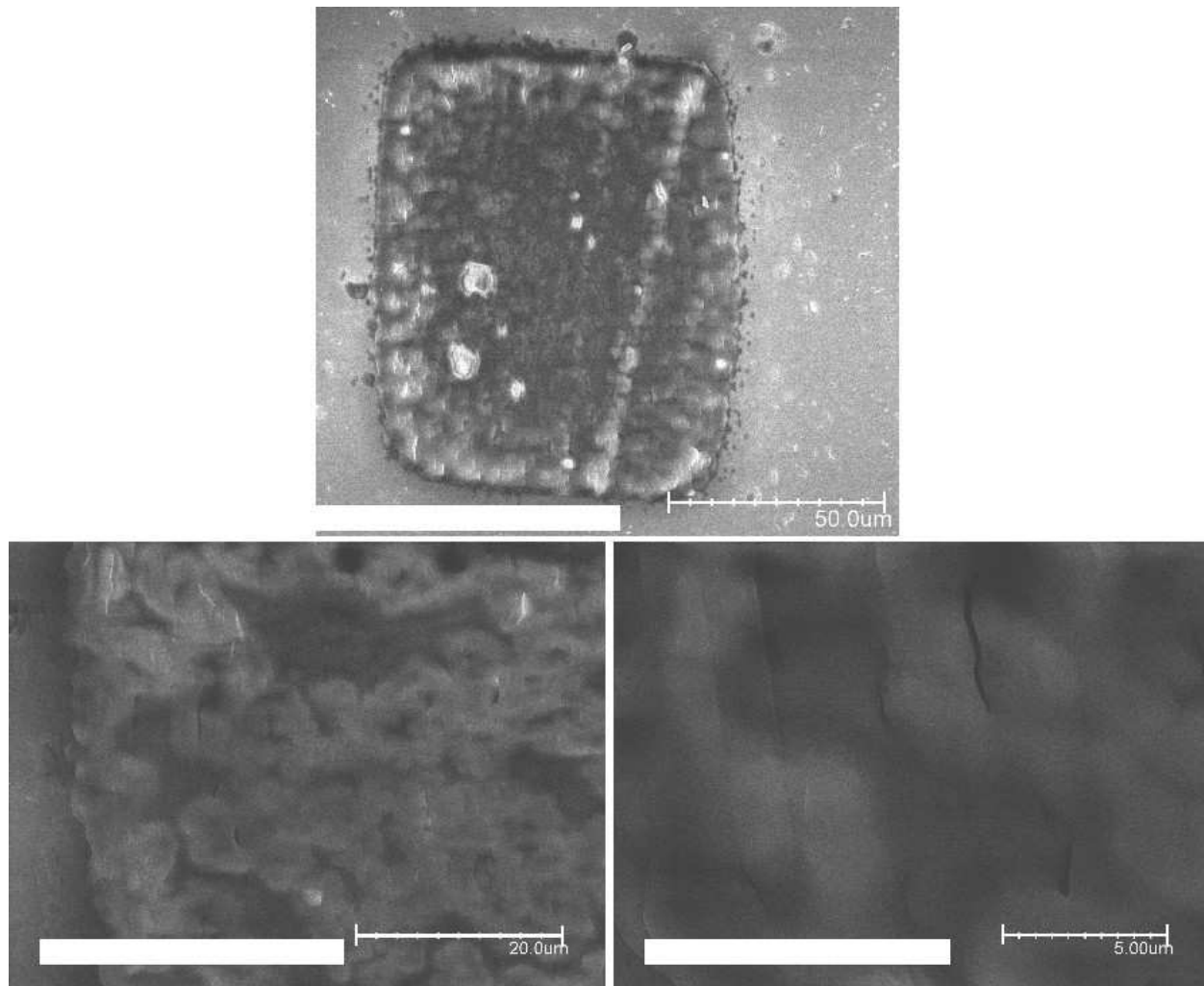
Figure IV.32 – *SEM images taken on one of the craters of the cell at $-5\,V$ presenting a huge "tail" of oxygen : Global view of the crater (scale of $50\,\mu m$ on the top graph) and close-ups on the "cracks" (scale of $20\,\mu m$ for the bottom left graph and of $5\,\mu m$ for the bottom right graph).*
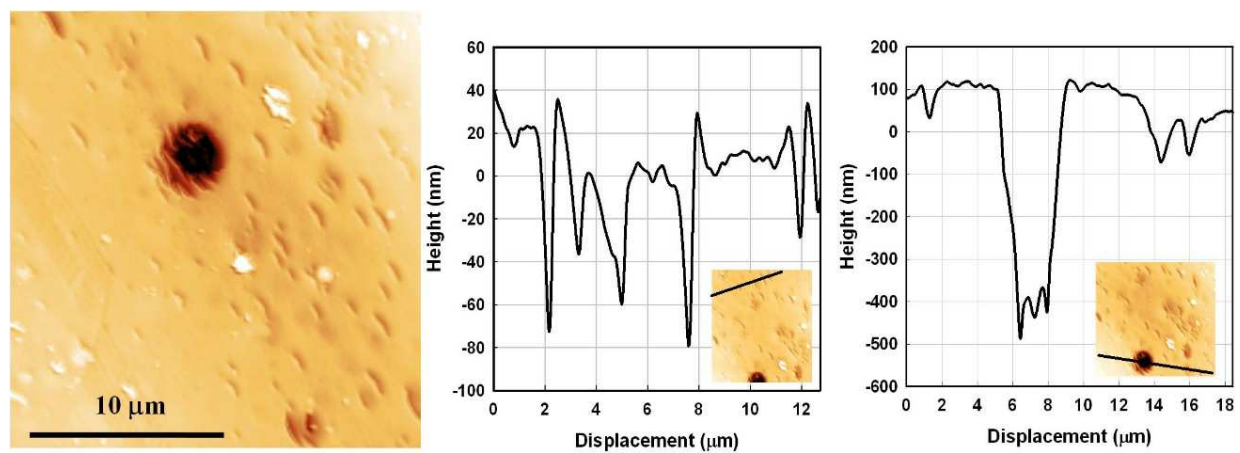

Figure IV.33 – *The left graph is an AFM image taken in the bottom of the same crater as the SEM images of Figure IV.32. The middle plot shows the depths of the "cracks" taken along the line shown in its inset and the right plot shows the depth of a hole taken along the line shown in its inset.*
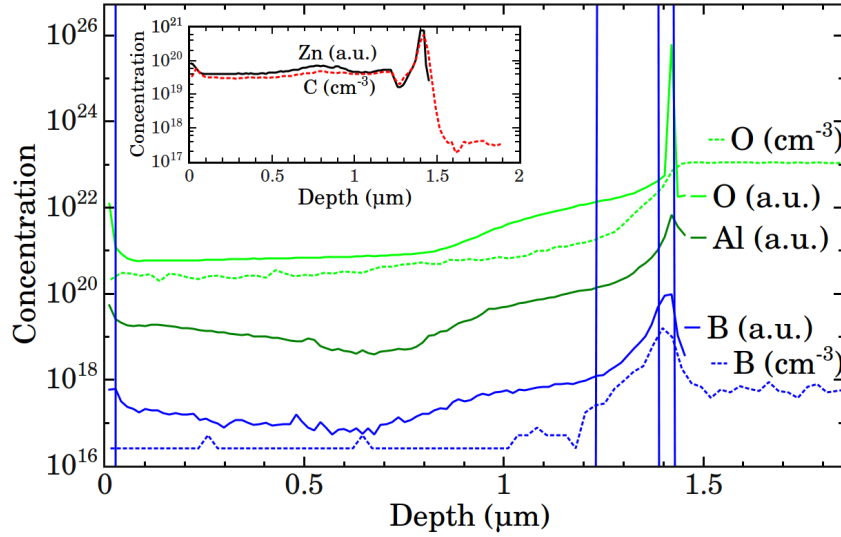
Figure IV.34 – *New measurement of the cell at $-5\,V$: The first measurement is in dashed lines (in cm^{-3}). The repetition is in solid lines (in arbitrary units). The detector (electron multiplier) saturated at the silicon/ZnO interface for the second measurement, thus, the signals in the ZnO should not be taken into consideration. The inset shows the superposition of the C profile of the first measurement with the mass 68 signal from the repetition.*

3.5.7.5   n-i-p cell

To be less sensitive to any oxygen that could diffuse from the ZnO and induce an n-type doping, we also studied an n-i-p structure :

- glass covered by textured Juelich ZnO
- n-doped amorphous layer made in the ARCAM reactor
- intrinsic amorphous buffer layer made in the ARCAM reactor (120 nm)
- air exposure
- H_2 treatment in the ATOS reactor
- intrinsic microcrystalline layer made in the ATOS reactor (1 µm) at $V_{bias} = -30\,V$
- air exposure
- H_2 treatment in the ARCAM reactor
- p-doped microcrystalline layer made in the ARCAM reactor
- ITO contacts (90 nm)

After the etching of the top p layer with an SF_6 plasma, the performance of the cell is FF of 26 %, R_p of 320 $\Omega\,cm^2$, R_s of 78 $\Omega\,cm^2$, J_{sc} of 3.0 mA/cm^2, V_{oc} of 216 mV and Efficiency of 0.2 %. Despite the etching of the high conductivity p layer, R_p stayed quite low and the n-i-p structure did not help us to improve the efficiency but the different layers and interface treatments were not optimized.

Conclusions from the first series in bias

It is difficult to propose a unified explanation to all the measurements or even to be sure of the bias leading to the best quality material since some apparent disagreements appear between them. This series clearly demonstrates that it could be very misleading to rely just on one diagnostic.

Still, we can notice that there is a qualitative agreement on the fact that the ion bombardment helps to obtain a dense material with a low hydrogen content, although the quantitative values differ between ellipsometry, exodiffusion and SIMS.

3.6   Second series in bias

Before the installation of the load-lock, we tried to explore another gas mixture. Not limiting ourselves to pure silane conditions anymore, we studied a mixture of 50 sccm of SiH_4, 5 sccm of Ar and 100 sccm of H_2. The goals of this change were to reduce the contaminantion concentrations by increasing the deposition rate (silane flow rate increased from 42 sccm to 50 sccm) and by reducing the residence time of the gas molecules (increase of the total flow rate). The other deposition parameters were a glass surface temperature of $\sim 239\,°C$, a gas pressure of 5 mTorr, a microwave power of 1.5 kW and a deposition time of 5 minutes and 30 seconds, corresponding to ~ 530 nm thick films. Five samples were deposited, varying the RF power from 31 W to 100 W, corresponding to bias voltages of -15 V to -61 V respectively.

All the samples have been characterized by ellipsometry. This new gas mixture allowed us to obtain very high crystalline fractions F_c (left graph of Figure IV.35). These conditions also allowed us to obtain the highest value at that time for the maximum of the imaginary part of the pseudo-dielectric function $\langle \varepsilon_i \rangle_{max} = 24.1$ and the lowest value of the bulk void fraction $F_v = 3.3\,\%$ (right graph of Figure IV.35). Judging from these results, the optimum in ion energy seems to be around -45 V.

The films are quite thick, around 530 nm, so that the informations on the incubation layer (IL) are not necessarily trustworthy. Still, we find trends similar to those of the first series, i.e. an increase of the IL thickness and crystalline fraction with higher ion bombardment (Figure IV.36).

Finally, basic electrical characterizations have been performed. As for the first series in bias, activation energy values and dark conductivity values typical of intrinsic microcrystalline silicon (i.e. $E_a \sim E_g/2$ and $\sigma_d \sim 1 \times 10^{-6}$ S·cm^{-1}) are obtained for low ion energies. But this time, the evolution is monotonous with the bias voltage (see Figure IV.37). The $V_{bias} = -15$ V condition has later been incorporated in a stack of layers for SIMS characterization. A high oxygen concentration $C_O = 1.1 \times 10^{20}$ cm^{-3} has been found, indicating that relating the E_a and σ_d values to the oxygen levels is not straightforward. The other species
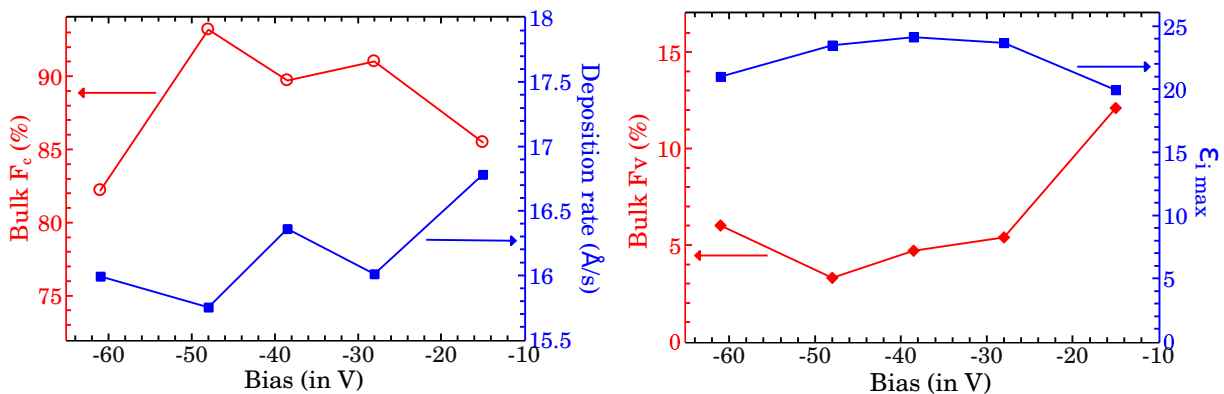

Figure IV.35 – *Ellipsometry results showing the bulk composition (crystalline fraction F_c and void fraction F_v), the deposition rate and the maximum value of the imaginary part of the pseudo-dielectric function $\langle \varepsilon_i \rangle_{max}$ as a function of the bias voltage.*
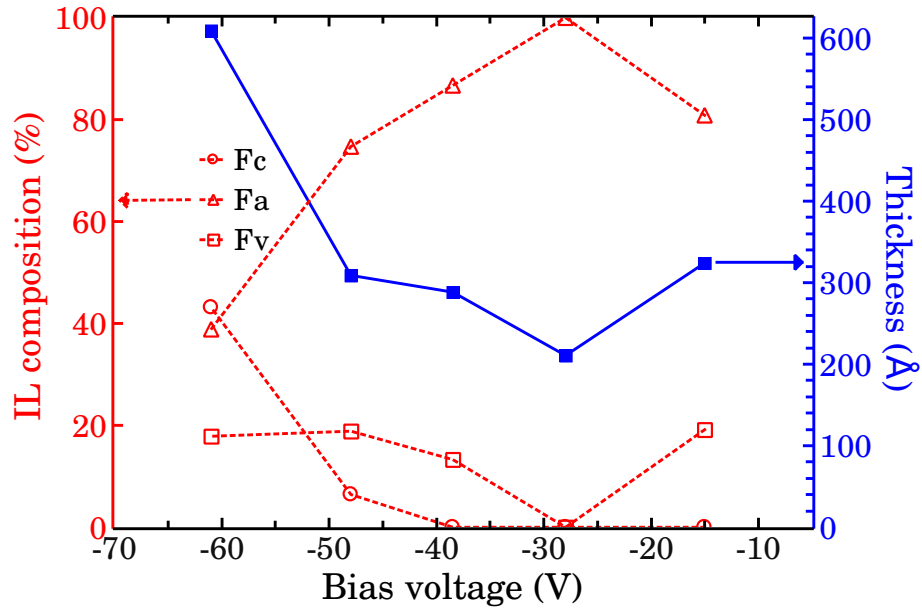
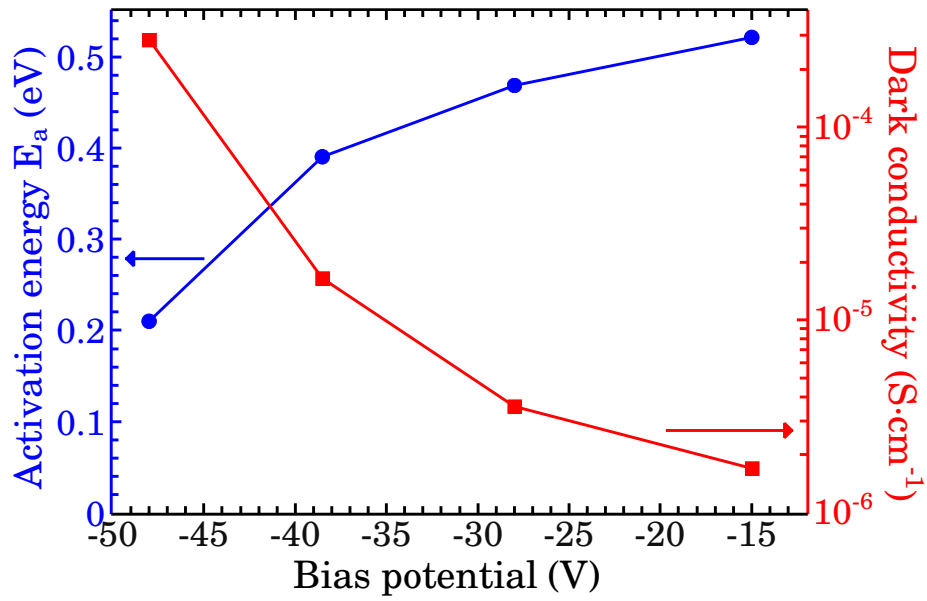Figure IV.36 – *Ellipsometry results showing the composition and the thickness of the incubation layer (IL).*

Figure IV.37 – *Activation energies and dark conductivities of the second series in bias.*

concentrations were $C_C \sim 8 \times 10^{19} \, \text{cm}^{-3}$, $C_F \sim 3 \times 10^{17} \, \text{cm}^{-3}$ and $C_N = 6 \times 10^{15} \, \text{cm}^{-3}$. The hydrogen signal has not been quantified but is a factor of 1.6 higher than the signal in the standard ARCAM microcrystalline layer.

As a conclusion, this second series in bias shows some differences with the first one due to the different plasma conditions used. This illustrates that finding "universal" behaviors (i.e. valid for the whole parameter space) is a major difficulty in this field of research. The condition at $-48 \, \text{V}$ has been chosen to study the effect of the argon dilution (see Section 3.3 page 106) because it has the highest F_c and the lowest F_v (3.3 %) in the bulk, and an $\langle \varepsilon_i \rangle_{max} > 23$.

3.7   Series in temperature

The variation of the substrate temperature has complex consequences. Increasing it in the range of $200 - 400 \, ^\circ\text{C}$ helps to enhance the mobility of radicals arriving on the surface. Above $400 \, ^\circ\text{C}$, dangling bonds are said to arise from thermal dissociation of Si–H bonds, and thus, to result in lower diffusion lengths of the radicals. This mechanism has been used to explain that too high temperatures can be detrimental for the crystalline fraction (e.g. see Figure 2 of [30]).

On the other hand, high temperatures help to promote the growth of bigger crystallites (Fig. 4 of [82] and [83]) and the grain coalescence threshold temperature is above $200 \, ^\circ\text{C}$ [49]. The effect of temperature on the defect density is not simple : in [65] (Figure 2), a continuous decrease of the defect density measured by Electron Spin Resonance (ESR) is evidenced when the temperature is increased in the range $100 - 250 \, ^\circ\text{C}$, while in [84] (Figure 6), the ESR spin density is linearly increasing from $100 \, ^\circ\text{C}$ to $400 \, ^\circ\text{C}$. An effect of the temperature on the preferred crystallographic orientation has also been noticed (increasing it from 60 to $400 \, ^\circ\text{C}$ favors the (110) orientation over the (111) orientation [83]).

Furthermore, the substrate temperature does not only have an influence on the film surface chemistry, but also on the sub-surface region. Indeed, the diffusion coefficient of atomic hydrogen [35] and its efficiency to etch depend on it.

For Electron Cyclotron Resonance high density plasmas, it seems that temperature can have reduced effects over large ranges : [40] found no significant influence of the temperature between $250 \, ^\circ\text{C}$ and $350 \, ^\circ\text{C}$ and similarly, [85] obtain close materials and devices between $270 \, ^\circ\text{C}$ and $340 \, ^\circ\text{C}$.

Understanding the multiple impacts of temperature is complicated as they seem to strongly depend on the deposition conditions (as emphasized in [86] for example). As a consequence, the effects of temperature on the film properties (e.g. creation of defects and dangling bonds) and on the nucleation dynamics (increase of the nucleation rate proposed in the model of [27]) is a fundamental question which has to be investigated in each deposition condition to find the optimum.

Concerning the amorphous/microcrystalline transition, it is well accepted that a certain level of atomic hydrogen flux has to arrive on the growing layer for it to crystallize. An interesting fact is that the hydrogen to silane ratio resulting in the transition is strongly affected by the temperature [63, 4] so that high temperatures can somehow balance too low atomic hydrogen fluxes (either because temperature and hydrogen have the same effect or because higher temperatures enhance the action of hydrogen).

It had been previously found [9, 72] that for the MDECR technology, a high temperature was necessary in order to crystallize the material deposited at high rate from pure silane. Progressively, it became a concern that these quite high substrate surface temperatures of $\sim 230\,°C$ could be the reason for the low performance of the cells so that we looked for new conditions to obtain a crystallized material at lower temperatures.

The most common process temperatures to deposit microcrystalline solar cells are below $200\,°C$. For higher temperatures, we can report here the results obtained with an Expanding Thermal Plasma source (ETP) [87]. They are of particular interest for us because their material and process present many similarities with ours : e.g. their FTIR spectra showing an absence of peak at $2000\,cm^{-1}$ for the conditions giving the highest crystalline fractions and often the narrow peaks doublet around $2100\,cm^{-1}$; a preferred (111) crystallographic orientation ; and plasma induced heating up to $450\,°C$. Their best cell has been deposited at $2\,Å/s$ at $T_{subtrate} = 250\,°C$ at $150 - 380\,mTorr$ and reached $1.9\,\%$. In other conditions giving a higher rate of $12.1\,Å/s$ and with an even higher temperature of $300\,°C$, they obtained a $1.5\,\%$ cell. The results of their cells at $350\,°C$ are unfortunately not reported.

Results of the depositions at temperatures lower than $230\,°C$

To study the effect of this important parameter for the growth of microcrystalline silicon, we deposited a series of five samples on glass and c-Si after the installation of the load-lock. Then, we processed three cells in order to check the resulting performance of these new materials. The temperature of the glass substrate surface, as indicated by the pyrometer, was varied from $195\,°C$ down to $125\,°C$. Additionally, one deposition at room temperature, without any heating was also tried. All the other deposition conditions were kept constant : $42\,sccm$ of pure silane, $\sim 41\,W$ of RF power, a gas pressure of $9\,mTorr$, a plasma pressure of $\sim 5.2\,mTorr$ and a microwave power of $1.5\,kW$ (same set of values as the first series in bias of Section 3.5 page 110).

The motivation of this series was to explore further the parameter space to obtain less crystallized films, which are reported by several groups to be better adapted for solar applications (see the discussion on this question in the Section 2.3 page 97). Another motivation was that one of the possible explanations of the SIMS signals at the silicon/ZnO interface (see for example Section 3.5.7.4 page 122) could have been that the high substrate surface temperature of $230\,°C$ results in a diffusion phenomenon of oxygen, aluminum and/or zinc from the ZnO substrate.

Another major potential interest of depositing at lower temperature would be to reduce the heating and cooling times, thus allowing to grow more samples per day. (We usually wait till the thermocouple reading is below $250\,°C$ to open the reactor.)

The really surprising discovery of this series is the ellipsometry results which are exposed in the left graph of Figure IV.38. It has indeed been found that for these conditions, the crystalline fraction of the bulk does not seem to be affected by the temperature, at least down to $155\,°C$. The last point, at $125\,°C$, should be considered with great care because its spectrum was impossible to fit with a satisfactory figure of merit with our standard model. A three layer model with a Tauc-Lorentz dispersion law for the amorphous component instead of the usual standard amorphous dielectric function (fit on 11 parameters instead of the usual 9 parameters) still gives a crystalline fraction in the bulk of $49\,\%$ (good figure of merit χ^2 of 0.4). In any case, in the range $155 - 195\,°C$, the crystalline fraction is very high and
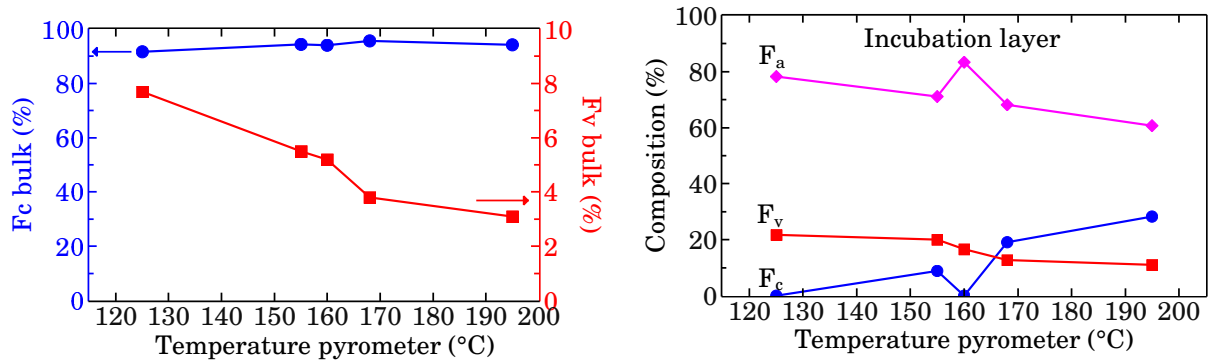
Figure IV.38 – *Effect of the surface temperature on the results of the ellipsometry models : The left graph shows the evolution of the bulk composition while the right graph shows the composition and the thickness of the incubation layer. The experimental spectrum of the sample grown at 125°C was unfortunately very difficult to fit with our usual model so that its points are probably not meaningful.*
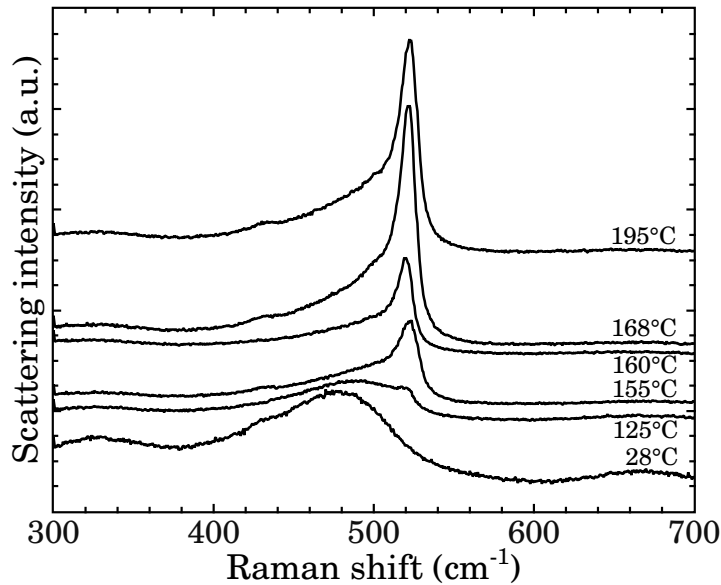

Figure IV.39 – *All the Raman spectra as a function of the deposition temperature.*

practically constant $(94-96\%)$. Additionally, the sample of the first series in bias (without the load-lock) at the usual $230\,°C$ with a close RF power had $F_c = 91\%$.

Although the crystalline fraction in the bulk does not vary a lot, changes in the material are still indicated by the other parameters of the models : the maximum value of the imaginary part of the pseudo-dielectric function, $\langle\varepsilon_i\rangle_{max}$, constantly increases with temperature (from 22.3 at $125\,°C$ up to 24.8 at $195\,°C$). Also, the global trend of the deposition rate is to go down with temperature (from $15.7\,\text{Å/s}$ at room temperature, to $11.8\,\text{Å/s}$ at $155\,°C$, to $10.8\,\text{Å/s}$ at $195\,°C$). Figure IV.38 also shows that higher temperatures help to reduce the bulk void fraction and favor the early crystallization of the incubation layer.

The sample grown at room temperature is completely amorphous and the Tauc-Lorentz model used to to fit its ellipsometry spectrum has an abnormally large band gap of $2.1\,\text{eV}$.

The onset of the crystallization at the temperature of $125\,°C$ and the global trend of an increase of the crystalline fraction with temperature are clearly evidenced by superposing the Raman spectra of the six films in Figure IV.39. This emphasizes that Raman spectroscopy
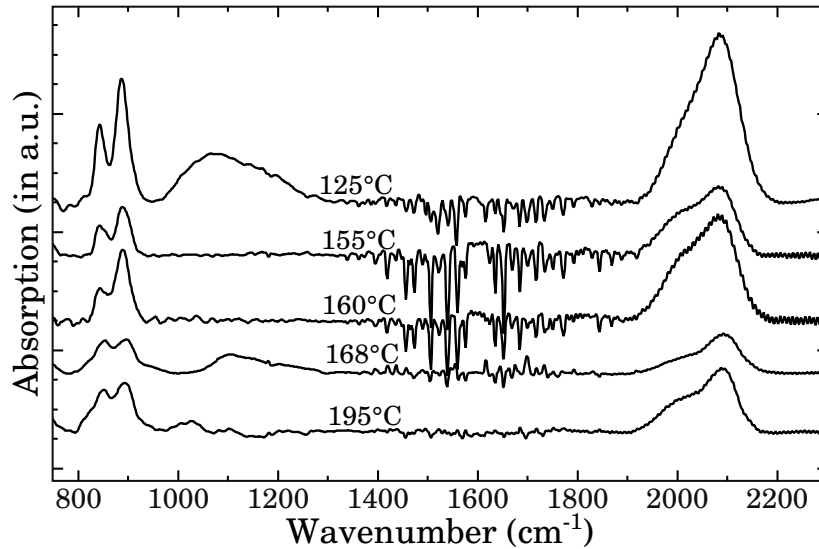
Figure IV.40 – *Comparison of the FTIR spectra as a function of the deposition temperature. The curves have been shifted for clarity.*

and ellipsometry bring complementary and sometimes different informations and that they have to be both implemented in order to maximize the understanding of the material.

The infra-red absorption modes of these samples are shown in Figure IV.40. A too low temperature of 125 °C results in oxygen contamination during the growth, as evidenced by the presence of a $\sim 1050 \, cm^{-1}$ peak (spectrum recorded just after having taken the sample out of the reactor). This could be explained by the temperature being too low to degas the water molecules adsorbed on the walls of the load-lock exposed to air. From the areas of the hydrogen mode peaks at ~ 840 and $\sim 890 \, cm^{-1}$, and $2000 - 2100 \, cm^{-1}$, we can also conclude that overall, the quantities of hydrogen incorporated in the films increase for lower temperatures.

We can notice that the spectra of these films grown at temperatures lower than 230 °C all show a $2000 \, cm^{-1}$ peak, which might be interpreted as an indication of dense films. Additionally, it was found that these materials seem to be less sensitive to oxydation when stored at ambient air : The film deposited at 195 °C has been re-measured two weeks after and the Si–O mode at $1050 \, cm^{-1}$ was small (graph not shown).

Finally, we selected three temperatures to process cells. The chosen structure was the following : textured ZnO / p-doped µc-Si:H layer (ARCAM) / intrinsic µc-Si:H buffer layer (ARCAM) / H_2 plasma treatment (ATOS) / 1 µm µc-Si:H layer at low temperature (ATOS) / H_2 plasma treatment (ARCAM) / n-doped a-Si:H layer (ARCAM) / silver back contacts. Glass substrates were also clamped on the substrate-holder to be co-deposited with each cell : their ellipsometry fits showed high crystalline fractions of 97 % or above, 0 % void fractions, and $\langle \varepsilon_i \rangle_{max}$ values of 24 or higher. Unfortunately, lowering the growth temperature does not seem to be the key solution to enhance MDECR solar cell performance, as can be seen in Table IV.8. The spectral responses showed the usual extremely low efficiency in the red part of the spectrum and also, a significant enhancement at negative bias voltage, indicating a problem of collection.

Information on the electrical properties of the µc-Si:H grown in these new conditions were needed so that we processed another cell at 189 °C. The co-deposited 1 µm film on glass has a 96 % crystalline fraction and an only 3 % void fraction, and was sent to the Laboratory

Temperature	FF	R_p	R_s	J_{sc}	V_{oc}	Efficiency
153 °C	21 %	319 Ω cm^2	121 Ω cm^2	5.0 mA/cm^2	420 mV	0.44 %
171 °C	36 %	470 Ω cm^2	33 Ω cm^2	6.2 mA/cm^2	330 mV	0.76 %
183 °C	43 %	455 Ω cm^2	20 Ω cm^2	5.8 mA/cm^2	300 mV	0.75 %

Table IV.8 – $J(V)$ *characteristics of the three cells of the temperature series.*

of Electrical Engineering of Paris for a complete characterization (with coplanar contacts). The results were an abnormally low activation energy of 0.2 eV, a too high dark conductivity of $\sim 3 \times 10^{-4}$ S·cm^{-1} and a too high $\mu_e \tau_e$ product of 2×10^{-4} cm^2 V^{-1} (flux of 10^{14} cm^{-2} s^{-1}), which is very surprising considering the low oxygen concentration of 1×10^{19} cm^{-3} found by SIMS for this condition. The other values were a conductivity prefactor of 0.81 S·cm^{-1} and a conductivity under illumination of $\sim 7.8 \times 10^{-4}$ S·cm^{-1}. The diffusion length is 115 nm, obtained with a flux of 10^{17} photons·cm^{-2}·s^{-1} at a wavelength of 677 nm corresponding to a power density of ~ 30 mW·cm^{-2}. The co-deposited cell (Structure : textured ZnO / p-doped layer / no ARCAM buffer layer / no plasma treatment in ATOS / intrinsic layer / H$_2$ treatment in ARCAM / n-doped layer / silver contacts) had the following $J(V)$ characteristics : FF of 52 %, R_p of 512 Ω cm^2, R_s of 13 Ω cm^2, J_{sc} of 5.3 mA/cm^2, V_{oc} of 285 mV and an efficiency of 0.78 %.

As a conclusion on the impact of the deposition temperature, the main surprising result is that we can obtain a crystallized material down to a temperature of ~ 150 °C at a high rate of ~ 12 Å/s, as proven by ellipsometry and Raman spectroscopy. Despite this interesting success, lowering the temperature did not help to enhance the cell performance. This series has been carried out after the installation of the load-lock and the oxygen concentration of the condition at ~ 180 °C has later been measured by SIMS (Section 4.4.3 page 173) and found to be satisfactory (1.1×10^{19} cm^{-1}), so that the limitation of the cells has to be found elsewhere.

Epitaxy at 10 Å/s

In addition to the glass and the ZnO substrates, pieces of monocrystalline silicon were also clamped to the substrate holder during these depositions and this brief section is dedicated to an interesting result (Figure IV.41). Indeed, unlike any other film grown in ATOS, the one at 189 °C shows epitaxy and the appearance of large grains. Fitting the film with the dielectric function of monocrystalline silicon results in a satisfactory figure of merit of 1.3 : The 754 nm thick bulk has 100 % of *monocrystalline* Si and the 68 nm thick interface layer consists of 96 % of monocrystalline Si, 2 % of large grain µc-Si and 2 % of void.

The films have also been carefully scratched from their c-Si substrate to characterize the flakes by Raman spectroscopy. It confirms that the sample grown at 189 °C is very particular : it presents a very sharp and intense Transverse Optical (TO) peak of crystalline silicon at 519.5 cm^{-1} with a Full Width at Half Maximum (FWHM) of ~ 4.6 cm^{-1}. The three other reference samples have microcrystalline spectra with crystalline peaks shifted in the range $507 - 515$ cm^{-1} and with FWHM ~ 16 cm^{-1}.

Around one year after their deposition, the chemical composition of this sample grown at 189 °C has been compared to the thinner sample grown at 195 °C by SIMS measurements. No tremendous variations have been found between the two films. The former seems dense and only its surface (50 nm) has been contaminated during the long stay at air. It has

$C_O = 1.7 \times 10^{19}\,\text{cm}^{-3}$, $C_C = 1.6 \times 10^{19}\,\text{cm}^{-3}$ and an atomic concentration of H of $\sim 10\,\%$. The latter is more affected by contaminations from the atmosphere and has $C_O = 3.0 \times 10^{19}\,\text{cm}^{-3}$, $C_C = 4.9 \times 10^{19}\,\text{cm}^{-3}$ and an atomic concentration of H of $\sim 13\,\%$.
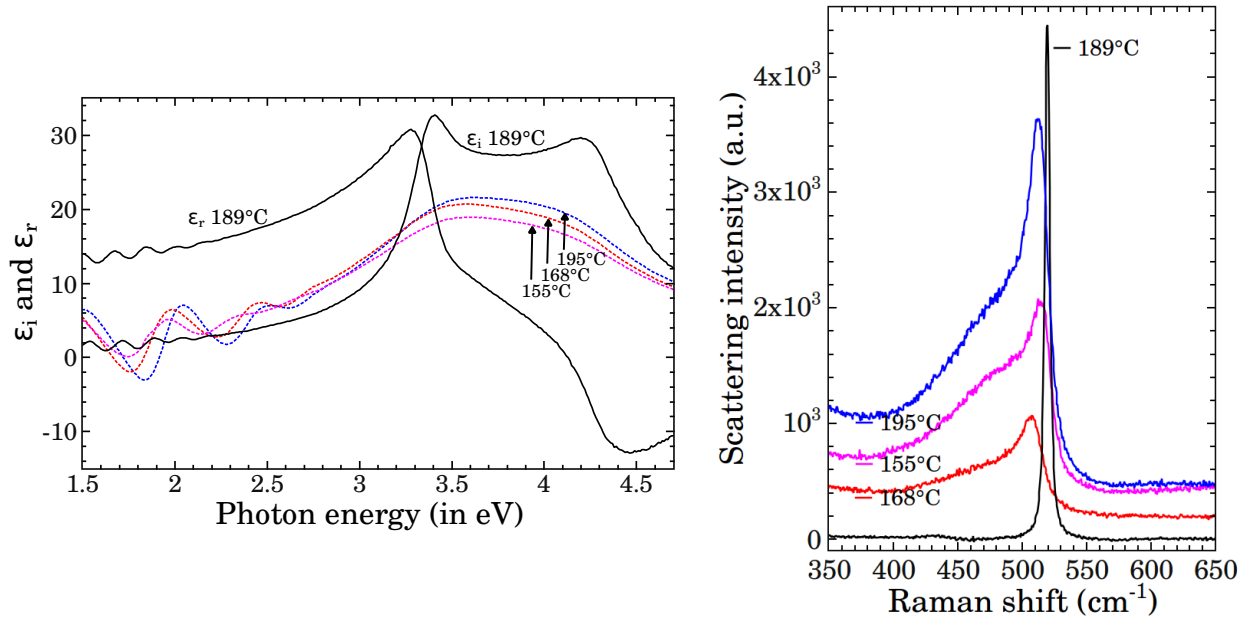

Figure IV.41 – *Left graph : Real and imaginary parts of the dielectric function of the $\sim 1\,\mu m$ thick film at 189°C (solid lines) compared to the imaginary parts of the dielectric functions of three other films of less than 300 nm grown at low temperatures (dashed lines). None of the c-Si substrates have been cleaned with HF so they all have a native oxide layer. Right graph : Raman spectra of flakes scratched from the c-Si substrates of the four same samples.*

3.8   Series in microwave power

The effect of this parameter was explored after the installation of the load-lock. The microwave (MW) power was varied from the usual 1.5 kW down to 0.55 kW (split on seven antennas). Four samples of ~ 300 nm and two samples of $\sim 1\,\mu m$ were deposited. The fixed conditions were a flow rate of pure silane of 42 sccm, a gas pressure of 9 mTorr, a plasma pressure of ~ 5.3 mTorr, a glass surface temperature of $\sim 230\,°C$ and an RF power of ~ 67 W.

This fixed RF power resulted in a DC bias voltage varying from -28 V to -51 V from 1.5 kW to 0.55 kW, which can be explained by the reduced electron density at lower MW powers. Furthermore, we can conclude from the evolution of the plasma emission showed in Figure IV.42 that the electron temperature also decreases with the MW power. Indeed, taking the ratio of the intensities of the Si line at 288.2 nm and of the SiH band around 414 nm allows to get rid of the dependence in the electron density. Thus, it can be used as a qualitative indicator of the electron temperature, at least if we suppose that the production of excited Si and SiH radicals mainly takes place directly from SiH_4. Indeed, in this case, the energy threshold for the production of excited Si is greater than the one for excited SiH.

Lowering the MW power, we can observe a transition from a highly crystallized material to an amorphous material in Figure IV.43. When using the usual three layer model to fit the spectrum at 0.55 kW, the figure of merit χ^2 cannot be smaller than 7.5 while a two layer model using a Tauc-Lorentz function to fit the amorphous component results in $\chi^2 = 1.7$. Thus, the graph shows $F_c = 0\,\%$ and $F_a = 100\,\%$ at 0.55 kW.
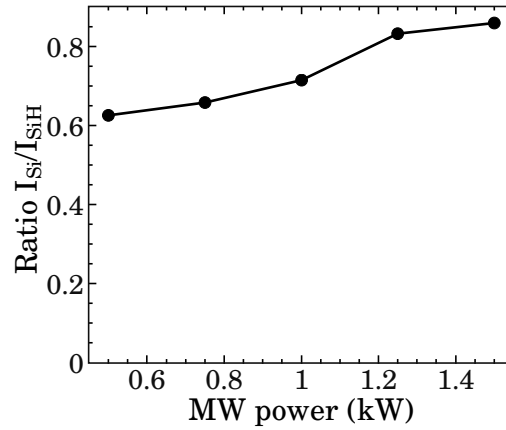
Figure IV.42 – *Ratio of the Si and SiH line intensities as a function of the MW power.*
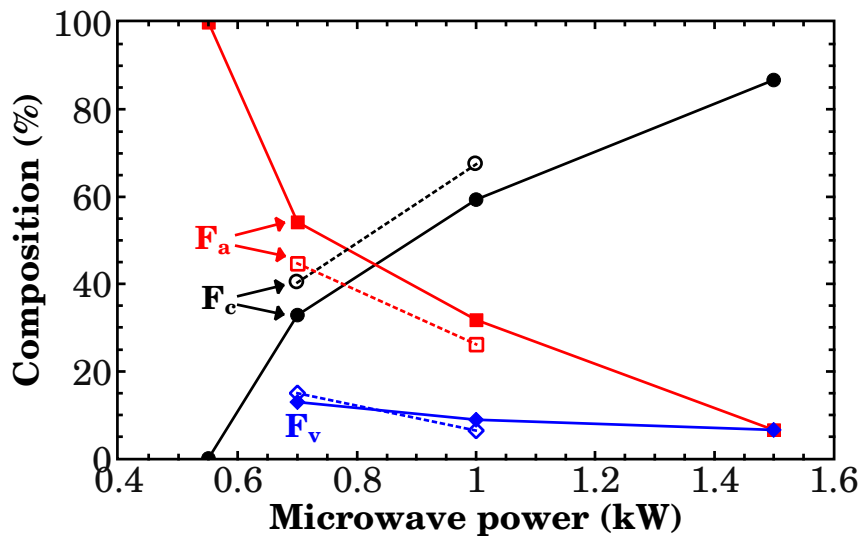

Figure IV.43 – *Composition of the bulk of the ellipsometry best fits as a function of the microwave power. The solid lines and filled symbols are for the 300 nm films, and the broken lines and open symbols are for the 1 μm films.*

The 1 μm thick films aimed at checking the evolution of the material properties with thickness. Indeed, the goal was to find conditions where it stays moderately crystallized throughout a thickness of 1 μm that will be used for the cells. To fit the thick films on glass, we used a three layer model, but with a sub-surface layer : surface layer / sub-surface layer / bulk / glass sample / void. Indeed, since the sensitivity goes down from the surface to the substrate, such a model is more adapted for thick films than a structure with an incubation layer.

At 0.7 kW, the crystalline fraction of the bulk evolves from 33 % to 40 % from 310 nm to 970 nm. At 1 kW, it evolves from 59 % to 68 % from 320 nm to 970 nm. Judging from these ellipsometry models, these sets of deposition conditions seem well adapted to grow materials which stay at the transition between amorphous and microcrystalline, even for 1 μm layers. What is more, the large (15 %) void fraction of the 1 μm film at 0.7 kW is a negative point while the value of 6 % at 1 kW is satisfactory.

The Raman spectra shown in Figure IV.44 bring slightly different results as compared to ellipsometry. Indeed, the crystalline component clearly increases from ∼300 nm to ∼1 μm.
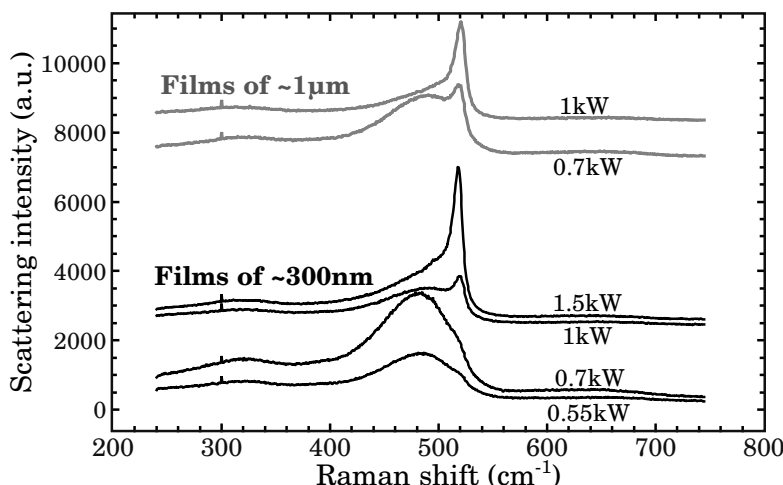
Figure IV.44 – *Superposition of the Raman spectra as a function of the MW power (curves shifted for clarity).*

This can be at least partially explained by the fact that the absorption of the red laser preferentially takes place close to the surface, which is probably more crystallized in the thick samples. (For the 0.55 kW spectrum, the little hump corresponding to a crystalline component is due to the crystallization by the laser and is not seen at lower magnification.)

The deposition rate does not increase very significantly with the MW power : from $\sim 12\,\text{Å/s}$ at 0.55 kW to $\sim 13\,\text{Å/s}$ at 1.5 kW. This means that most probably, silane is already completely dissociated at 0.55 kW. Furthermore, the crystalline fraction evolves from 0 % to 87 % at almost constant deposition rate just by increasing the MW power. This also demonstrates that it is not necessary to reduce the deposition rate to crystallize the material with the MDECR technology and that modifying the chemical composition of the plasma (even as "simple" as a pure silane gas) can have a striking impact on the material properties. Most probably, what takes place at greater microwave powers is that the hydrogen and silane molecules are further dissociated, thus increasing the atomic hydrogen flux on the growing surface.

In accordance with the strong changes of crystalline fractions, the Atomic Force Microscopy (AFM) images of the films surface show unique new properties. Indeed, it can be seen in Figure IV.45 that at MW powers lower than 1.5 kW, the crystallized grains are packed in larger "cauliflower-like" structures while they are *always* homogeneously distributed at the maximum power of 1.5 kW. But these structures can probably not be called "columns". In particular, the formation of column boundaries should affect the transport parallel to the surface and result in conductivity prefactors of the order of magnitude of $1\,\text{S·cm}^{-1}$ [76] while we found higher values (see Table IV.9). Also, the AFM image at 0.55 kW shows "grains" while we know from ellipsometry and Raman spectroscopy that the film is completely amorphous, which reminds us that the surface topography can be misleading. Figure IV.46 sums up the root-mean-square roughness values. The fact that the result at 0.7 kW depends on the scan size is due to the presence of bubbles for this film, as seen by naked eye and revealed by a $10\,\mu\text{m} \times 10\,\mu\text{m}$ image (Figure IV.47). Nonetheless, the 9.5 nm rms roughness at 0.7 kW for a scan area of $1\,\mu\text{m} \times 1\,\mu\text{m}$ is still valid. This value corresponds to a really large roughness. For example, we can compare it to the maximum one of the first bias series (page 110) for the same film thickness and AFM scan area, which was only of 2.3 nm.
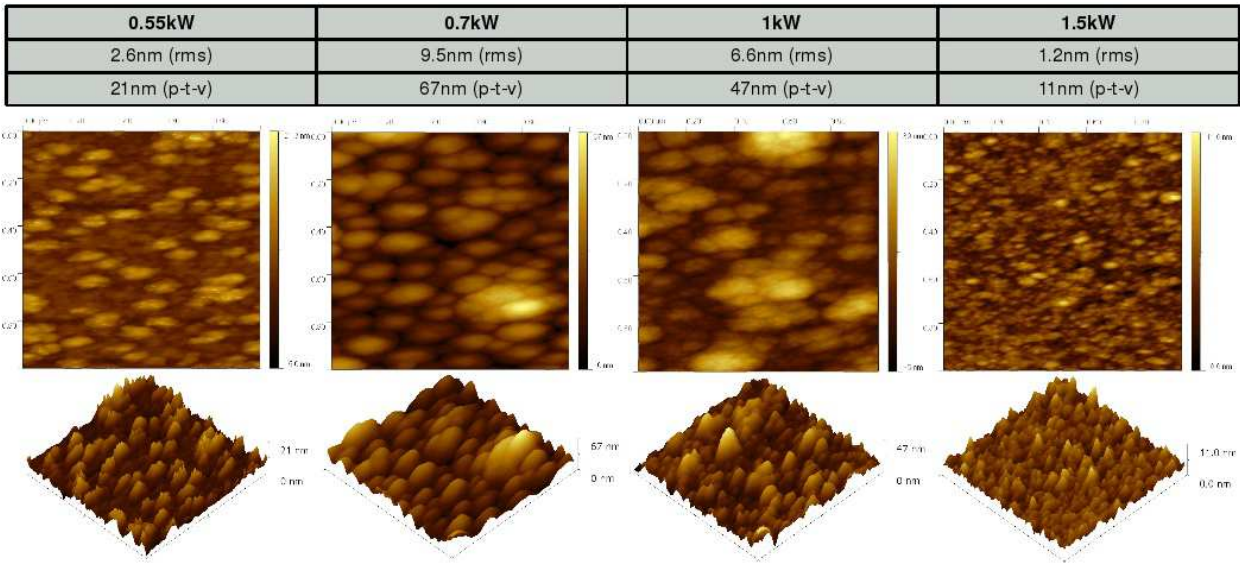
0.55kW	0.7kW	1kW	1.5kW
2.6nm (rms)	9.5nm (rms)	6.6nm (rms)	1.2nm (rms)
21nm (p-t-v)	67nm (p-t-v)	47nm (p-t-v)	11nm (p-t-v)

Figure IV.45 – *AFM results for the films of 300 nm with a scan area of 1 μm × 1 μm. The table on the top sums up the root-mean-square (rms) and peak-to-valley (p-t-v) roughness values. The first row of images are 2-dimensional top views and the second row, 3-dimensional views.*
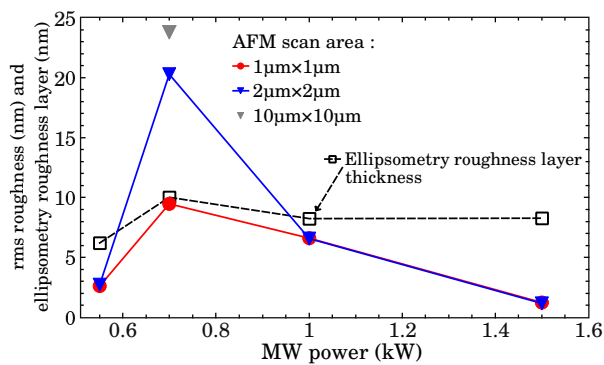

Figure IV.46 – *Comparison of the roughnesses of the 300 nm thick films obtained by AFM (root-mean-square roughness for different scan areas) and obtained by ellipsometry (thickness of the top layer).*

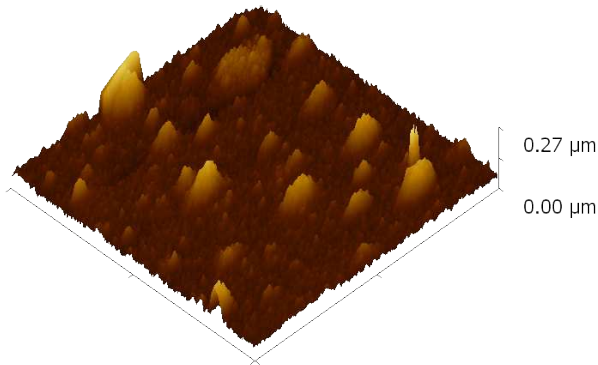Figure IV.47 – *3-dimensional image of the 300 nm thick sample at 0.7 kW with a large scan area of 10 μm × 10 μm to reveal the presence of bubbles. The rms roughness is 23.8 nm and the peak-to-valley roughness is 270 nm (similar to the film thickness).*
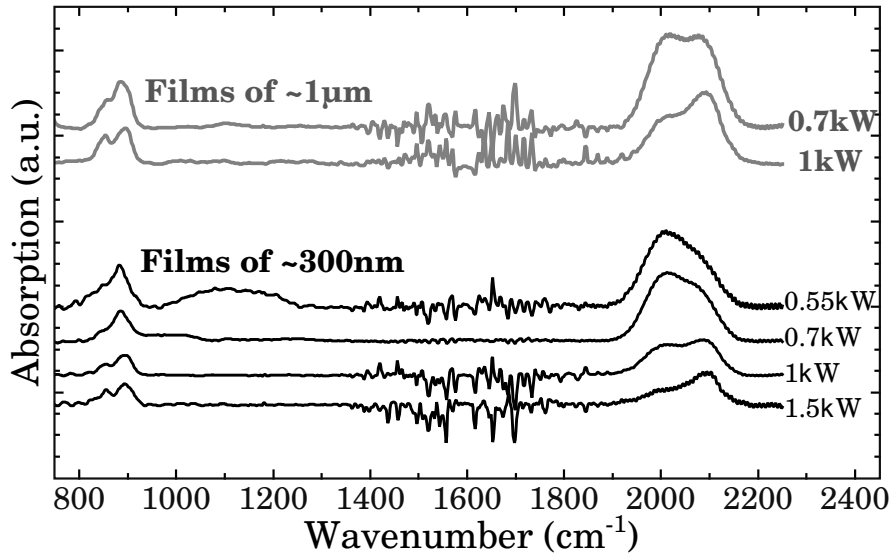
138

Figure IV.48 – *FTIR spectra as a function of MW power (curves shifted for clarity).*

The infra-red absorption spectra of these films are presented in Figure IV.48. As expected during the amorphous to microcrystalline transition, the concentration of incorporated hydrogen globally decreases when the MW power is increased as qualitatively indicated by the total area under the hydrogen-related peaks. Lowering the MW power has a strong effect on the Si–H streching modes : the $2000\,cm^{-1}$ mode dominates the one at $2100\,cm^{-1}$ at lower powers, due to less crystallized films (similar evolution can be seen in [55], in Figure 4 of [88] and Figure 3 of [38]).

The H_2 exodiffusion profiles of the samples are shown in Figure IV.49. As a first general remark, we see an unexpected absence of signal below $350\,°C$. In the first series of bias (MW power used : $1.5\,kW$), this feature had only been found for the sample deposited at the highest ion bombardement energy (Section 3.5.4 page 114). The $0.7\,kW$ condition appears to be very particular : The huge hydrogen content found by the exodiffusion technique fits with the high void fractions found by ellipsometry ($13\,\%$ at $300\,nm$ and $15\,\%$ at $1\,\mu m$).

A higher total H concentration was expected at low MW powers, the material becoming more amorphous. Furthermore, the different curve shapes at $300\,nm$ and $1\,\mu m$ for a MW power of $1\,kW$ can be explained by the phenomenon of diffusion through the thicker layer which delays the exit of hydrogen and consequently shifts the peaks at higher temperatures. We can notice that they have close total hydrogen concentrations.

The electrical properties of the two samples of $1\,\mu m$ have been measured at the Laboratory of Electrical Engineering of Paris (with coplanar contacts). The results can be seen in Table IV.9 and in Figure IV.50. The lower activation energy and higher dark conductivity for the sample at $1\,kW$ could be explained by the greater sensitivity to oxygen for the more crystallized film, although their oxygen contamination level should be low with the load-lock. The low dark conductivity of the $0.7\,kW$ sample (in the $10^{-8}\,S{\cdot}cm^{-1}$ range while our "standard" samples at $1.5\,kW$ are always in the $10^{-6}\,S{\cdot}cm^{-1}$ range) clearly indicates it is close to the amorphous/microcrystalline transition [63]. The exciting result of these measurements is the very high diffusion length values of $225\,nm$ and $250\,nm$. They have been obtained by the technique of steady-state photocarrier grating (SSPG) with a flux of $10^{17}\,photons{\cdot}cm^{-2}{\cdot}s^{-1}$ at a wavelength of $677\,nm$ corresponding to a power of $\sim 30\,mW{\cdot}cm^2$.
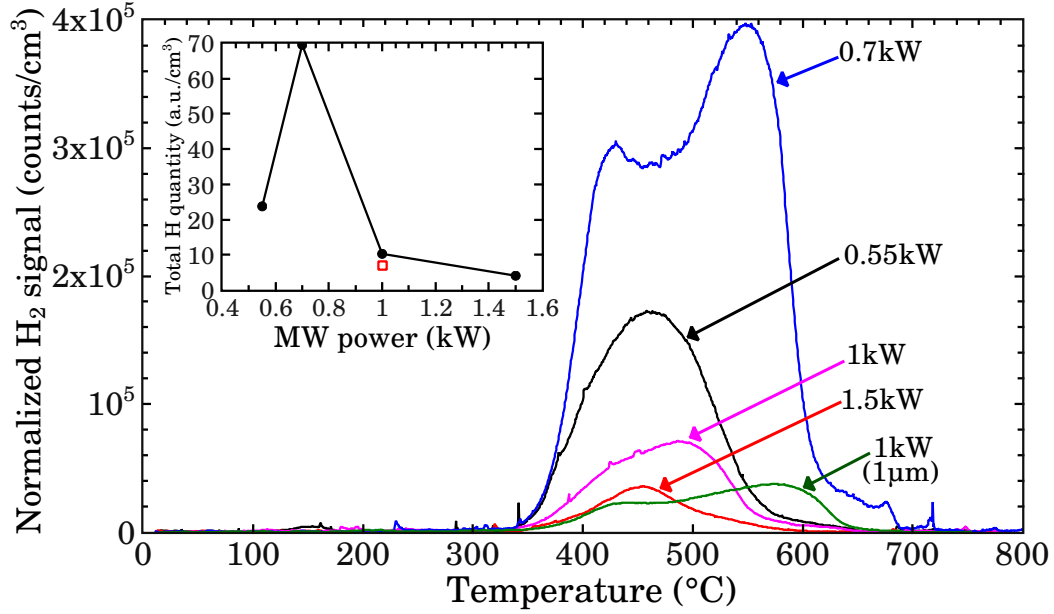
Figure IV.49 – *Exodiffusion spectra as a function of the MW power (films of ∼ 300 nm unless otherwise indicated). The inset shows the total areas under the curves, which represent the total hydrogen contents of the films per volume unit : the open symbol is the 1 μm film.*

MW power	$F_{c\ bulk}$	E_a	σ_d	σ_0	σ_{photo}	σ_{photo}/σ_d	$\mu_e \tau_e$	$\mathbf{L_d}$
0.7 kW	40 %	0.54 eV	5.4×10^{-8} S·cm^{-1}	57 S·cm^{-1}	7.0×10^{-6} S·cm^{-1}	∼ 130	4.5×10^{-6} cm^2 V^{-1}	**250 nm**
1 kW	68 %	0.35 eV	1.6×10^{-5} S·cm^{-1}	14 S·cm^{-1}	1.0×10^{-4} S·cm^{-1}	∼ 6.5	3.2×10^{-6} cm^2 V^{-1}	**225 nm**

Table IV.9 – *Impact of the MW power on the electrical properties of the films. The columns are : the bulk crystalline fraction, the activation energy, the dark conductivity, the conductivity prefactor, the photoconductivity, the photosensitivity, the electron mobility-lifetime product and the hole diffusion length.*
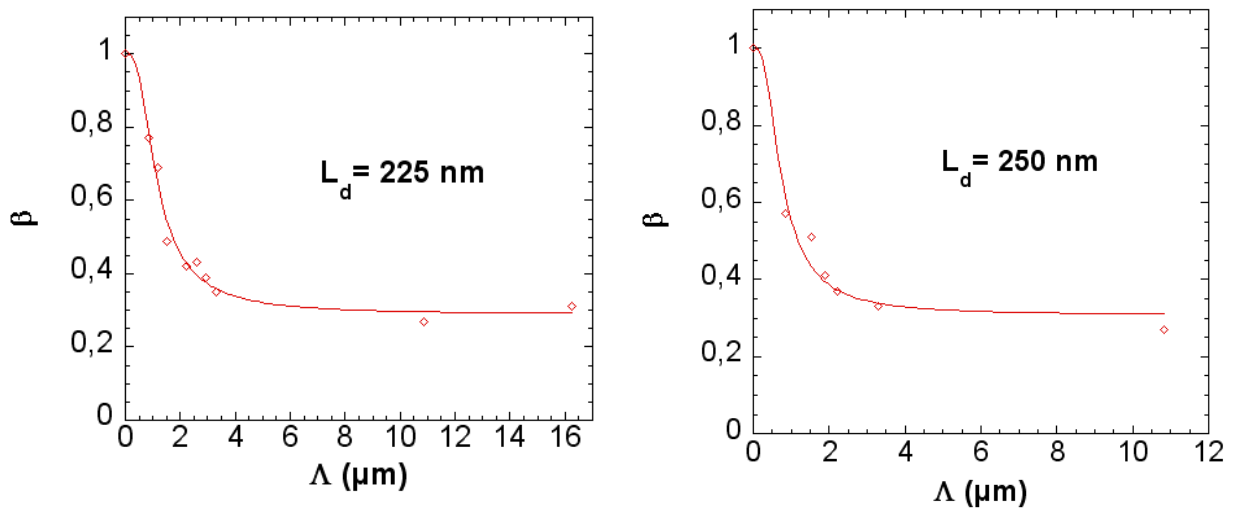

Figure IV.50 – *Steady-state photocarrier grating (SSPG) results : The points are the experimental data and the lines are the fits to obtain the diffusion length L_d. β is the ratio of the currents with and without interferences and Λ is the grating period.*

The fits of the experimental data to extract de diffusion length values are shown in Figure IV.50 and are explained in the litterature [89, 54] and in Section 8 page 46. The values of the other fitting parameter Φ are 0.36 and 0.35 respectively. The high values of the diffusion lenghts can be explained by a better passivation of defective grain boundaries by the amorphous tissue as compared to the highly crystallized samples obtained at the maximum MW power of 1.5 kW. These improved values are now close from the highest published values (e.g. 300 nm in [24, 25] and 320 nm $\pm$ 10 nm in [17]). The density of band gap states could unfortunately not be determined by modulated photocurrent method (MPC) for these samples due to some technical issues with the experimental setup at that time. However, the high value of the photoconductivity of the 1 kW sample, along with its high diffusion length, can be taken as a proof of its excellent transport properties.

Two cells have been processed, with 0.7 kW and 1 kW of MW power. Their structure is : textured ZnO substrate / p-doped µc-Si:H layer (ARCAM) / $\sim$ 120 nm intrinsic µc-Si:H buffer layer (ARCAM) / H_2 treatment (ATOS) / 1 µm thick µc-Si:H layer (ATOS) / n-doped a-Si:H layer (ARCAM) / H_2 treatment (ARCAM) / silver back contacts. Their performance is presented in Figure IV.51 and Table IV.10. The spectral responses show the usual very low efficiency in the red and the only difference between the two cells is the enhanced response in the blue at 0 V for 0.7 kW. Yet, these are the highest values of current density ever obtained. The other parameters being very poor, this does not result in better efficiencies.
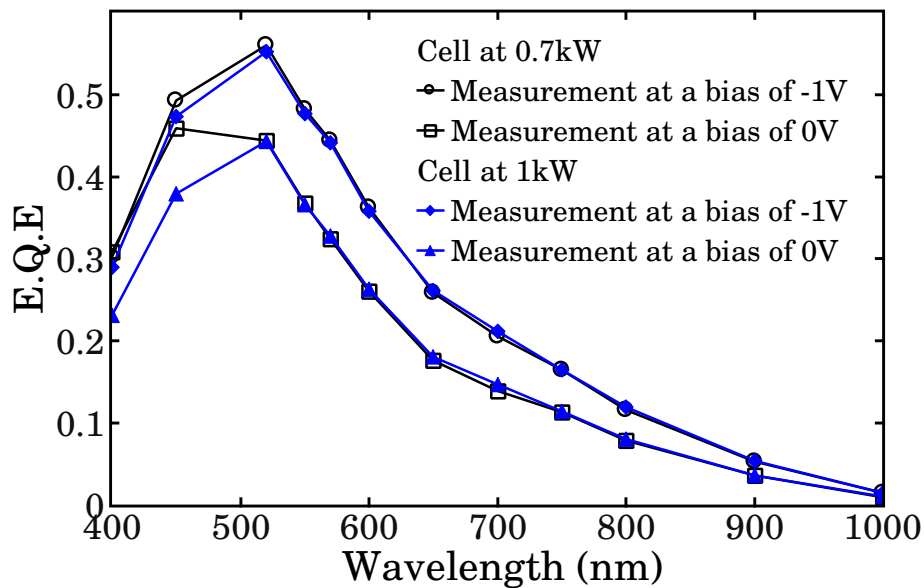
Figure IV.51 – *External Quantum Efficiencies (EQE) as a function of the MW power.*

MW power	FF	R_p	R_s	J_{sc}	V_{oc}	Efficiency
0.7 kW	50 %	398 Ω cm^2	11 Ω cm^2	7.3 mA/cm^2	280 mV	1.0 %
1 kW	49 %	426 Ω cm^2	11 Ω cm^2	7.0 mA/cm^2	260 mV	0.9 %

Table IV.10 – *J(V) characteristics as a function of the MW power.*

Discussion and conclusion of the series in microwave power

Several of the diagnostics used revealed problems for the 0.7 kW condition : the F_v in the bulk of the 1 µm thick film is 15 % and the hydrogen concentration evaluated by exodiffusion is by far the highest of the series. Despite these indications, the diffusion length is the highest ever obtained and the cell at 0.7 kW is slightly better than the one at 1 kW. Once again, this illustrates the absolute necessity to implement multiple characterization techniques.

The improvement of the electrical properties, and in particular of the diffusion length, at the amorphous/microcrystalline transition has been reported by other groups. In [89], the diffusion lengths of µc-Si deposited by Hot Wire CVD reach a maximum of 271 nm at a Raman crystalline fraction around 50 % and decrease for higher crystalline fractions. In [54], the maximum of L_d for Very High Frequency PECVD µc-Si is 200 nm at the transition between highly crystallized and amorphous material, obtained by adjusting the silane concentration to 5 %, which also fits with their highest efficiencies in solar cells [49].

$\mathbf{L_d}$	T_{pyro}	Gases	MW power	**Efficiency**	Page of the section
40 nm	$\sim 230\,°C$	$SiH_4 = 55\,sccm$	1.5 kW	**0.8 − 1.1 %**	100
50 − 110 nm	$\sim 275\,°C$	$SiH_4 = 55\,sccm$	1.5 kW	**⩽ 0.5 %**	102
105 nm	$\sim 275\,°C$	$SiH_4/SiF_4 = 55/1\,sccm$	1.5 kW	**⩽ 0.5 %**	102
115 nm	$\sim 190\,°C$	$SiH_4 = 42\,sccm$	1.5 kW	**0.8 %**	130
225 nm	$\sim 230\,°C$	$SiH_4 = 42\,sccm$	1 kW	**0.9 %**	135
250 nm	$\sim 230\,°C$	$SiH_4 = 42\,sccm$	0.7 kW	**1.0 %**	135

Table IV.11 – *Comparison of the diffusion length values (first column) with the efficiencies of the cells made with the corresponding material (fifth column) as a function of the main varied deposition parameters (second to fourth column). Note that the structures of the cells (buffer layer, interface treatments) are not exactly the same so that their efficiencies can only be used as an indicative comparison.*

Unfortunately, for the MDECR material, we cannot see *any* impact of the successful improvement of the diffusion length values achieved over time on the cell performance, as clearly shown in Table IV.11. One has to remember that these SSPG measurements are made in coplanar configuration and thus, characterize the transport properties parallel to the film. Moreover, the material grown on glass and on a ZnO/p-doped µc-Si/buffer µc-Si stack may be different. Nonetheless, such a complete decorrelation seems to indicate that the limitation of the cell performance comes from the cell processing itself. The possible causes could be :

- the oxidation of the interfaces during the transfers from one reactor to another,
- the degradation of the p-doped layer and/or of the TCO by the aggressive and hydrogen-rich MDECR plasma,
- the elevated deposition temperature detrimental for the device,
- or the presence of a thin amorphous incubation layer which could affect the cells but not the SSPG values.

All these potential sources of limitation will be studied in detail in the next part of this chapter (Section 4 page 145).

Nevertheless, the interesting point of this series is that the microwave power has a strong influence on the film properties (i.e. crystalline fraction, hydrogen concentration, hydrogen

configuration, surface topology, crystallite organization and electrical properties), thus enabling us to explore new types of materials. Unfortunately, the high diffusion lengths did not lead to improved cells. *Once again, a radical change in the MDECR material does not necessarily have an impact on the cell quality.*

3.9   Conclusion on the optimization of the deposition conditions of the microcrystalline films and solar cells

In this part, we have explored the effects of the most important deposition parameters. Holding all the other deposition conditions constant and varying only one parameter enables to isolate its impact. Thus, it is a necessary first step in our experimental field of research. But this approach is also limited. Indeed, the interactions between the numerous deposition parameters are very complex and the trends found for one set of deposition conditions are not necessarily universally true in all the parameter space (see for example the results of the two series in bias pages 110 and 128).

We have studied the effects of the gas composition (pure silane or with hydrogen, argon and/or silicon tetrafluoride added), of the ion bombardment energy, of the substrate temperature and of the microwave power. Despite clear improvements of the material properties, all the cells showed quite poor characteristics, in particular, very low response in the red.

We can remind here some of the most important results obtained during these series : The addition of a small flow rate of SiF_4 unfortunately did not help to solve the problem of too high oxygen concentrations before the installation of the load-lock. The ion bombardment has been seen to increase the intra-grain defect densities (lower TRMC local mobilities). The MDECR microcrystalline films often present high hydrogen concentrations but the film density has been successfully improved (as indicated by the ellipsometry void fractions of $\sim 15\,\%$ in the first films, reduced to normal values of a few percents). At low microwave powers, the materials with lower crystalline fractions showed very high diffusion lengths (up to $250\,\mathrm{nm}$), probably due to better grain passivation by the amorphous component.

The material quality can still be improved. The presence of large grains have never been detected on the ellipsometric spectra and most of the time (except for low microwave powers), no columnar organization of the crystallites can be seen on AFM images. The TRMC mobilities and lifetimes are also lower than the device quality values obtained in the other reactors of the laboratory. The photosensitivity is often very limited and the current densities of our MDECR cells are always $\leqslant 7.3\,\mathrm{mA/cm^2}$. Finally, another concern was the oxygen signal at the Si/ZnO interface seen on the SIMS profiles, and the risk of diffusion from the ZnO will be ruled out in the next part.

Other parameters have been studied by colleagues, such as the antennas-substrate distance and the pressure (varied in the range $2-35\,\mathrm{mTorr}$). The idea was to increase the secondary reactions in the gas phase in order to favor the formation of low sticking coefficient radicals (SiH_3). But once again, the outcome of these series was that the MDECR technology does not exhibit a very strong dependence on these parameters and that it did not help to improve the cell performance.

Scanning all the combinations of deposition parameters is of course impossible to do. In our low pressure reactor, due to inefficient thermal contact between the heated substrate holder

and the substrate, the very long heating and cooling times did not allow us to deposit more than three samples per day. As a consequence, it was necessary for us to adopt a strategy based on detailed characterizations of our samples with a large set of diagnostics.

Several diagnostics have been compared : The crystalline fraction can be obtained from ellipsometry and from Raman spectroscopy. The hydrogen concentrations can be characterized from ellipsometry, SIMS and exodiffusion. The crystallite sizes can be obtained from XRD and seen on the AFM images. The surface roughness can be deduced from ellipsometry models and from AFM images.

These analyses led to important conclusions. First, the MDECR process is not always very "reactive", i.e. it seems that some parameters only have a reduced effect on the material properties and in particular on the crystalline fraction (e.g. the argon dilution or the surprisingly low influence of the temperature on the crystalline fraction). Then, every diagnostic suffers from some artefacts or limitations or can sometimes be difficult to interpret. For example, Raman spectroscopy cannot indicate if a film is very porous or not and "normal" values of the activation energy (i.e. around half the band gap energy) and of the dark conductivity (i.e. around $1 \times 10^{-6}\,\mathrm{S \cdot cm^{-1}}$) do not guarantee low n-type donor concentrations (oxygen and nitrogen). It is therefore necessary to implement as many characterization techniques as possible in order to be able to determine where the optimum is. Finally, there seems to be a decorrelation between the successive improvements of the material properties achieved over time and the solar cell efficiencies, which stayed below $2\,\%$.

In the last part of this chapter, we will keep on using all these diagnostics in order to focus on the potential problems of the material and cell quality.

4   Investigations into the limitations of the microcrystalline material and solar cells

This part presents our detailed studies on all the potential origins of the low cell efficiencies. We will successively focus our attention on the design of the reactor, the characteristics of the plasma, the quality of the material and the potential problems during the processing of the devices.

4.1   Design of the reactor : Can oxygen come from the water cooling system of the antennas ?

The abnormally high concentrations of oxygen incorporated in the material for many of our deposition conditions were a great concern before the installation of the load-lock. In this section, we will expose how we checked a potential weak point of our reactor design.

Cold water is circulating inside the magnets of the microwave antennas in order to prevent them from heating too much. The water cooling system is only isolated from the vacuum chamber by a toroidal joint pressed when the magnet is screwed (see Figure IV.52).
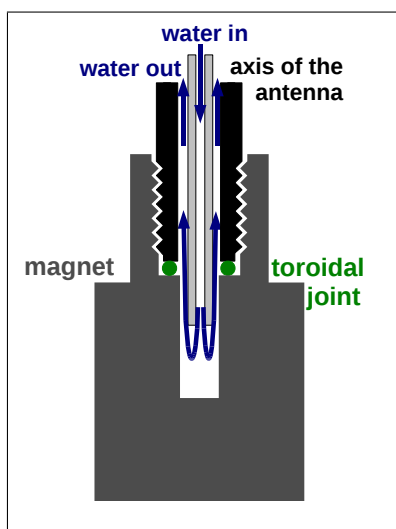

Figure IV.52 – *Schematic view of the end of an antenna with the central axis, the magnet and the water cooling system sealed by the toroidal joint.*

This design could have been a weak point resulting in water being introduced in the vessel. To rule out this risk, we carried out two tests.

The first test consisted of mass spectroscopy measurements : we connected a mass spectrometer with a differential pumping to the vessel of the reactor. The vessel of the mass spectrometer was heated in order to degas it to avoid misleading signals of hydrogen or water that would interfere with the real signals coming from the vessel of ATOS. The signal of water was found to stay constant (H_2O partial pressure of $\sim 2 \times 10^{-9}$ Torr) during a silane plasma of 14 minutes (typically corresponding to a 1 μm thick deposition) in the usual conditions, i.e. at a high microwave (MW) power of 1.5 kW and a substrate holder surface temperature of 350 °C. Thus, even though the magnets are heated during such a long plasma, no water release is detected.

The second test consisted in an individual leak detection for each antenna. To do so, each antenna was put under a pressure of ~ 3 bars of Helium. The two antennas which were found to leak under these conditions have been fixed and checked again until we were sure that the water cooling system of each antenna was vacuum tight. (Note that this test could only be performed without any heating in order not to damage the magnets in the absence of water flowing.)

After these careful tests, we concluded that there was no risk of water leaking from the cooling system of the antennas.

As a conclusion, the exact origin of the oxygen contaminations in our films remained unclear. We can remind here that gas purifiers were installed on the H_2 and the SiH_4 lines in November 2008 and that we systematically let the gases flow during a few minutes before starting the depositions but these precautions did not help to improve the cell performance. The large pressure increase observed during static vacuum tests with heating also remained unexplained (see Section 6.1 page 74).

4.2   The incubation layer

4.2.1   Studies of the incubation layer in the reactor Domex

The formation of the incubation layer was studied at the very beginning of my PhD in the reactor Domex (see Section 4 page 66 for its description). We chose two sets of conditions which had been found to be in the microcrystalline regime and we varied the deposition times to obtain thicknesses ranging from 67 nm to 773 nm.

A group of 11 samples has been grown with a pure silane flow rate of 63 sccm and another group of 5 samples has been deposited with 50 sccm of pure silane. The plasma pressure was ~ 7 mTorr, the temperature of the substrate holder surface was $\sim 335\,°C$, six microwave applicators injected ~ 188 W each and the RF power of ~ 30 W gave a DC bias of $+30$ V. The substrates were small 1" $\times$ 1" glass substrates which were not glued to the substrate holder. To reach a higher substrate temperature necessary to crystallize the material, we applied the so-called "pre-heating procedure" described in the Section 4 page 66. This allowed us to start the depositions at a temperature of $\sim 270\,°C$, as indicated by the pyrometer (instead of the maximum $T_{pyrometer} \sim 230\,°C$ at the end of the heating phase).

Figure IV.53 compares the results obtained by Raman spectroscopy and spectroscopic ellipsometry. The crystalline fraction was estimated by Raman spectroscopy using a three Gaussian fit :

$$X_c = \frac{I_{500\,cm^{-1}} + I_{520\,cm^{-1}}}{I_{500\,cm^{-1}} + I_{520\,cm^{-1}} + 0.8\,I_{480\,cm^{-1}}} \tag{IV.1}$$

where I represents the integrated area of the peak at the indicated wavenumber.

One can see that the two films of ~ 200 nm of the 63 sccm series are very different, thus revealing problems of process reproducibility. The large number of samples still allows us to draw some trends : As expected, the films with a very short deposition time are completely amorphous. The two diagnostics indicate that the crystallization starts for thinner thicknesses for the 50 sccm condition. The material then becomes more crystallized with thickness, the 50 sccm condition leading to greater crystalline fractions. These results can be at least partially explained by a lower deposition rate for the reduced flow rate ($\sim 12.4\,\text{Å/s}$
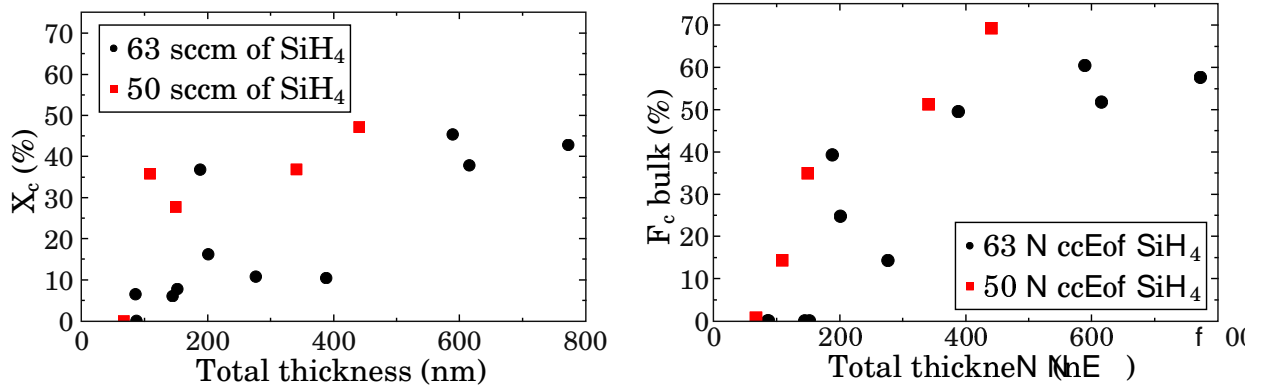
Figure IV.53 – *Crystalline fractions obtained by Raman spectroscopy (left graph) and by spectroscopic ellipsometry (rigth graph) as a function of the total thickness of the films of the two groups.*
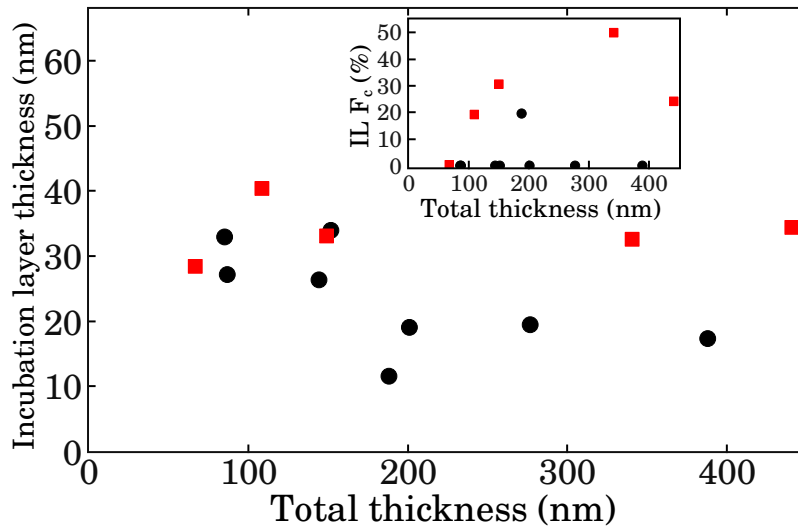

Figure IV.54 – *Thicknesses of the incubation layers (IL) from the ellipsometry fits. The inset shows the crystalline fractions (F_c) of the IL. The black points correspond to the 63 sccm samples and the red squares to the 50 sccm samples.*

and $\sim 16.5\,\text{Å/s}$). Furthermore, comparing the two graphs reveals us that this way of estimating the crystalline fraction from the Raman spectra gives lower values than our ellipsometry models most of the times.

The main goal of this series was initially to study the evolution of the incubation layer thickness with the deposition time. The material gets crystallized at the surface and subsurface of the growing film but we wanted to detect an evolution deeper, due to the diffusion of atomic hydrogen and/or to the plasma induced heating. It is difficult to really see a trend of a decrease of the incubation layer thickness during the deposition from the results of Figure IV.54. The analysis has been stopped at 450 nm because the sensitivity to the incubation layer (IL) for films thicker than that is not satisfactory anymore. The inset of the graph shows that while the IL is almost always completely amorphous for 63 sccm of silane, reducing the flow rate (and thus, the deposition rate) is an effective way to promote the early crystallization of the film. A solution to combine a crystallized incubation layer and a high deposition rate could be to start with 50 sccm and to switch at 63 sccm, after 300 nm for example.

Several cells have been deposited with these two conditions for the intrinsic layer and we will compare two of them which have the same structure :

- Glass substrate
- Textured ZnO
- Microcrystalline p-doped layer deposited in the reactor ARCAM ($\sim 20\,\mathrm{nm}$)
- Microcrystalline intrinsic layer deposited in the reactor ATOS ($\sim 1\,\mu\mathrm{m}$)
- Amorphous n-doped layer deposited in the reactor ARCAM ($\sim 20\,\mathrm{nm}$)
- Silver back contacts

The performance of the two cells are compared in Figure IV.55 and in Table IV.12. The spectral responses show the usual very low efficiency of the MDECR cells in the red part of the spectrum as well as a great enhancement under a negative bias of $-1\,\mathrm{V}$. The cell at 63 sccm has a higher efficiency, which is somewhat in contradiction with the result of the crystallized incubation layer at 50 sccm.
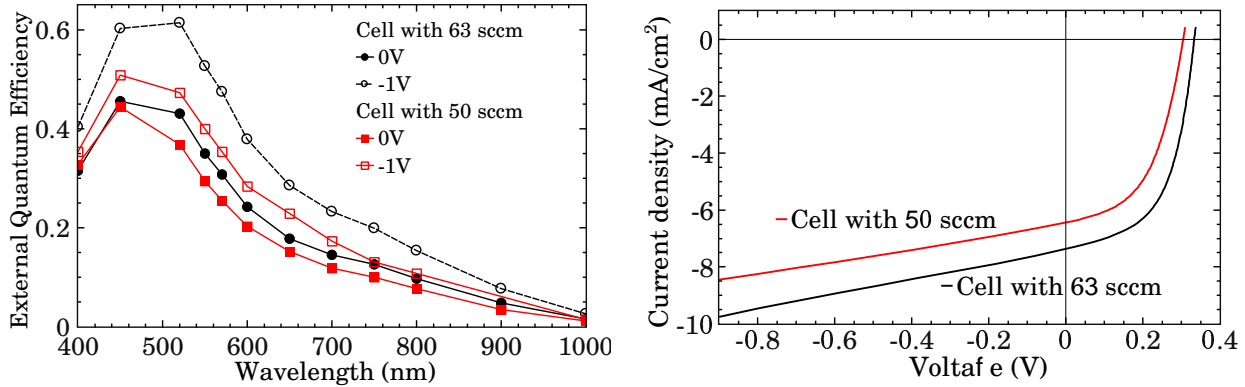

Figure IV.55 – *Spectral responses (left graph) and current–voltage curves (right graph) of the two cells after annealing.*

Silane flow rate	FF	R_s	R_s	J_{sc}	V_{oc}	Efficiency
63 sccm	55 %	$390\,\Omega\,\mathrm{cm}^2$	$7.8\,\Omega\,\mathrm{cm}^2$	$7.4\,\mathrm{mA/cm}^2$	$334\,\mathrm{mV}$	1.4 %
50 sccm	51 %	$470\,\Omega\,\mathrm{cm}^2$	$12\,\Omega\,\mathrm{cm}^2$	$6.4\,\mathrm{mA/cm}^2$	$305\,\mathrm{mV}$	0.99 %

Table IV.12 – *$J(V)$ characteristics of the two cells.*

As a conclusion, the samples of this series in the reactor Domex have been processed using the "pre-heating" procedure, which results in a not very well controlled initial temperature. This could explain the scattering of the Figures IV.53 and IV.54. Finally, after this preliminary study, we disassembled the reactor Domex to install the new MDECR reactor. Indeed, we wanted to be able to go at higher temperatures with the specially designed substrate holder of ATOS in order to try to crystallize the layers right from the beginning.

4.2.2   Transient regime in the plasma chemistry after ignition

Since an incubation layer was systematically seen on the ellipsometry models for the films on glass, we studied the plasma chemistry evolution after ignition to determine if a transient regime could be responsible for the growth of an initial less crystallized layer. To do so, this section reports the results of Optical Emission Spectroscopy (OES) measurements carried
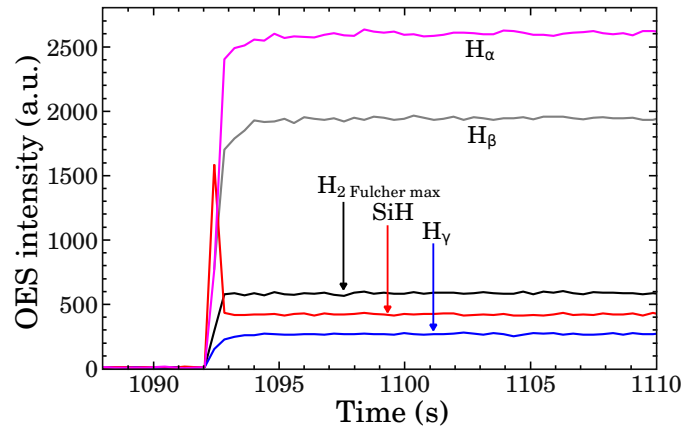
Figure IV.56 – *Blow-up on the evolution of the emission lines of H_α (656.5 nm), H_β (486.1 nm), H_γ (434 nm), SiH (415.2 nm) and of the highest peak of the Fulcher band $H_{2\,Fulcher\,max}$ (602.7 nm) just after plasma ignition.*

out in the reactor Domex. Their validity has also been later checked and confirmed by new measurements in the reactor ATOS (not shown here).

The spectrometer used (Model USB2000 from Ocean Optics with a CCD detector) allowed us to monitor the main emission lines of the pure SiH_4 plasma as a function of time with a resolution of 400 ms (integration time of 35 ms and one point every 400 ms).

The plasma conditions were exactly the same as the ones used in the previous section to study the incubation layer formation. We turned the plasma on and off several times to check the reproducibility. One of these "pulses" is shown in Figure IV.56.

The SiH line can be seen to have a peak before going down to its steady-state regime value. All the other lines increase monotonically. The time resolution of the spectrometer does not allow us to really study in detail the plasma dynamics after ignition, but we can see that no noteworthy changes take place after one second. This time corresponds to thicknesses of less than 20 Å and thus, these OES measurements established that the presence of an incubation layer (of typical thickness of 150 Å or more) in the MDECR films cannot be explained by the evolution of the plasma chemistry after ignition. This underlines a great difference between our MDECR reactor and an RF-CCP reactor having a volume of gas around the plasma region, where the equilibration time can be as long as 40 seconds [41]. These authors evidenced the link between the presence of an incubation layer in their films and the back diffusion in their process reactor. This explanation cannot be used to understand the formation of an incubation layer in our case.

4.2.3   Depositions without heating from the substrate holder

The heating element of the first substrate holder of the new ATOS reactor (see description in Section 5.3.1 page 72) unfortunately got broken after around six months. Since this element is welded inside a disk of the substrate holder, it was impossible to fix it.

This section also deals with the incubation layer and more precisely with the question : "Why does nucleation start ?" A possible answer could be that the plasma induced heating (see Section 6.2.1 page 76) helps the substrate to reach the high temperature to crystallize the material deposited at high rate. Here, we will explain in which conditions we established

that an increase of the substrate surface temperature is not necessary for the crystallization to start.

As a consequence of the heating system failure, we temporarily tried to deposit films without heating from the back, from the substrate holder. Instead, we carried out an argon or argon/hydrogen plasma before the deposition. A remarkable result is that with a sufficiently high RF bias of the substrate holder during this pre-heating plasma, we managed to obtain the typical glass substrate surface temperature of $\sim 230\,°C$, as indicated by the pyrometer. This temperature is normally obtained for a substrate holder surface temperature of around $350\,°C$. The typical conditions used for the pre-heating plasma were a high RF power of $70 - 200\,W$ resulting in voltage drops as high as $-80\,V$, flow rates of argon and hydrogen of $100\,sccm$, microwave powers of $1 - 1.5\,kW$, heating times between 20 and 40 minutes, and plasma pressures of $1 - 4\,mTorr$.

As far as thin ($\lesssim 300\,nm$) films on glass are concerned, some interesting results could be obtained. One sample, obtained from a mixture of SiH_4, Ar and H_2 (flow rates of 41, 100 and $100\,sccm$ respectively), seemed to be crystallized right from the beginning, without amorphous incubation layer. The film is thin enough ($\sim 209\,nm$) for ellipsometry to be sensitive to the interface and the best fit gave an interface layer of $13\,nm$ with $F_c = 77\,\%$ ($F_a = 23\,\%$). The bulk composition is $F_c = 81\,\%$, $F_a = 4\,\%$ and $F_v = 15\,\%$. We etched the sample during 60 seconds and re-measured it after : it was confirmed on the thinned ($\sim 144\,nm$) film that the interface layer is crystallized ($F_c = 93\,\%$). Unfortunately, two attempts to repeat this film failed. Indeed, the first problem of the depositions made during this period is that the heating procedure is not very reproducible. For example, one of the difficulties is that it takes a few minutes to stop the pre-heating plasma and to set the chosen conditions for the deposition (gas flow rates, adjustment of the gate valve in front of the turbo molecular pump controlling the gas pressure, microwave and RF power levels). In absence of ion bombardment during this short time period, the substrate surface temperature drops (see Figure IV.57).
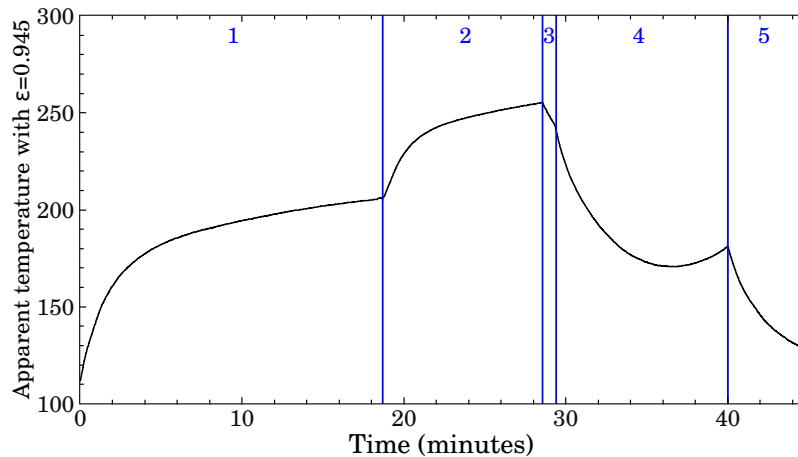

Figure IV.57 – *Temperature evolution recorded by the pyrometer during the deposition of the sample A080403a. The different steps of the process are : 1) First phase of heating with $100\,sccm$ of pure argon, $V_{bias} = -80\,V$ and $P_{MW} = 1\,kW$ 2) Second phase of heating with $100\,sccm$ of pure argon, $V_{bias} = -80\,V$ and $P_{MW} = 1.5\,kW$ 3) The heating plasma is stopped and the temperature drops while adjusting the new conditions for deposition 4) Deposition at $P_{MW} = 1.5\,kW$ and $V_{bias} = -15\,V$ 5) Plasma stopped.*

Figure IV.57 also shows a very interesting feature : Due to the absence of heating from

the back and to the reduced ion bombardment during the deposition as compared to the pre-heating phase, the temperature of the sample surface is measured to drop during the deposition. The film has been characterized by ellipsometry and the best model has an amorphous ($F_a = 98\%$) incubation layer of 20 nm and then a high crystalline fraction of 84 % in the bulk. This brings new insights for the understanding of the formation of the incubation layer because it suggests that the phenomenon of nucleation, of crystallization, takes place even if the temperature is decreasing.

The second problem of this procedure is that although low void fractions in the bulk can be obtained for thin ($\sim 200-300$ nm) films, the void fraction goes up again for thicker films, most probably due to the dropping temperature.

Finally, the third issue is that this pre-heating plasma damages the p or n layers of the substrates for p-i-n or n-i-p cells respectively. Some heating conditions led to the complete sputtering of a p-doped microcrystalline layer on glass and of an n-doped amorphous layer on SnO_2. We were even able to completely sputter a 120 nm layer of evaporated chromium on glass.

Attempts of pre-heating have also been carried out with mixtures of argon and hydrogen. We evidenced a phenomenon of chemical transport. For example, the Raman spectrum of an amorphous n-doped layer on SnO_2 showed a clear small crystalline peak around $520\,\mathrm{cm}^{-1}$ after a 34 minute heating plasma with $V_{bias} = -30$ V. On glass, amorphous silicon is seen to be chemically transported with the in-situ ellipsometer.

When cells are processed with this heating procedure, some have S-shaped $J(V)$ curves, probably due to defects induced by the heating treatment, and they very often show extremely low currents of less than $1\,\mathrm{mA/cm^2}$. In order to deposit the intrinsic layer of cells with this heating procedure, an optimum in the ion energy is to be found : if the bombardment is too energetic, the doped layer will be damaged or even sputtered, and if it is low, the crystalline fraction of the film will be small, due to a low temperature. What is more, the MDECR layers often exhibited "bubbles" measured with a microscope and a profilometer to be on the whole thickness of the 1 µm film and with diameters as large as several tens of microns.

Conclusion : To optimize one set of plasma parameters for deposition is already a very difficult problem. The optimization of the pre-heating plasma conditions increases tremendously the number of possible combinations. Although some exciting results have been obtained during this period, the whole procedure of heating by ion bombardment seems to be very difficult to adapt for cell deposition. As a consequence, we replaced the broken substrate holder by the one of an other MDECR reactor (described in Section 5.3.2 page 73).

4.3   Quality of the material

4.3.1   Metallic impurities

After having assembled the new ATOS reactor, one of our first tests has been to check for the presence of metallic impurities by Secondary Ion Mass Spectrometry measurements (SIMS, see page 41). We were concerned by the risk of contamination by aluminum, copper, iron, nickel or chromium in our films. Indeed, nickel and iron could for example come from the stainless steel covering the magnets of the antennas which are certainly heated by the very dense ECR plasma and could even be sputtered. The top plate of the first substrate holder

was in Inconel 600, an alloy containing more than 72 % of nickel, $14-17$ % of chromium and $6-10$ % of iron. What is more, the first metallic frame used to clamp the substrates was in aluminum. It was then replaced by another one in stainless steel. (Aluminum and copper are also present in a few stainless steel alloys.)

Detecting metals by the SIMS technique is carried out by bombarding the sample with a primary beam of negatively charged oxygen ions and by collecting the sputtered positively charged ions. It can be tricky to analyze the results due to the small concentrations involved and to the large masses of these species which give rise to a lot of possibilities of mass interferences. For example, a Si–Si$^+$ molecular ion can have masses ranging from 56 to 60 with all the combinations of the three isotopes of silicon (of masses 28, 29 and 30).

4.3.1.1   First sample

The first sample for SIMS consisted in the following stack of five layers :

- a-Si:H ; ~ 1000 Å ; $T_{\text{thermocouple surface}} = 250\,^{\circ}\text{C}$
- a-Si:H ; ~ 1000 Å ; $T_{\text{thermocouple surface}} = 291\,^{\circ}\text{C}$
- µc-Si:H ; ~ 1000 Å ; $T_{\text{thermocouple surface}} = 350\,^{\circ}\text{C}$; $P_{\text{gas}} = 9\,\text{mTorr}$
- µc-Si:H ; ~ 1000 Å ; $T_{\text{thermocouple surface}} = 350\,^{\circ}\text{C}$; $P_{\text{gas}} = 4.6\,\text{mTorr}$
- a-Si:H ; ~ 1000 Å ; $T_{\text{thermocouple surface}} = 350\,^{\circ}\text{C}$
- SnO_2:F
- Glass Substrate

The substrate was glass covered by fluorine-doped SnO_2. Unfortunately, since SnO_2 is naturally textured, this choice led to a lack of resolution in all the SIMS profiles : no sharp changes between the five stacked layers can be seen. For example, it takes around 1000 Å for the $^{30}\text{Si}^+$ signal to go down by a factor of 10 at the silicon/SnO_2 interface (curve not shown). This very smooth decrease, of the order of magnitude of the layer thicknesses, clearly indicates that the concentrations of the successive layers are averaged.

The studied species for this first measurement were aluminum, copper, iron and nickel. The isotopes ^{27}Al (unique isotope of aluminum), ^{63}Cu and ^{65}Cu, ^{54}Fe (the main isotope of iron ^{56}Fe cannot be used because it interfers with ^{28}Si-^{28}Si) and ^{61}Ni, ^{62}Ni and ^{64}Ni were monitored.

After the procedure of normalization to convert the raw signals (in counts per second) in number of atoms per cubic centimeter, the isotopes ^{61}Ni, ^{62}Ni and ^{63}Cu were found to lead to overestimated concentrations. For example, the total concentration of nickel deduced from its isotope of mass 61 was around 3×10^{20} atoms/cm^3, which is of course an artefact, most likely due to the molecular ion $^{30}\text{Si}^{30}\text{SiH}^+$. Since all the different isotopes of an element should lead to the same total concentration of this element, only the isotopes giving the lowest total concentrations were selected in order to minimize the overestimation, they are : ^{54}Fe, ^{64}Ni and ^{65}Cu (see Fig. IV.58). But as usual, one cannot be sure that these are the real concentrations, they are just upper limits. For example, ^{64}Ni only has a relative abundance of 0.93 % so that its signal must be very weak. It could then be possible that the molecular ion $^{28}\text{Si}^{12}\text{C}_3$ lead to its overestimation since the carbon concentration in these layers is $\sim 3 \times 10^{19}$ cm^{-3}.

Unfortunately, from this first measurement, it is hard to conclude whether the nickel, iron and copper quantities are small enough to realize good solar cells with such a material. To
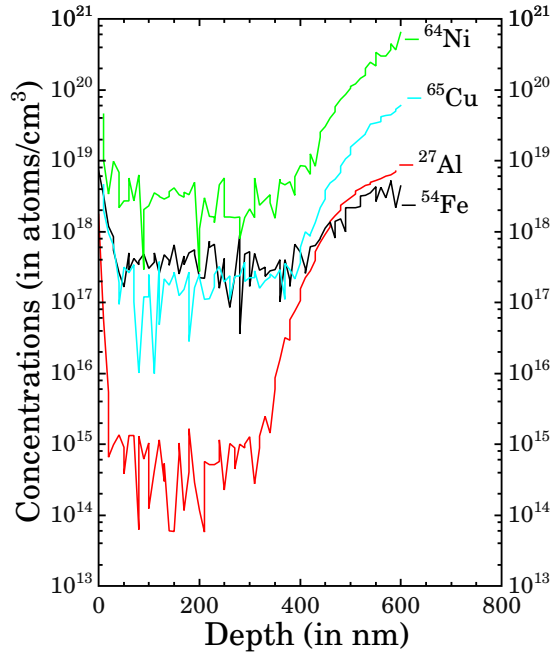
Figure IV.58 – *The first SIMS measurement in the new ATOS reactor : Study of the potential presence of metallic impurities. The graph shows the depth profiles of the total concentrations of nickel, copper, aluminum and iron deduced from their respective ^{64}Ni, ^{65}Cu, ^{27}Al and ^{54}Fe isotopes. The surface of the stack is at 0 nm and the SnO_2 substrate is at ~ 500 nm.*

be sure that the recorded signals are not overestimated, SIMS measurements with high mass resolution should be performed (see the results of the second sample below). What is more, these profiles should be considered with caution because the different layers are obviously overlapped and averaged due to the SnO_2 roughness and to the sputtering conditions with 5.5 keV O^- ions which are likely to create a roughness as well. Also, the fact that all the metal concentrations increase in the SnO_2:F remains unexplained.

At least, the clear result of this first SIMS measurement is that there is no aluminum contamination in our films : $C_{Al} < 1 \times 10^{15}$ cm^{-3}. It was a significant risk since the cylinder tube of the microwave antennas are in aluminum. In the previous reactor Domex, it had been found that the aluminum concentration just after manual cleaning could be as high as 4×10^{18} cm^{-3} but would go down to $\sim 4 \times 10^{14}$ cm^{-3} after the coating of the transfer plate, the antennas and substrate holder by several depositions.

4.3.1.2   Second sample

The sample A071218a was a stack of five layers :

- a-Si:H ; ~ 1000 Å
- μc-Si:H ; ~ 1000 Å ; SiH_4 + 50 sccm H_2
- μc-Si:H ; ~ 1000 Å ; SiH_4 + 50 sccm Ar
- μc-Si:H ; ~ 1000 Å ; pure SiH_4 ; $V_{bias} = -15$ V
- μc-Si:H ; ~ 1000 Å ; pure SiH_4 ; $V_{bias} = -80$ V
- Float-Zone monocrystalline silicon (FZ c-Si)

All the layers were deposited at the usual $T_{thermocouple\ surface} = 350$ °C. The top amorphous layer is a capping film to protect the stack from any post-oxidation.
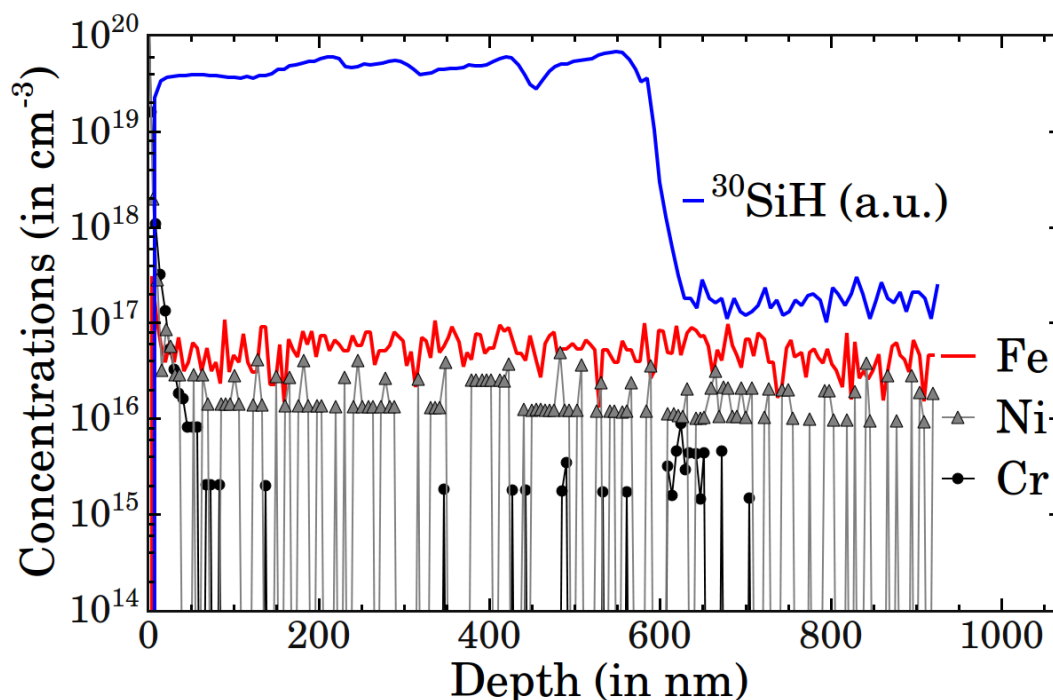
Figure IV.59 – *Results from the second SIMS sample in the new ATOS reactor. The iron, nickel and chromium concentrations have been obtained with high mass resolution to avoid any misleading mass interference. The hydrogen profile (^{30}SiH in arbitrary units) is also superposed to the metallic species profiles in order to indicate the interfaces of the five layers and of the c-Si substrate.*

The mass resolution necessary to distinguish two atomic or molecular ions of masses M_1 and M_2 is defined as $M_1/(M_1-M_2)$. As an example, the exact mass of ^{56}Fe is $55.93494 \, g \cdot mol^{-1}$ and the exact mass of $^{28}Si^{28}Si$ is $55.95386 \, g \cdot mol^{-1}$. Then, to separate the two signals, one has to have a minimum mass resolution of 2956. In the results presented here (see Fig. IV.59), all the metallic species were measured with at a high mass resolution of 3800, thus ensuring that the signals are free from any interference : e.g. the mass resolution to separate ^{58}Ni from $^{30}Si^{28}Si$ is 3777.

The evolution of hydrogen is also shown (in arbitrary units) in the Figure IV.59. Its drop at a depth of $\sim 0.6 \, \mu m$ corresponds to the c-Si wafer and the fact that it is a sharp decrease indicates that there is no roughness issue for this measurement as opposed to the previous one. Within the four µc layers, the H signal goes down with the deposition time. This "transient" could be explained by the plasma-induced heating. This fits with the fact that the H signal does not vary in the amorphous layer which is grown at a lower microwave power (875 W vs 1500 W).

This measurement has been mainly focusing on the risk of iron contamination. Indeed, the iron concentration has been calculated by comparison with a reference c-Si sample containing a known quantity of iron while the chromium and nickel concentrations have simply been obtained by calibration with Relative Sensitivity Factors (RSF) found in the literature. What is more, the SIMS equipment has been adjusted specifically for iron and the two other metallic species have been measured without changing its configuration. Thus, the signal intensities of chromium and nickel might not be optimal. It is obvious from Fig. IV.59 that their signals are extremely low, or even just noise. Indeed, the raw signals before

calibration are just a few counts per second or none at all (which has to be compared to the typical $140\,000$ counts per second of ^{30}Si for example). This could either mean that the chromium and nickel concentrations are really very low (lower than $\sim 2 \times 10^{15}\,cm^{-3}$ and $\sim 2 \times 10^{16}\,cm^{-3}$ respectively) or these concentrations might be underestimated due to the fact that the adjustment of the equipment was optimized for iron. A reference sample implanted with known concentration profiles of chromium and nickel would be necessary to determine their detection limit in the used sputtering conditions.

The obtained apparent concentration of iron is around 5.5×10^{16} atoms/cm^3. But one can see that this concentration does not decrease in the monocrystalline silicon wafer while the iron impurity level in FZ c-Si is several orders of magnitude lower. This indicates that the recorded signal is the detection limit of the SIMS analyser. This is also proved by the fact that in the implanted reference sample, the measured Fe concentration is saturating around the same value of 6×10^{16} atoms/cm^3 and is not going lower. Therefore, this value is the noise level. As a conclusion, this proves that our iron contamination level is equal to or lower than 5.5×10^{16} atoms/cm^3.

Conclusion on the metallic impurities

The main results can be summarized as :

- $C_{Al} \leqslant 1 \times 10^{15}$ atoms/cm^3
- $C_{Fe} \leqslant 5.5 \times 10^{16}$ atoms/cm^3
  This value, obtained with high mass resolution, proves that the first measurement, which was $\sim 4 \times 10^{17}$ atoms/cm^3 was severely overestimated.
- $C_{Cu} \leqslant 2 \times 10^{17}$ atoms/cm^3
  The internal walls of the vessel were initially protected by a copper foil which has been replaced by a stainless steel one and as a consequence, this species was not a concern anymore and has not been re-measured.
- Finally, in the absence of a reference sample implanted with chromium and nickel, it is unfortunately impossible to be sure that their measured low quantities ($\sim 2 \times 10^{15}\,cm^{-3}$ and $\sim 2 \times 10^{16}\,cm^{-3}$ respectively) are valid.

4.3.2   Presence of fluorine

The fluorine signals observed in some SIMS measurements a very long time after having used SiF$_4$ were puzzling. For some of the antennas, the toroidal joint of the magnet (see Figure IV.52 page 145) had been replaced by teflon tape wound around the thread. Such teflon tape can be a potential source of fluorine, e.g. if this part of the antenna gets heated and/or exposed to plasma. Indeed, teflon is polytetrafluoroethylene, which consists of carbon and fluorine atoms. Thus, we tried to investigate whether the high fluorine and carbon levels sometimes revealed by SIMS measurements could come from the antennas by depositing amorphous silicon without feeding any microwave power, the plasma being sustained only with the RF power injected on the surface plate of the substrate holder.

Figure IV.60 shows the SIMS profiles of the following stack :

- Layer 1 : Intrinsic a-Si:H layer in the ATOS reactor without microwave power ($\sim 430\,\mathrm{nm}$)
- Layer 2 : Intrinsic a-Si:H layer in the ATOS reactor (200 nm)
- Layer 3 : Intrinsic µc-Si:H layer in the ATOS reactor (400 nm)
- Layer 4 : Intrinsic µc-Si:H buffer layer in the ARCAM reactor (100 nm)
- Layer 5 : p-doped µc-Si:H layer in the ARCAM reactor (30 nm)
- Flat ZnO : The substrate has been annealed under vacuum overnight as a degassing procedure and exposed to a one minute argon plasma treatment to clean it.
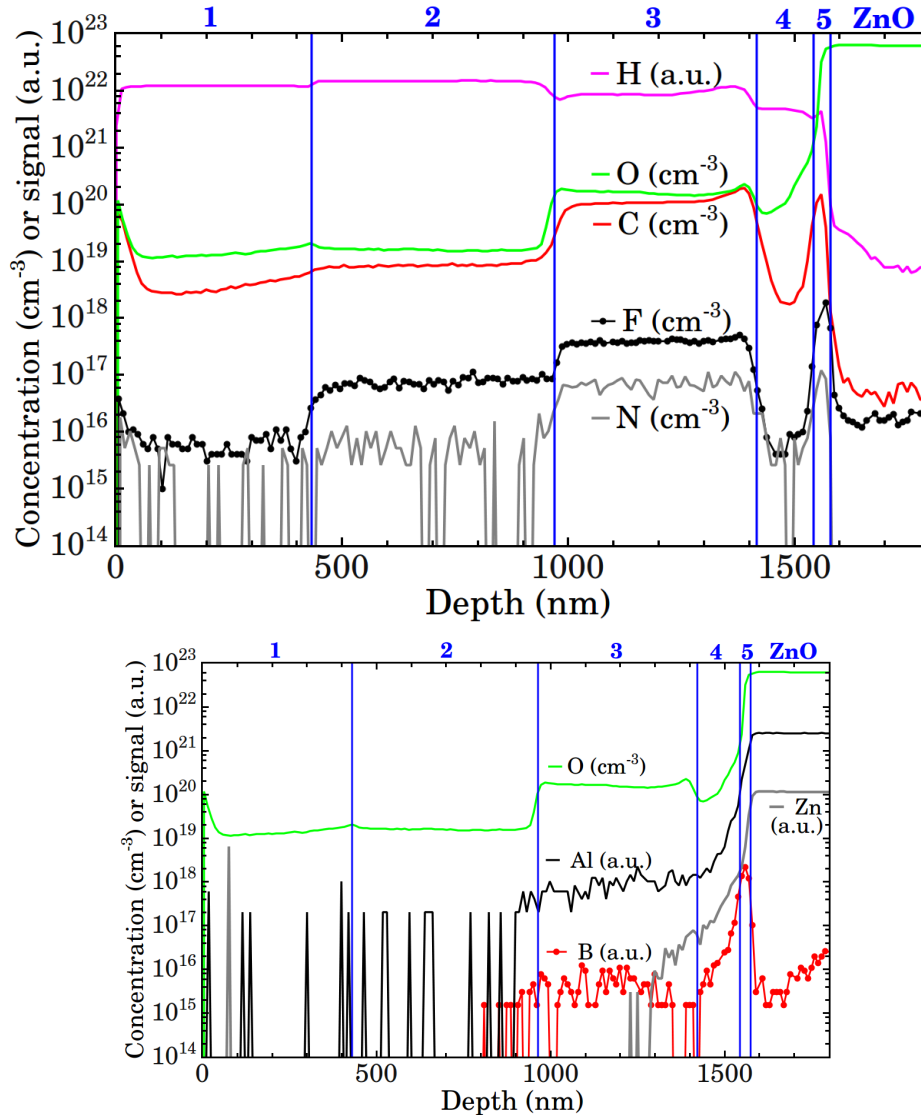- Glass

Figure IV.60 – *SIMS profiles of the stack. The species have been separated in two groups for clarity : The bottom graph shows the O, Zn, Al and B profiles, of interest for the study of the Si/ZnO interface.*

First, one can notice the very high C concentration in the ATOS µc-Si:H layer (Layer 3) : $\sim 1 \times 10^{20}\,\mathrm{cm}^{-3}$, i.e. two orders of magnitude higher than in the ARCAM buffer layer. The N level is very satisfactory in this ATOS layer ($8 \times 10^{16}\,\mathrm{cm}^{-3}$).

The bottom graph of Figure IV.60 focuses on the silicon/ZnO interface. Once again, we

see that the oxygen rise is not sharp. This would probably have been even more clear if the ARCAM buffer layer had been thicker than 100 nm. What is more, the aluminum and zinc species have also been measured and they show "tails" on a depth of several hundreds nanometers as well. These non-sharp variations are compared in detail with a reference sample entirely deposited in the ARCAM reactor in the Section 4.4.4.1 page 177.

The main goal of this stack was the layer 1 : We switched off the microwave power once the desired thickness was reached for the layer 2 and as a result, the plasma was only sustained by the RF power injected on the substrate holder. Looking through the window of the ellipsometer during this deposition, we could see the glowing volume being reduced to a thin volume in front of the substrate holder. The RF power was fixed to 53 W and from layer 2 to layer 1, the DC self-polarization voltage dropped from -42 V to -75 V, the pressure dropped from 7.5 mTorr to 4.6 mTorr and the deposition rate from ~ 16 Å/s to ~ 3.6 Å/s.

In this particular mode of deposition, the carbon concentration C_C drops from 8×10^{18} cm^{-3} to 2.8×10^{18} cm^{-3} and the variation of oxygen C_O is very small (from 1.7×10^{19} cm^{-3} to 1.2×10^{19} cm^{-3}) although the deposition rate has been greatly reduced. Interestingly, we observe a significant step in C_F : from 8×10^{16} cm^{-3} down to 6×10^{15} cm^{-3}, which means that the teflon tapes of the antennas could be a source of fluorine when they are exposed to the plasma.

4.3.3   Generalities about contamination by oxygen and nitrogen impurities

Oxygen, nitrogen and carbon atoms can come from the process gases, from air leaks, from pump oil or from degassing from the walls exposed to air during the loading of the samples. The solutions for the first and third cases are the installation of gas purifiers and of a loading chamber respectively. Apart from reducing the incorporation, two other methods are available : It is also possible to try to better passivate the incorporated oxygen atoms, which can be achieved at temperatures less than 140 °C for the deposition process of [65], as indicated by their Hall effect carrier concentration measurements (in agreement with the series in temperature of [43]). Finally, one can also balance the n-type doping effect of oxygen or nitrogen by an intentional p-type doping. It is the so-called microdoping solution that has been implemented for example for the first all-microcrystalline cell [2].

Contamination by oxygen or nitrogen leads to an n-type doping, an increased dark conductivity ($\sigma_{dark} \sim 10^{-3}$ S·cm^{-1} for [O] $\sim 10^{21}$ atoms/cm^3 in [90]), a decreased activation energy and an increased charge carrier density because the oxygen or nitrogen atoms in the silicon matrix behave as donor states [90]. Oxygen has also been observed to limit the crystallization and in particular, to limit the size of the grains [91]. Indeed, it is believed that oxygen donors precipitate at the grain boundary regions and that they are electrically active there. Then, depending on their incorporation configuration, they can act as negatively charged deep defects in the amorphous tissue of the grain boundaries leading to a decrease of $\mu_h \tau_h$ without affecting $\mu_e \tau_e$ [25], or they can be positively charge shallow defects below the conduction band.

For Kilper *et al.* [92], the oxygen concentration above which the efficiencies of their microcrystalline cells start to be affected is 1.2×10^{19} cm^{-3} to 2×10^{19} cm^{-3}. These concentrations are quite high, which means that probably most of the oxygen atoms are bound to two silicon atoms, which is a non-doping configuration. It affects the fill factor as well as the spectral response of the cells in the red and thus, the short-circuit current [90]. Indeed, the

negatively ionized oxygen atoms will perturb the internal electric field and thus, prevent the drift-assisted transport of holes to the p-doped layer. On the other hand, it seems to have nearly no effect on the V_{oc} for these authors even for concentrations up to 10^{21} cm^{-3}, while other authors [65] talk about a reduction of the V_{oc} due to shunt leakage. But in any case, even in the extreme case of $C_O = 10^{21}$ cm^{-3}, it is possible to obtain a 2.6 % cell with $J_{sc} = 9.0$ mA/cm^2.

The nitrogen threshold of degradation is even lower (6×10^{18} cm^{-3} to 8×10^{18} cm^{-3}) and the quality of the cells starts to decrease for ratios of air leak over the total gas flow of 140 ppm to 200 ppm.

The oxygen and nitrogen concentrations measured by SIMS are important information. However, as always, the configuration of the incorporated impurities has to be taken into account. First, the active or inactive configuration of the incorporated oxygen atoms could depend on the plasma chemistry and of the nature of the incoming molecules : Sources of oxygen like the gas lines will tend to produce siloxane molecules and could result in lower doping efficiencies than a contamination from the walls which will produce H_2O or OH molecules, as proposed recently to explain the degradation of amorphous solar cells by these different controlled sources [93]. Then, one has to keep in mind that the passivation of the donors is another very important parameter : Indeed, it has been reported that at low deposition temperatures, donors were not activated (< 180 °C for [94] or < 140 °C for [65]). Once again, hydrogen can play a crucial role, e.g. by breaking a bond of an electrically active oxygen bonded to three silicon atoms and leaving an electrically inactive Si–O–Si configuration.

4.3.4   Installation of the load-lock

In this section, we will report on the positive changes the modification of the reactor design brought. Secondary Ion Mass Spectrometry (SIMS) has been used to quantify the impact of this improvement on the material chemical composition.

4.3.4.1   First stack for SIMS with the load-lock

The detailed structure of this stack is the following :

- 120 nm of a-Si:H (ATOS)
- 200 nm of µc-Si:H with 42 sccm of pure silane at floating potential (ATOS)
- 100 nm of µc-Si:H with a gas mixture Ar/H$_2$/SiH$_4$ = 5/100/50 sccm and an RF power of 29 W (ATOS)
- 200 nm of µc-Si:H with a gas mixture Ar/H$_2$/SiH$_4$ = 5/100/50 sccm and an RF power of 45 W (ATOS)
- $\sim$ 400 nm of intrinsic µc-Si:H (ARCAM)
- $\sim$ 40 nm of p-doped µc-Si:H (ARCAM)
- Flat ZnO substrate, heated one hour to degas it.

The main result of Figures IV.61 and IV.62 is of course the success of the load-lock with the lowest oxygen concentration ever reached for the ATOS reactor : 2.1×10^{19} cm^{-1}. As a matter of fact, this level is now even lower than the one of the ARCAM microcrystalline layer for the sets of deposition conditions used.
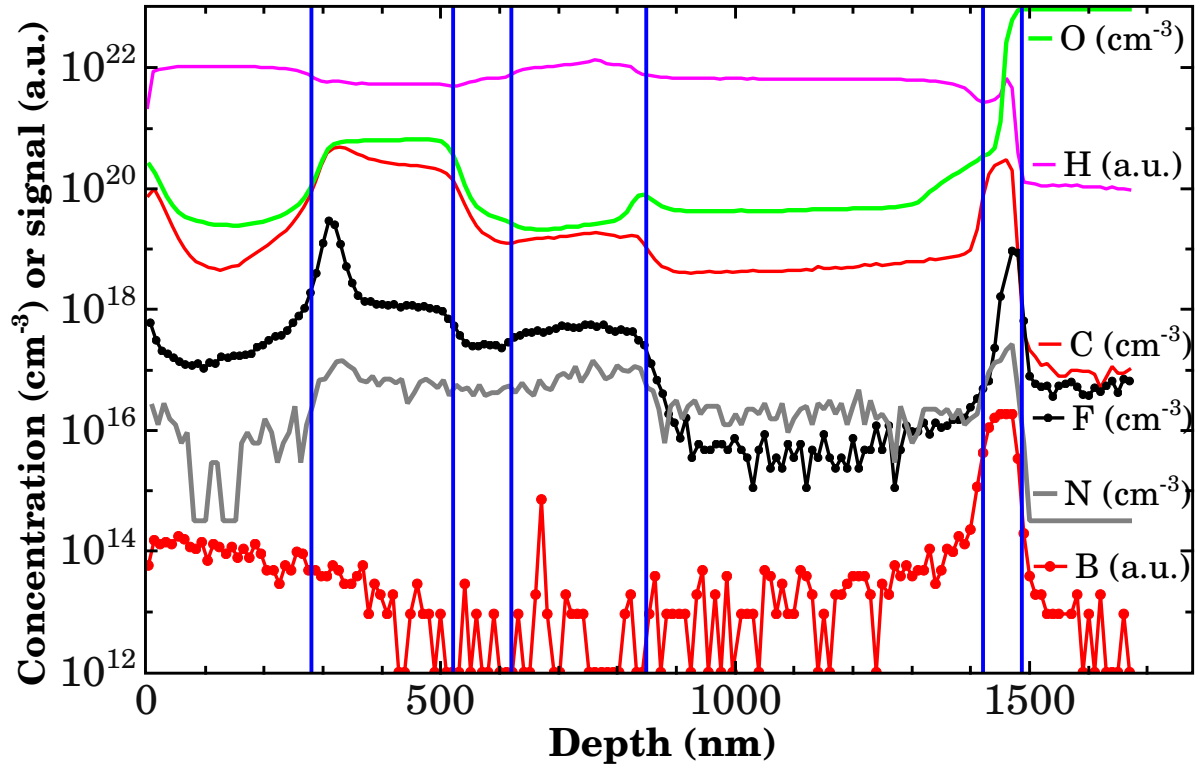
Figure IV.61 – *Hydrogen, carbon, oxygen, nitrogen, fluorine and boron SIMS profiles after the installation of the load-lock. The strange unexplained F and C peaks appearing at the end of the layer at floating potential do not correspond to any particular event during the deposition.*
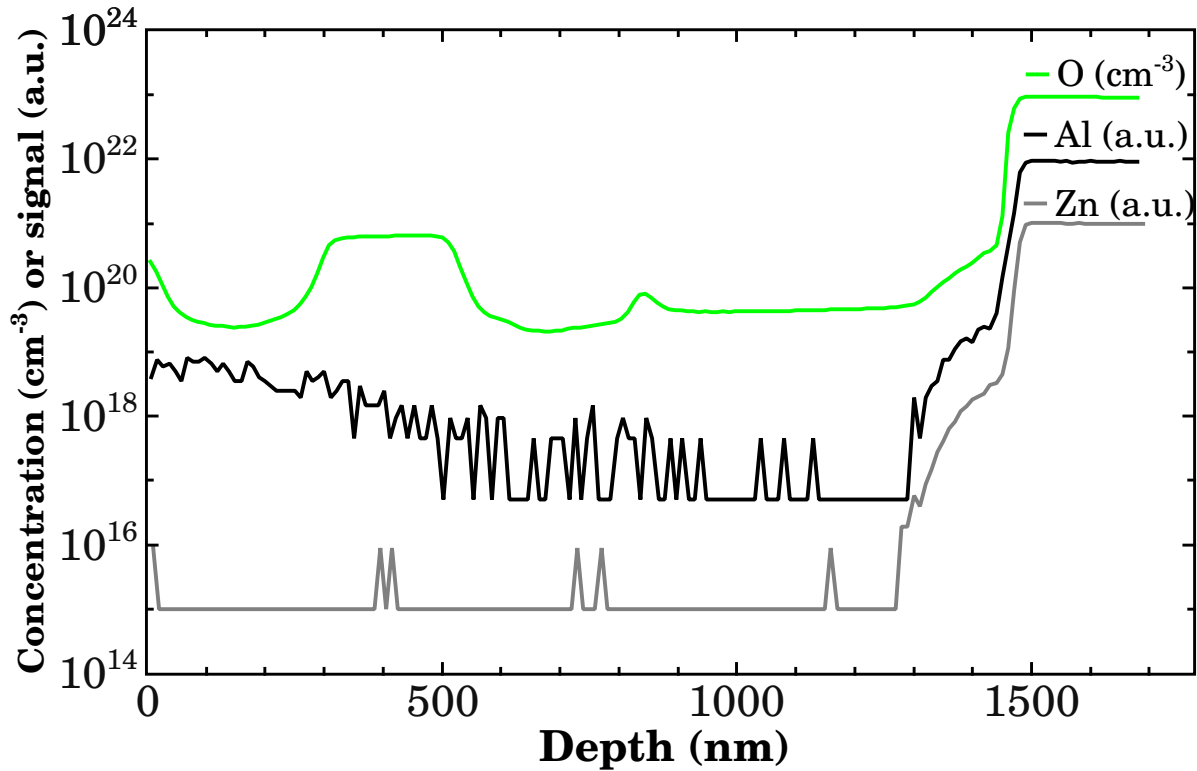

Figure IV.62 – *O, Al and Zn SIMS profiles after the installation of the load-lock.*

While the H concentrations in the ARCAM and ATOS µc-Si layers are close, the C, F and N concentrations are still respectively 4, 75 and 2 times higher in the latter reactor. Finally, we can notice that the ion bombardment energy still has a tremendous influence on the incorporation of contaminants after the load-lock installation. Indeed, the layer deposited at floating potential still has a huge oxygen content of $6.4 \times 10^{20} \, \text{cm}^{-1}$ and an abnormally high carbon content of $\sim 3 \times 10^{20} \, \text{cm}^{-1}$.

Figure IV.62 shows the superposition of the O, Al and Zn profiles which once again, present the characteristic feature of all the samples on flat ZnO having one or several layers from the ATOS reactor : the three species have non-sharp variations at the silicon/ZnO interface on a depth of $\sim 150 \, \text{nm}$.

4.3.4.2   Second sample for SIMS with the load-lock

This sample is commented in detail in Section 4.4.3 page 173 : It is a p-i-n cell on flat ZnO with 400 nm of its intrinsic layer deposited in the ARCAM reactor and the remaining 600 nm deposited in the ATOS reactor. For the deposition conditions used, the oxygen concentration reached the level of $1.1 \times 10^{19} \, \text{cm}^{-3}$. It can be reminded here that some authors [65] still manage to obtain cell efficiencies of more than $8 \, \%$ with oxygen concentrations of $2 \times 10^{19} \, \text{cm}^{-3}$.

4.3.5   FTIR and Raman combined investigations

These two techniques have been used to study the quality of the material and more precisely, its porosity and the presence of "cracks". Indeed, FTIR spectroscopy and Raman spectroscopy are powerful complementary tools to study the configurations of hydrogen incorporated in the microcrystalline material and the environment of these hydrogen atoms. The studies presented in the next sub-sections are based on the work of A. H. M. Smets and co-workers [46]. They recently stated that the presence of two peaks at $\sim 2080 \, \text{cm}^{-1}$ and $\sim 2100 \, \text{cm}^{-1}$, which they call Narrow High Streching Modes (NHSMs), could be qualitatively used as a signature of porous, highly crystallized samples presenting interconnected voids or cracks. Such samples are prone to post-oxidation, which can be put into evidence by the time evolution of the infra-red (IR) spectra, and are said to result in poor solar cells. Other authors have emphasized the importance of having dense grain arrangement [95] and attributed their high performance ($9.13 \, \%$ at a deposition rate of $2.3 \, \text{nm/s}$) to the absence of oxidation during vacuum break between the intrinsic and doped layer or after deposition. Although the exact configurations giving rise to these peaks are still under debate [96], their detection can be used to quickly rule out the corresponding deposition conditions.

4.3.5.1   Samples A080929b

These samples have been grown from the decomposition of a mixture of 8 sccm of SiH_4, 5 sccm of Ar and 75 sccm of H_2, resulting in a very low deposition rate of around 5 Å/s, due to the very small flow rate of SiH_4 (different Mass Flow Controller used). The gas pressure, the microwave power, the substrate surface temperature and the RF power were respectively 5 mTorr, 1.5 kW, 237 °C and 11 W. The samples have been co-deposited on two substrates : a glass substrate and a monocrystalline silicon substrate. The ellipsometry results are film thicknesses of $\sim 990 \, \text{nm}$ and $\sim 906 \, \text{nm}$, crystalline fractions in the bulk of $81 \, \%$ and $77 \, \%$, and very high void fractions of $18 \, \%$ and $22 \, \%$ respectively. The crystalline fraction of the
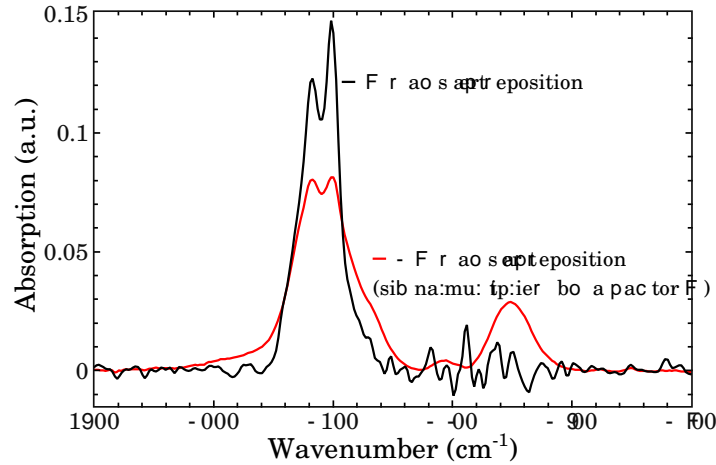
Figure IV.63 – *Evolution with time of the FTIR absorption spectra of the film on monocrystalline silicon.*

film on glass deduced from the deconvolution of its Raman spectrum around $520\,cm^{-1}$ is $63\,\%$ (see inset in the left graph of Figure IV.64).

For the comparison of FTIR and Raman spectroscopy to be valid, the film must not be too thick. Indeed, the former technique probes the whole thickness of the layer while the laser beam of the latter technique is preferentially absorbed near the surface of the sample. At the $632\,nm$ excitation wavelength of the Raman laser, the absorption length of the material, $1/\alpha$, is around $1\,\mu m$, as deduced from the ellipsometry results. Thus, we can consider that the whole thickness of the film is probed during the Raman measurement and that the comparison of the two methods is valid.

The first FTIR spectrum has been recorded four days after the deposition (black curve of Figure IV.63). We can notice that there is no absorption at all around $2000\,cm^{-1}$ and the two narrow peaks around $2100\,cm^{-1}$ appear very clearly. 24 days after the deposition, the infra-red absorption decreased a lot. (Note that the signal has been multiplied by a factor of 4 for clarity : red curve of Figure IV.63). This could be explained by the post-oxidation, with the hydrogen atoms at the crystalline surface of the cracks being replaced by oxygen. Indeed, an oxygen-related peak around $2250\,cm^{-1}$ appeared, as well as an intense one around $1050\,cm^{-1}$ (not shown). What is more, it seems that the two NHSM peaks are not evolving at the same rate, the one at $\sim 2100\,cm^{-1}$ disappearing faster.

Raman spectra have been acquired for the two substrates. The narrow peaks are put into evidence for both of them (see left graph of Figure IV.64). Interestingly, this proves that the NHSMs are not due to the silicon substrate and that it is possible to detect them for films on glass with the Raman technique. The major interest of this finding is that porous films can be evidenced even for non-IR transparent substrates. Although the signal of the narrow peaks is higher on c-Si, Raman spectroscopy can still be a fast method for μc-Si:H optimization of the material on glass or even directly on a solar cell. Being able to characterize the material directly on a solar cell has the additional advantage of suppressing any risk of misinterpretation if the growth is substrate-dependent. This approach has been proposed by our group in 2009 (see [96] and [97]).

The evolution with time of these peaks has been monitored, both on c-Si and on glass. The right graph of Figure IV.64 shows the spectra on c-Si. The signal decreases with time and the narrow peaks vanish. No oxydation peak around $2250\,cm^{-1}$ can be seen clearly (but this region has not been measured systematically).
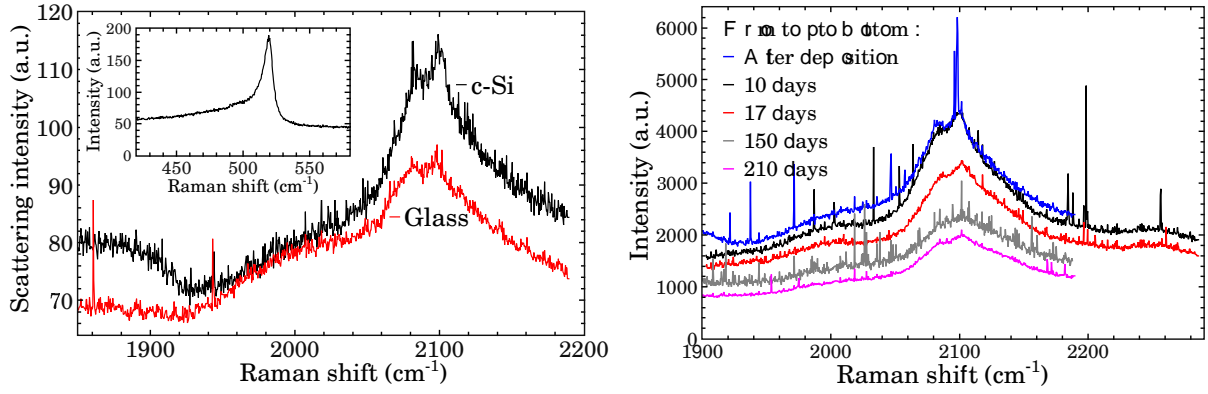
Figure IV.64 – *Raman characterizations. Left graph : Comparison of the signals of the films co-deposited on glass and on c-Si. Inset of the left graph : Crystalline peak at $\sim 520\,cm^{-1}$. Right graph : Evolution with time of the spectra (sample on c-Si).*

4.3.5.2   Samples A100315

For this run, the exact same deposition conditions as the previous section have been used, but we have clamped two monocrystalline silicon substrates : one is in the corner and is therefore tightly clamped by the metallic frame (A100315a), the other one is loosely clamped (A100315b). The c-Si substrate of the previous section was loosely clamped.

The goal of this run was to study the crystallographic orientation of the co-deposited films on glass and on the two crystalline substrates. The results of X-Ray Diffraction (XRD) measurements can be seen in Figure IV.65 and in Table IV.13. For the spectra on the (100) crystalline substrates, two peaks appear at 32.96 ° and 33.04 °, corresponding to the $K_{\alpha 1}$ and $K_{\alpha 2}$ lines respectively, because the Bragg condition is fulfilled by the (800) planes. These very sharp peaks can be used to confirm that not correcting for the instrumental broadening in the Scherrer formula is reasonable for our crystallite sizes estimations : for the sample A100315b, the Full Width at Half Maximum (FWHM) in terms of 2θ of these peaks is smaller than 0.04 ° while the FWHM of the (111), (220) and (311) peaks are ~ 0.42, ~ 0.73 and ~ 0.86 respectively.

A significant difference between samples a and b is seen in Table IV.13. While sample a has a (110) preferred orientation, sample b shows a strong (111) texture. In our opinion, this result fits with the trend observed in the series in bias (see Section 3.5.3 page 112). Indeed, since the loosely clamped sample b is slightly bent, the ion bombardment on its surface is probably reduced, which has been seen to lead to (111)-oriented films. It is more difficult to explain the difference between sample a (on c-Si) and sample e (on glass) : it could be due to a substrate dependent growth mechanism or to the lower temperature on the crystalline substrates (they are on top of the glass substrate and not directly on the heated substrate holder).

Applying the Scherrer formula, we found that the (111) grains are around a factor of 2 bigger than the (110) and (311) grains. This time, the greater ion bombardment for sample a as compared to sample b has no influence on the (110) crystallite size (opposed to the series in bias).
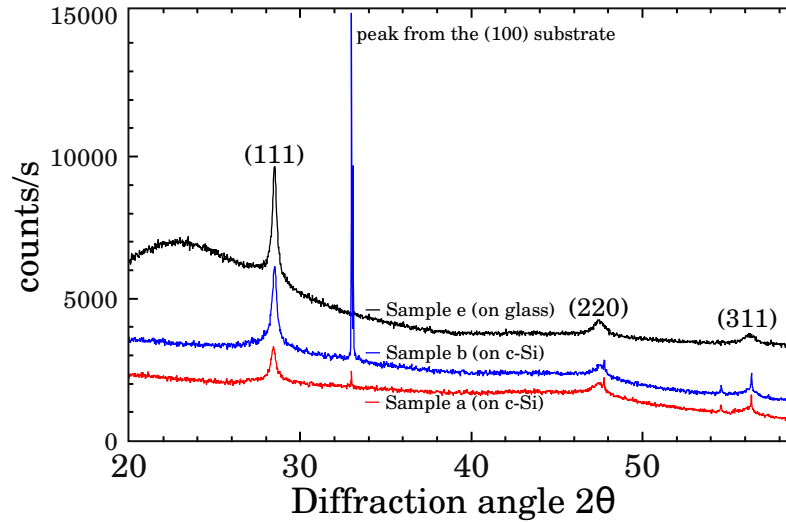
Figure IV.65 – *XRD spectra of the three co-deposited films of the batch A100315.*

Name	Fraction (111)	Fraction (110)	Fraction (311)	Size (111)	Size (110)	Size (311)
A100315a (c-Si)	0.23	0.40	0.38	271 Å	110 Å	118 Å
A100315b (c-Si)	0.57	0.21	0.22	215 Å	133 Å	117 Å
A100315e (glass)	0.49	0.24	0.27	282 Å	122 Å	113 Å

Table IV.13 – *Results deduced from the analysis of the peaks of the XRD spectra.*

4.3.5.3   Samples A090514

Another run with the exact same deposition conditions has later been carried out to quantify the post-oxidation with SIMS. To do so, the samples have been let at air 21 weeks before the measurement. The results seen on Figure IV.66 strongly confirm that the sample a, tightly clamped in the corner, is denser than the co-deposited sample b, which is loosely clamped and which presents intense double peaks around $2100\,\mathrm{cm^{-1}}$ in its FTIR spectrum.

Indeed, oxygen has completely contaminated sample b (solid lines in the graph) on its whole $1\,\mathrm{\mu m}$ thickness while only the top $100\,\mathrm{nm}$ of sample a is affected by post-oxidation. Similarly, the carbon penetration depth is $\sim 400\,\mathrm{nm}$ for sample b and $\sim 100\,\mathrm{nm}$ for sample a. There is a factor of 2 for nitrogen but no penetration tail can be seen. In parallel to the very high level of oxygen in sample b, its hydrogen content is $\sim 18\,\%$ less than for sample a (atomic percentages of $7.6\,\%$ and $6.2\,\%$), which could correspond to the narrow peaks on the FTIR spectra disappearing with time due to oxygen replacing hydrogen in interconnected cracks (mechanism proposed in [46]).

It can be noticed that although co-deposited, the film thicknesses are quite different. What is more, the oxygen base level of sample a, of $\sim 6 \times 10^{19}\,\mathrm{cm^{-3}}$, is too high despite the load-lock. This could be due to the very low growth rate of less that $5\,\mathrm{Å/s}$ obtained for these deposition conditions. Also, there are broad peaks of contamination at the film/substrate interface which had never been observed before.

We can now link the previous XRD results with the post-oxidation data of this batch, which are in very good agreement with published studies :

- In [98], their randomly oriented samples get post-oxidized ($C_O \sim 10^{20}\,\mathrm{cm^{-3}}$) while their samples without any (111) peak do not ($C_O \sim 10^{18}\,\mathrm{cm^{-3}}$).

- The SIMS results (Figure 4) of [99] are very similar to ours : One year after deposition, their (111)-oriented sample got contaminated over the whole $\sim 1\,\mu m$ depth at $2 \times 10^{20}\,cm^{-3}$, while oxygen only penetrates on a depth of $\sim 350\,nm$ in the case of a (110) orientation. They explain their different textures by different radicals coming at the surface, which is not our case since the samples are co-deposited.

As an additional remark, it has to be made clear that post-oxidation is just used as a way to reveal poor film quality but should not really affect the cells, since the amorphous n-doped top layer as well as the metallic contact protect the absorber layer from any chemical contamination [18, 11].
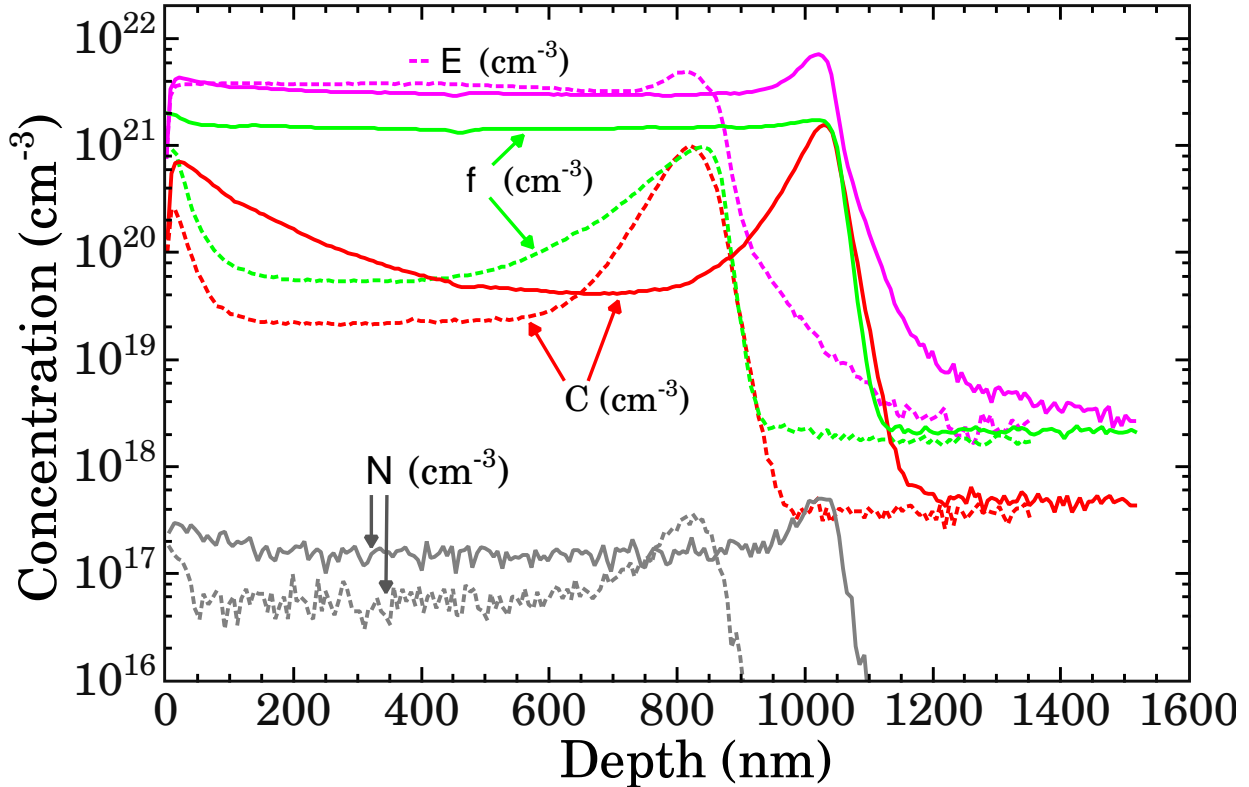

Figure IV.66 – *SIMS profiles of two co-deposited samples stored at air during 21 weeks. Sample a is tightly clamped in the corner (dashed lines), sample b is loosely clamped (solid lines).*

4.4   Investigations into the cells

4.4.1   Cell degradation induced by annealing in ATOS

SIMS measurements carried out on two cells made in ATOS had shown an apparent signal of oxygen coming from the ZnO (see Section 3.5.7.4 page 122). Thus, we were concerned by a risk of diffusion of oxygen from the ZnO due to the high surface temperature of $\sim 230\,°C$ used most of the time to obtain highly crystallized material at high rate. We tried to investigate the potential detrimental effect of temperature on the cells. To do so, we used cells entirely made in the ARCAM RF-CCP reactor, which are of high quality. We cut them after deposition, kept one piece as a reference, annealed the other pieces in the ATOS reactor and then, evaporated contacts and compared their performance.

4.4.1.1   Polymorphous cell

We first carried out this test on a standard polymorphous (pm-Si:H) p-i-n cell on SnO_2 entirely made in the ARCAM reactor. A piece of it has been heated in ATOS at the usual temperature ($T_{pyrometer} = 230\,°C$ and $T_{surface} = 535\,°C$) during 2H54 : it took around 1H15 to reach the saturation temperature (second substrate holder) and then it stayed around 1H39 at the maximum temperature before cooling down slowly. Aluminum contacts have been evaporated afterwards. The results are compared in Figure IV.67.

A huge degradation of the external quantum efficiency can be seen in the blue part of the spectrum, up to $\sim 600\,nm$. Problems of collection appear after annealing, as indicated by the great enhancement of the spectral response at negative bias. This annealing treatment results in a strong degradation of the PV characteristics of the cell, as shown in the table.
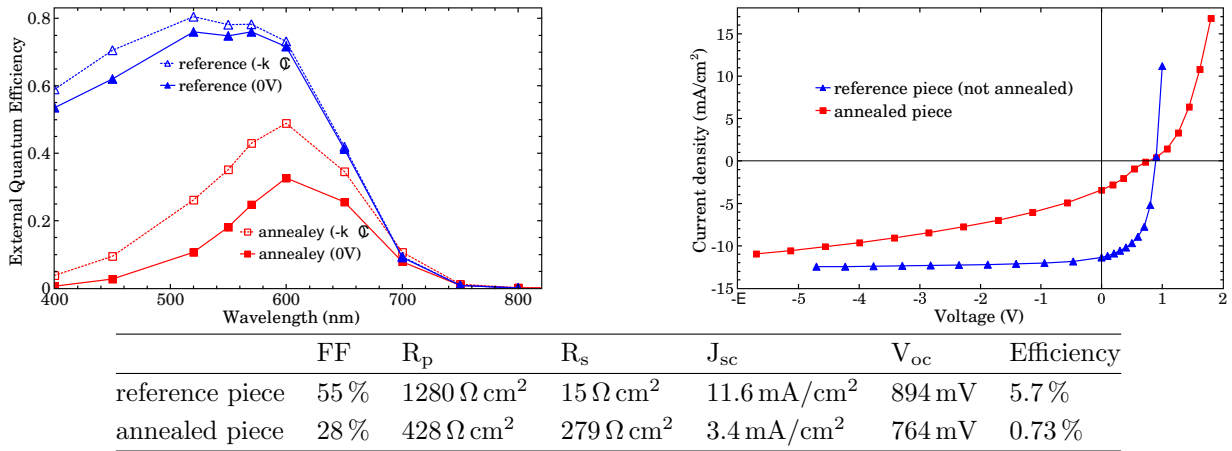

	FF	R_p	R_s	J_{sc}	V_{oc}	Efficiency
reference piece	55 %	$1280\,\Omega\,cm^2$	$15\,\Omega\,cm^2$	$11.6\,mA/cm^2$	$894\,mV$	5.7 %
annealed piece	28 %	$428\,\Omega\,cm^2$	$279\,\Omega\,cm^2$	$3.4\,mA/cm^2$	$764\,mV$	0.73 %

Figure IV.67 – *Degradation induced by a 2H54 annealing in ATOS on a p-i-n pm-Si:H cell.*

4.4.1.2   Microcrystalline cells

Two microcrystalline cells have been deposited in the ARCAM reactor on two different ZnO : on a ZnO deposited at high temperature (Juelich ZnO) and on one deposited at ambient temperature (IRDEP ZnO). The transparent conducting oxides have not been textured in order to carry out SIMS measurements afterwards, in case a degradation was observed. The back contacts are in aluminum.

The initial characteristics of the cell on Juelich ZnO are : FF of 61 %, R_p of $754\,\Omega\,cm^2$, R_s of $4.8\,\Omega\,cm^2$, J_{sc} of $14\,mA/cm^2$ and V_{oc} of $420\,mV$, resulting in a 3.6 % efficiency. On the IRDEP ZnO, we obtained a lower initial performance : FF of 56 %, R_p of $627\,\Omega\,cm^2$, R_s of $7.5\,\Omega\,cm^2$, J_{sc} of $10\,mA/cm^2$ and V_{oc} of $380\,mV$, Efficiency of 2.1 %. The relative evolutions of these parameters are presented on the graphs of Figure IV.68 as a function of the annealing times of the different pieces.

We can see on the two graphs that some of the parameters are improved by the treatment, at least up to a certain annealing duration. Interestingly, the degradation of the current densities for the two cells mainly takes place in the blue part of the spectrum : e.g. on Juelich ZnO, the relative degradation between the reference piece and the one heated 4H26 is 34 % at 400 nm and only 26 % at 750 nm. The efficiency of the piece annealed during a very long time of 4H26 went down to 2.9 %, corresponding to a relative degradation of only 20 %. The efficiency drops a bit more for the second ZnO but in any case, they still perform much better that the cells of less than 1 % that we often obtain in the MDECR reactor.
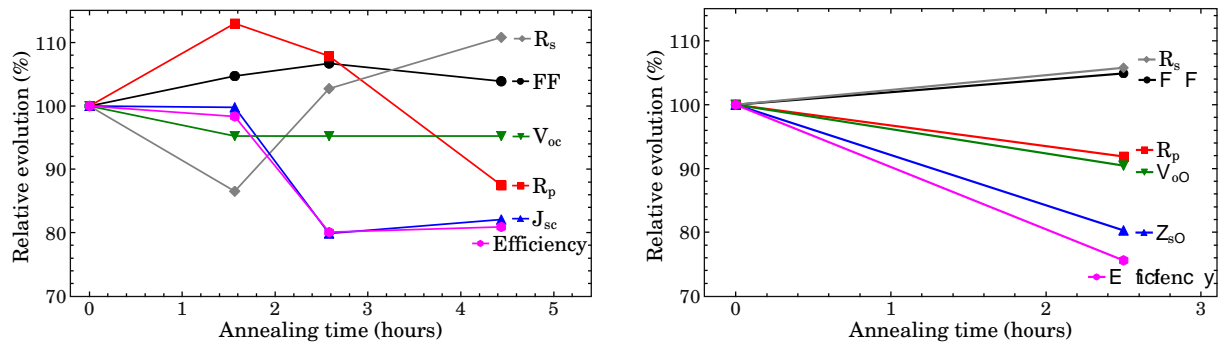
Figure IV.68 – *Degradation induced by an annealing treatment in ATOS (230°C) on the PV parameters of two microcrystalline cells : on Juelich ZnO (left graph) and on IRDEP ZnO (right graph). The lines are just guides to the eye.*

Conclusion : One has of course to keep in mind that heating *after* the structure is completed and heating *during* its deposition can have very different effects (e.g. for the boron diffusion from the p-doped layer as emphasized in [51]). The strong degradation observed for the polymorphous cell can probably be explained by the evolution of hydrogen at the high annealing temperature for this type of material. But as far as microcrystalline cells are concerned, we think that the risk of thermal diffusion of oxygen from the ZnO is ruled out by these experiments because in such a case, a much greater degradation of the cells would be observed.

4.4.2   The half-ARCAM half-ATOS cell (without load-lock)

We had seen that the addition of a "buffer layer" between the p-doped layer and the intrinsic layer could help to improve the cells. Here, we have deposited a cell with a very particular structure. Its spectral response and SIMS characterization have brought many highly valuable information.

4.4.2.1   Description

After the deposition of the µc p-doped layer in the RF-CCP multi-chamber reactor ARCAM, we sometimes add an intrinsic microcrystalline "buffer layer" on top of it, grown in another chamber of the same reactor. Such layers, with typical thicknesses ranging from 70 to 120 nm, have proven to be beneficial for the cell performance (see for example the early results in Table IV.4 page 102). Pushing this idea further, we decided to do a particular cell : half of its 1 µm-thick absorber layer was made in ARCAM before transfering it to the MDECR reactor for the high rate ($\sim 16.7\,\text{Å/s}$) deposition of the second half. This procedure allowed us to be absolutely sure that :

- The p-i interface is free from any oxidation since it is not exposed to air and is of good quality since the cells entirely done in ARCAM have high performances.
- There is no risk of damage of the ZnO by the hydrogen-rich MDECR plasma since 0.5 µm of dense microcrystalline silicon is protecting it from diffusing hydrogen atoms.

One has to keep in mind the following limits of this cell : it is exposed to air in the middle of the absorber layer and also, in order to be suitable for SIMS measurements, the ZnO used has not been textured. The ZnO substrate has been kept in ARCAM under vacuum and

166

annealed at a temperature in the range of $150-210\,°C$ the previous night in order to outgas it and it has been treated with a one minute argon plasma before the deposition of the p µc layer. Despite these precautions, the absence light trapping by a textured ZnO as well as its potential lack of cleanliness can affect the cell performances. What is more, the back contacts are in aluminum and not in silver.

The deposition conditions used for the ATOS layer were the ones found to give the lowest oxygen content at that time (i.e. $\sim 10^{20}\,cm^{-3}$ before the installation of the load-lock) : with a gas mixture of 5 sccm of Ar, 100 sccm of H_2 and 50 sccm of SiH_4, and an RF power of 42 W.

4.4.2.2   Performance of the cell

The film co-deposited on glass was found to have a high crystalline fraction of 91 % and a void fraction of 5.5 % by ellipsometry. The film co-deposited on c-Si for FTIR characterization unfortunately peeled.

No hydrogen treatment has been performed before the deposition in ATOS nor before the n layer deposition and the performance of the cell are reported in the Figure IV.69 and in Table IV.14.
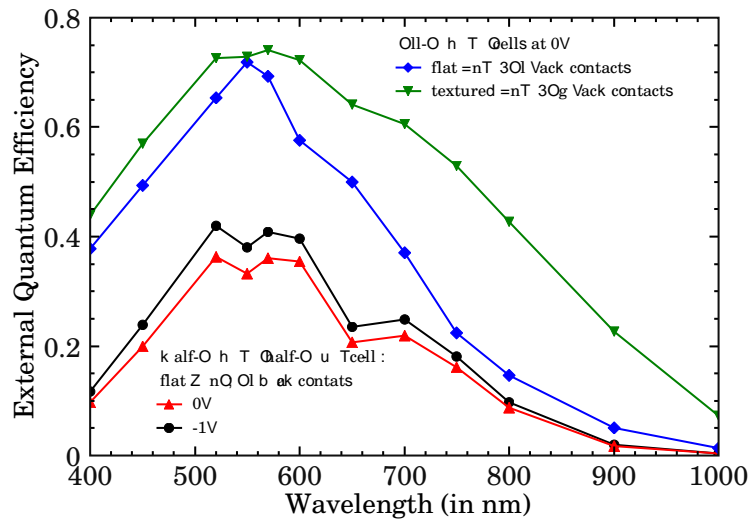

Figure IV.69 – *Spectral Responses of the half-ARCAM half-ATOS cell at 0 V and $-1\,V$ after annealing. For this cell, the temperature in ARCAM was $T_{ARCAM} = 150\,°C$. The two top curves are reference cells : They are two µc cells entirely done in ARCAM (with $T_{ARCAM} = 170\,°C$). One is on flat ZnO with aluminum back contacts and one is on textured ZnO with silver back contacts. They aim at illustrating the degradation induced by the $0.5\,\mu m$ MDECR layer as well as the importance of light trapping.*

	FF	R_p	R_s	J_{sc}	V_{oc}	Efficiency
Half-ARCAM half-ATOS (before annealing)	54 %	$1050\,\Omega\,cm^2$	$20.4\,\Omega\,cm^2$	$6.7\,mA/cm^2$	405 mV	1.45 %
Half-ARCAM half-ATOS (after annealing)	64 %	$1130\,\Omega\,cm^2$	$8.1\,\Omega\,cm^2$	$6.6\,mA/cm^2$	404 mV	1.71 %
All-ARCAM (flat ZnO ; Al back contacts)	64 %	$939\,\Omega\,cm^2$	$4.7\,\Omega\,cm^2$	$12.5\,mA/cm^2$	417 mV	3.37 %
All-ARCAM (textured ZnO ; Ag back contacts)	54 %	$448\,\Omega\,cm^2$	$4.8\,\Omega\,cm^2$	$20.8\,mA/cm^2$	397 mV	4.41 %

Table IV.14 – *Results of the half-ARCAM half-ATOS cell before and after a 30 minute annealing at $150°C$. On the third and fourth lines, the characteristics of the reference cells are shown for comparison.*

The very surprising result is the lack of collection in the blue part of the spectrum even though the p-i region, which is entirely done in the ARCAM reactor, is known to be of high quality. This would mean that the oxide in the middle of the absorber layer and/or the quality of the ATOS 0.5 µm layer and/or the i-n interface are very harmful for the transport of the electrons to the n layer.

Table IV.14 shows that the 30 minute annealing at 150 °C has an remarkable effect on the fill factor, the parallel resistance and the series resistance and allowed a relative improvement of the efficiency of around 18 %. It is worth noticing that such an enhancement never occured before on cells done in ATOS and is thus thought to be related to the ARCAM material.

The results of a µc p-i-n on flat ZnO entirely done in the ARCAM reactor and with aluminum back contacts are also reported to have a reference to estimate the degradation. We can see that the main parameter affected by the two air exposures (in the middle of the i layer and before the n layer), the heating in ATOS and the ATOS material quality is the current density, which dramatically drops from $12.5\,\mathrm{mA/cm^2}$ to $6.6\,\mathrm{mA/cm^2}$. The spectral responses are quite close in the red part of the spectrum ($\geqslant 750\,\mathrm{nm}$) due to the absence of light trapping so that this huge difference in current densities arises from a degradation of the efficiency of the half-ARCAM half-ATOS cell in the range of $400-750\,\mathrm{nm}$.

4.4.2.3   SIMS profiles

Without any chemical etching, this type of ZnO has an rms roughness of less than 15 nm and is thus suitable to obtain SIMS profiles with well resolved interfaces : see Figure IV.70. This sample turned out to be extremely useful to compare the chemical composition of the ATOS material to the one of the standard microcrystalline silicon deposited in the RF-CCP reactor ARCAM :

- The oxygen concentration in the ATOS µc-Si:H is ~ 25 times higher than in the ARCAM material and such a contamination is known to have a very detrimental effect on the cell performance (see discussion in Section 4.3.3 page 157).
- The carbon level shows an impressive jump of a factor ~ 39 at the ARCAM/ATOS interface.
- The fluorine signal in ATOS is $\sim 2 \times 10^{17}\,\mathrm{cm^{-3}}$ and at least 200 times higher than the ARCAM level, which is below the detection limit.
- The nitrogen concentration in ATOS is $\sim 5 \times 10^{16}\,\mathrm{cm^{-3}}$, corresponding to at least 20 times more than in ARCAM, which is below the detection limit.

Figure IV.70 shows again an oxygen "bump" between $1200-1370\,\mathrm{nm}$, i.e. $\sim 170\,\mathrm{nm}$ before the silicon/ZnO interface. The measurement of this sample has been repeated and the same feature appears for the two recordings. On Figure IV.71, this suspicious oxygen profile is shown again and superposed with the signals of boron, zinc and aluminum. These effects will be studied in detail in Section 4.4.4.2 page 177.
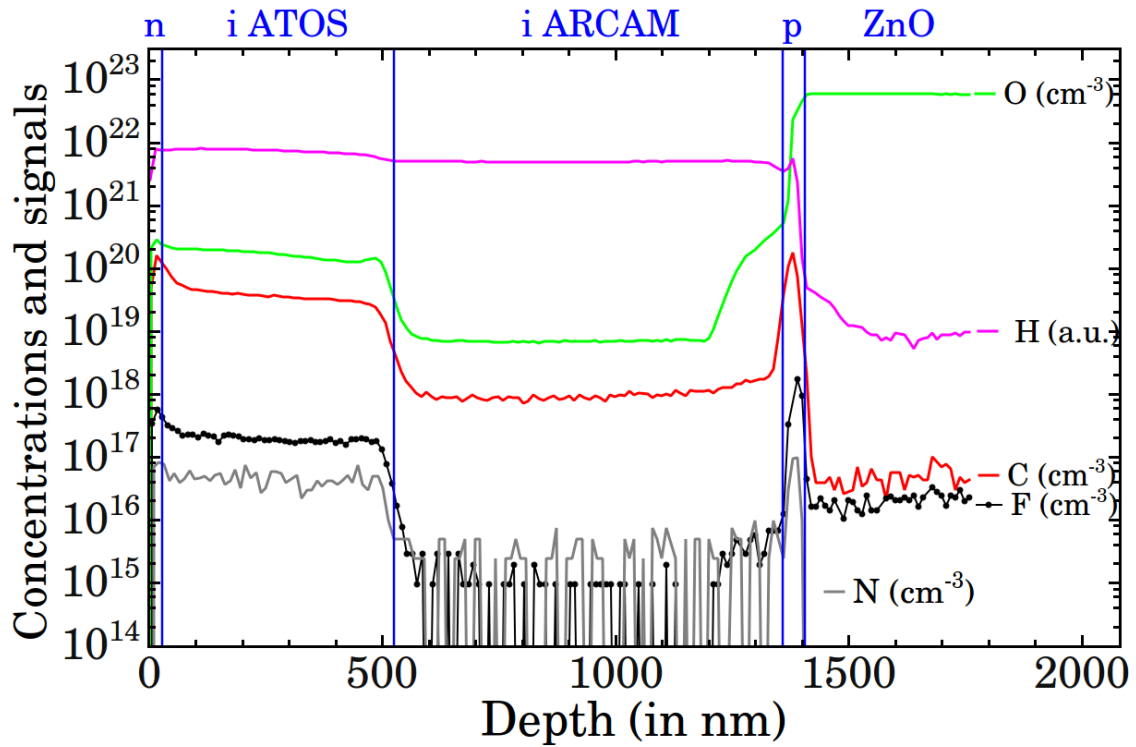
Figure IV.70 – *Oxygen, hydrogen, carbon, fluorine and nitrogen concentration and signal profiles in the half-ARCAM half-ATOS cell. Its structure is indicated on the top of the figure and the different layers are identified by vertical lines. The low quality of the ATOS material before the installation of the load-lock is remarkably illustrated by the great step of all the species at the ARCAM-ATOS interface.*
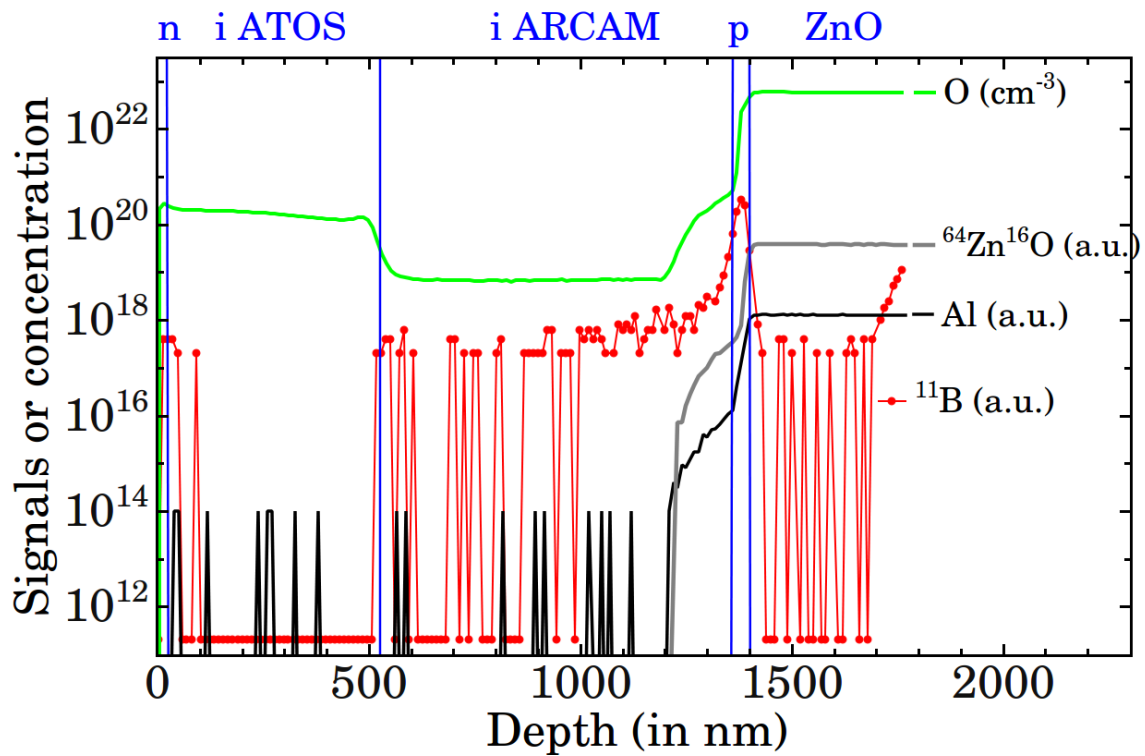

Figure IV.71 – *Superposition of the oxygen concentration with the signals (in arbitrary units) of boron, zinc and aluminum of the half-ARCAM half-ATOS cell to study the risk of diffusion from the ZnO.*

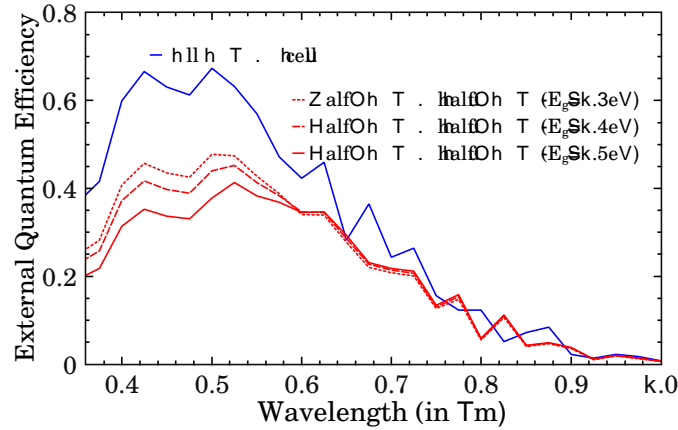## 4.4.2.4   Simulation of the half-ARCAM half-ATOS cell

Figure IV.72 – *External Quantum Efficiencies of the all-ARCAM cell and the half-ARCAM half-ATOS cell (for three different values of the mobility band gap of the ATOS material indicated in parentheses).*

The results presented in this section have been obtained by Parsathi Chatterjee (Energy Research Unit of the Indian Association for the Cultivation of Science, Kolkata, India) using her model named Amorphous Semiconductor Device Modeling Program (ASDMP). It has already been successfully implemented to understand the behavior of microcrystalline cells [60] and extended to heterojunctions [100, 101].

This model uses a set of one-dimensional equations to take into account the electrical and optical phenomena. The electrical part of the model uses the Poisson's equation and the two carrier continuity equations under steady state conditions. The optical part simulates the generation of the carriers taking into account specular interference effects and diffused reflectances and transmittances due to interface roughness. The materials are defined by their band-gap energy and their band-tail and mid-gap defect densities of states. The needed inputs are the complex refractive indexes for each layer, which are obtained from ellipsometry, and the structure of the cell. The model outputs are the external quantum efficiency and the $J(V)$ characteristics.

The goals of this simulation study were to explain the drop of the external quantum efficiency (EQE) taking place mainly in the blue part of the spectrum and to reproduce the trends of the all-ARCAM and of the half-ARCAM half-ATOS cells, i.e. the identical fill factors, the close values of open-circuit voltages and the significant drop in the short circuit currents.

The two cells were simulated with an "almost flat" ZnO. A small roughness was left in order to create the scattering corresponding to the internal scattering taking place at the grain boundaries of µc-Si:H. The mobility band gap of the ARCAM µc-Si:H has been taken to be 1.33 eV, as obtained from previous studies [59]. Taking into account the SIMS results, the ATOS material has been set as n-type. The doping concentration in the MDECR material has been varied in the range of $5 \times 10^{17} - 1 \times 10^{19}$ cm^{-3} but as expected, the effect of this variation is small since the layer is close to the n layer [92]. The results presented here are for a doping level of $\sim 5 \times 10^{17}$ cm^{-3}. Accordingly, the defect density is also higher in the ATOS layer than in the ARCAM one.

One of the results of this modelling is that a 100 nm layer with a high defect density of 10^{19} cm^{-3} has to be added at the beginning of the ATOS layer to be able to reproduce the fall of the EQE for the short wavelengths.

	FF	J_{sc}	V_{oc}	Efficiency
Experimental results				
All-ARCAM (flat ZnO ; Al back contacts)	64 %	12.5 mA/cm^2	417 mV	3.4 %
Half-ARCAM half-ATOS	64 %	6.6 mA/cm^2	404 mV	1.7 %
Simulation results				
All-ARCAM (flat ZnO ; Al back contacts)	57 %	14.8 mA/cm^2	463 mV	3.9 %
Half-ARCAM half-ATOS	39 %	9.5 mA/scm	430 mV	1.6 %

Table IV.15 – *Comparison of the experimental and simulated $J(V)$ data.*
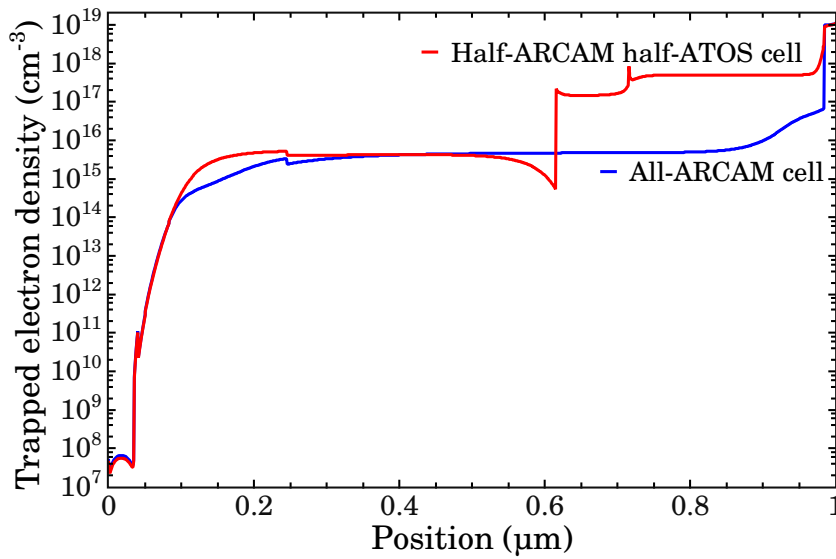
Figure IV.73 – *Profiles of the trapped electron densities in the two cells. E_g=1.5eV for the ATOS material. x=0 corresponds to the p layer and x=1µm, to the n layer.*
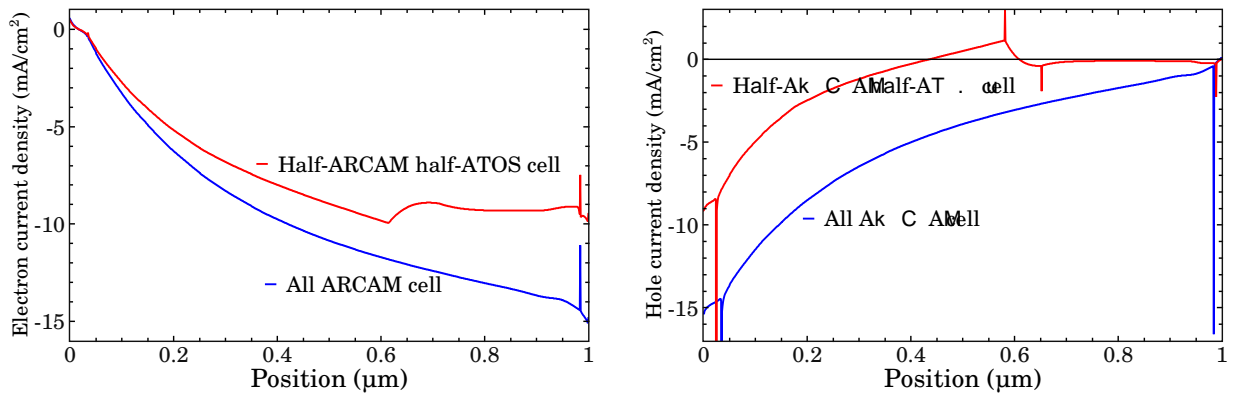
Figure IV.74 – *Profiles of the electron (left graph) and hole (right graph) current densities in the two cells. Chosen sign convention : The electron current density is integrated from x = 0 to x and is negative when flowing towards the n layer. The hole current density is integrated from x = 1 µm to x and is negative when flowing towards the p layer.*

The effect of the mobility band gap of the ATOS layer on the EQE can be seen in Figure IV.72. The higher it is, the better the model reproduces the experimental data of Figure IV.69. This corresponds to our experimental characterization of this material : we know from ellipsometry, Raman spectroscopy and AFM images that it is not as highly crystallized as the ARCAM µc-Si (no large grains). All the other results presented thereafter have been obtained with the MDECR material having a gap of 1.5 eV.

The $J(V)$ parameters for the two cells are shown in Table IV.15. The main limitation of the model is obviously that the fill factor does not reproduce the experimental data : the simulated value drops from 57 % to 39 %. For the other parameters, the model matches the experimental values and their degradation fairly well.

The ASDMP program mainly helped us to understand that the drop of the current density can be explained because of the repulsion of the electrons generated in the ARCAM layer by the high density of trapped electrons in the ATOS layer (see Figures IV.73 and IV.74). This repulsion can also be clearly seen on the hole current (right graph of Figure IV.74) : indeed, over a small region around the ARCAM/ATOS interface, there is a net hole current towards the n layer (with the chosen sign convention, it corresponds to positive values).

As a conclusion, this model is an initial step into the simulation of the MDECR cells and is not complete since it does not allow to perfectly reproduce the evolution of the fill factor, the very low experimental EQE in the blue nor the values of J_{sc}. Nonetheless, its first outcome is that it points out to a defect-rich ARCAM/ATOS interface and it explains the sharp drop of the current density in the half-ARCAM half-ATOS cell by the repulsion of the electrons and the attraction of the holes by the high density of trapped electrons in the MDECR layer.

One also has to keep in mind that in the simulation, it has been assumed that the p-i interface is the same in the all-ARCAM cell and in the half-ATOS half-ARCAM cell. Trying to introduce a degradation of this region in the half-ATOS half-ARCAM cell could help to better reproduce the experimental results and would be an interesting future work.

4.4.2.5   Conclusion on the half-ARCAM half-ATOS cell

The comparison of the SIMS profiles and the current densities of the half-ARCAM half-ATOS cell and of the all-ARCAM cell showed very clearly the poor quality of the ATOS material before the installation of the load-lock in terms of chemical composition and degraded photovoltaic performance.

With controllable oxygen, nitrogen and air leaks, Kilper *et al.* [92] have studied the effect of the contamination levels of O and N on microcrystalline cells as well as the effect of the depth distribution of these impurities. They concluded that the presence of high concentrations of O and N ($\sim 8 \times 10^{19}$ cm^{-3} and $\sim 2 \times 10^{20}$ cm^{-3} respectively) in the ~ 400 nm close to the n layer is not harmful at all for the cell performance : they could obtain efficiencies as high as 7.4 % with FF $= 72.4$ % and $J_{sc} = 19.1$ mA/cm^2. Since a degradation is observed in our case when the half of the absorber layer close to the n side is made in ATOS, this would indicate that this is not due to its high oxygen level but to some other factor such as air exposure and/or heating. This was later confirmed by the fact that the tenfold reduction of the oxygen level in ATOS enabled by the installation of a load-lock did not result in a clear improvement of the cells. What is more, the degradation they observe is mainly due to a lower current density in the red part of the spectrum and a lower Fill Factor, which is not our case.

4.4.3   The 40%-ARCAM 60%-ATOS cell (with load-lock)

After the installation of the load-lock on the vessel of the MDECR reactor, the idea of the previous particular structure (Section 4.4.2) has been repeated in a similar way.

4.4.3.1   Structure

The structure of the cell was the following :

- Silver contacts
- Amorphous n-doped layer in ARCAM
- One minute hydrogen plasma treatment in ARCAM
- Air exposure : transfer to the ARCAM reactor
- $\sim 600\,nm$ layer of intrinsic microcrystalline silicon in ATOS :
  This layer has been deposited at a rate of $\sim 12\,\text{Å}/s$ from pure silane (42 sccm). Also, due to the concern about a risk of thermal diffusion from the ZnO substrate, the deposition temperature in ATOS has been lowered to $T_{pyrometer} = 182\,°C$ instead of the usual $\sim 230\,°C$.
- Air exposure : transfer to the ATOS reactor
- $\sim 400\,nm$ layer of intrinsic microcrystalline silicon in ARCAM (at $175\,°C$)
- p-doped microcrystalline layer in ARCAM
- Non-textured ZnO
- Glass substrate

4.4.3.2   Characterizations of the ATOS material

Different substrates (glass and monocrystalline silicon) have been co-deposited with the cell. The ellipsometry spectrum of the 600 nm of ATOS µc-Si:H on glass is fitted with a 95 % crystalline fraction and a 5 % void fraction in the bulk. The film on crystalline silicon has been characterized by FTIR (see Fig IV.75). The $2100\,cm^{-1}$ mode dominates the one at $2000\,cm^{-1}$ and an oxygen-related peak appears around $1100\,cm^{-1}$ after a few days of air exposure corresponding to Si–O bounds. This probably indicates that the material density has to be improved.
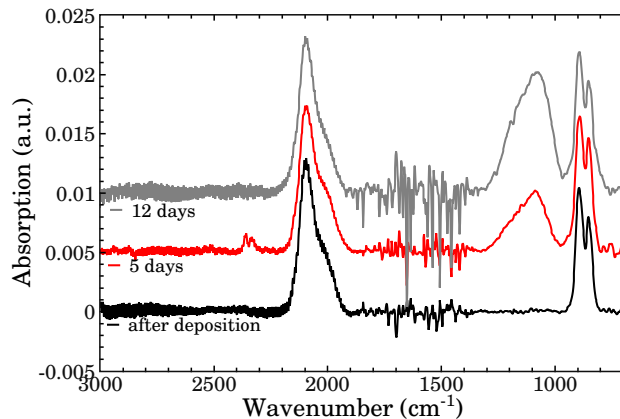

Figure IV.75 – *Evolution with time of the FTIR spectra of the 600 nm thick ATOS layer : just after deposition, 5 days after deposition and 12 days after deposition. The curves are shifted for clarity.*

4.4.3.3   Cell results

Scanning Electron Microscopy (SEM) images of this cell can be seen on Figure IV.76. The SEM resolution is unfortunately too low to distinguish the doped layers or an incubation layer at the beginning of the ATOS layer. The appearances of the materials from the two reactors seem a bit different. While the ARCAM µc-Si seems to have vertical structures, the ATOS µc-Si seems to show horizontal structures. But this may well be due to the manual breaking of the sample.
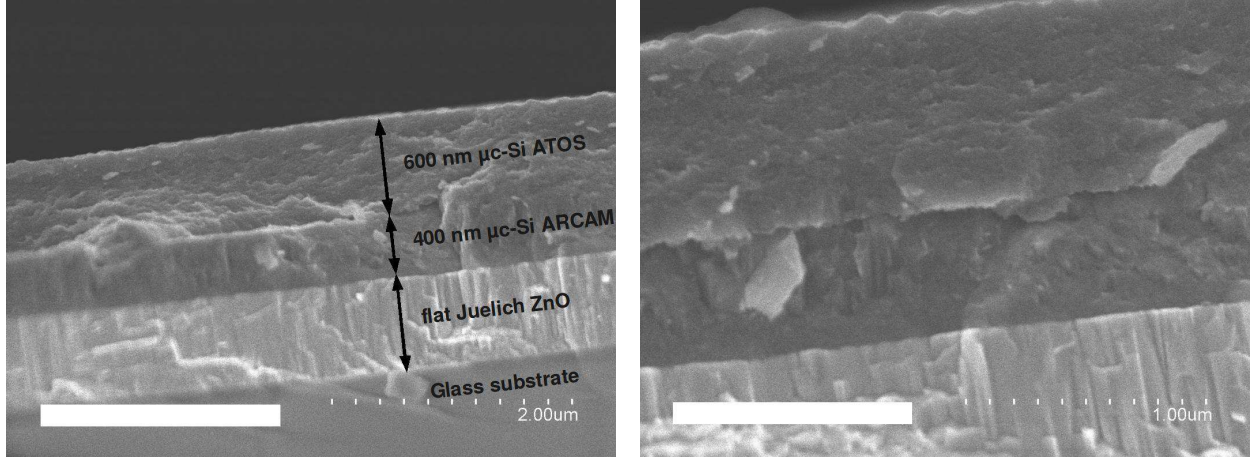

Figure IV.76 – *Scanning Electron Microscopy (SEM) images of the 40%-ARCAM 60%-ATOS cell. The right image is a zoom on the silicon layers.*

It has to be kept in mind that the deposition conditions of the ARCAM and ATOS layers are not the same as the ones of the previous cell. The characteristics of the 40%-ARCAM 60%-ATOS cell are reported in the Table IV.16. The parallel resistance is abnormally low and apart from the current density, all the parameters are worse than the ones of the half-ARCAM half-ATOS cell. The silver contacts are not responsible for the $\sim 13\,\%$ relative improvement of J_{sc}, as proved by the spectral response curves in Fig. IV.77 : Indeed, the enhancement of the current density of the 40%-ARCAM 60%-ATOS cell arises from a better response in the blue.

4.4.3.4   SIMS results

With the help of the load-lock, the base pressure at the end of the heating phase in ATOS was as low as 1.8×10^{-7} Torr, which is one order of magnitude below the typical values obtained when the entire vessel was exposed to air between each deposition. The SIMS profiles are shown in Figure IV.78.

The most striking consequence of the installation of the load-lock is of course the tenfold reduction of the oxygen content, down to $\sim 1.1 \times 10^{19}\,\mathrm{cm}^{-3}$. This demonstrates the usefulness and the very positive impact of the modification of the reactor. What is more, this value is now below the critical threshold value for the degradation of the cell performance of $1.2 \times 10^{19}\,\mathrm{cm}^{-3}$ to $2 \times 10^{19}\,\mathrm{cm}^{-3}$ found by Kilper *et al.* [92].

The signal of hydrogen (not quantified, in arbitrary units) is a factor of 2 higher in the ATOS µc-Si:H than in the ARCAM one. Another interesting feature can be noted in this graph : at the ATOS/ARCAM interface, we can see a peak of oxygen. It simply corresponds to oxidation during the air exposure but this phenomenon is revealed here for the first time due to the oxygen reduction in the ATOS material.

	FF	R_p	R_s	J_{sc}	V_{oc}	Efficiency
Before annealing	53 %	165 $\Omega\,cm^2$	11.6 $\Omega\,cm^2$	7.4 mA/cm^2	380 mV	1.49 %
After annealing	53 %	248 $\Omega\,cm^2$	11.6 $\Omega\,cm^2$	7.5 mA/cm^2	379 mV	1.50 %

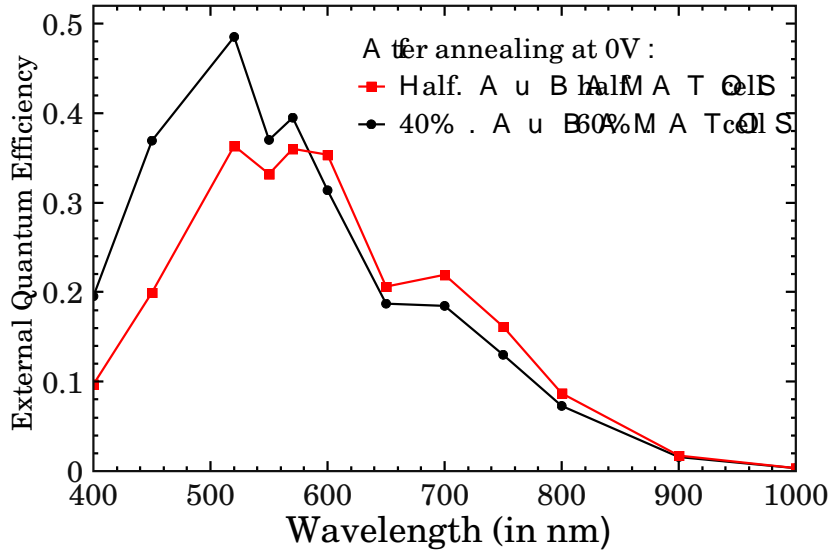Table IV.16 – *Results of the 40%-ARCAM 60%-ATOS cell before and after a 30 minute annealing at 150°C.*

Figure IV.77 – *Spectral Responses of the 40%-ARCAM 60%-ATOS cell (silver contacts) compared to the previous half-ARCAM half-ATOS cell (aluminum contacts). It can be seen that the higher current density of the 40%-ARCAM 60%-ATOS cell is not due to the more efficient back reflector.*

Table IV.17 sums up the main results of the two cells. One can clearly see the consequences of the different deposition conditions for the two ARCAM layers : most probably due to the higher temperature for the second cell (175 °C vs 150 °C), the contamination levels of the four species are worse. Thus, the ratios of the second cell appear as artificially good. Despite this, the improvement of the ATOS material is clear.

As a conclusion, the main goal of the load-lock, i.e. the reduction of the O content, has been fulfilled. The fluorine level should not be harmful for the cells, although its source remains unknown. The nitrogen level is two orders of magnitude below the critical threshold of $6 \times 10^{18}\,cm^{-3}$ to $8 \times 10^{18}\,cm^{-3}$ found in [92] but the carbon concentration is probably still abnormally high.

For the Si/ZnO interface, we can see the same oxygen "bump" before the ZnO as in the previous cell (see Figure IV.79). This time, the depth is only $\sim 100\,nm$ (vs $\sim 170\,nm$ for the previous cell at $T_{pyrometer} = 226\,°C$). This phenomenon is explained in Section 4.4.4.2 page 177.
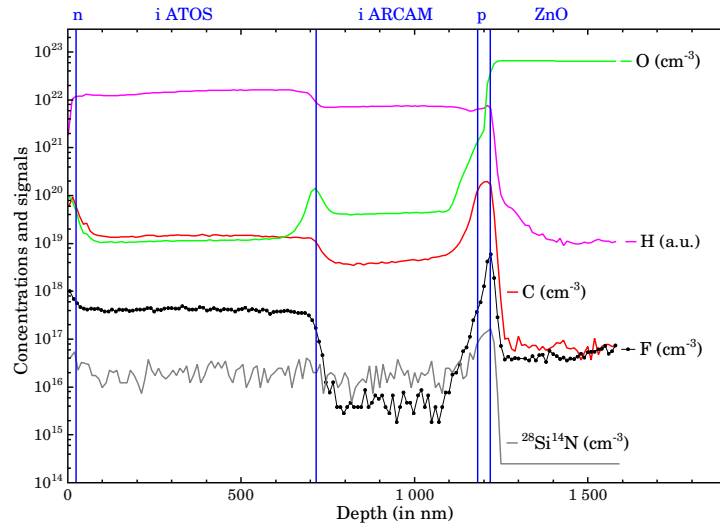
Figure IV.78 – *The O, H, C, F and N signal and concentration profiles in the 40%-ARCAM 60%-ATOS cell. Its structure is indicated on the top of the graph and the different layers are identified by vertical lines. This measurement has to be compared to Figure IV.70, carried out before the installation of the load-lock.*

	Before load-lock			After load-lock		
	ATOS	ARCAM	Ratios	ATOS	ARCAM	Ratios
Oxygen	1.7×10^{20}	6.7×10^{18}	25	1.1×10^{19}	4.3×10^{19}	0.3
Carbon	3.4×10^{19}	8.7×10^{17}	39	1.4×10^{19}	4.2×10^{18}	3
Nitrogen	4×10^{16}	$< 2 \times 10^{15}$	> 20	2×10^{16}	2×10^{16}	1
Fluorine	1.8×10^{17}	$< 9 \times 10^{14}$	> 200	4.2×10^{17}	3.8×10^{15}	110

Table IV.17 – *Comparison of the concentrations (in atoms/cm³) of four impurities in the half-ARCAM half-ATOS cell (Column "Before load-lock") and in the 40%-ARCAM 60%-ATOS cell (Column "After load-lock"). The columns "Ratios" correspond to the concentrations in ATOS divided by the concentrations in ARCAM. Although the layers are not deposited in the same conditions, it still gives a summary of these two experiments and an idea of the progress brought by the load-lock.*
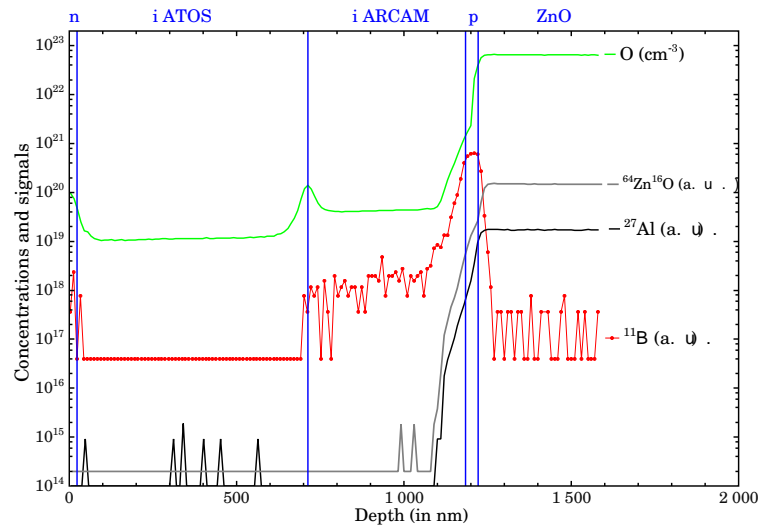

Figure IV.79 – *Superposition of the O concentration with the signals (in arbitrary units) of B, Zn and Al of the 40%-ARCAM 60%-ATOS cell to study the risk of diffusion from the ZnO substrate.*

4.4.4   The zinc oxide (ZnO)

The possibility of damaging the ZnO is a great concern, especially in high density plasmas. For example, to fit the ellipsometry spectra of their microcrystalline films deposited on ZnO at a high rate of 20 Å/s, the authors of [102] used an optical model including a fraction of ZnO in the first layer in order to take into account a phenomenon of mixing. We processed several samples to specifically study this layer of our cells.

4.4.4.1   The all-ARCAM sample on flat ZnO

This sample has been deposited entirely in the ARCAM reactor during the same series as the sample of Section 4.3.2 page 155 and the sample of Section 4.4.2 page 166. It will be used as a reference, especially for the silicon/ZnO interface. Its structure is the following :

- Intrinsic a-Si:H layer (200 nm)
- Intrinsic µc-Si:H layer (200 nm)
- p-doped µc-Si:H layer (30 nm)
- Ar plasma : one minute treatment to clean the ZnO surface and to improve adhesion
- Flat ZnO : heated a few hours to degas it
- Glass

The SIMS results of this stack are presented in Figure IV.80. Here, for this sample entirely made in the ARCAM reactor, the oxygen, aluminum and zinc variations are very sharp at the Si/ZnO interface. On the contrary, *all* the stacks on flat ZnO containing one or several layers deposited in the ATOS reactor show non-sharp variations of these species at the Si/ZnO interface. Furthermore, these "bumps" or "tails" are seen for a great range of thicknesses of the buffer layer deposited in the ARCAM reactor on top of the ZnO substrate (between 30 nm and 500 nm).

In Figure IV.81, the oxygen, zinc and aluminum profiles of the all-ARCAM sample are compared to those of the two other samples deposited on flat ZnO in the same series :

- The sample of Section 4.3.2 page 155 is a stack with an amorphous layer deposited in ATOS without microwave power to study teflon inside the antennas as a potential source of fluorine and carbon contamination.
- The sample of Section 4.4.2 page 166 is the half-ARCAM half-ATOS cell before the load-lock.

Such a superposition enables to emphasize the striking difference in the SIMS evolutions at the silicon/ZnO interface. For the all-ARCAM sample, the signals of the three species sharply drop below the detection level in a few tens of nanometers (i.e. on the scale of the peak-to-valley roughness of the non-textured ZnO), while the samples containing one or several layers from ATOS exhibit apparent signals expanding in the silicon matrix on depths of up to several hundreds of nanometers.

4.4.4.2   Sample A090429 : Detailed study of the SIMS craters

We have established that the oxygen non-sharp signals at the silicon/flat ZnO interfaces could not be caused by hydrogen diffusing from the MDECR plasma. Indeed, this signature was found even in the case of a 500 nm protective layer deposited in the ARCAM (sample in Section 4.4.2 page 166). Furthermore, we tried to decrease the temperature down to
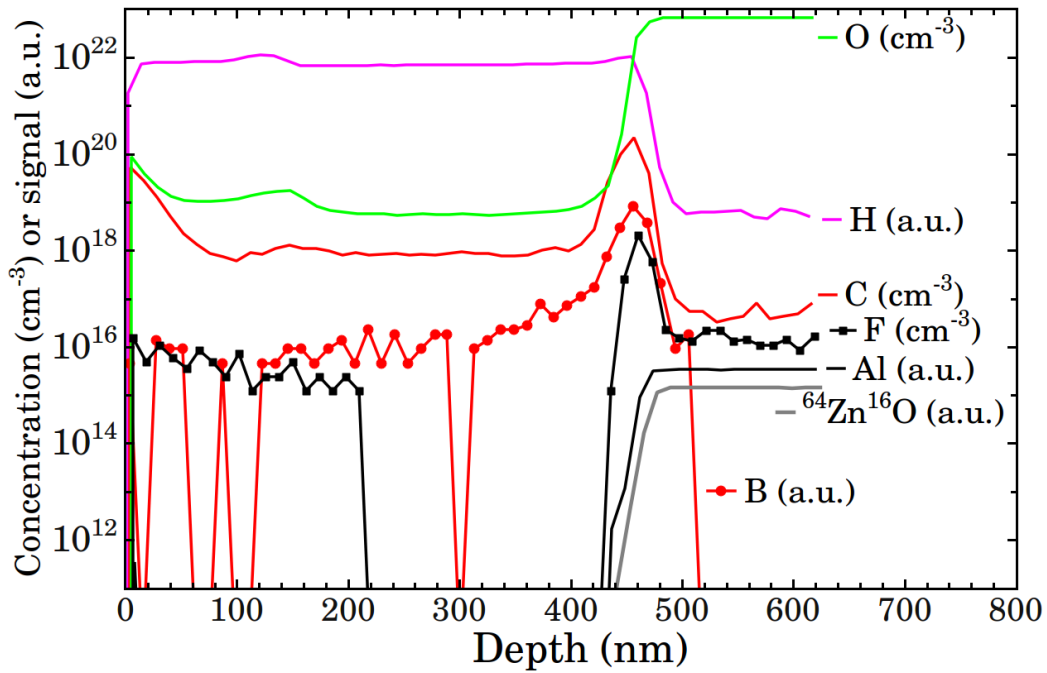
Figure IV.80 – *SIMS profiles of the all-ARCAM reference sample on flat ZnO. Nitrogen is below the detection limit everywhere except at the ZnO/Si interface and has therefore not been included. The Zn, O and Al profiles are further studied in the next graph.*
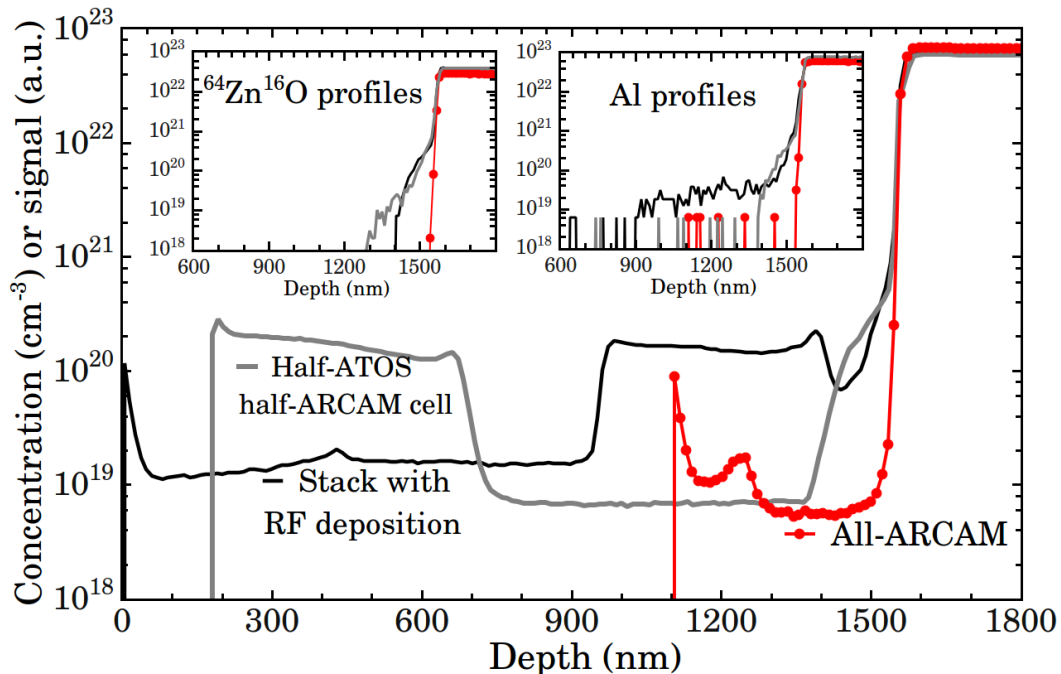

Figure IV.81 – *Comparison of three samples on flat ZnO : The profiles of the all-ARCAM sample are the red curves with symbols. The profiles of the stack of Section 4.3.2 page 155 are the black curves. The profiles of the half-ARCAM half-ATOS cell of Section 4.4.2 page 166 are the grey curves. The main graph is the superposition of the three oxygen profiles while the insets show the zinc and aluminum profiles.*

$T_{pyrometer} = 182\,°C$ to check if it could a thermally induced phenomenon but it did not supress the signal either (sample in Section 4.4.3 page 173).

The biggest "tail" of oxygen in the SIMS profiles had been found for a sample with a thin buffer layer of 120 nm (Section 3.5.7.4 page 122). We wanted to check the potential risk of oxygen diffusion with a thin buffer layer again. The structure of this stack was the following :

- ~ 120 nm intrinsic a-Si:H layer (ATOS) to encapsulate the stack
- ~ 600 nm intrinsic µc-Si:H layer in ATOS with a mixture of 5 sccm of Ar, 100 sccm of H_2 and 50 sccm of SiH_4
- 30 second H_2 plasma treatment (ATOS)
- ~ 120 nm intrinsic µc-Si:H buffer layer (ARCAM)
- ~ 30 nm p-doped µc-Si:H layer (ARCAM)
- flat ZnO substrate annealed overnight under vacuum to degas it

What is more, we wanted the total thickness to be a bit less than the usual one of the previous samples for SIMS (i.e. $\sim 0.8\,\mu m$ instead of $\sim 1\,\mu m$), in order to limit as much as possible the risk of formation of a roughness during the sputtering. The main idea of this stack was to study the SIMS craters. To do so, we sputtered five craters, to check the reproducibility of the oxygen "tail". For three of these five craters, we sputtered until the ZnO and for the two others, the primary ion beam was intentionally stopped as soon as the oxygen signal started to rise in order to perform SEM and profilometry analyses of the crater bottom surface at this stage.

The ATOS layers were also co-deposited on a monocrystalline silicon (c-Si) substrate cleaned with hydrofluoric acid (HF) and a glass substrate. Figure IV.82 shows the SIMS profiles of the stack on ZnO. The satisfactory oxygen level of $\sim 2 \times 10^{19}\,cm^{-3}$ enabled by the load-lock is confirmed and a huge "tail" of oxygen is found to start $\sim 0.6\,\mu m$ before the silicon/ZnO interface for the five craters. The bottom graph shows that this rise of oxygen is not present in the stack co-deposited on c-Si (see dashed green line) and that Al and the molecular ions $^{64}Zn^{16}O$ and $^{70}Zn^{16}O$ follow the exact same shape, thus suggesting that all these signals are due to some kind of "holes". The Al signal on the c-Si substrate is not shown because it is below the detection level throughout the stack and the Zn species have unfortunately not been recorded on c-Si.

Figure IV.83 shows some Scanning Electron Microscopy (SEM) images of the craters for different magnifications. It reveals that craters sputtered until the ZnO and craters whose sputtering has been interrupted before the ZnO have very different appearances. At the bottom of the former type of craters, we can see features which are like aligned "scratches" while the latter type exhibits "bubble-like" features which are more than 250 nm deep. Thus, stopping the sputtering was necessary to really understand what is going on during the SIMS measurement.

The image 1 of Figure IV.84 shows the spatial distribution of the oxygen signal during the SIMS measurement. If the oxygen "tail" had been due to diffusion, we would have seen a uniform signal from the whole crater. Instead, the bright spots of the image 1 correspond to holes, as seen by SEM (images 2 and 3) and with depths ranging from $\sim 0.2\,\mu m$ to $\sim 0.45\,\mu m$, as measured by profilometry (images 4 and 5).

It is now established that the oxygen rise before the Si/ZnO interface is due to the presence of holes during the SIMS sputtering. The question of their origin and of their exact location still remains. It could be due to a problem of adherance on the flat ZnO causing bubbles to
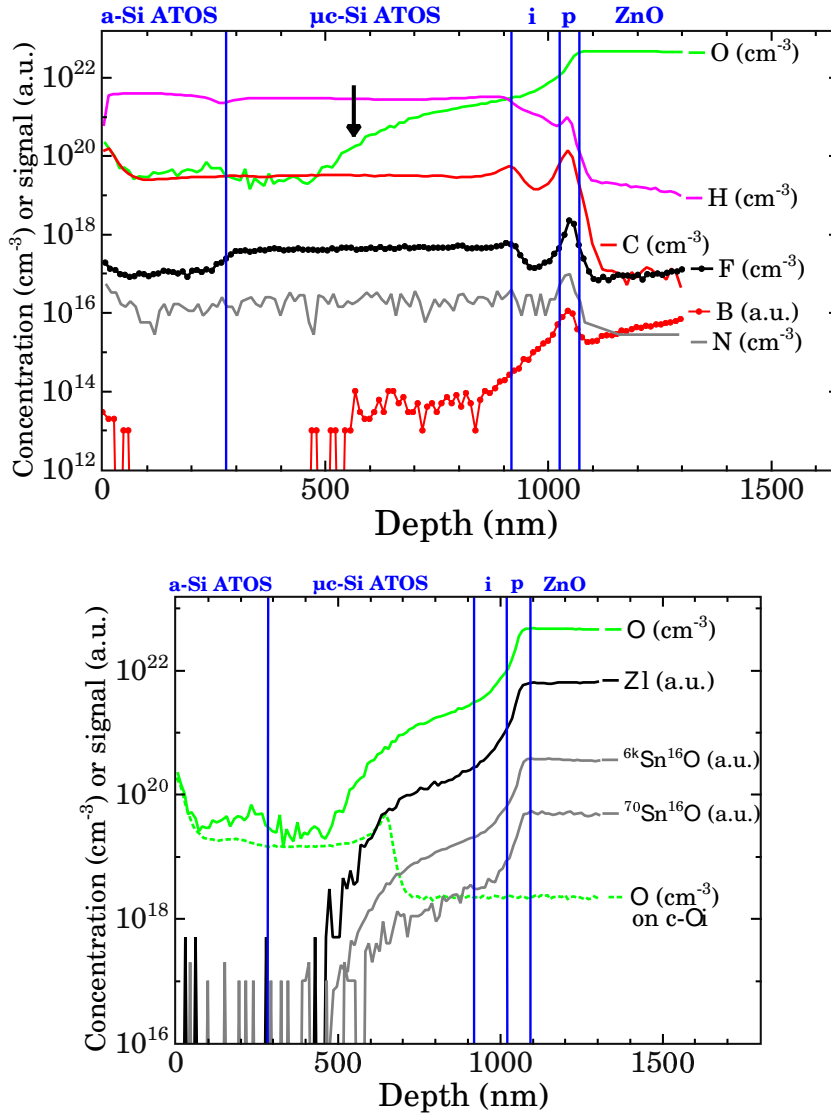
Figure IV.82 – *SIMS profiles of the stack on ZnO. The species have been separated in two groups for clarity. The green dashed line in the bottom graph is the oxygen profile of the ATOS layers on the c-Si substrate, superposed for comparison, and the arrow in the top graph indicates the depth at which two of the five craters have been stopped.*

form at the ZnO/p interface. To investigate this possibility, we performed an exodiffusion measurement. Indeed, such bubbles, if filled with H_2, can give a typical signature with this techique consisting of "spikes" of hydrogen appearing at low temperature. This phenomenon has not been observed in our case, as shown in Figure IV.85. The interesting result of this measurement is the comparison of the signals on ZnO and on glass. It has to be kept in mind that the two stacks are not exactly the same (absence of the two ARCAM layers on glass and different effect of the H_2 plasma treatment), but still, we can clearly see that the total hydrogen concentration on glass is higher (by 58 %) and also, that hydrogen is present in weaker configurations on glass (effusion starts at lower temperature). This would correspond to the surface temperature being higher on the ZnO substrate than on the glass substrate. The possible reasons for this difference, such as the absorption of microwaves heating the TCO, are still being studied.
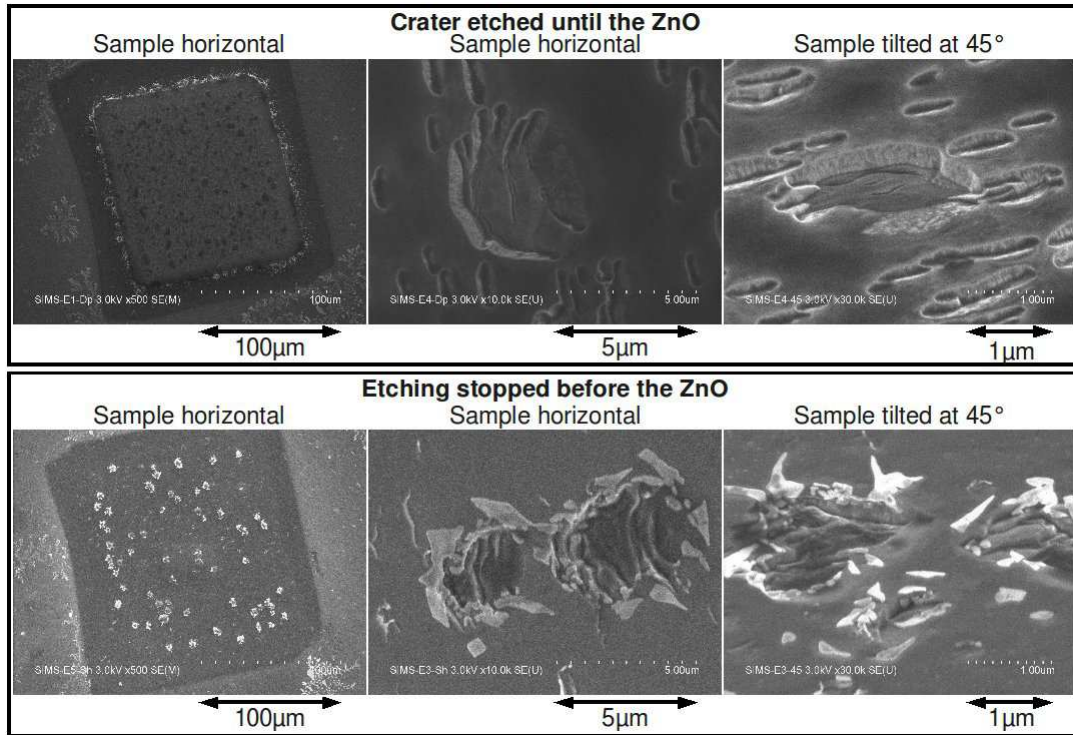
Figure IV.83 – *SEM top views of the two types of craters : sputtered until the ZnO or intentionally stopped just after the beginning of the oxygen signal rise.*
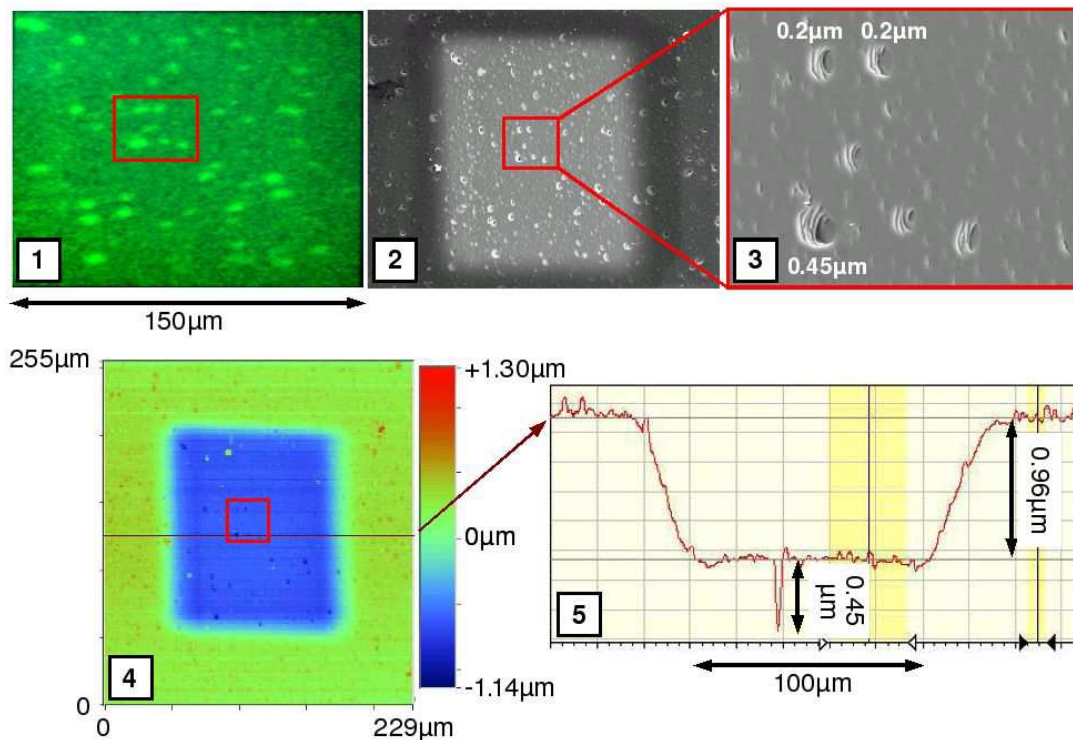

Figure IV.84 – *Image 1 is the spatial repartition of the oxygen signal as seen by the electron multiplier detector during the measurement, deduced knowing the scanning rate of the primary ion beam. The same six "bright spots", marked by the red rectangles, have then been studied by SEM (images 2 and 3) and by profilometry (images 4 and 5). The image 5 is the surface profile taken on the red horizontal line of image 4. One of the six holes is on this line and has a depth of $\sim 0.45\,\mu m$. The depths of the holes measured by profilometry are reported on the image 3.*
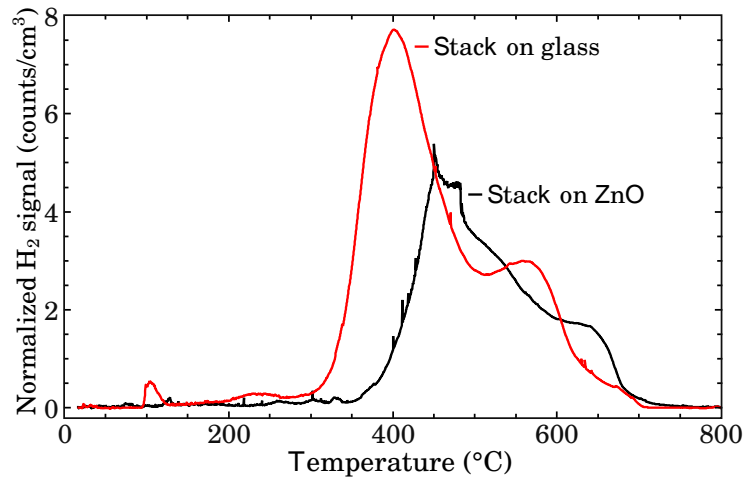
181

Figure IV.85 – *Qualitative comparison of the exodiffusion profiles of the stacks on glass and on ZnO.*

Conclusion on the SIMS measurements at the silicon/ZnO interface

The SIMS technique has been used a lot through the course of this doctoral work. For example, we studied the presence of metallic impurities (Section 4.3.1 page 151) and tried to find plasma conditions reducing the too high levels of oxygen we had before the installation of the load-lock. Then, we decided to study the interfaces in a real device. For this purpose, we did a cell on non-textured ZnO (Section 3.5.7.4 page 122). It was the first time we saw what we then called a "tail" of oxygen and it brought a whole new topic of studies and new hopes that understanding it would enable us to improve the cell efficiencies. The idea of stopping the SIMS sputtering before the Si/ZnO interface finally allowed us to prove that there is no oxygen diffusion.

The "tails" had depths of $\sim 100\,nm$ to $\sim 600\,nm$ and were observed for *every* sample deposited on non-textured ZnO having at least one layer deposited in ATOS. This represents six samples, some of which have been measured several times (total number of measurements : 14). On the other hand, one sample entirely grown in the ARCAM reactor on flat ZnO has been mesured twice and showed a sharp Si/ZnO interface (Section 4.4.4.1 page 177), so that we will keep on dedicating efforts to explain this strong difference, which hopefully could lead us to discover the origin of the poor efficiencies of the MDECR solar cells.

4.4.5   Other potential problems during the processing of the cells

In this section, we will very briefly review some potential sources of limitation of the MDECR microcrystalline cells and remind the experiments and results which rule them out.

4.4.5.1   The doped layers   The exact same doped layers can lead to $8.3\,\%$ solar cells when the intrinsic layer is deposited in another RF-CCP reactor from the decomposition of SiF_4, Ar and H_2 [47]. This is a strong indication that the problem is not the doped layers.

4.4.5.2   The hydrogen-rich MDECR plasma   At the beginning of the deposition of the intrinsic layer in ATOS, hydrogen from the MDECR high density plasma could diffuse inside the thin p-doped layer and react with the boron atoms to form boron hydrides which
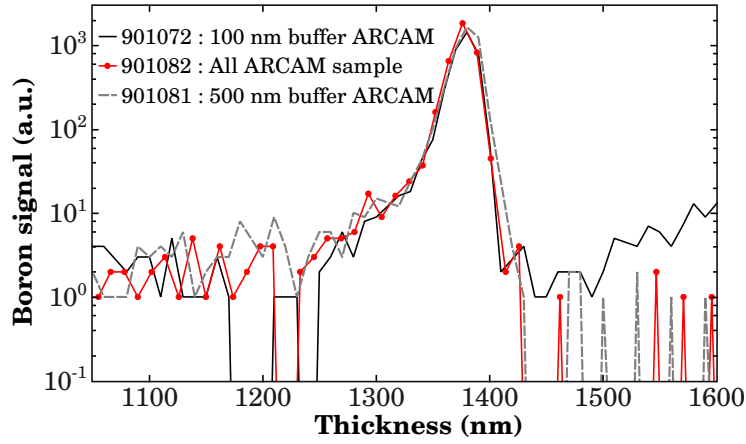
Figure IV.86 – *Superposition of the boron profiles of three different samples : See text for their detailed description.*

would then be pumped away. Such a phenomenon would create defects, reduce the electric field and cause the p/i interface not to be sharp. But again, the special cells which had an ARCAM buffer layer of 400 nm or more have shown no noteworthy improvement, thus demonstrating that this potential problem is not responsible for the limitation of our cells.

To further prove this point, Figure IV.86 shows the superposition of the SIMS boron profiles of three different samples. They are all on non-textured ZnO substrates with p-doped microcrystalline layers deposited with the *exact same* conditions in the reactor ARCAM. Sample 901072 has a 100 nm thick µc buffer layer from the ARCAM (sample from Section 4.3.2 page 155). Sample 901082 is the sample entirely deposited in the ARCAM (Section 4.4.4.1 page 177) and sample 901081 has a very thick 500 nm buffer layer (cell of Section 4.4.2 page 166). One can see that there is an excellent reproducibility of the boron signal in the p-doped layers and that there is no difference at all between the stack entirely processed in ARCAM and the ones having layers grown in ATOS, and no difference either as a function of the protective buffer layer thickness.

4.4.5.3   Boron diffusion from the p-doped layer   Some authors (like in [51]) attribute the degradation of their microcrystalline cell performance at high temperatures to enhanced diffusion of boron from the p layer and to defect formation at the p/i interface. Again, the cells we deposited at low temperatures (down to 150 °C, see Section 3.7 page 130) showed no enhanced performance and the comparisons of Figure IV.86 show no degradation of the p-doped layer due to the MDECR plasma.

4.4.5.4   Heating of the Transparent Conductive Oxide due to microwave absorption   This question is still currently studied but the first pyrometry tests carried out on glass covered by SnO_2 exposed to 20 seconds of microwave injection (1 kW) *without plasma* resulted in an increase of only 5 °C for an initial temperature of around 150 °C. This amplitude of heating is very different from the increase from 0 °C to 175 °C in 1.6 second presented in [103].

Furthermore, for magnetic field intensities lower than 875 Gauss, the left hand polarized (LHP) and the right hand polarized (RHP) modes of the microwave electric field cannot propagate for densities higher than a value between n_c and $2 n_c$, depending on the magnetic field intensity (see the solutions of the dispersion relation as a function of the magnetic field

intensity and of the plasma density page 318 of [104]) : n_c is the critical density, defined by $\omega_{pe} = \omega_{MW}$, where ω_{pe} is the plasma pulsation and ω_{MW} is the microwave pulsation. This gives a critical density $n_c = \omega_{MW}^2 \, \varepsilon_0 \, m_e \, / \, q_e^2 = 7.5 \times 10^{10} \, \mathrm{cm}^{-3}$ for our $2.45\,\mathrm{GHz}$ electric field. As a consequence, the microwave power can reach the substrate only if there is a "path" of low density, which is not very likely.

4.4.6   Interface treatments

The quality of the interfaces is of course of crucial importance for the cell performance. On the other hand, it is certainly very difficult to quantify it precisely. It is generally thought that e.g. oxidation or a too energetic ion bombardment can have detrimental effects on the interfaces, such as creating defects which will enhance recombination or trapping. If the latter phenomenon occurs preferentially for one carrier type, it can also induce a charging effect.

To test different plasma treatments at the p-i and i-n interfaces is obviously extremely time-consuming and it was not possible to make a systematic study of their impact. Nonetheless, a few attempts have been carried out and one is exposed here.

The following comparison of two plasma treatments has been done after the installation of the load-lock, during the series in microwave power (Section 3.8 page 135). The structure of the two cells was exactly the same : textured ZnO / p-doped µc-Si:H layer (ARCAM) / 120 nm of intrinsic µc-Si:H buffer layer (ARCAM) / treatment in ATOS / 1 µm intrinsic µc-Si:H layer at a reduced MW power of 1 kW (ATOS) / H_2 plasma treatment (ARCAM) / n-doped a-Si:H layer (ARCAM) / silver contacts. The difference between the two cells is the treatment between the buffer layer and the ATOS layer :

- One cell has been exposed to a pure H_2 plasma (flow rate of 50 sccm) during 30 seconds without any RF power fed to the substrate holder (floating potential).
- The other cell has been exposed to a H_2/Ar plasma (both flow rates of 50 sccm) during 40 seconds with 5 W of injected RF power.
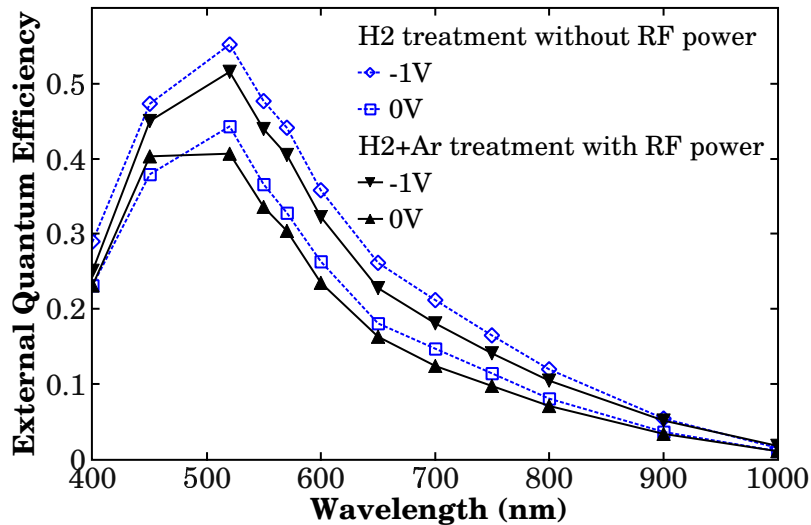

Figure IV.87 – *Effect of two different plasma treatments at the ARCAM/ATOS interface on the spectral responses measured at 0V and −1V.*

ATOS treatment	FF	R_p	R_s	J_{sc}	V_{oc}	Efficiency
H_2	49 %	426 $\Omega\,cm^2$	10.8 $\Omega\,cm^2$	7.0 mA/cm^2	260 mV	0.89 %
H_2+Ar	47 %	443 $\Omega\,cm^2$	15.9 $\Omega\,cm^2$	6.6 mA/cm^2	304 mV	0.94 %

Table IV.18 – *Effect of two different plasma treatments at the ARCAM/ATOS interface on the cell performance.*

The spectral responses of the cells and their $J(V)$ characteristics are presented in Figure IV.87 and Table IV.18 respectively. One can see that the variation due the two plasma treatments is quite small. The two cells present a problem of collection, as seen on their external quantum efficiencies measured with a negative bias voltage (e.g. a relative increase of 27 % from 0 V to −1 V at 520 nm for the H_2+Ar treatment case). The higher ion bombardment energy of the H_2+Ar treatment results in a lower current density but in a higher open-circuit voltage.

As a conclusion, a systematic optimization of such plasma treatments at the ARCAM/ATOS and ATOS/ARCAM interfaces, with and without buffer layers, with different gas mixtures and plasma conditions could be a promising topic of research if the cell performance is affected by oxidation during the transfers from one reactor to the other.

4.5 Conclusion on the investigations into the limitations of the microcrystalline material and solar cells

This part of this chapter was a discussion on all the potential sources of limitation of our material and devices that we have reviewed during this three year project.

With the use of a large range of diagnostics and of numerous original tests, we have been able to successfully solve or rule out several potential risks :

- We studied the design of the reactor and the possibility of a leak of water from the antenna cooling system. We made sure they are vacuum tight at room temperature.

- We carried out two SIMS measurements to ensure that the metallic species contaminations are low in the reactor ATOS.
- We investigated on the origin of fluorine and carbon. Indeed, the concentration of F in the MDECR films can be up to 75 times higher than in the RF-CCP layers. Depositing a-Si:H without microwave power, only with RF power on the substrate holder, led to a reduction of F by a factor 13, so that the teflon of the antennas could be its source.
- Depending on the deposition conditions, the oxygen concentrations in the reactor ATOS had always been in the range $10^{20} - 10^{21}\,cm^{-3}$. The technical solution of the installation of a load-lock reduced this level to the satisfactory value of $\sim 1 \times 10^{19}\,cm^{-3}$. The N level has also been improved and could reach values as low as $2 \times 10^{16}\,cm^{-3}$.
- The rise of the oxygen signal seen on the SIMS profiles before the Si/ZnO interface could have been due to a diffusion of oxygen from the ZnO inside the silicon matrix, but it has been proven to be due to the presence of holes at the bottom of the craters.
- SIMS has also been used to make sure that the boron concentration profile of the p-doped layer is not affected by the MDECR plasma.

- We also focused on the issue of the incubation layer. The evolution of the plasma emission monitored by OES allowed us to conclude that its formation is not correlated with the transient in plasma chemistry after the ignition, which lasts less than one second. We found out that an increase of the substrate surface temperature is not necessary to induce the start of the crystallization and that reducing the deposition rate seems to help to promote the early crystallization of the growing film.

- We have proposed Raman spectroscopy at high wavenumbers as a new method to quickly identify deposition conditions leading to highly crystallized materials with interconnected voids prone to post-oxidation. The advantage of this method is that it can be used for films on glass or even directly on cells. By combining XRD, Raman spectroscopy, FTIR and SIMS, a link between the crystallographic orientation, the presence of narrow peaks of absorption around $2100\,\mathrm{cm}^{-1}$ and the post-oxidation has been established.

- The risk of degradation of the cell performance due to too high substrate temperatures has been studied by annealing tests on cells entirely processed in the RF-CCP reactor and no tremendous degradation of the microcrystalline cell has been found.

Interestingly, the failure of the heating element of the first substrate holder led us to the discovery of the possibility to heat the glass substrates at high temperatures by accelerating the argon ions with a high RF power. One sample with a highly crystallized incubation layer (F_c of 77 %) has been obtained with this pre-heating procedure.

We also analyzed the effect of some interface treatments on the cells and of buffer layers. We processed very particular structures with several hundreds of nanometers of the intrinsic layer deposited in the RF-CCP reactor and concluded that these cells are still degraded by the ATOS layer, even with the load-lock. Simulation proposed that the high density of trapped electrons in the ATOS layer repels electrons away from the n-doped layer and to attracts the holes away from the p-doped layer.

Some questions still remain unexplained, such as the tremendous effect of the ion energy on the chemical composition, even after the installation of the load-lock (e.g. factor 7 in O, factor 42 in C, factor 2 in H). Also, the possible dependence of the material properties as a function of the substrate (glass vs texturized Transparent Conductive Oxide with a p-doped µc-Si:H layer on top) has to be further studied.

Conclusion of the chapter on microcrystalline silicon films and solar cells

This chapter has first presented some general aspects of the microcrystalline silicon material and solar cells. Then, we analyzed in detail the results of the extensive parametric studies that we carried out. Finally, we ruled out or solved many potential sources of limitation of the material and device quality.

Since there is not only one microcrystalline silicon but many different types of microcrystalline silicon, we will now sum up the main original characteristics of the Matrix Distributed Electron Cyclotron Resonance material. We will also remind the unique properties of the MDECR solar cells.

The MDECR microcrystalline silicon :

- It can be deposited at very high rates (up to $28\,\text{Å/s}$). Provided the microwave power is sufficient, the growth rate scales linearly with the silane flow rate. It is possible to obtain a crystallized material from the decomposition of pure silane, without addition of hydrogen. This is due to the very efficient dissociation achieved in the plasma and to the resulting high atomic hydrogen flux on the surface. Uniform depositions on substrates as large as wanted can be easily achieved, just by expanding the matrix of microwave applicators.
- With the MDECR technology, the transition from amorphous to microcrystalline material can take place at *constant* deposition rate by increasing the microwave power (Section 3.8 page 135).
- The films can show great electrical properties, e.g. diffusion lengths of holes in the direction parallel to the substrate as high as $250\,\text{nm}$ as measured by the SSPG technique and densities of states as low as $5 \times 10^{15}\,\text{cm}^{-3}\,\text{eV}^{-1}$ at $0.6\,\text{eV}$ below the conduction band as estimated by the MPC diagnostic.

- Before the installation of the load-lock, great levels of contaminations could be observed (see for example Figure IV.70 page 169 for a striking comparison with the material from the RF-CCP reactor ARCAM). With the load-lock, satisfactory levels of oxygen and nitrogen ($1 \times 10^{19}\,\text{cm}^{-3}$ and $2 \times 10^{16}\,\text{cm}^{-3}$ respectively) have been achieved.
- The hydrogen concentration is always high in the MDECR material, as compared to the reference RF-CCP µc-Si:H. For example, a ratio of 3.8 was found by SIMS for the very porous condition at floating potential of the first series in bias. On the other hand, we managed to significantly reduce the void fraction obtained in our ellipsometry fits from values that could be as high as $\sim 15\,\%$ for some initial depositions, down to $\sim 3\,\%$. Despite this, problems of post-oxidation are often noticed.

- Although on glass the models of ellipsometry always indicate a less crystallized layer at the beginning of the growth, it seems to be possible to partially crystallize it by reducing the deposition rate and with energetic ion bombardment.

- From the few XRD measurements carried out, the films can be preferentially (111), (110) or (311) oriented, depending on the deposition conditions. Ion bombardment seems to favor the (110) orientation and sometimes also to promote the growth of bigger (110) crystallites. There seems to be two size populations : the (111) grains are

always around a factor of 2 bigger than the (110) and (311) grains.

- A surprising property of MDECR µc-Si:H is that the material does not seem to evolve a lot with thickness. For example, no columnar structures can be seen on AFM images, even for 1.5 µm thick films (except at microwave powers lower than 1.5 kW). The size of the crystallites is not seen to increase for thicknesses of 1 µm to 1.5 µm on XRD spectra. The electrical properties of the 0.3 µm and 1 µm thick films in the first series in bias have been found to be close.

The MDECR microcrystalline cells :

- They unfortunately always showed very low current densities ($< 8\,\mathrm{mA/cm^2}$), in particular, due to a very low response in the red.
- The spectral responses are often greatly enhanced with a negative voltage applied.
- Surprisingly, the annealing treatment (30 minutes at 150 °C) never improves the cell performance.
- Despite the reduction of the oxygen concentration by a factor of ten after the installation of the load-lock, the cell performance stayed unchanged. In addition to the chemical composition, the diffusion length has also been tremendously improved, from 40 nm to 250 nm, without any effect on the cell efficiencies (see Table IV.11 page 142). This further supports the fact that there is some sort of decorrelation between the material quality and the cell performance.

Future work

We will now list some ideas to continue the optimization of the MDECR deposition of microcrystalline solar cells.

The reactor :

- The size of the substrate holder could be drastically reduced (as well as the size of the substrates, e.g. from $10\,\mathrm{cm} \times 10\,\mathrm{cm}$ to $2.5\,\mathrm{cm} \times 2.5\,\mathrm{cm}$) in order to lower its thermal mass and to limit the heating and cooling times. This way, more depositions per day could be performed.
- In order to avoid the formation of high sticking coefficient radicals, the gas injection configuration could be modified to use hydrogen as a "vector gas", introduced behind the ECR zones, and to inject silane close to the substrate holder, like in [85].
- Finally, a pulsed microwave generator could be used to see if it brings any improvements.

Some of the material properties could still be improved :

- the photo- to dark conductivity ratios,
  As a comparison, the high efficiency cells of the authors of [63] all correspond to materials having ratios of ~ 400 or more, while our values have always been significantly lower. They propose that the optimization of the material at the amorphous/microcrystalline transition on glass should be based on improving this parameter.
- the TRMC mobilities and lifetime,
- the presence of a less crystallized incubation layer for all the films deposited on glass,
- the absence of large grains on the ellipsometry spectra,

- also, the preferential (111) orientation of some films should also be avoided.

The diagnostics :

- The sensitivity of ellipsometry to the crystalline fraction could maybe be improved by fitting the amorphous fraction with a Tauc-Lorentz dispersion law instead of using a standard dielectric function.

- The usefulness of new diagnostics like Electron Spin Resonance, the Time Of Flight technique to measure the mobility-lifetime product of electrons and holes [25], Diffusion-induced time resolved microwave conductivity to determine the ambipolar mobility [23], Small Angle X-ray Scattering, Photothermal Deflection Spectroscopy or Constant Photocurrent Method should be explored in order to look for other limitations of the material.

- New ways to really characterize the transport *perpendicular* to the substrate have to be used, for example :
    - the Surface Photovoltage method (SPV) to obtain the diffusion length of holes perpendicular to the substrate with sandwich contacts, which can even be performed directly on a solar cell [17],
    - AFM with a conductive cantilever [15],
    - or AC conductivity measurements.

- Transmission Electron Microscopy (TEM) should be carried out to better evidence the presence or the absence of a less crystallized layer *in the cells* at the beginning of the intrinsic layer growth.

The depositions :

- Optimizing depositions from SiF_4+H_2 mixtures could bring breakthroughs with a completely new chemistry and a control of the hydrogen flux on the growing surface (by the H_2 flow rate) independent from the deposition rate (given by the SiF_4 flow rate).

- The effect of the addition of a very small flow rate of trimethylboron (TMB, $B(CH_3)_3$), resulting in micro-doping, could be tested.

- A detailed study of the influence of the substrate type has to be carried out (e.g. isolating *vs* conducting, floating *vs* in contact with the RF biased part of the substrate holder, flat *vs* rough, glass *vs* p-doped µc-Si:H layer).

- The emission of energetic UV radiations by excited hydrogen molecules in the plasma could be a problem for the film quality.

- Finally, we mainly worked on high crystallinity materials during this PhD and conditions close to the a-Si:H/µc-Si:H transition should now be invested.

The cells :

- The greater H concentration on glass than on ZnO for co-deposited films has to be confirmed. A potential explanation could be the risk of absorption of the microwaves by the TCO.

- The systematic presence of holes in the craters during SIMS sputtering when the sample contains layers from ATOS, and their absence when the sample is entirely processed in the RF-CCP reactor, should be investigated.

- Depositing the intrinsic layer with deuterated silane and measuring the profile of deuterium by SIMS would show how deep it is diffusing in the buffer layer and would be an additional way of studying the risk of deterioration of the p-doped layer and of the ZnO by hydrogen.

- Although it is an extremely time-consuming task, more efforts could be dedicated to a systematic optimization of the interface treatments.
- During this work, we focused on the p-i-n structure. More efforts have to be dedicated to n-i-p cells, with an amorphous or a microcrystalline n-doped layer.

Bibliography

[1] Satyendra Kumar, B. Drevillon, and C. Godet. In situ spectroscopic ellipsometry study of the growth of microcrystalline silicon. *Journal of Applied Physics*, 60(4):1542–1544, 1986.

[2] J. Meier, R. Flückiger, H. Keppner, and A. Shah. Complete microcrystalline p-i-n solar cell – Crystalline or amorphous cell behavior ? *Applied Physics Letters*, 65(7):860–862, 1994.

[3] J. P. Kleider, C. Longeaud, R. Brüggemann, and F. Houzé. Electronic and topographic properties of amorphous and microcrystalline silicon thin films. *Thin Solid Films*, 383(1-2):57 – 60, 2001.

[4] S. Ray, S. Mukhopadhyay, T. Jana, and R. Carius. Transition from amorphous to microcrystalline Si:H: effects of substrate temperature and hydrogen dilution. *Journal of Non-Crystalline Solids*, 299-302(Part 2):761 – 766, 2002.

[5] P. St'ahel, S. Hamma, P. Sládek, and P. Roca i Cabarrocas. Metastability studies in silicon thin films: from short range ordered to medium and long range ordered materials. *Journal of Non-Crystalline Solids*, 227-230(Part 1):276 – 280, 1998.

[6] F. Finger, R. Carius, T. Dylla, S. Klein, S. Okur, and M. Günes. Stability of microcrystalline silicon for thin film solar cell applications. *IEE Proc. – Circuits Devices Syst.*, 150(4):300–308, August 2003.

[7] E. A. G. Hamers, A. Fontcuberta i Morral, C. Niikura, R. Brenot, and P. Roca i Cabarrocas. Contribution of ions to the growth of amorphous, polymorphous, and microcrystalline silicon thin films. *Journal of Applied Physics*, 88(6):3674–3688, 2000.

[8] U. Kroll, J. Meier, P. Torres, J. Pohl, and A. Shah. From amorphous to microcrystalline silicon films prepared by hydrogen dilution using the VHF (70 MHz) GD technique. *Journal of Non-Crystalline Solids*, 227-230(Part 1):68 – 72, 1998.

[9] P. Roca i Cabarrocas, P. Bulkin, D. Daineka, T. H. Dao, P. Leempoel, P. Descamps, T. Kervyn de Meerendre, and J. Charliac. Advances in the deposition of microcrystalline silicon at high rate by distributed electron cyclotron resonance. *Thin Solid Films*, 516(20):6834–6838, August 2008.

[10] L. Houben, M. Luysberg, P. Hapke, R. Carius, F. Finger, and H. Wagner. Structural properties of microcrystalline silicon in the transition from highly crystalline to amorphous growth. *Philosophical Magazine A*, 77, 1998.

[11] J. Meier, S. Dubail, J. Cuperus, U. Kroll, R. Platz, P. Torres, J. A. Anna Selvan, P. Pernet, N. Beck, N. Pellaton Vaucher, Ch. Hof, D. Fischer, H. Keppner, and A. Shah. Recent progress in micromorph solar cells. *Journal of Non-Crystalline Solids*, 227-230(Part 2):1250 – 1256, 1998.

[12] N. Beck, J. Meier, J. Fric, Z. Remes, A. Poruba, R. Flückiger, J. Pohl, A. Shah, and M. Vanecek. Enhanced optical absorption in microcrystalline silicon. *Journal of Non-Crystalline Solids*, 198-200(Part 2):903 – 906, 1996. Amorphous Semiconductors-Science and Technology.

[13] A. Poruba, A. Fejfar, Z. Remeš, J. Špringer, M. Vaneček, J. Kočka, J. Meier, P. Torres, and A. Shah. Optical absorption and light scattering in microcrystalline silicon thin films and solar cells. *Journal of Applied Physics*, 88(1):148–160, 2000.

[14] R. Brenot, R. Vanderhaghen, B. Drévillon, and P. Roca i Cabarrocas. Real-time measurement of the evolution of carrier mobility in thin-film semiconductors during growth. *Applied Physics Letters*, 74(1):58–60, 1999.

[15] B. Rezek, J. Stuchlík, A. Fejfar, and J. Kočka. Local characterization of electronic transport in microcrystalline silicon thin films with submicron resolution. *Applied Physics Letters*, 74(10):1475–1477, 1999.

[16] J. Kocka, A. Fejfar, H. Stuchlíková, J. Stuchlík, P. Fojtík, T. Mates, B. Rezek, K. Luterová, V. Svrcek, and I. Pelant. Basic features of transport in microcrystalline silicon. *Solar Energy Materials and Solar Cells*, 78(1-4):493 – 512, 2003. Critical review of amorphous and microcrystalline silicon materials and solar cells.

[17] V. Svrcek, A. Fejfar, P. Fojtik, T. Mates, A. Poruba, H. Stuchlikova, I. Pelant, J. Kocka, Y. Nasuno, M. Kondo, and A. Matsuda. Importance of the transport isotropy in μc-Si:H thin films for solar cells deposited at low substrate temperatures. *Journal of Non-Crystalline Solids*, 299-302(Part 1):395 – 399, 2002.

[18] A. V. Shah, J. Meier, E. Vallat-Sauvain, N. Wyrsch, U. Kroll, C. Droz, and U. Graf. Material and solar cell research in microcrystalline silicon. *Solar Energy Materials and Solar Cells*, 78(1-4):469 – 491, 2003. Critical review of amorphous and microcrystalline silicon materials and solar cells.

[19] John Y. W. Seto. The electrical properties of polycrystalline silicon films. *Journal of Applied Physics*, 46(12):5247–5254, 1975.

[20] C. Droz, M. Goerlitzer, N. Wyrsch, and A. Shah. Electronic transport in hydrogenated microcrystalline silicon: similarities with amorphous silicon. *Journal of Non-Crystalline Solids*, 266-269(Part 1):319 – 324, 2000.

[21] M. Goerlitzer, P. Torres, C. Droz, and A. Shah. Extension of the a-Si:H electronic transport model to μc-Si:H: use of the $\mu^0\tau^0$ product to correlate electronic transport properties and solar cell performances. *Solar Energy Materials and Solar Cells*, 60(2):195 – 200, 2000.

[22] J. Hubin, A. V. Shah, E. Sauvain, and P. Pipoz. Consistency between experimental data for ambipolar diffusion length and for photoconductivity when incorporated into the "standard" defect model for a-Si:H. *Journal of Applied Physics*, 78(10):6050–6059, 1995.

[23] R. Brenot, R. Vanderhaghen, B. Drévillon, P. Roca i Cabarrocas, R. Rogel, and T. Mohammed-Brahim. Transport mechanisms in hydrogenated microcrystalline silicon. *Thin Solid Films*, 383(1-2):53 – 56, 2001.

[24] M. Goerlitzer, N. Beck, P. Torres, J. Meier, N. Wyrsch, and A. Shah. Ambipolar diffusion length and photoconductivity measurements on "midgap" hydrogenated microcrystalline silicon. *Journal of Applied Physics*, 80(9):5111–5115, 1996.

[25] M. Goerlitzer, P. Torres, N. Beck, N. Wyrsch, H. Keppner, J. Pohl, and A. Shah. Structural properties and electronic transport in intrinsic microcrystalline silicon deposited by the VHF-GD technique. *Journal of Non-Crystalline Solids*, 227-230(Part 2):996 – 1000, 1998.

[26] Yasuo Yamamoto, Hideshi Nomura, Takao Tanaka, Mineo Hiramatsu, Masaru Hori, and Toshio Goto. Measurement of Absolute Densities of Si, SiH and SiH_3 in Electron Cyclotron Resonance SiH_4/H_2 Plasma. *Jpn. J. Appl. Phys.*, 33:4320–4324, 1994.

[27] John Robertson. Thermodynamic model of nucleation and growth of plasma deposited microcrystalline silicon. *Journal of Applied Physics*, 93(1):731–735, 2003.

[28] S. Veprek, Z. Iqbal, and F.-A. Sarott. A thermodynamic criterion of the crystalline-to-amorphous transition in silicon. *Philosophical Magazine B*, 45:137–145, 1982.

[29] R. A. Street. Hydrogen chemical potential and structure of a-Si:H. *Phys. Rev. B*, 43(3):2454–2457, Jan 1991.

[30] Akihisa Matsuda. Growth mechanism of microcrystalline silicon obtained from reactive plasmas. *Thin Solid Films*, 337:1–6, 1999.

[31] C. C. Tsai, G. B. Anderson, R. Thompson, and B. Wacker. Control of silicon network structure in plasma deposition. *Journal of Non-Crystalline Solids*, 114:151–153, December 1989.

[32] T. Akasaka and I. Shimizu. In situ real time studies of the formation of polycrystalline silicon films on glass grown by a layer-by-layer technique. *Applied Physics Letters*, 66(25):3441–3443, 1995.

[33] Chisato Niikura, Naho Itagaki, and Akihisa Matsuda. High rate growth of high-quality microcrystalline silicon films from plasma by interconnected multi-hollow cathode. *Surface and Coatings Technology*, 201(9-11):5463 – 5467, 2007. Proceedings of the Fifth Asian-European International Conference on Plasma Surface Engineering - AEPSE 2005, Proceedings of the Fifth Asian-European International Conference on Plasma Surface Engineering.

[34] S. Hamma and P. Roca i Cabarrocas. In situ correlation between the optical and electrical properties of thin intrinsic and n-type microcrystalline silicon films. *Journal of Applied Physics*, 81(11):7282–7288, 1997.

[35] A. Fontcuberta i Morral and P. Roca i Cabarrocas. Etching and hydrogen diffusion mechanisms during a hydrogen plasma treatment of silicon thin films. *Journal of Non-Crystalline Solids*, 299–302(1):196–200, April 2002.

[36] A. Fontcuberta i Morral and P. Roca i Cabarrocas. Role of hydrogen diffusion on the growth of polymorphous and microcrystalline silicon thin films. *The European Physical Journal Applied Physics*, 35(3):165–172, September 2006.

[37] K. Saitoh, M. Kondo, M. Fukawa, T. Nishimiya, A. Matsuda, W. Futako, and I. Shimizu. Role of the hydrogen plasma treatment in layer-by-layer deposition of microcrystalline silicon. *Applied Physics Letters*, 71(23):3403–3405, 1997.

[38] A. Asano. Effects of hydrogen atoms on the network structure of hydrogenated amorphous and microcrystalline silicon thin films. *Applied Physics Letters*, 56(6):533–535, 1990.

[39] A.A. Howling, B. Strahm, and Ch Hollenstein. Non-intrusive plasma diagnostics for the deposition of large area thin film silicon. *Thin Solid Films*, 517(23):6218 – 6224, 2009. Proceedings on the Sixth Symposium on Thin Films for Large Area Electronics.

[40] P. Bulkin, A. Hofrichter, R. Brenot, and B. Drévillon. Deposition of microcrystalline silicon in an integrated distributed electron cyclotron resonance PECVD reactor. *Thin Solid Films*, 337:37–40, 1999.

[41] M. N. van den Donker, B. Rech, F. Finger, W. M. M. Kessels, and M. C. M. van de Sanden. Highly efficient microcrystalline silicon solar cells deposited from a pure SiH_4 flow. *Applied Physics Letters*, 87(26):263503, 2005.

[42] Hajime Shirai, Debajyoti Das, Jun ichi Hanna, and Isamu Shimizu. A novel preparation technique for preparing hydrogenated amorphous silicon with a more rigid and stable si network. *Applied Physics Letters*, 59(9):1096–1098, 1991.

[43] S. Hamma and P. Roca i Cabarrocas. Low-temperature growth of thick intrinsic and ultrathin phosphorous or boron-doped microcrystalline silicon films: Optimum crystalline fractions for solar cell applications. *Solar Energy Materials and Solar Cells*, 69(3):217 – 239, 2001.

[44] K. Postava, H. Sueki, M. Aoyama, T. Yamaguchi, K. Murakami, and Y. Igasaki. Doping effects on optical properties of epitaxial ZnO layers determined by spectroscopic ellipsometry. *Applied Surface Science*, 175-176:543 – 548, 2001.

[45] P. Roca i Cabarrocas, J. B. Chévrier, J. Huc, A. Lloret, J. Y. Parey, and J. P. M. Schmitt. A fully automated hot-wall multiplasma-monochamber reactor for thin film deposition. *Journal of Vacuum Science & Technology A: Vacuum, Surfaces, and Films*, 9(4):2331–2341, 1991.

[46] A. H. M. Smets, T. Matsui, and M. Kondo. Infrared analysis of the bulk silicon-hydrogen bonds as an optimization tool for high-rate deposition of microcrystalline silicon solar cells. *Applied Physics Letters*, 92(3):033506, 2008.

[47] Q. Zhang, E. V. Johnson, Y. Djeridane, A. Abramov, and P. Roca i Cabarrocas. Decoupling crystalline volume fraction and V_{oc} in microcrystalline silicon pin solar cells by using a μc-Si:F:H intrinsic layer. *Physica Status Solidi (RRL) - Rapid Research Letters*, 2(4):154–156, 2008.

[48] Y. Mai, S. Klein, R. Carius, H. Stiebig, X. Geng, and F. Finger. Open circuit voltage improvement of high-deposition-rate microcrystalline silicon solar cells by hot wire interface layers. *Applied Physics Letters*, 87(7):073503, 2005.

[49] O. Vetterl, F. Finger, R. Carius, P. Hapke, L. Houben, O. Kluth, A. Lambertz, A. Muck, B. Rech, and H. Wagner. Intrinsic microcrystalline silicon : A new material for photovoltaics. *Solar Energy Materials and Solar Cells*, 62:97–108, April 2000.

[50] O. Vetterl, A. Lambertz, A. Dasgupta, F. Finger, B. Rech, O. Kluth, and H. Wagner. Thickness dependence of microcrystalline silicon solar cell properties. *Solar Energy Materials and Solar Cells*, 66(1-4):345–351, February 2001.

[51] Yoshiyuki Nasuno, Michio Kondo, Akihisa Matsuda, Hitoshi Fukuhori, and Yoshihiko Kanemitsu. Formation of interface defects by enhanced impurity diffusion in microcrystalline silicon solar cells. *Applied Physics Letters*, 81:3155–3158, 2002.

[52] S. Guha and J. Yang. Microcrystalline silicon solar cells. Technical report, National Renewable Energy Laboratory (NREL) and United Solar Ovonic Corporation, August 2005. `www.nrel.gov/docs/fy05osti/38355.pdf`.

[53] A. Gross, O. Vetterl, A. Lambertz, F. Finger, H. Wagner, and A. Dasgupta. N-side illuminated microcrystalline silicon solar cells. *Applied Physics Letters*, 79(17):2841–2843, 2001.

[54] S. Okur, M. Günes, O. Göktas, F. Finger, and R. Carius. Electronic transport properties of microcrystalline silicon thin films prepared by VHF-PECVD. *Journal of Materials Science: Materials in Electronics*, 15:187–191, 2004.

[55] U. Kroll, J. Meier, A. Shah, S. Mikhailov, and J. Weber. Hydrogen in amorphous and microcrystalline silicon films prepared by hydrogen dilution. *Journal of Applied Physics*, 80(9):4971–4975, 1996.

[56] K. Yamamoto, M. Yoshimi, Y. Tawada, Y. Okamoto, A. Nakajima, and S. Igari. Thin-film poly-Si solar cells on glass substrate fabricated at low temperature. *Applied Physics A : Materials Science & Processing*, 69:179–185, 1999.

[57] Takuya Matsui, Masaharu Tsukiji, Hiroyuki Saika, Toshihiko Toyama, and Hiroaki Okamoto. Correlation between Microstructure and Photovoltaic Performance of Polycrystalline Silicon Thin Film Solar Cells. *Jpn. J. Appl. Phys.*, 41:20–27, 2002.

[58] Stefan Klein, Friedhelm Finger, Reinhard Carius, and Jan Lossen. Improved deposition rates for µc-si:h at low substrate temperature. *Thin Solid Films*, 501(1-2):43 – 46, 2006. Proceedings of the Third International Conference on Hot-Wire CVD (Cat-CVD) Process.

[59] Madhumita Nath, P. Roca i Cabarrocas, E.V. Johnson, A. Abramov, and P. Chatterjee. The open-circuit voltage in microcrystalline silicon solar cells of different degrees of crystallinity. *Thin Solid Films*, 516(20):6974 – 6978, 2008. Proceedings on Advanced Materials and Concepts for Photovoltaics EMRS 2007 Conference, Strasbourg, France.

[60] E.V. Johnson, M. Nath, P. Roca i Cabarrocas, A. Abramov, and P. Chatterjee. Why does the open-circuit voltage in a micro-crystalline silicon PIN solar cell decrease with increasing crystalline volume fraction? *Journal of Non-Crystalline Solids*, 354(19-25):2455 – 2459, 2008. Amorphous and Nanocrystalline Semiconductors, 22nd International Conference on Amorphous and Nanocrystalline Semiconductors - Science and Technology.

[61] M. N. van den Donker, S. Klein, B. Rech, F. Finger, W. M. M. Kessels, and M. C. M. van de Sanden. Microcrystalline silicon solar cells with an open-circuit voltage above 600 mV. *Applied Physics Letters*, 90(18):183504, 2007.

[62] E. Iwaniczko, Y. Xu, R. E. I. Schropp, and A. H. Mahan. Microcrystalline silicon for solar cells deposited at high rates by hot-wire CVD. *Thin Solid Films*, 430(1-2):212 – 215, 2003. Proceedings of the Second International Conference on Cat-CVD (Hot Wire CVD) Process.

[63] O. Vetterl, A. Groß, T. Jana, S. Ray, A. Lambertz, R. Carius, and F. Finger. Changes in electric and optical properties of intrinsic microcrystalline silicon upon variation of the structural composition. *Journal of Non-Crystalline Solids*, 299-302(Part 2):772 – 777, 2002.

[64] R. B. Bergmann and J. H. Werner. The future of crystalline silicon films on foreign substrates. *Thin Solid Films*, 403-404:162–169, February 2002.

[65] Y. Nasuno, M. Kondo, and A. Matsuda. Microcrystalline silicon thin-film solar cells prepared at low temperature using PECVD. *Solar Energy Materials and Solar Cells*, 74(1-4):497 – 503, 2002.

[66] A. Abramov and P. Roca i Cabarrocas. Addition of SiF_4 to standard SiH_4+H_2 plasma: an effective way to reduce oxygen contamination in µc-Si:H films, 2010.

[67] Jr. G. E. Jellison, M. F. Chisholm, and S. M. Gorbatkin. Optical functions of chemical vapor deposited thin-film silicon determined by spectroscopic ellipsometry. *Applied Physics Letters*, 62(25):3348–3350, 1993.

[68] E. A. G. Hamers, J. Bezemer, and W. F. van der Weg. Positive ions as growth precursors in plasma enhanced chemical vapor deposition of hydrogenated amorphous silicon. *Applied Physics Letters*, 75(5):609–611, 1999.

[69] J. K. Rath. Low temperature polycrystalline silicon: a review on deposition, physical properties and solar cell applications. *Solar Energy Materials and Solar Cells*, 76(4):431 – 487, 2003.

[70] B. Kalache, A. I. Kosarev, R. Vanderhaghen, and P. Roca i Cabarrocas. Ion bombardment effects on microcrystalline silicon growth mechanisms and on the film properties. *Journal of Applied Physics*, 93(2):1262–1273, 2003.

[71] H. Jia, J. K. Saha, N. Ohse, and H. Shirai. High-density microwave plasma of SiH_4/H_2 for high rate growth of highly crystallized microcrystalline silicon films. *Eur. Phys. J. Appl. Phys.*, 33:153–159, 2006.

[72] Thien Hai DAO. *Dépôt de couches minces de silicium à grande vitesse par plasma MDECR*. PhD thesis, École Polytechnique, May 2007.

[73] D. L. Williamson. Microstructure of amorphous and microcrystalline Si and SiGe alloys using X-rays and neutrons. *Solar Energy Materials and Solar Cells*, 78(1-4):41 – 84, 2003. Critical review of amorphous and microcrystalline silicon materials and solar cells.

[74] Mario Birkholz, Erhard Conrad, and Walther Fuhs. Crystallinity of Thin Silicon Films Deposited at Low Temperatures: Combined Effect of Biasing and Structuring the Substrate. *Japanese Journal of Applied Physics*, 40(Part 1, No. 6A):4176–4180, 2001.

[75] Sanjay K. Ram, Laurent Kroely, Pavel Bulkin, and Pere Roca i Cabarrocas. Effect of ion energy on structural and electrical properties of intrinsic microcrystalline silicon layer deposited in matrix distributed electron cyclotron resonance plasma reactor, 2010.

[76] J. Kocka, H. Stuchlíková, J. Stuchlík, B. Rezek, T. Mates, V. Svrcek, P. Fojtík, I. Pelant, and A. Fejfar. Model of transport in microcrystalline silicon. *Journal of Non-Crystalline Solids*, 299-302(Part 1):355 – 359, 2002.

[77] M. Konuma, H. Curtins, F.-A. Sarott, and S. Veprek. Dependence of electrical conductivity of nanocrystalline silicon on structural properties and the effect of substrate bias. *Philosophical Magazine B*, 55:377–389, 1987.

[78] P. Bulkin, R. Brenot, B. Drévillon, and R. Vanderhaghen. Structure and transport properties of integrated distributed electron cyclotron resonance grown micro-crystalline silicon. *Journal of Non-Crystalline Solids*, 231(3):268 – 272, 1998.

[79] Samir Kasouit. *Mécanismes de croissance et transport dans le silicium microcristallin fluoré. Application aux transistors en couches minces et transfert technologique*. PhD thesis, École Polytechnique, October 2003.

[80] T. Söderström, F.-J. Haug, V. Terrazzoni-Daudrix, X. Niquille, M. Python, and C. Ballif. N/I buffer layer for substrate microcrystalline thin film silicon solar cell. *Journal of Applied Physics*, 104(10):104505, 2008.

[81] J. Meier, S. Dubail, S. Golay, U. Kroll, S. Faÿ, E. Vallat-Sauvain, L. Feitknecht, J. Dubail, and A. Shah. Microcrystalline silicon and the impact on micromorph tandem solar cells. *Solar Energy Materials and Solar Cells*, 74(1-4):457 – 467, 2002.

[82] Y. Nasuno, M. Kondo, and A. Matsuda. Passivation of oxygen-related donors in microcrystalline silicon by low temperature deposition. *Applied Physics Letters*, 78(16):2330–2332, 2001.

[83] Yong Sun, Tatsuro Miyasato, and J. K. Wigmore. Possible origin for (110)-oriented growth of grains in hydrogenated microcrystalline silicon films. *Applied Physics Letters*, 70(4):508–510, 1997.

[84] Jhantu Kumar Saha, Naoyuki Ohse, Kazu Hamada, Hiroyuki Matsui, Tomohiro Kobayashi, Haijun Jia, and Hajime Shirai. Fast deposition of microcrystalline Si films from SiH_2Cl_2 using a high-density microwave plasma source for Si thin-film solar cells. *Solar Energy Materials and Solar Cells*, 94(3):524 – 530, 2010.

[85] V.L. Dalal, J.H. Zhu, M. Welsh, and M. Noack. Microcrystalline Si:H solar cells fabricated using ECR plasma deposition. *IEE Proceedings – Circuits, Devices and Systems*, 150(4), August 2003.

[86] M.N. van den Donker, R. Schmitz, W. Appenzeller, B. Rech, W.M.M. Kessels, and M.C.M. van de Sanden. The role of plasma induced substrate heating during high rate deposition of microcrystalline silicon solar cells. *Thin Solid Films*, 511-512:562–566, 2006.

[87] C. Smit, A. Klaver, B.A. Korevaar, A.M.H.N. Petit, D.L. Williamson, R.A.C.M.M. van Swaaij, and M.C.M. van de Sanden. High-rate deposition of microcrystalline silicon with an expanding thermal plasma. *Thin Solid Films*, 491(1-2):280 – 293, 2005.

[88] Cheng-Zhao Chen, Sheng-Hua Qiu, Cui-Qing Liu, Yan-Dan Wu, Ping Li, Chu-Ying Yu, and Xuan ying Lin. Low temperature fast growth of nanocrystalline silicon films by rf-PECVD from SiH_4/H_2 gases: microstructural characterization. *Journal of Physics D: Applied Physics*, 41, 2008.

[89] S. Okur, M. Günes, F. Finger, and R. Carius. Diffusion length measurements of microcrystalline silicon thin films prepared by hot-wire/catalytic chemical vapor deposition (HWCVD). *Thin Solid Films*, 501(1-2):137 – 140, 2006. Proceedings of the Third International Conference on Hot-Wire CVD (Cat-CVD) Process.

[90] T. Kilper, U. Zastrow, D. Hrunski, R. Carius, and A. Gordijn. The influence of oxygen incorporation on the properties μc-si and the performance of μc-si based solar cells, 2008. EMRS conference.

[91] Satoru Somiya, Hirotaka Toyoda, Yoshihiko Hotta, and Hideo Sugai. Suppression of Oxygen Impurity Incorporation into Silicon Films Prepared from Surface-Wave Excited H_2/SiH_4 Plasma. *Japanese Journal of Applied Physics*, 43(11A):7696–7700, 2004.

[92] T. Kilper, W. Beyer, G. Bräuer, T. Bronger, R. Carius, M. N. van den Donker, D. Hrunski, A. Lambertz, T. Merdzhanova, A. Mück, B. Rech, W. Reetz, R. Schmitz, U. Zastrow, and A. Gordijn. Oxygen and nitrogen impurities in microcrystalline silicon deposited under optimized conditions: Influence on material properties and solar cell performance. *Journal of Applied Physics*, 105(7):074509, 2009.

[93] Jan Woerdenweber, Tsvetelina Merdzhanova, Helmut Stiebig, Wolfhard Beyer, and Aad Gordijn. Critical oxygen concentration in hydrogenated amorphous silicon solar cells dependent on the contamination source. *Applied Physics Letters*, 96(10):103505, 2010.

[94] Michio Kondo. Microcrystalline materials and cells deposited by RF glow discharge. *Solar Energy Materials and Solar Cells*, 78(1-4):543 – 566, 2003. Critical review of amorphous and microcrystalline silicon materials and solar cells.

[95] Takuya Matsui, Akihisa Matsuda, and Michio Kondo. High-rate microcrystalline silicon deposition for p-i-n junction solar cells. *Solar Energy Materials and Solar Cells*, 90:3199–3204, November 2006.

[96] E.V. Johnson, L. Kroely, and P. Roca i Cabarrocas. Raman scattering analysis of SiH bond stretching modes in hydrogenated microcrystalline silicon for use in thin-film photovoltaics. *Solar Energy Materials and Solar Cells*, 93(10):1904 – 1906, 2009.

[97] Erik V. Johnson, Laurent Kroely, Mario Moreno, and Pere Roca i Cabarrocas. Characterization of Microcrystalline Silicon by High Wavenumber Raman Scattering. In *MRS Spring Meeting Symposium A proceedings*, 2009.

[98] K. Brühne, M. B. Schubert, C. Köhler, and J. H. Werner. Nanocrystalline silicon from hot-wire deposition – a photovoltaic material? *Thin Solid Films*, 395(1-2):163 – 168, 2001.

[99] M. Fonrodona, D. Soler, J. M. Asensi, J. Bertomeu, and J. Andreu. Studies on grain boundaries in nanocrystalline silicon grown by hot-wire CVD. *Journal of Non-Crystalline Solids*, 299-302(Part 1):14 – 19, 2002.

[100] Madhumita Nath, P. Chatterjee, J. Damon-Lacoste, and P. Roca i Cabarrocas. Criteria for improved open-circuit voltage in a-Si:H(N)/c-Si(P) front heterojunction with intrinsic thin layer solar cells. *Journal of Applied Physics*, 103(3):034506, 2008.

[101] Antara Datta, J. Damon-Lacoste, P. Roca i Cabarrocas, and P. Chatterjee. Defect states on the surfaces of a P-type c-Si wafer and how they control the performance of a double heterojunction solar cell. *Solar Energy Materials and Solar Cells*, 92(11):1500 – 1507, 2008.

[102] Haijun Jia and Hajime Shirai. In situ study on the growth of microcrystalline silicon film using the high-density microwave plasma for si thin film solar cells. *Thin Solid Films*, 506-507:27 – 32, 2006. The Joint Meeting of 7th APCPST (Asia Pacific Conference on Plasma Science and Technology) and 17th SPSM (Symposium on Plasma Science for Materials) - 7th APCPST/17th SPSM.

[103] T. F. Schulze, H. N. Beushausen, T. Hansmann, L. Korte, and B. Rech. Accelerated interface defect removal in amorphous/crystalline silicon heterostructures using pulsed annealing and microwave heating. *Applied Physics Letters*, 95(18):182108, 2009.

[104] James E. Stevens. Electron cyclotron resonance plasma sources. In Oleg A. Popov, editor, *High Density Plasma Sources*, pages 312 – 379. William Andrew Publishing, Park Ridge, NJ, 1996.

Conclusion

The very challenging goal of this work was the high rate deposition of hydrogenated microcrystalline silicon with a Matrix Distributed Electron Cyclotron Resonance (MDECR) plasma source and the incorporation of the optimized material in p-i-n solar cells.

Microcrystalline silicon is a quite "young" material which has only been used as the absorber layer of p-i-n and n-i-p structures for the first time in 1994. MDECR is an even younger technology and our laboratory is the first and only one in the world to use such a prototype for photovoltaic applications. Both this material and this deposition technology carry promises of cost reduction, which is our motivation

This unique project allowed me to discover the whole chain of this research field and resulted in a very satisfactory *global approach*. The first phase was the assembling of this complex new plasma reactor. I was then responsible for its maintenance and its improvement (installation of a load-lock). The second phase consisted in scanning the deposition parameters to optimize the material quality, evaluated by many characterization techniques, and to select the interesting conditions to process p-i-n solar cells.

Chapter I emphasized the strong difference between having good material properties, as characterized by a few diagnostics, and the possibility to obtain a high performance cell with this material. We have also stressed that only a very small number of technologies and laboratories or companies are successful in addressing the very challenging issues specific to high rate deposition of microcrystalline silicon solar cells. In particular, this seems universally very difficult for all high density sources. This is confirmed by the fact that the best microcrystalline cell processed with an ECR plasma source only has a 4.7 % efficiency.

Chapter II gave an overview of some of the most used diagnostics during this PhD. They have been powerful tools to characterize the microstructure of the films, their crystallinity, their chemical composition, their electrical properties and to measure the cell performance. The limitations and potential artefacts of the different techniques have been underlined throughout this manuscript. The question of the *best diagnostic* on which the process of optimization of the material and cell quality should be based is of course a central and crucial debate in this field of research.

Chapter III gave a short historical overview of the evolutions of ECR sources until MDECR in order to better show its numerous advantages : high plasma densities, high deposition rates (up to $60\,\text{Å/s}$ for a-Si:H and $28\,\text{Å/s}$ for µc-Si:H), possibility to expand the matrix of microwave applicators on very large areas, absence of powders, independent control of

the ion bombardment energy. The two reactors used in this work have been presented and characterized.

Section 1 of Chapter IV first exposed some general points about the microcrystalline material. Its complexity has been clearly shown, which induces that the comparison of the samples has to be very methodic. Furthermore, its growth mechanism and its exact transport model are still under debate and require more fundamental research.

Section 2 of Chapter IV gave general points about microcrystalline solar cells and the steps of the µc-Si:H p-i-n cell processing in our laboratory have been detailed.

Section 3 of Chapter IV showed the parametric studies we carried out : we studied the impacts of the gas composition (pure silane or with hydrogen, argon and/or silicon tetrafluoride added), of the ion bombardment energy, of the substrate temperature and of the microwave power. The most important results and the original properties of the MDECR material and cells are summarized in pages 143 to 144. Despite the numerous diagnostics implemented, it is not always straightforward to determine where the optimum in the scan is. The film density and the values of the diffusion length of holes parallel to the substrate (up to 250 nm) have been improved and the initially too high hydrogen, oxygen and nitrogen contents have been reduced, but unfortunately, no impact has been observed on the cell efficiencies, which stayed below 2 %.

Section 4 of Chapter IV is probably the most original part of our work, where we tried to rule out all the potential limitations we could think of. We successfully studied : the risk of water leak from the cooling system of the antennas ; the origin of the fluorine and carbon contaminations in our films ; the levels of metallic impurities ; the degradation of µc p-i-n cells induced by an annealing treatment at high temperature ; the post-oxidation, analyzed by combined Raman spectroscopy, XRD, SIMS and FTIR measurements ; the protection of the p-doped layer by buffer layers of thicknesses in the range $100-500$ nm ; some interface treatments on the cells to "clean" the oxidized surface after the transfers from one reactor to the other. Furthermore, we found out that the p-doped layer does not seem to be damaged by the MDECR hydrogen-rich plasma and that the signal of oxygen before the Si/ZnO interface seen on all the SIMS profiles is not due to oxygen diffusion but to holes at the bottom of the craters. It has been established that the formation of the incubation layer is not related to a transient phase in the plasma chemistry after ignition and that the start of the nucleation is not thermally induced. Finally, the installation of a load-lock helped us to reduce the oxygen levels in our films by a factor of 10.
(A more detailed summary of these results can be found in pages 185 to 186.)

Ideas for further work have been listed in detail in the conclusion of the Chapter IV, page 188.

The MDECR technology has a great potential for photovoltaic application. Yet, the time-scale of a PhD was not enough to solve all the challenges of this exploratory research project. Efforts will keep on being devoted to the improvement of the reactor and the process.

It has to be emphasized that this was the first PhD entirely dedicated to microcrystalline solar cells deposited by MDECR in our laboratory. Thus, the method to study these devices

was not clear at the beginning of my work and had to be optimized. Since the solar cell performance has always been poor, we constantly tried throughout this work to find new diagnostics indicating a problem in the material or in the devices. The *apparent decorrelation* between the material quality and the cell efficiencies forced us to explore a very large set of characterization methods (not all of them were successful and all the results could not be reported in this manuscript) : OES, Langmuir probes, emissive probes, mass spectroscopy, pyrometry, spectroscopic ellipsometry, in-situ real-time multi-wavelengths ellipsometry, polarized and non-polarized Raman spectroscopy, FTIR spectroscopy, activation energy and dark conductivity measurements, SSPC, MPC, SSPG, TRMC, Schottky diodes, SIMS, GD-OES, GD-TOF, EGA, DSC, XRD, AFM, SEM, spectral response measurements, dark and illuminated $J(V)$ curves, variable intensity $J(V)$ curves and computer simulation of the cells. Some of them have only been used qualitatively or briefly tried and it is of course impossible to become an expert in all these methods in three years.

We can once again underline the unique diversity of this rich experimental work : Two different MDECR reactors (Domex and ATOS) have been used, the second one has been assembled from scratch in collaboration with the technicians and engineers of our laboratory. We tried a lot of different configurations with ATOS : we added a load-lock and three different substrate holders were successively used, heated by a resistive element or by lamps. Without heating the substrate holder, we also managed to "pre-heat" the glass substrates with intense ion bombardment. Additionally, the plasma could be sustained only by RF power, without microwave power fed to the antennas. Depositions with a grid installed in front of the substrate holder (in order to reflect the microwaves which might heat the conductive substrates) have also been tried.

More efforts should be dedicated to the improvement of the material itself. Once a deposition condition leading to a material presenting *only* good properties has been found and characterized by *all* the available diagnostics, the next step would be to focus on the interface quality of the cells. A program of detailed ideas for future work has been proposed pages 188 to 190.

Publications

Articles published in peer-reviewed journals

S. N. Abolmasov, **L. Kroely** and P. Roca i Cabarrocas. Negative corona in silane-argon-hydrogen mixtures at low pressures. *Journal of Physics D: Applied Physics*, 41(16):165203 (6pp), July 2008.

S. N. Abolmasov, **L. Kroely** and P. Roca i Cabarrocas. Negative corona discharge: application to nanoparticle detection in rf reactors. *Plasma Sources Science and Technology*, 18(1):015005(6pp), November 2008.

E. V. Johnson, **L. Kroely** and P. Roca i Cabarrocas. Raman scattering analysis of Si–H stretching peaks in hydrogenated microcrystalline silicon. *Solar Energy Materials & Solar Cells*, 93(10):1904-1906, October 2009.

Peer-reviewed proceedings

E. V. Johnson, **L. Kroely**, M. Moreno and P. Roca i Cabarrocas. Characterization of Microcrystalline Silicon by High Wavenumber Raman Scattering. *2009 MRS Spring Meeting Symposium A proceedings*.

S. K. Ram, **L. Kroely**, P. Bulkin and P. Roca i Cabarrocas. Effect of ion energy on structural and electrical properties of intrinsic microcrystalline silicon layer deposited in matrix distributed electron cyclotron resonance plasma reactor. *Physica Status Solidi A*, 207(3):591-594, January 2010.

L. Kroely, S. K. Ram, P. Bulkin and P. Roca i Cabarrocas. Microcrystalline silicon films and solar cells deposited at high rate by Matrix Distributed Electron Cyclotron Resonance (MDECR) plasma. *Physica Status Solidi C*, 7(3-4):517-520, February 2010.

S. K. Ram, **L. Kroely**, S. Kasouit, P. Bulkin and P. Roca i Cabarrocas. Plasma emission diagnostics during fast deposition of microcrystalline silicon thin films in matrix distributed electron cyclotron resonance plasma CVD system. *Physica Status Solidi C*, 7(3-4):553-556, February 2010.

E. V. Johnson, **L. Kroely** and P. Roca i Cabarrocas. Assignment of High Wave-number Absorption and Raman Scattering Peaks in Microcrystalline Silicon. Accepted for publication in the *2010 MRS Spring Meeting proceedings*.

Posters presented in international conferences and workshops

Laurent Kroely, Pere Roca i Cabarrocas, Sergey Abolmasov, Pavel Bulkin, Dmitri Daineka and Thien Hai Dao. Transient effects in the growth of microcrystalline silicon films from pure silane in MDECR plasmas. *CIP07 – 16th International Colloquium on Plasma Processes*, in Toulouse (France), June 2007.

Laurent Kroely, Sanjay K. Ram, Pere Roca i Cabarrocas and Pavel Bulkin. Optimization of microcrystalline silicon thin film solar cells deposited at high rate by distributed microwave plasma. *European School "Physics of solar cells : from basics to last developments"*, in Les Houches (France), February 2009.

Posters presented in national conferences and workshops

Laurent Kroely, Pere Roca i Cabarrocas, Dmitri Daineka, Pavel Bulkin and Tatiana Novikova. Optimisation de cellules photovoltaïques multispectrales à base de couches minces de silicium déposées à grande vitesse. *Électricité solaire photovoltaïque, Colloque national ADEME–ANR*, in Aix-les-Bains (France), March 2007.

Laurent Kroely, Pere Roca i Cabarrocas, Sergey Abolmasov, Pavel Bulkin and Dmitri Daineka. Comment mesurer la température du substrat dans un réacteur MDECR de dépôt de silicium microcristallin ? *6èmes Journées du Réseau Plasmas Froids*, in Bonascre (France), October 2007.

Acknowledgements

Acknowledgements

Including my Master internship, I stayed in this lab around four years, during which I bought $\sim 3 \times 10^3$ coffees to Chantal Geneste. I also would like to thank the two other secretaries Laurence Corbel and Carine Roger, and Frédéric Liège and Éric Paillassa for their help with computers.

This lab is so full of great people that I am $100\,\%$ sure that I will forget several in this list but I hope they will forgive me : Nans Pham, Tran Thuat Nguyen, Yassine Djeridane, Thien Hai Dao, Pierre-Jean Alet, Grygoriy Dolgonos, Martin Foldyna, Jérôme Damon Lacoste, Yvan Bonnassieux, Antonello De Martino, Bicher Haj Ibrahim, Oumkelthoum Mintmoustapha, Bernd Marquardt, Ning Ning, Ingrid Stenger, Tatiana Novikova, Jon Mapel, Rosaria Antonelli, Mathieu Diers, Jérémi Bézin, Xavier Renault, Paul Finger, Jean-Éric Bourée, Laurent Baraton, Changseok Lee, Chang-Hyun Kim, Poncho Torres, Marc Chaigneau, all the workers from Total and my badminton partners.

In particular, it was wonderful being followed by so friendly new PhD students such as Martin Labrune[1], Benedict O'Donnell and James Ka-Hyun Kim.

Roelene Botha has been very kind to lend me her substrate holder while mine was broken !

I liked all my office neighbors during these years and they can now leave the door open ...

To sum it up, I think of most of the people from the LPICM as friends rather than as colleagues !

More generally, I would like to warmly thank again :
all the people who corrected this manuscript or gave me feedback on it,
the few people who tried *not* to ask me how the writing was going at the end of my PhD,
all the people who helped me with the preparation of the defense,
and all the people who helped me in some way for my "job hunting".

My family also played a great role during my studies and my PhD and I would like to thank my parents, Matthieu, Mara, Aude, my godmother, my godfather and my grand parents for their support.

It was great being able to relax and exchange with my friends, especially during the intense times of writing : Jérôme, Marie, Arthur, Sophie, Raphaël, Simoné, Camille T, Samuel, Élodie, Cédric, Hélène, Rachael, Julien S, Nathalie (who taught me LaTeX a very very long time ago...), Benoît, Hélène, David, Benoîte, Florence, Olivier, Laurent, Virginie, Camille V, Julien A, Vincent etc ...

Merci à Andrea pour sa patience, son humour et sa douceur ...

---

[1]Stop reading my acknowledgements and go back to work !

Summary in English

High deposition rates on large areas are industrial needs for mass production of microcrystalline silicon (µc-Si:H) solar cells. This doctoral work aims at exploring the usefulness of Matrix Distributed Electron Cyclotron Resonance (MDECR) plasmas to process the intrinsic layer of µc-Si:H p-i-n solar cells at high rates.

With the high dissociation of silane achieved in MDECR plasmas, deposition rates as high as $60\,\text{Å/s}$ and $28\,\text{Å/s}$ have been demonstrated in our lab for amorphous and microcrystalline silicon respectively, without hydrogen dilution. This technique is also promising because it can be easily scaled up on large areas, just by extending the matrix of elementary microwave applicators.

This subject was a unique opportunity to cover the whole chain of this field of research :

A new MDECR reactor has been specially designed and assembled during this project. Its maintenance and its improvement have been important technical challenges : for example, the addition of a load-lock enabled us to lower the oxygen concentration in our films by a factor of 10.

The impact of the deposition parameters (e.g. the ion energy, the substrate temperature, different gas mixtures, the microwave power) has been explored in extensive parametric studies in order to optimize the material quality. Great efforts have been invested in the characterization of the films. Our strategy has been to develop a wide range of diagnostics (ellipsometry, Raman spectroscopy, SIMS, FTIR, XRD, electrical characterizations etc.). Finally, p-i-n cells have been processed with the selected interesting materials.

The successive successful improvements in the material quality (e.g. diffusion lengths of holes parallel to the substrate as high as $250\,\text{nm}$) did unfortunately not result in high efficiency solar cells. Their limited performance is in particular due to a very poor response in the red part of the spectrum resulting in low current densities. Consequently, the potential sources of limitation of the reactor, the material and the device have been studied : e.g. the presence of "cracks" prone to post-oxidation in the highly crystallized materials and the risk of deterioration of the ZnO substrate or of the p-doped layer by a too high process temperature or by hydrogen diffusing from the plasma.

Résumé en Français

La réduction des coûts de production des cellules solaires en silicium microcristallin (µc-Si:H) nécessite de nouvelles techniques innovantes capables de réaliser des dépôts à grande vitesse sur de grandes surfaces. Cette thèse a pour but d'étudier les avantages des sources plasma matricielles distribuées à effet de résonance cyclotronique électronique (MDECR) pour le dépôt de la couche intrinsèque µc-Si:H de cellules p-i-n.

Grâce à la forte dissociation du gaz dans les plasmas MDECR, des vitesses de croissance allant jusqu'à $60\,\text{Å/s}$ pour le silicium amorphe et $28\,\text{Å/s}$ pour le µc-Si:H ont pu être démontrées dans notre laboratoire, et ce, sans dilution du silane dans de l'hydrogène. De plus, par simple répétition du motif des sources micro-onde, la surface traitée peut être augmentée sans limitation technique.

Cette thèse a été l'occasion de découvrir tous les aspects de ce domaine de recherche très riche :

Un nouveau réacteur de dépôt MDECR a été spécialement conçu et assemblé pour ce projet. Son entretien et son amélioration constante ont été des défis techniques importants : l'ajout d'un sas de chargement nous a notamment permis de réduire les niveaux de contamination en oxygène de nos couches par un facteur 10.

Les effets des paramètres de dépôt (énergie des ions, température du substrat, différents mélange de gaz, puissance micro-onde) ont été étudiés en détail au cours de nombreuses études paramétriques pour optimiser la qualité du matériau. La caractérisation des couches a été un enjeu primordial. Pour cela, nous avons choisi de développer une palette très large de diagnostiques (ellipsométrie, spectroscopie Raman, SIMS, FTIR, XRD, mesures électriques etc). Les matériaux intéressants ont été incorporés dans des cellules p-i-n.

Les améliorations successives de la qualité du matériau (par exemple, longueurs de diffusion des trous parallèle au substrat jusqu'à $250\,\text{nm}$) ne se sont malheureusement pas répercutées au niveau des cellules solaires. Leurs rendements limités sont en particulier dûs à de très faibles réponses spectrales dans le rouge, donnant des densités de courants basses. En conséquence, les sources potentielles de limitations au niveau du réacteur, du matériau et des cellules ont été passées en revue : en particulier, nous avons étudié la présence de joints de grains sensibles à la post-oxydation dans le cas des matériaux fortement cristallisés, ainsi que le risque de détérioration du substrat de ZnO ou de la couche de type p dûe à des températures de dépôt trop hautes ou à un effet de l'hydrogène pouvant diffuser du plasma.